Electron Microscopy Characterisation of Size-Selected Pd Clusters and Industrial Pd Catalysts

by

David Pearmain

A thesis submitted to the University of Birmingham for the degree of
DOCTOR OF PHILOSOPHY

Nanoscale Physics Research Laboratory

School of Physics and Astronomy

The University of Birmingham

January 2011

UNIVERSITYOF BIRMINGHAM

University of Birmingham Research Archive

e-theses repository

THE UNIVERSITY OF BIRMINGHAM

Abstract

This thesis presents an investigation into the morphology of palladium (Pd) size selected clusters and industrial Pd catalysts using high angle annular dark field scanning transmission electron microscopy (HAADF-STEM) technique. The driving force of this work is to establish reliable and efficient methods for the structural characterisation of nanostructures. The characterisation of nanostructures is essential to our fundamental understanding of cluster use within applications, such as catalysis. The complexity of the morphology of industrial catalysts presents a significant challenge to rapid screening techniques.

This thesis presents an efficient method which uses size selected clusters as mass standards in STEM based mass spectrometry. Size selected clusters were created using a radio frequency magnetron sputtering cluster beam source in conjunction with a lateral time of flight mass selector, Pd clusters were soft-landed onto amorphous carbon grids between the size range of N = 454 to 10,000 ($\pm 4\%$), with a deposition energy of 500 eV. The quantitative image analysis allows one to gain insight into each catalytic Pd particle and, in combination with two-dimensional diameter measurements, evaluate the three dimensional morphology of the particles.

The use of the cluster source has also allowed investigation into the formation mechanisms of nanostructures, finding specific size-dependant morphological features for Pd clusters. Elongation of Pd clusters has been observed for cluster sizes of ≥ 2000 atoms, as well as the onset of voids within the cluster structure for sizes ≥ 2622. HAADF-STEM analysis has proved to be an invaluable tool in the determination of cluster size, independent of morphology, as well as enabling specific structural features within clusters to be revealed. An investigation into the atomic structure of supported Pd_{887} clusters is also presented. Specific structural motifs are identified using aberration corrected STEM within the sample range via direct comparison with simulated HAADF-STEM images of structures simulated using global minimum techniques.

Acknowledgements

Contents

List of Figures

Authors Contribution

All of the electron microscopy and analysis presented in this thesis was conducted in the laboratory at the University of Birmingham and was carried out by myself.

Size-selected cluster sample preparation was performed co-operatively between myself and Ahmed Abdela, Feng Yin or Sunjin Park. Few samples were prepared without my presence in the laboratory, but on these occasions the samples were prepared by Feng or Sunjin. All catalytic samples were prepared by Johnson Matthey and sent to the laboratory for analysis. The preparation of these samples for microscopy analysis was then performed by myself.

Simulated Pd cluster work was performed by Andrew Logsdail and Prof. Roy Johnston. The simulated z-contrast images were then generated by myself using a MatLab script written by Dongshen He.

Abbreviations

ADF Annular Dark Field

AFM Atomic Force Microscopy

BF Bright Field

DF Dark Field

fcc Face Centered Cubic

FEG Field Emission Gun

HAADF High Angle Annular Dark Field

HCA Hemispherical Cluster Approximation

LECBD Low Energy Cluster Beam Deposition

MD Molecular Dynamics

RF Radio Frequency

SCA Spherical Cluster Approximation

STEM Scanning Transmission Electron Microscopy

STM Scanning Tunnelling Microscopy

sr Steradian

TEM Transmission Electron Microscopy

ToF Time of Flight

WPOA Weak Phase Object Approximation

Chapter 1

Introduction

The properties of matter at the nanoscale differ dramatically from that at macro-scales. To gain some perspective of how small 1×10^{-9} m (1 nm) is, it is useful to think of a size $1/100{,}000^{th}$ the diameter of a human hair. At this scale the structure and properties of materials change in comparison to that of the bulk. It is only recently that the tools to characterise, fabricate, or manipulate nanoscale objects (0.5-100 nm) have become available. Fabrication in this sense refers to the "top down" method of nanostructure creation; lithographic methods such as electron beam writing are capable of creating features down to the sub 100 nm range [1]. The manipulation of atoms to form nanostructures relates to the "bottom up" or "self assembly" approach where atoms and molecules are guided into organised structures through processes inherent in the manipulated system [1]. Complex structures are made by self assembly frequently in nature, but technology at present is not capable of reproducing such results and is limited to relatively simple systems [2]. However, recent times have provided large advances in the tools to characterise and study nanostructures. Methods such as Scanning Tunneling Microscopy (STM) [3], Atomic Force Microscopy (AFM) [4] and Transmission Electron Microscopy (TEM)/Scanning TEM [5], to name a few, can all be employed within nanoscale research to analyse structural features or characterise the size of nanostructures.

An aggregate of a countable number of atoms localised within a nanoscale volume [6] defines what is known as a "cluster". Clusters can contain any number of elements and their properties depend on the number of atoms, N, within the cluster. The atomic

arrangement and geometric structure are also dependant on this factor of N. Whilst it may be shown that for a cluster with a certain number of atoms a certain structure is energetically favoured, a group of clusters with an equal N, may show a range of structural forms [6]. Factors contributing to the atomic scale structure of any nanocluster include thermodynamics and kinetics. External factors, such as substrate condition or temperature may both contribute to vary the structure considerably [7].

Clusters are seen to have physical properties intermediate between atoms, molecules and bulk material [8]. They have many different technological applications ranging from protein immobilisation [9] to opto-electronics [10] but a large interest is taken in the use of clusters within catalysis [11]. This area has applications within industry due to an improved yield which results from an increase in the active areas of a material for any given reaction. An example of such an application can be found in fuel processing. Ten catalysts are required during the production of petroleum from crude oil, and an increase in efficiency of any of these process steps would save a considerable amount of resources. To make steps towards the improvement of such processes, controlled production and detailed characterisation of clusters is required, along with a deeper understanding of why particular atomic-scale structures of nanoclusters produce an improvement in catalytic activity [11].

Specifically, examples of where Pd is used within industry as a catalyst to accelerate de/hydrogenation reactions and petroleum cracking. There is a continual need for greater efficiency of catalysts. This may occur by improved catalytic design, making the catalyst more reactive for its purpose, this can be due to the structure of the catalytic particle and therefore the number of reactive sites on it suitable for application. In turn then, a challenge is to control the structure of catalytic particles. The lifetime of a catalyst is also an issue within catalyst particle efficiency, with catalysts becoming de-active or damaged by secondary processes in a reaction. For each potential improvement in catalytic design, the understanding of catalytic mechanisms requires the characterisation of catalytic particles in order to establish how the design of the catalyst may have suited the outcome of the reaction.

A prominent tool utilised in the world of materials science is the Transmission Electron Microscope (TEM) or Scanning TEM (STEM). It is a tool capable of structural analysis for the characterisation of newly developed materials or in this case, clusters. Many

different techniques are available within an electron microscope for sample analysis, for example, atomic resolution can be achieved in both STEM and TEM for structural analysis whilst electron energy loss spectroscopy offers insight into the electronic structure of samples. Advances in the synthesis of new materials would not be possible if not for the advances in the methods of characterisation. For example, the discovery of the carbon nanotube was first seen under an electron microscope [12]. The study presented in this thesis utilises High Angle Annular Dark Field STEM (HAADF-STEM) as a tool for the purpose of nanocluster investigation, in a detailed study into the world of catalytic and size-selected Pd clusters.

This thesis presents the development of nanometrology methods to characterise the size, in terms of number of atoms, N, and morphology of commercial Pd catalyst clusters, using size selected clusters as a mass standard in HAADF-STEM analysis. HAADF-STEM is also shown to be a useful tool in the characterisation of size selected cluster size, N, independent of its morphology. Investigation into structural features of size selected Pd clusters are presented, and the mechanisms of cluster formation for inert gas magnetron sputtered clusters are discussed in detail. A spherical aberration (C_s) corrected microscope is also employed for investigation into the size-selected cluster Pd_{887} to determine its predominant structural form when soft landed on an amorphous (a-C) substrate. The atomic resolution provided by a C_s corrected probe in STEM is key to help identify specific structural features which may exhibit specific properties for application as well as deepen our understanding of nanostructure formation. The methods of characterisation of structural features for both size-selected clusters and catalytic particles described in this thesis present a contribution to the industry of catalysis by the design of efficient characterisation methods. Both broad brush and detailed techniques have been developed and presented here. This is key to the understanding of catalytic processes at each stage of thier life time and can be employed through design production and use.

Chapter 2

Cluster Physics

2.1 Cluster Structures

The concept that structure determines function [9, 13–15] is appreciated across many disciplines. For example, in biology, the role of proteins in specific chemical pathways is determined by the way in which the biomolecules fold to form structures. The same concept is true for clusters. The aggregation of a given number of atoms within a nanoscale volume will produce a varied number of different structures and hence properties. There is a large amount of interest, both experimental and theoretical, regarding the study of clusters, spanning a variety of different elements such as Au, Pd, Pb, Al, Ni, Na or Ar, to name some examples [14]. This thesis is predominantly concerned with metallic clusters, specifically Palladium (Pd). A good review concerning cluster structure and function can be found by Baletto and Ferrando [14].

A cluster's structure is determined by the most energetically favourable configuration for any particular size, and is dependant on its surrounding conditions and formation kinetics. There is a wide range of structures available for any given cluster size. This is due to many different energy minima found close together, governed by the thermodynamics or kinetics of the clusters formation. The physics behind such processes is addressed in greater detail in chapter 3 and more specific formation mechanisms for size-selected clusters are discussed in chapter 6. Many theoretical techniques have been used to determine the growth sequences of various clusters at the nanoscale [16], but up until

today there is a considerable lack of experimental evidence to bridge the gap between theory and physical phenomenon. Although much work is done regarding the determination of cluster structure, three-dimensional imaging and reliable cluster production make for tricky experiments when trying to confirm exact theoretical predictions. Figure 2.1 shows a theoretical phase diagram of the structure of Au clusters. The diagram displays the basic phases of cubic crystal, decahedral and icosahedral structures which are commonly found within small cluster structure. However, other literature [17–19] would suggest that this is a simplified diagram, with many experiments showing many different structural regimes for any particular given size of a cluster.
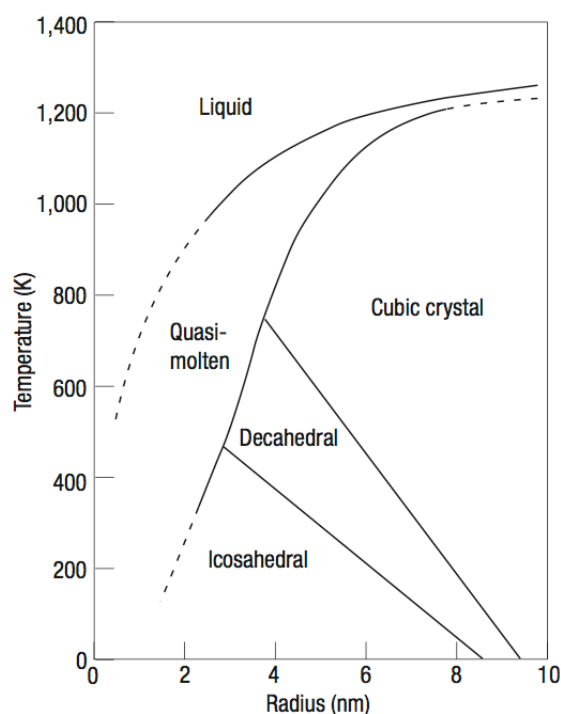
FIGURE 2.1: Theoretical phase diagram of the structure of small Au clusters [17, 18].

Before addressing the detailed quasi-spherical nature of cluster morphology it is important to note how the reduction in size for a given material permits structural variety. Crystallography and the development of X-ray diffraction has allowed the measurement of the periodicity of crystal structures found in bulk materials [20]. This periodicity is lost at the nanoscale. By taking a result from the spherical cluster approximation (SCA), which is to be discussed in greater detail later, we can show that the percentage of surface atoms to that within the volume is greatly increased approaching the nanoscale. The number of surface atoms in a cluster (N_s) is given by dividing the surface area of

the cluster by the cross sectional area of an atom. Thus, $N_s = 4N^{\frac{2}{3}}$ [21]. For example; the percentage of surface atoms compared to that of the entire cluster in Pd_{887} is 41% with an estimated diameter of 2.65 nm. A Pd_{10000} cluster has only 18% of its atoms situated at the surface, which is less than half that of the Pd_{887} cluster, and with an estimated diameter of 5.95 nm, it is still very much within the nanoscale regime. Now if we were to consider a bulk structure, say 10μm in diameter, when using the SCA this corresponds to 0.011% of atoms situated at the surface. It is then easy to see how one can class the role of surface atoms in bulk materials as negligible in many situations. On the nanoscale however, in order to maximise the surface to volume ratio, quasi spherical structures must have closely packed facets deviating from structures seen in bulk material. The number of atoms at the surface is therefore a key point in determining the structure of a cluster.

The binding energy E_b of a cluster of size N, can be written as: [14]

$$E_b = aN + bN^{\frac{2}{3}} + cN^{\frac{1}{3}} + d. \tag{2.1}$$

The first term represents a volume contribution and the other terms represent surface contributions such as those from vertices, facets or edges. The symbols a, b and c represent the contribution to each term for varying atomic arrangements and d is the empirical constant [14]. In any cluster, volume and surface contributions are in competition with each other. For example, clusters can optimise their surface to volume ratio by adopting quasi-spherical shapes if they have a low surface energy. It is also not possible to build up clusters with a spherical shape without internal strain, hence there has to be a volume contribution [14].

As mentioned previously, many different structural formations have been proposed for clusters of different sizes. Figures 2.2 and 2.3 display examples of structural motifs from fcc clusters to non-crystalline decahedral clusters.

A possible shape for a cluster resulting from the bulk fcc crystal structure is the octahedron. This structure has a high surface to volume ratio so does not optimise surface energy. Cutting the vertices of this shape produces a truncated octahedron (2.2). A
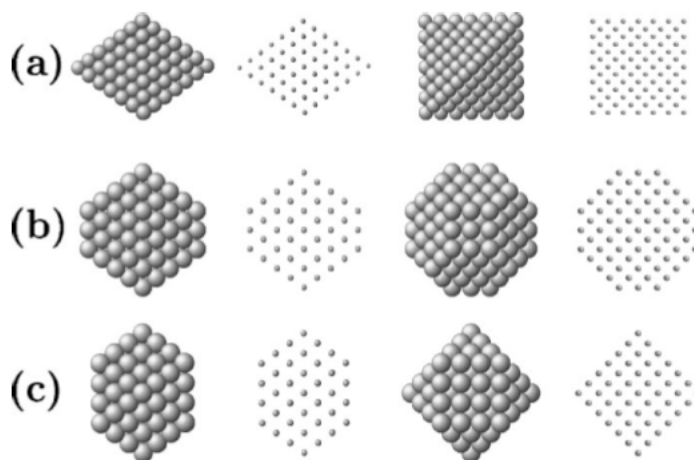
FIGURE 2.2: Fcc clusters (a) Octahedron - two square pyramids sharing the same basis with 8 triangular (111) facets (b) Truncated Octahedron (c) Cuboctahedron. Each cluster is shown in four views: On the left a hard ball model of the cluster is viewed from the side and second in from the right shows this model of the cluster viewed from the top down. The remaining images show the atom locations of the hard ball model in two-dimensional projection. Figure adapted from Baletto and Ferrando [14].

more quasi spherical structure that can be produced is the icosahedron. This structure offers low surface energy although it has high strain within its internal structure. Like the icosahedron, other non-cystalline structures have been proposed to form cluster structures. For example, at a particular size the internal strain within an icosahedron would no longer be favourable as an equilibrium structure.
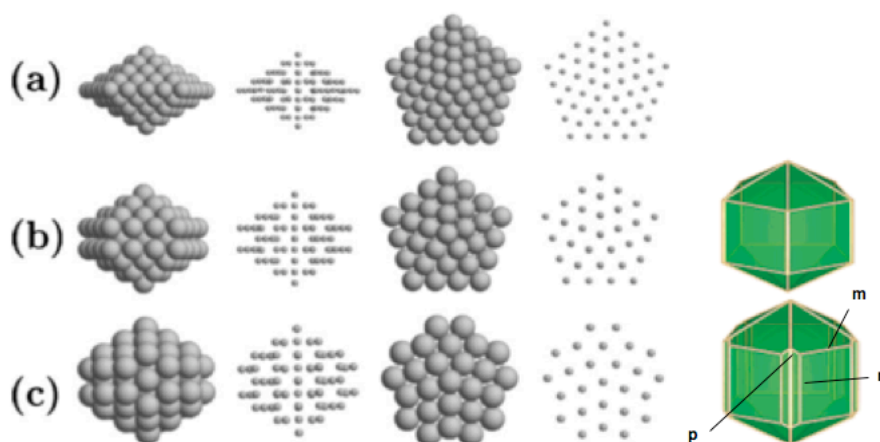
FIGURE 2.3: Decahedral Clusters (a) Regular decahedra (b) Ino-Truncated Decahedra (c) Marks Truncated Decahedra (See text for details). Each cluster is shown in four views and (b) and (c) have an extra image showing a clearer structural display. Source adapted from Baletto and Ferrando [14] and Barnard [22].

At this size, decahedral structures give less internal strain than that of the icosahedron.

For certain forms of decahedron, the surface energy is better optimised than that of octahedron structures. A decahedra is formed of two pentagonal pyramids. In 1969 Ino proposed a truncated version of the decahedron whereby the common pyramid base's size is reduced and (100) facets exposed. This served to improve the surface to volume ratio but the large (100) surfaces did not optimise surface energy. In 1984, Marks proposed an improvement on this structure by exposing re-entrant facets between each (100) face [14]. There is however, an associated strain with the decahedral motif of cluster structure. There is a volume contribution to the excess energy seen, particularly for clusters with large N, although the strain at these sizes remains smaller than that of the icosahedral motif. Johnson *et al* [23] studied the strain distributions of decahedral Au nanoparticles and Figure 2.4 illustrates how a cluster of a certain structure must contain strain or defects. The decahedron shown is made from five tetrahedral units, all with fcc structure and (111) crystallographic faces. The units share one edge with their neighbour, making the five fold symmetrical axis, and are joined together by twin boundaries. The right hand side of Figure 2.4 shows that tetrahedral units packed in this way do not complete the pentagonal projection, a solid angle remains of 7.35 degrees [23].
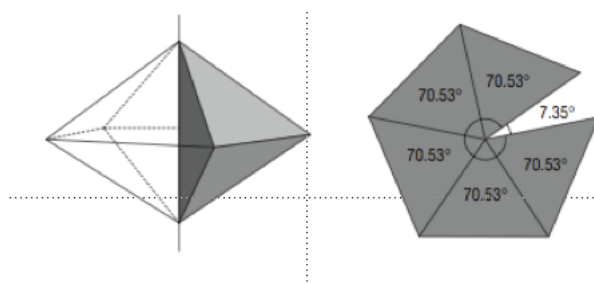
FIGURE 2.4: Left hand side: The tetrahedral units are shown shaded, they have (111) crystal faces and are organised around the verticle line which represents the five fold rotational axis. The light grey shades represent the (111) faces and the dark grey the internal twinned interfaces. Right hand side: Birds eye view down the (110) face of the decahedron. Perfect fcc tetrahedral units arrange together leaving a solid angle of 7.35 degrees. Consequently, real clusters must contain defects or be intrinsically strained. Figure taken from Jonhson *et al* [23].

In summary, the cluster morphology provided by fcc crystalline structures, such as the octahedron or truncated octahedron do not optimise surface energy and thus are less suitable for small clusters. Non-crystalline structures were then proposed with fivefold symmetry such as icosahedral and decahedral clusters which are able to optimise surface energy well by introducing closely packed (100) or (111) like facets [14]. It was concluded

in the review by Baletto and Ferrando that the icosahedral structure should be the most common at small sizes, truncated octahedrons at larger sizes and then truncated decahedral forms for the intermediate range. It has been stated previously how the periodicity of bulk material morphology is not present within nanoscale volumes, there does however exist an apparent periodicity for the cluster morphologies addressed so far. This is a "shell periodicity" and is apparent because the clusters grow with the addition of shells or layers of atoms [24].

The concept of geometric magic numbers is brought about by the completion of polyhedral shells for all the polyhedral cluster structures described previously. These full shells are considered to form a more stable structure. Many sequences exist for geometric magic numbers dependant on the specific structure in question. These can be found documented within the work of Martin [24]. Martin states also that the shell structure by definition may lead to confusion; for example, when thinking about the structure of a cube consisting of atoms placed at the sites of a simple cubic lattice. The first shell placed around a central atom will make a cube with three atoms on each side. In order to complete a second shell, 125 atoms are required, creating a cube with five atoms on each side. It is clear though that the cube with four atoms on each side has been overlooked, this can be solved by adding atoms to only half the surface of the core cube, thus creating the four atom sides [24]. This outlines the fact that a shell does not always constitute to a complete layer of atoms around the original structure, but only enough atoms added to retain the original symmetry.

One particular sequence covers non-crytalline icosahedra, Ino-truncated decahedra and cubotahedral fcc type structures. The number of atoms in each complete shell forms the numerical sequence; 1, 13, 55, 147, 309, 561 etc. The growth sequence for icosahedral clusters can be defined by the relation:

$$N(k) = \frac{1}{3}(10k^3 + 15k^2 + 11k + 3) \tag{2.2}$$

where N is the number of atoms in a cluster with k shells [24]. Figure 2.5 shows a graphical example of clusters with an icosahedral morphology as they increase in size with the completion of outer shells.
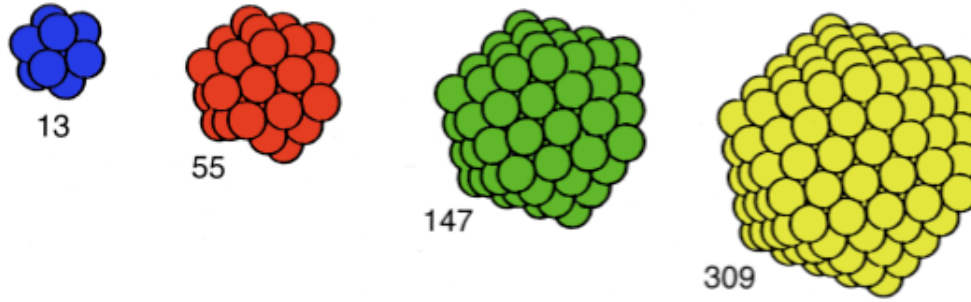
FIGURE 2.5: Models of icosahedral clusters with geometric magic numbers defined by the relation given in equation 2.2. Each different size corresponds to the completion of an outer layer of atoms. Figure adapted from reference [6].

A more complex relationship exists for the completion of full shells for the Marks decahedra [14];

$$
\begin{aligned}
N_{mdh} = \quad & [\frac{(30p^3 - 135p^2 + 207p - 102)}{6} \\
& + \frac{(5m^3 + (30p - 45)m^2 + [60(p^2 - 3p) + 136]m)}{6} \\
& + n\frac{(15m^2 + (60p - 75)m + 3(10p^2 - 30p) + 66)}{6}] - 1
\end{aligned}
$$

where m, n and p are integer indicies representing the lengths of the (100) facets and the depth of the re-entrant respectively and can be seen labelled in Figure 2.3 (c). Due to the delicate nature of the type of structure that a cluster of N atoms may form, and indeed, the small spatial difference between two similarly sized clusters, it is useful to use an approximate method of cluster size estimation. This is known as the spherical cluster approximation [21]. Prior to using the approximation it is vital to realise that the relation is an over simplification of the true physical scenario. The spherical cluster approximation is physically impossible within the real world since hard spheres cannot pack exactly into a spherical volume. As a concept though, the SCA does give a reasonable projection of cluster sizes and diameters.

The spherical cluster approximation is as follows; a cluster with N atoms is modelled by a sphere with a volume V_c;

$$V_c = NV_a, \tag{2.3}$$

where V_a is the atomic volume. In terms of cluster and atomic radii this becomes,

$$\frac{4}{3}\pi R_c^3 = N\frac{4}{3}\pi R_a^3. \tag{2.4}$$

The radius of the cluster is represented as,

$$R_c = N^{\frac{1}{3}}R_a. \tag{2.5}$$

Whilst shell sequences are extremely useful to identify sizes of stable cluster formation, there remain many structures that any cluster of N atoms may form, this has been outlined in previous discussion. It should be noted at this point that electronic magic numbers also occur in cluster formation, leading to stable sizes of clusters for specific elements [21]. Electronic structure is governed by delocalised valence electrons whereby the completion of outer electronic shell constitutes to a stable structure, this is closely related to the well-known nuclear shell structure [25]. An example of electronic magic numbers is given in Figure 2.6, taken from research performed by Knight *et al* [26]. The spectrum shows large peaks for Na clusters at sizes N = 8, 20, 40, 58 and 92, which corresponds to the closed electronic shell model. A rule of thumb for the closed shell structure of a stable cluster is that electronic magic numbers tend to dominate at smaller nuclearities and then geometric effects are more important for larger clusters [6].

Experimentally, the ability to produce clusters of N atoms accurately remains challenging, as well as the ability to accurately characterize the cluster morphology to a high degree of certainty. This thesis attempts to address some of these issues for Pd, and the remainder of this chapter looks into some of the structural studies of Pd and other materials both theoretically and experimentally.

Zhang *et al* [27] have studied the stability of palladium (Pd) clusters using density functional theory for N⩽13, with the comparison of several 1D, 2D and 3D isomers and selected structures at N=19 and 55. The results indicated that icosahedral structures are favoured over both decahedral and cuboctahedral for structures where N=13 and
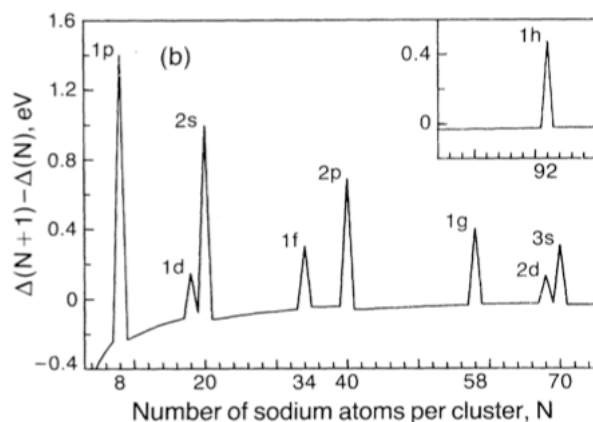
FIGURE 2.6: A figure to illustrate the electronic magic numbers as seen for Na clusters. The calculated change in electronic energy difference vs the cluster size, N. Labels on the peaks correspond to the closed shell orbitals of electrons. Figure taken from reference [26]. For more information refer to this reference.

55. Contrary to these results Watari and Ohnishi [28] found that at N=13 atoms, the cuboctahedron is more stable than the icosahedron according to density functional calculations. For larger sizes of clusters, results are few [14]. Kumar and Kawazoe [29] compared icosahedron with cuboctahedron and Ino decahedron clusters at N=55 and 147. The lowest energy for both cases was found to be slightly distorted icosahedral structures. Using tight binding calculations Barreteau *et al* [30] studied Pd clusters at N=309 and 561, finding that the icosahedron is still lower in energy than the cuboctahedron when N=309 but not at N=561. Global optimisation studies using the Sutton and Chen potential [31] for N up to 100 give the same results for Pd as for Silver (Ag), with icosahedron structure at N=55. Baletto *et al* [32] performed semi-empirical calculations to compare different material's (Ag, Cu, Au, Pd, and Pt) structural preferences for different size ranges of cluster. The favoured structure was found to be dependent on the metal in question. Cu presents a large window of sizes for decahedral preference but at small sizes up to N=100 favours icosahedral motifs. Au clusters on the other hand take up fcc structures for N>600, but with the marks decahedral motif favoured up to this point. Pd clusters are found to favour iscosahedral structure at small sizes and then the transition from decahedral to fcc is found at around 6000 atoms. It is interesting to note the preferential values for the integer indicies m, n and p of marks decahedral clusters. For all metals m=n is preferred due to these values making the cluster more spherical. For the indices p; at small sizes m=p, and at larger sizes p=m-2 or m-3 is preferred [32].

Theoretical calculations have also predicted structures that take on the form of less

conventional motifs. Structural predictions using the n-body Gupta potential have been performed for Au, Ni and Ag clusters of sizes 6, 7, 12, 14, 19, 38, 55 and 75 atoms by Michaelian *et al* [33]. The study finds the existence of disordered global minima for gold clusters with 19, 38 and 55 atoms. Clusters such as Au_{75} and other Ni and Ag clusters were found not among the global minima, but instead existed as low energy isomers. Of interest, is that this study suggests the disordered states of Au would most probably be results from cluster condensation from a gas or liquid, as is the case for the formation of size-selected clusters presented in this thesis. Doye *et al* [34] also found that many Zinc and Cadmium clusters with up to 125 atoms show no overall order. This is done by global optimization methods. It is found however, that many of the clusters are based upon distorted oblate Marks decahedra. The distortion in this case is the fusion of the re-entrant groove atoms.

Theoretical work carried out with more relevance to experimental work is done by Zachariah *et al* [35]. This study uses molecular dynamics simulations of silicon nanoparticles which form via particle-particle interactions at varying temperatures. Findings show that cluster morphology sometimes forms agglomerated or partially sintered structures formed by solid state diffusion mechanisms. These structures are far from the proposed general motifs of the icosahedron etc, but are important to note at this stage due to the nature of the formation of size selected clusters discussed in this study. It is apparent from the literature that the subject of disordered cluster structure is one relating to the many different possibilities of cluster formation mechanisms and the presence of many different global minimums and low energy isomers. The physics of such processes is mentioned in chapter 3, and then discussed in detail in chapter 6.

2.2 Structure of Clusters on Surfaces

Theoretical studies into the structure of clusters provides an excellent body of data and the knowledge to determine the application of clusters along with our fundamental understanding of nanoscale building blocks. In recent years, due to significant advancement in the application of experimental techniques, it has become possible to study cluster structure experimentally. When the structure under question is complicated, or the overall morphology is not well characterised, as is the case for clusters, X-ray diffraction

and electron microscopy techniques have become extremely useful in the last few years [18] (see chapter 4). However, in order to study clusters using these techniques it is often necessary to deposit them upon a substrate or support (see chapter 3). In the same way that it is difficult to determine how the interaction of ligands in passivated clusters deforms the atomic structure [36], it is also believed that the interaction between cluster and substrate could lead to a re-arrangement of the cluster morphology [21]. A prime example of this was found where a gold nanocluster on MgO support was seen to sink into the MgO surface after prolonged irradiation under an electron flux [37, 38]. It was found that the inclination of the cluster to sink into its substrate was dependent on changes to the surface free energy of the cluster, in this case, provided by the electron flux, but sinking could also be induced by chemisorption of impurities at the cluster surface.

The present study concerns Palladium (Pd). As a bulk material Pd belongs to the transition metals. It has an atomic number, Z, of 46 and forms a face-centred-cubic (fcc) structure [39]. The nearest neighbour distance is 2.76 Å [20] giving an atomic radius of 1.38 Å. There is evidence for contraction of Pd lattice parameter, and other metallic clusters bond lengths, for decreasing cluster sizes [40–42]. This is attributed to an increase in cluster surface stress. This has been found by Lamber *et al* [40] for small palladium particles of sizes 1.4 to 5 nm in diameter using electron diffraction. Bond length contraction has also been reported by Huang *et al* [41] for Au clusters of 3 to 5 nm in diameter. They state that due to surface atoms of clusters having fewer interatomic bonds than bulk atoms, they often relax and reconstruct when on two dimensional surfaces. From coherent diffraction patterns and molecular dynamics simulation they report bond length contraction of around 0.2 Å for edge atoms; around 0.13 Å for (100) surface atoms and only 0.05 Å for atoms in the middle of (111) facets. Free Pd nanoparticles with diameters of 1.2 to 5.4 nm have been studied more recently by Qi *et al* [42] using tight binding molecular dynamics simulations, finding a contraction of bond length for the outermost layers of atoms of 0.24 nm, irrespective of cluster size. The bond length for the core interior atoms was found to correspond to the bulk value.

Conversely previous experiments by Lamber *et al* [43] and Heinemann *et al* [44] report an increase in bond length for Pd nanoparticles on surfaces such as mica and carbon respectively. The former attributes the lattice parameter change to the incorporation of

carbon atoms from the amorphous carbon substrate into the Pd structure. In this case the Pd was evaporated onto the substrate. Other reasons proposed for the dilation of Pd lattice constant include; pseudomorphism [44], which can be descibed as an uncharacteristic cystalline form taken by the Pd as it assumes the form of the substrate it is upon, as well as the dissolution of oxygen within the Pd clusters [45]. Heinemann's work [44] finds an increase in the lattice parameter of 2.9% for clusters with a diameter of 1.5 nm, but for particles with a 5 nm diameter the lattice constant is believed to be that of the bulk value. This effect is attributed to a structural change due to a decrease in atomic packing density. It is of interest to note that pseudomorphism being accountable for the dilation is ruled out due to the lack of epitaxy from a unclean substrate surface. Oxygen presence is also ruled out as a cause due to tests that were run with exposure to oxygen atmospheres resulting in no measured lattice parameter change. In a theoretical study by Vervisch *et al* [46] experimentally observed pyramidal Pd clusters are modelled on a MgO (100) surface. The interesting result from this study is that a lateral dilation of the lattice parameter for Pd at the interface is observed, matching that of the substrate. As the size of the Pd cluster increases, the lattice mismatch becomes apparent once again as the dilation of the Pd cluster can no longer accommodate the small Pd cluster's structure.

Wang *et al* [47] used substrates such as TiO_2 and $SrTiO_3$ to deposit Au clusters finding that when annealed, the Au atoms substitute for cations in these systems thus altering the morphology of the cluster. Cluster deposition on amorphous carbon (a-C) substrates is discussed in more detail in chapter 3. Molecular Dynamic simulations performed by Kuo *et al* [48] show that Au cluster structure was strongly influenced by the substrate. The authors conclude that the structural characteristic of the Au shapes is not only a function of size, but also depends on the contact area with the surface. High-resolution electron microscopy has been utilised by Koga *et al* [49]. By annealing Au clusters at 1173 to 1373 K, over a size range of 3 to 14 nm in diameter using a helium bath, a structural change from icosahedral to decahedral motifs was observed just below the melting point, 1337 K, of the clusters. The formation of bulk crystalline structures from decahedral morphology requires a large energy barrier to be overcome, thus in order to achieve this transition it is stated that a melt-freeze process would be required.

An interesting approach to the structural determination of clusters is to utilise electron

microscopy techniques alongside direct theoretical modeling of the system for comparison. This has been done by Li *et al* [5] for Gold (Au) 309 clusters. Here studies using HAADF-STEM identified Au 309 clusters to have either Ino-decahedral, cuboctahedral or icosahedral structures. Comparison with simple kinematical imaging simulations and multi slice techniques assisted structural identification and suggested that there are a series of energy minima with small energy barriers between them, which govern the overall structure of clusters within this experiment. Similar techniques to this study have been employed for a size-selected cluster of Pd containing 887 atoms (Pd_{887}), and this will be presented within chapter 7. Of interest within the present study is to choose clusters of a size which may represent different geometry based upon theoretical predictions. This project has used clusters with the following sizes, N = (454, 887, 1103, 1389, 2046, 2622) $\pm$ 4%. These sizes were chosen as they represent Mark's Decahedral structures suggested by Cleveland *et al* [50, 51] and Jiang *et al* [52]. The theoretical cluster size predictions are in agreement with each other across these different works. Energy-minimisation [50], many body potential [51] and Lenard-Jones potentials [52] have been used to calculate the Marks decahedral magic numbers respectively. The sizes of clusters chosen have been identified within this study to have a theoretical closed shell structure. This was confirmed utilising the equation for Marks decahedral magic numbers mentioned previously. For clusters larger than that of N = 2622 no theoretical structural motif has been followed. This is because the mass resolution of the time of flight cluster source used in this study (see chapter 3) would produce an associated error in N for clusters above this size, which would correspond to many structural motifs. For example, a cluster with N=4500 would have an associated error in N of $\pm$ 180 atoms, meaning that the variety of cluster sizes produced could not be attributed to any specific structural motif. Clusters with N= 3000, 3500, 4500 and 10000 have also been studied in this size range.

Another investigation which bridges the gap between theory and experiment can be found in the work of Ascencio *et al* [53]. Again, multi-slice simulations, fast fourier transforms and high-resolution TEM images are used for the structural determination of small particles through comparison. Images of gold clusters with fcc, decahedral, icosahedral and amorphous structures are reported. The study discusses the fact that other investigations into the structural characterisation of clusters, only look at the most common orientations of cluster, as upon a substrate surface, particles will be inevitably

be orientated at random. Very often this will lead to one of the low index crystallographic planes not being parallel to the electron beam and hence be harder to identify.

Experimentally Jose-Yacaman [54] investigated thiol-passivated Pd nanoparticles by transmission electron microscopy. Clusters ranged from 1-5 nm in diameter and a variety of structures were seen. It is thought that the use of alkyl thiols to passivate the clusters does not alter their morphology, it does however produce distortions along some crystal planes. Structures ranged from icosahedral, to fcc, to decahedral forms. Figure 2.7 shows a series of HRTEM images taken of Decahedral Pd clusters. Each micrograph is taken to show different orientations about the five fold axis parallel to the electron beam and it is interesting to see how the cluster image projection changes with orientation.
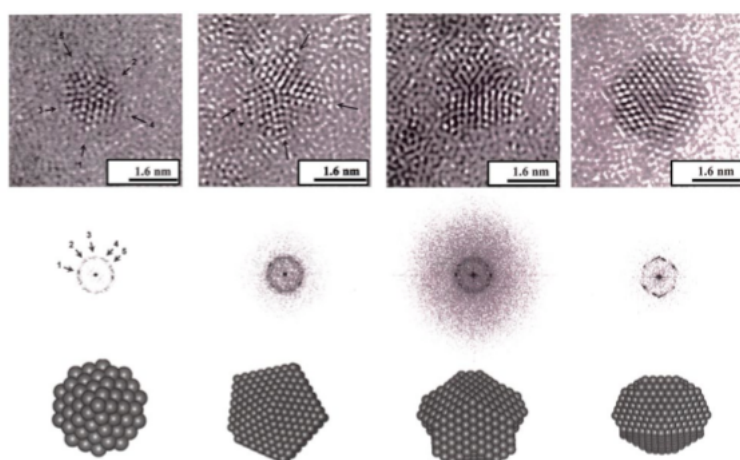
FIGURE 2.7: Decahedral Pd particles taken at different orientations about the five fold axis parallel to the electron beam. FFT's are also shown and models are displayed to show the orientation of the cluster in three-dimensions. Figure taken from Jose-Yacaman *et al* [54].

In many occasions the FFT of imaged Pd clusters was undefined and noisy. For these clusters no real order and geometry could be established. These clusters were said to have an amorphous structure and can be seen in Figure 2.8.

Soler *et al* [55] have studied the amorphous structure of metals, specifically Au, finding that amorphous structures are found even for closed shell sizes for which very ordered structures are thought to exist. By analysing the local stresses in clusters, the study concludes that the tendency of metallic bonds to contract at the surface, due to a reduced co-ordination number, is the primary factor that favours the amorphization of the cluster structure.
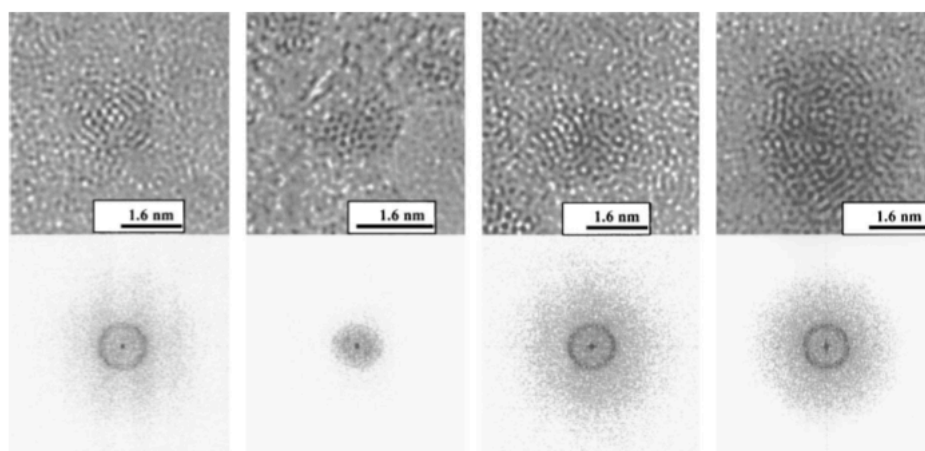
FIGURE 2.8: HRTEM images of amorphous Pd clusters, the corresponding FFT is shown for each case. Figure taken from Jose-Yacaman *et al* [54].

Problems associated with accurate measurement of true cluster structure on any substrate using TEM/STEM methods is that the structure may be changed under the highly energetic electron beam. Iijima *et al* [56] found this to be the case for clusters under 5 nm in diameter deposited on crystalline silicon. The evolution of the structure is reported to have slowed under the electron beam when deposited onto a-C substrates. Baston [57] also reports the movement of single Au atoms on graphite under an aberration corrected scanning transmission electron microscope beam, and Yacaman *et al* [54] discussed how an interaction of the cluster with an electron beam may induce a structural change. An excitation would not be required to be of a large magnitude due to the many local minima configurations which correspond to different structures.

2.3 Motivation and Application

Precise control in the synthesis of nanomaterials such as clusters, alongside accurate characterisation techniques will ultimately enable the association of structure with biological, chemical and physical properties [58]. The motivation is therefore the ability to produce structurally monodisperse clusters suitable for the given application and understand their formation mechanism [59, 60]. In order to do this structural characterisation is needed. Pd clusters show potential in a variety of technological applications including, hydrogen storage [61] and hydrogen detection devices [62]. But perhaps one of Pd's

most significant applications will be that of catalysis, not only for Pd but other metallic clusters also [7].

An entity that accelerates a chemical reaction without being consumed is the definition of a catalyst [58] and plays an important role in many processes that govern our everyday lives. Catalysis at the atomic level has been realised both experimentally and theoretically in recent years. Specifically, Starchevsky *et al* [63] have found Pd 561 clusters in solution to undergo lower alcohol oxidation at room temperature, giving a range of products. In this case, the surroundings were essential to the catalytic process. Ahmadi *et al* [64] highlight the importance of the size and shape of the cluster in its suitability as a catalyst. Their experiment into colloidal shape controlled growth of Pt nanoclusters begins to study the means to reliably create a structure displaying useful catalytic properties. Hvolbaek *et al* [11], in agreement with Ahmadi, state that the main scientific and technological challenge with the use of nanoparticles as catalysts is the understanding of how the atomic scale structure produces the best catalytic activity. Also stated is that the ability to synthesize these particles with maximum control over the structure, is equally important. This study performed density functional theory calculations and showed that Au structures with atoms at low-coordinated sites have increased reactivity for oxidation reactions. These reactions, intriguingly, were done at temperatures at or below room temperature. Their work states that not all factors that may affect the increased reaction rates at atomic level have been considered or understood, but a main affect discovered.

Other factors such as electronic effects can modulate the effect of a clusters catalytic activity for clusters below 1.5 nm in diameter [65, 66]. However, as already discussed, the most apparent factor to determine the catalytic activity of metalic clusters is dependent on the number of reaction sites provided by the structure [11, 67, 68], and this in turn is determined by N. Hence, with knowledge of the reactivity for catalytic clusters used within industry, the characterisation of such clusters could begin to determine experimentally the particular size of cluster that produces high catalytic activity. Currently, little data exists bridging the gap between reaction rates and the size of a cluster in terms of the number of atoms it contains outside that of theoretical simulations. Experimental work that has been done in this field using X-ray diffraction and TEM to characterise Pd catalysts prepared by chemical reduction methods. A study, performed by Gniewek

et al [68] characterised the clusters in terms of morphology and diameter, finding that smaller Pd nanoclusters were more chemically reactive. Chapter 5 of this thesis tackles this problem, a new technique for the efficient characterisation of catalytic Pd particles is presented and a more detailed review of the subject area given.

2.4   Conclusion

The experiments and investigations within the present study address the motivations for cluster research. Theoretical simulations of cluster structure, on the whole, appear limited to N < 100 atoms. Experimentally using high-resolution TEM it is evident that a variety of cluster structures can be determined for a range of measured diameters. This project however, provides a unique opportunity to study cluster morphologies with a pre-knowledge of the number of atoms contained in a cluster (see chapter 3). Thus it may be possible to offer clues between theoretical simulations for N atom Pd clusters and their physical structure. The range of cluster size experimentally is also far less limited than that of theoretical simulations.

Much research into clusters has found that achieving the correct thermodynamically stable structure can be difficult. On experimental time scales rather than thermodynamics, it is often kinetics that obscures the stable state of a cluster [14]. This does not mean though, that we cannot perhaps control the cluster structure and hence its properties. Schebarchov and Hendy [69], in a theoretical study, report structural control with respect to temperature. They report structural transitions of Pd clusters from decahedral to icosahedral structures near the melting point over a range of sizes from N=561 to several thousand. This was performed by molecular dynamic simulations.

Mass selected cluster beam deposition has been utilised in the experiments presented in this thesis (see chapter 3). This process itself offers scientific questions which need to be answered before true characterisation of cluster structure and size can be determined. Questions such as, is the gas phase cluster structure maintained exactly upon landing on the substrate? Or, are produced structures governed by deposition thermodynamics or kinetics? The following chapters will discuss the methods of imaging and cluster deposition used within this research.

The characterisation of clusters, experimentally, may involve large errors, and accurate three dimensional imaging at the nanoscale is hard to achieve to any degree of certainty. The understanding of cluster structure property relations in nanoscience requires progress so as to make technological advances in areas such as catalysis. Methods to characterise clusters are required and further experimental investigations into structure are needed. This thesis presents an insight into investigations towards the characterisation and reliable production of Pd clusters as is required in the field.

It is widely believed that an integral step towards technological application of clusters is to be able to produce clusters with full control over size, shape and uniform structure [53]. Hence there is a requirement for the full characterisation of such variables. Electron microscopy is utilised within this study in the development of techniques to achieve these goals.

Chapter 3

Cluster Production

3.1 Methods of Cluster Production

Development in the understanding of nanocluster properties is highly dependant on the technology and methods available for their production. Unless studied in the gas phase as free clusters [14], there is a requirement to support the nanoclusters by deposition on a substrate for analysis. Many technologies exist to satisfy such a requirement and include cluster beam methods, atomic vapour deposition and wet chemical techniques.

For size selected cluster samples presented within this thesis, the clusters are formed in the gas phase prior to deposition [25] and then combined with cluster beam mass selection technology [70] before being deposited upon the surface of a substrate. Cluster beam methods of production allow the morphology of the cluster to be formed prior to interaction with the substrate surface, examples of which include laser ablation [71], seeded supersonic nozzle sources, and sputtering [25]. This chapter's aims are two fold: to give an overview of cluster production methods and the physics behind their formation; and to present the methods of cluster production for clusters used within this study. Size selected Pd cluster samples investigated within this thesis have been prepared my myself with invaluable assistance from colleagues at the laboratory. Industrial Pd catalytic samples were prepared by Johnson Matthey and sent to myself for deposition onto TEM grids and analysis.

3.1.1 Atomic Vapour Deposition

One approach to cluster production is by atomic vapour deposition [72, 73]. A large amount of control within this process is given to the production rate of deposition and surface temperature of the substrate. Other factors which can control the size of cluster formed within the production of the vapour is the atmosphere in which it is produced [73]. Thermal evaporation or plasma sputtering are two common forms of vapour deposition, and tend to produce a wide size distribution of clusters on the deposited surface. This is sometimes due to aggregation of clusters post deposition upon the substrate. For instance, Au clusters produced by thermal evaporation and deposited onto an amorphous carbon (a-C) substrate were found to be hemispherical in morphology and have a range of sizes from 2 to 5.5 nm [74]. Figure 3.1 (a) shows a TEM image of clusters prepared by this method. The size distribution can however be controlled using lithographic masks, for example, by using nanosphere lithography clusters of Ag were tuned from 21 to 126 nm in diameter [75]. Size control has also been achieved through the use of lasers. In a study by Bosbach *et al* [76] Ag clusters with a broad size distribution were deposited on quartz substrates. The width of the size distribution was able to be reduced by 40 % through irradiation of the clusters with short laser pulses. This was achieved by tuning the laser to a frequency that only the smallest and largest clusters would absorb. Deposition by thermal evaporation can be used in the production of thin films [77] which are essential in many lithographic techniques and other applications.

3.1.2 Liquid Phase Chemical Methods

Perhaps the most widely used method of cluster production is to synthesize clusters in solution. For example, for seed mediated growth, metal clusters are produced by reducing metal ions with a suitable agent [78]. The seed clusters can then to added to growth solutions, which may contain other metal ions and other additives such as ligands, which then allows the nanocluster to grow via nucleation at the surface of the seeds. Once growth is complete the solution can then be dropped onto a substrate which will then evaporate leaving clusters upon the substrate surface. Such methods can easily produce bi-metallic particles [79] allowing more diverse research into nanocluster properties. Lin

et al [80] utilised the advantages of wet chemical methods by adding dodecanethiol ligands around nanoclusters to fabricate nanoscale structures such as superlatices. An example image of nanoclusters produced by wet chemical methods can be found in Figure 3.1 (b).

The main advantage of deposition of clusters formed in a solution is that a large amount of clusters can be deposited in a short time period and are under equilibrium conditions [21]. The material involved can very often be reduced much quicker than using physical methods as discussed in section 3.1.4. Disadvantages of this method are that the clusters may have residual surfactants/impurities present upon their surface present from the solution that they were formed in [21]. As mentioned previously, clusters can be passivated with ligands in order to prevent aggregation, and minimize cluster-surface interaction. However, the presence of ligands also inhibits the direct application of these clusters to catalytic reactions [81]. Many methods have been developed to instigate the removal of the surrounding ligands from a cluster. For example, the electron beam from a scanning electron microscope (SEM) can be used to burn off ligands from Au clusters [82] and other methods such as UV-ozone cleaning [83] have also been employed.

3.1.3   Self Assembly

Self organisation is seen around us in our daily lives. It is apparent in the growth of any living organism, whereby the coding in the DNA enables the formation of cells and proteins without control from any external means. The principle here is to provide conditions for the system or material being used to "let nature do it herself" [85]. Nanostructures can then be formed by spontaneous organisation; the constituents arrange themselves in order to minimise surface energy, thus providing an organised pattern. For example, structure in the growth of Ge nano-crystal islands on a Si(100) surface is able to be controlled by the coverage of the Ge deposits and the temperature at which the growth occurs [85]. A substrate surface can be used to create organised superlattices of clusters, Al_6 atoms occupying specific regions on a Si (111) 7 by 7 surface is a prime example of this [85]. Other examples of substrates being used with clusters of specific properties to self organise nanostructures is the nucleation of C_{60} to the naturally occurring steps present in highly ordered pyrolytic graphite (HOPG) [77]. The diffusive

(a)

(b)
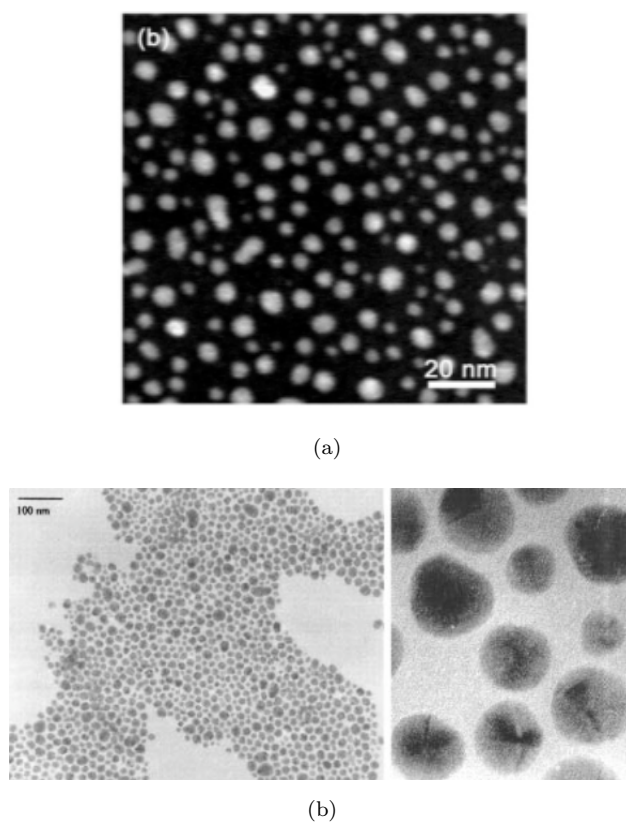
FIGURE 3.1: (a) HAADF-STEM image of Au nanostructures formed by atomic vapour deposition of Au onto a-C [74] (b) TEM image of Au/Ag alloy colloidal clusters [84].

properties of C_{60} have also also been used to assist the growth of Au nanowires by Young *et al* [86]. Au atoms were transported by the C_{60} molecules to step edges by increasing the diffusive length of the materials through heating. The methods described so far in this section refer to self-assembly of nanostructures at surfaces, self assembly within the gas phase also occurs when forming clusters using cluster beam methods. Gas phase formation mechanisms are discussed later on in this chapter and in chapter 6 of this thesis.

An advantage to these methods is that they are highly suited to industrial application, however, the structures produced are often limited to the the specific circumstances in which they are produced. For every possible application the surface functionalisation of the material in question determines the interaction it will have with its environment, which in turn enables oragnised assembly [87].

3.1.4 Cluster Beam

Many different types of cluster beam techniques are in operation within nanoscale research and this section looks into specific types of cluster sources in common use. The physics behind each cluster beam method shares common themes with the cluster source used to create samples studied in this thesis. A detailed description of the cluster source used for the present study can be found in the next section of this chapter. Each cluster beam type has its own drawbacks, but all cluster beam technology has significant strengths in certain aspects of cluster production. Key characteristics of cluster beam production are as follows; clusters are not passivated allowing direct experimentation of their catalytic activity; the beam position can be altered for specific cluster patterning of surfaces; and similarly, the cluster density deposited on a surface can be controlled by altering the deposition flux; furthermore the morphology can be controlled to an extent by manipulation of the deposition energy. Perhaps the most significant advantage though is that cluster beams allow size selection techniques to be applied to them. Figure 3.2 displays an example of Pd clusters produced by cluster beam technology and size selected using a time of flight mass selector.
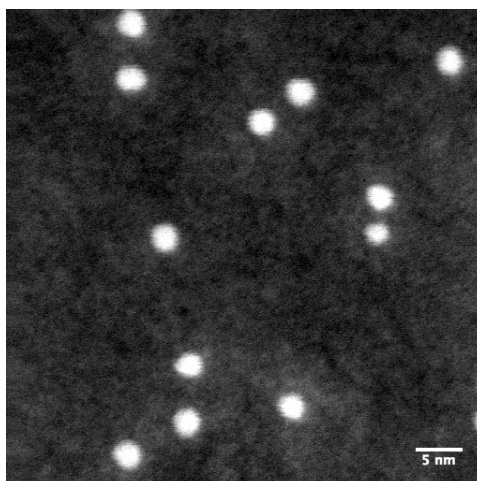
FIGURE 3.2: HAADF-STEM image of supported Pd nanoclusters obtained from a cluster beam source. Clusters formed in the gas phase via radio frequency magnetron sputtering and size selected to have 887 ± 35 atoms using a time of flight mass filter.

3.1.4.1 Gas Condensation / Nozzle expansion

Cluster production in the gas condensation source begins with the heating of the cluster material in order to create a high pressure vapour. An inert carrier gas is added such

as Ar or He to promote cluster condensation [88]. The metal vapour and carrier gas mixture is then expanded through a small nozzle via a large pressure gradient. This is where the term "supersonic nozzle source" comes from [25]. The supersonic expansion of the clusters into the vacuum is an adiabatic process, and thus promotes cluster cooling. Super saturation then allows the condensation of the metal vapour to form clusters, and clusters will form until the quickly expanding vapour density becomes too low.

The sizes of clusters produced using this set up can be varied. When no carrier gas is used, small clusters up to tens of atoms are produced. When a carrier gas is used however, the mass of its constituents influences the size of clusters produced. For example, a heavy gas will be slower providing more time for the aggregation process, promoting larger cluster growth [88]. Cluster sizes can also be influenced by the alteration of temperature (i.e. evaporation rate), carrier gas pressure, and growth distance [89]. This type of source is limited to materials of relatively low melting points, and the difficulty in material evaporation rate regulation means that the cluster beam intensity can vary during cluster production.

3.1.4.2   Laser Ablation

The laser ablation cluster source uses a high powered pulsed laser that is directed onto a target material. The laser pulse induces surface melting of the target, and then in turn vapourises and ionises the material. The ablation of atoms and clusters from the target surface is a simultaneous event with a pulse of inert gas. Although some clustering occurs from the plasma plume created by laser ablation, the carrier gas is able to induce more collisions between ablated atoms and the gas, thus allowing larger clusters to form. Using the same principles as the gas condensation source the cluster and gas mixture then undergo supersonic expansion. In order to ensure the same condition of the target, and hence ablated cluster yield, between each laser pulse the target is rotated or moved to find a new area of unused target surface. The use of laser ablation techniques for cluster generation produces both ionic and neutral clusters and it provides a stable, high cluster density beam. Pulsed lasers are used as this type of laser can achieve energy densities of a far higher magnitude than that of a continuous beam [81]. This type of cluster source is very versatile and is capable of producing a wide range of cluster sizes. One of the main drawbacks of this process is the extensive cost of the high power lasers required. A

more detailed introduction to the working of laser ablation cluster sources can be found
in references [25, 88].

3.1.4.3 Ion Sputtering

High energy incident ions when bombarded against any target surface cause a domino
effect of atomic collisions within the target material. The result is that many atoms and
small clusters are ejected from the surface. This is the principle of an ion sputtering
source which accelerates heavy inert gas ions with energies from 10 to 20 keV towards
the target material [25]. The incident ion beam angle can be adjusted in many cases to
optimise the cluster flux achieving higher yields [89]. In this case high purity clusters are
produced as there is no carrier gas used, thus making the ion sputtering cluster source
suitable for ultra high vacuum (UHV) set up [90].

Ion sputtering techniques have been improved upon in recent years with the development
of magnetron sputtering [81]. This is where a plasma is ignited over the target material
by applying a DC or RF potential to the target. The plasma is confined by magnetic
fields and ions are accelerated into the target resulting in sputtering. Plasma sputtering
methods have improved the cluster yields from standard ion sputtering techniques by
ensuring a large area of the target is sputtered, even with less acceleration potential.
Magnetron sputtering is the technique employed in this study for the creation of size-
selected clusters; a more detailed overview of the Birmingham cluster source can be
found in the next section of this chapter.

3.1.5 Mass Selection

After clusters have been produced there is a need to determine the size range of clusters
within the cluster beam, be it for apparatus develpoment or experiments directly with
the cluster beam. It has been discussed previously in chapter 2 that the size, N, of a
cluster can determine its physical properties. In which case it is necessary to select a
certain size of cluster for further investigation. In order to be able to do this, clusters need
to be ionised, if this is not already the case from the cluster formation mechanism, then
electron beams or lasers can be used to perform this function [91]. A thorough review

of the types of mass analysers can be found in the work of de Heer [25]. Types of mass selection devices in use within cluster beam sources include Wien filters, quadrupole mass filters and time of flight mass selectors. Full details upon the workings of these devices is behond the scope of this thesis. The latter however, is implemented within experiments presented in this thesis, this type of mass selection will therefore be discussed in the next section which provides an overview of the cluster source used.

3.2 Cluster Source Overview

A radio frequency (RF) magnetron sputtering gas condensation cluster beam source with mass selection has been used for the purpose of cluster production at the Nanoscale Physics Research Laboratory. This instrument is capable of reliably producing size selected clusters for a range of materials under controlled conditions, making it ideal for the experimental methods required. This is due to the control over the energy of the deposition (as will be discussed in the next section) and the ability to deposit upon standard 3 mm TEM grids. This chapter provides a short summary of the basic principles involved with this type of cluster production. A schematic of the system can be seen in Figure 3.3.
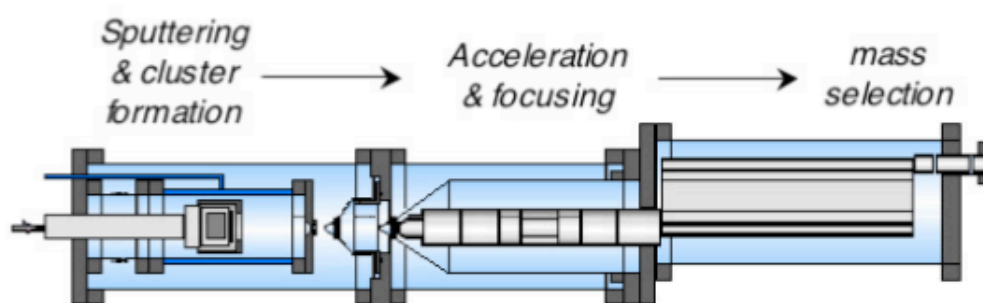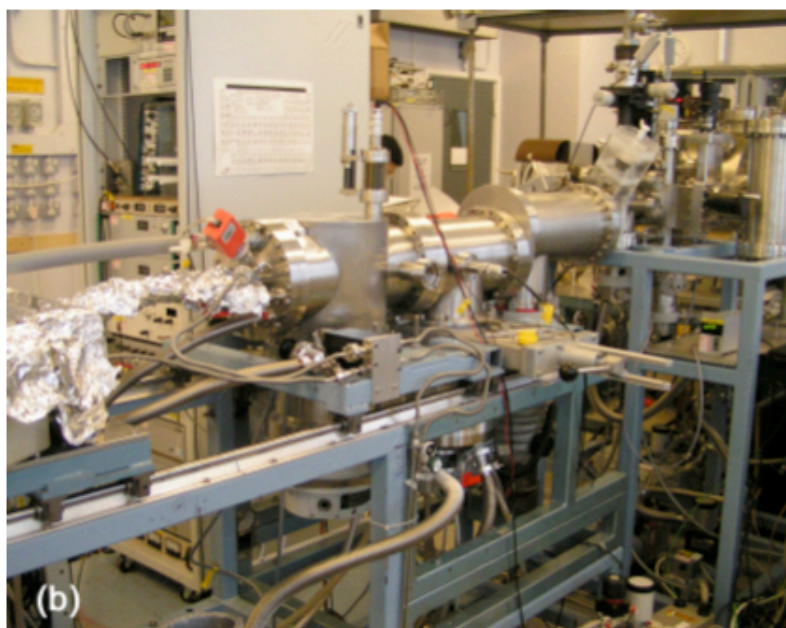
FIGURE 3.3: The Birmingham magnetron sputtering gas condensation cluster beam source. a) Schematic showing the three main chambers of the system. From left to right these are responsible for cluster generation, acceleration and focussing and time of flight mass selection respectively. b) Photograph of the laboratory set up. Both the figure and caption have been taken from the PhD thesis of N. P. Young (2007) [6].

3.2.1 Sputtering Cluster Formation

Clusters investigated in the experiments within this study are formed through RF sputtering and gas condensation techniques. RF sputtering has great advantages over other cluster production methods: There is flexibility of the target materials that can be used, and this does not rely on melting temperatures being reached, which means a wide range of cluster types can be studied. As sputtering produces a large quantity

of small clusters, when combined with gas condensation a whole range of cluster sizes are available. Plasma sputtering also produces ionised clusters, thus negating the need for an ionisation stage, as is needed with some sources. Figure 3.4 shows a simplified schematic of the formation chamber within the cluster source. The grey and white area on the left of the image contains the target material (Pd), a high strength magnet, a cavity that is used for water cooling, a magnetron head, shielding and Ar/He gas flow lines. A mixture of Ar and He gases are injected near the Pd target and ignited as an RF plasma. By definition, a plasma is a condition of matter containing freely moving charged particles [92], in this case, electrons and Ar^+ ions. A high voltage RF signal is applied to the isolated Pd target, and by nature will fluctuate between a positive and negative potential. During the positive part of the RF cycle electrons are attracted to the Pd target, and vice versa for the Ar^+ ions during the negative cycle. The mass of the plasma constituents is vital here, the electrons have less mass than the Ar^+ ions and therefore have a greater mobility within the plasma. Therefore, the overall result of the RF cycle is that the Pd target builds up a net negative bias. The bias on the target can be varied by the applied voltage, power to the magnetron and applied frequency [93]. When the potential difference is large enough Ar^+ ions are accelerated to the target causing sputtering. During this process the plasma is confined above the target surface with a strong magnetic field.

Sputtering can be thought of as a cascade of collisions in the target material due to an impinging ion. The breaking away of atoms from the target surface is due to the energy of the collision and some atoms being given a velocity component in that direction [94]. The sputtering process creates small clusters and atomic species, but the larger cluster formation process is induced by the flow of He gas into the formation chamber [93]. The He gas cools the sputtered Pd atoms allowing them to nucleate into small clusters within the dense atomic vapour produced. These smaller "seed" clusters are then able to form larger clusters via further collisions and aggregation. The principles of this process are discussed in greater detail in a later section of this chapter. Many of the clusters within the formation chamber are ionised by the presence of a plasma allowing them to pass to the mass selection stage without further ionisation.
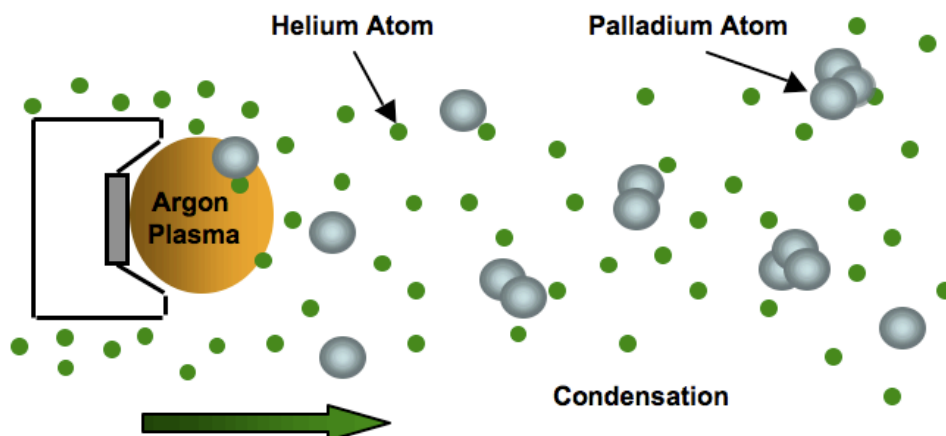
FIGURE 3.4: Formation chamber within the Birmingham Cluster source: RF magnetron sputtering and gas condensation. Argon ion bombardment of the Pd target causes sputtering with the He gas promoting cluster formation

3.2.2 Acceleration and focusing

All sections of the cluster source are differentially pumped. The operating pressures of chambers decrease progressively from cluster formation to deposition. Pressures of 0.02-0.03 mbar to $\approx 10^{-7}$ mbar are reached, respectively. This pumping creates a pressure gradient within the apparatus which transports the clusters into the ion optics chamber. The cluster beam is supersonically expanded via a nozzle at the end of the formation chamber, which halts the formation process of clusters. The nozzle is adjustable thus allowing control over gas pressure and flow rate. Positively charged clusters then pass through two skimmers and are accelerated by an element with high voltage (extractor plate) in order to attract as many of the cluster ions as possible. Ion optics consisting of two einzel lenses and x-y deflection plates [93] then focus the beam.

3.2.3 Mass Selection

A time of flight mass filter is utilised to achieve mass selected clusters from the cluster beam. In simple terms, this is done through high voltage pulses applied for a pre-determined length of time to the cluster beam in order to displace it in a perpendicular direction from its original course of travel. Plates are positioned parallel to the direction

of travel of the cluster beam at the top and bottom of the chamber , as displayed in part (a) of figure 3.3. Upon cluster beam entry, the plates within the mass selection chamber are biased to the same negative potential corresponding to the cluster beam energy. A high frequency high voltage switch is set to both top and bottom plates. The bottom plate is used to provide a perpendicular acceleration pulse to the cluster beam. The plates potential is raised to zero for the duration of this pulse. All plates are then restored back to the beam potential, allowing the accelerated portion of the cluster beam to drift upwards through the central field-free region of the chamber. The upwards motion of the cluster beam is then halted by an identical pulse as the first, but applied to the top plate. The time that it takes any cluster to travel from the accelerated region to the deceleration region is dependant on its mass. Therefore the time between the two pulses defines the mass of the cluster allowed through to the deposition chamber.

The mass resolution of this selection technique is constant over the entire mass range. The mass resolution for size selected clusters presented in this thesis is M / Δ M $\approx$ 12. Thus for example, a Pd_{887} cluster denotes a Pd cluster containing 887 ± 35 atoms. This value was calculated by recording a mass spectrum for Ar_1 during the deposition of samples used in this study. Figure 3.5 displays this data. The plot shows measured beam current as a function of atomic mass units for the cluster source when tuned to produce single Ar atoms. The atomic mass unit for a Ar is 39.948, and it is shown in Figure 3.5, that the maximum beam current is achieved at this point, with a distribution around this value. By taking the full width at half maximum of the peak and dividing it by the maximum value one can obtain the mass resolution (as stated above) of the cluster source at the time of sample production. Theoretically the mass resolution is related to the physical properties of the time of flight mass selector by the equation [95],

$$\frac{l}{\Delta X} \approx \frac{M}{\Delta M},$$
(3.1)

Where l, is the vertical distance travelled by clusters within the time of flight chamber and is a fixed physical value, and ΔX is the diameter of the exit aperture from the time of flight chamber. This equation, however, is only theoretical as it assumes that the cluster beam is focused to a sharp point. In reality the beam width is dependent on the formation variables and the settings within the acceleration and focussing chamber,

as well as the bias applied to the third einzel lens just before cluster deposition (see next subsection). Equation 3.1 does however give a good idea of the limiting factors to the mass resolution that can be achieved with the cluster source used to create samples within this thesis. The size of the exit aperture can be adjusted to alter the resolution achieved. However, reducing the size of this aperture will result in a loss of the amount of clusters of a specific size being deposited upon the TEM grid. Also the area of the TEM grid exposed to the cluster beam will be reduced, limiting the area of interest to investigate within the TEM. Discussion as to the development of the time of flight mass selector and intricate details in how the resolution may be improved are beyond the scope of this thesis.
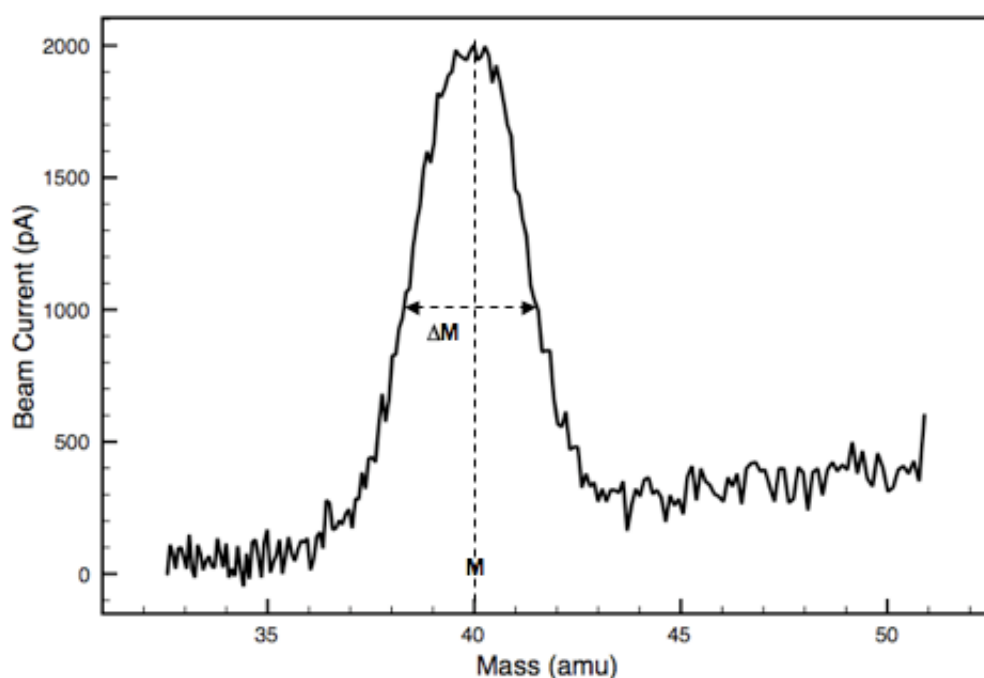
FIGURE 3.5: Mass spectrum of Ar_1 taken during the creation of size-selected Pd cluster samples used within this thesis. Plot is used to calculate mass resolution of the cluster source at the time of sample deposition, see text for details.

3.2.4 Cluster Deposition Chamber

Prior to leaving the mass selection chamber the beam is focused by a third einzel lens [93]. The beam then passes through to the sample holder which is held at a negative bias. The magnitude of this bias determines the deposition energy of the clusters on the substrate. The energy range over which clusters can be deposited is from 500 eV to 1500

eV, and the deposition energy will be varied subject to the needs of the experiment (see section 3.4.1). The sample holder is capable of holding ten different 3 mm TEM grids at a time. This is useful as each one of the size selected cluster samples involved in a specific experiment was able to be produced under the same conditions, as ten samples can be made in each batch.

At the base of the substrate holder is a Faraday cup which can measure the cluster beam current. This is typically measured to a few tens of picoamps (pA). Each separate Pd cluster size produced for experiments presented within this study has been deposited for 2000 C (pAs). For example, if the cluster beam current for a specific size of cluster is measured to be 40 pA, then the deposition was performed for 50 s, giving a total deposition of 2000 C. This value was decided upon via trial and error methodology by studying the cluster density upon the a-C TEM grids from deposition over a varied C magnitudes. The value used gave a good cluster density upon the surface allowing multiple clusters to be imaged when using standard 1.8 Mx magnification (see chapter 4) with Tecnai F20 microscope. The cluster density was not too large either allowing distance between the clusters upon the surface. A cluster density that was too large would; greatly increase the risk of clusters landing upon each other (and hence no longer being of the desired mass); would increase the risk of clusters merging together via surface diffusion across the substrate (see section 3.3.2); and would not allow background subtraction protocol. For this to be feasible, a certain amount of substrate must visible surrounding the imaged cluster in order to estimate its scattering contributions from beneath the cluster. For more details see Chapter 4.

Cluster formation of specific sizes requires the tuning of many parameters to achieve the beam current for that size. These parameters are discussed in the cluster formation section of this chapter. After the source is tuned for specific requirements, it is possible to scan across a large mass range to see what sized clusters are being produced under the conditions set. This is done by measurement of the beam current using the Faraday cup for all atomic mass units of the target material. Figure 3.6 shows the mass spectrum for Pd taken during the creation of the size selected clusters that were investigated in this study. For Pd_{55}, the peak shows a high beam current for low cluster masses (amu) of Pd, showing that under the conditions in the cluster source at the time, small clusters were being produced. For Pd_{10000}, however, the cluster beam shows no small clusters

being produced, but a wide range of large clusters are. The peak has the highest beam
current at around 490,000 amu, which corresponds to the Pd_{4500} cluster. The amu for
Pd is taken to be 106.42.
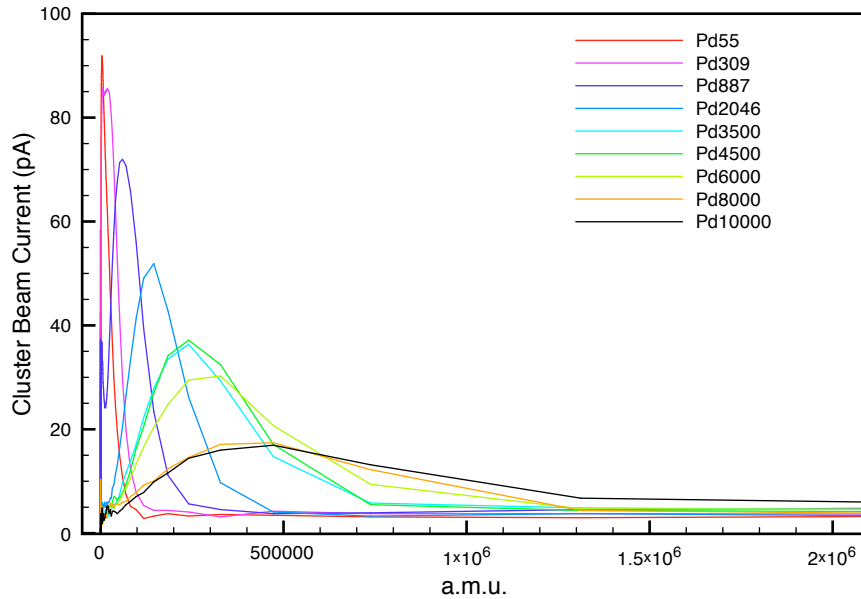
FIGURE 3.6: Mass spectrum of Pd clusters as measured in the Birmingham Cluster
Source. Figure from data taken during deposition of samples presented in this thesis
for Pd 887 to 10000 and provided by Ahmed Abdela, University of Birmingham

3.3 Cluster Formation

3.3.1 Formation of Free Clusters

A key point to take away from Chapter 2 of this thesis was that structure determines
function. Hence the formation mechanisms that take place within the formation cham-
ber and on surfaces are vital in determining the properties of the cluster. Previously the
sputtering mechanism was explained in the cluster source overview, but now the atten-
tion is turned to the formation of clusters. The cluster source is highly tuned for each
size of cluster required, this section discusses how tuning different parameters effects the
formation, and looks into the physics of formation itself. The formation of clusters can
be considered to have two stages [93]: the formation of small seed clusters via surface
growth, and the sticking of seed clusters to create larger structures via inelastic particle
- particle collisions [96].

The nucleation of small clusters involves a three-body collision. Two sputtered atoms collide with the He atom removing excess kinetic energy from the two other colliding atoms. This process will occur frequently in a supersaturated vapour. To achieve this, there must be a high sputtering rate, and hence a high Ar pressure [93]. The supersaturation of a vapour is given by the natural log of the actual pressure within the formation chamber over the saturated vapour pressure [97]. In order to increase the supersaturation of the vapour and promote further small cluster growth, the temperature is reduced by cooling the He with liquid nitrogen to a temperature of 90 K, as measured by a K-type thermocouple. Temperature reduction causes an increase in ambient pressure, thus achieving this goal.

Atom attachment to clusters is an exothermic process and as clusters grow they will become vibrationaly hot [91]. Cooling methods are therefore essential in achieving thermodynamically stable clusters. Clusters within the formation chamber will cool by two methods [21]. Firstly; collision with a He atom to remove excess kinetic energy thus allowing them to condense to form the small seed clusters required for further growth, and secondly; evaporative cooling. The later is where the internal energy of a cluster is channeled into the clusters vibrational mode/modes. The energy is enough to overcome the barrier to bond breaking and the resulting loss of atom/atoms carries away this excess energy.

When larger clusters are formed within the supersaturated vapour the energy of the system will decrease, however, in the event of large cluster formation work will be done against the surface tension, Γ, of the cluster. It is useful to consider the surface tension of the cluster as an increase in energy at its surface, due to a reduction in the number of nearest neighbour atoms. From reference [97] it can be written that the free energy of a system is,

$$\Delta G = -kTln\frac{P}{P_s}\frac{4\pi r^3}{3V_a} + 4\pi r^2\Gamma \qquad (3.2)$$

where k is Boltzmann's constant, r is cluster radius, P is the bulk vapour pressure, P_s the saturation vapour pressure, and V_a the volume of one atom. As long as the criteria are met for the supersaturation of the system (P $>P_s$), this equation is true. Equation

3.2 will rise to a maximum free energy value for a critical radius r_c, at which point it will then fall. r_c can be written as,

$$r_c = \frac{2\Gamma V_a}{kTln\dfrac{P}{P_s}} \tag{3.3}$$

As the energy of a cluster is maximum at the critical radius, in order to become larger than this value, they are required to overcome an energy barrier. After this is met it is then energetically favourable to grow in size [98]. To summarise, as super saturation is increased, the the critical radius of cluster formation is decreased and the energy barrier acting against cluster formation is also lowered. The energy barrier can be written by substituting equation 3.3 into equation 3.2,

$$E_b = \frac{4}{3}\pi\Gamma(r_c)^2 \tag{3.4}$$

The growth of large clusters occurs via two body cluster-cluster collisions, and also the condensation of atomic species onto already larger clusters [93]. Two clusters will then coalesce to form a larger cluster via sintering [96]. This process can only be completed to form a stable quasi spherical cluster depending on the temperature, particle size and the material involved. The sintering process will be driven by surface energy minimisation and may occur via viscous flow (for liquid droplets) or solid state diffusion (for solid particles) [35, 96].

Temperature will play a large role in the time it takes for sintering to complete for any cluster. This may result in the formation of agglomerates, rather than quasi-spherical shaped clusters. Definition of these terms is important here; quasi-spherical shapes refers to structures found from fully sintered seeds that have found their energy minimum, such as those discussed in Chapter 2. The term agglomerates, refers to metastable structures that are often elongated or oblate, whereby only partial sintering was achieved before cluster production was halted. It should be noted that the morphology of a cluster may effect the rate of the particle growth. For two clusters of the same mass, one agglomerated and the other spherical, the agglomerate will collide much faster with other clusters than the spherical cluster [96]. The growth rate of clusters is controlled

by the sticking probability of a certain face. Taking an fcc structure for example, the (001) face has a higher sticking probability than that of the (111) face due to a higher surface free energy [18]. Therefore, cluster formation governed by kinetics would lead to a cluster growth with (111) faces due to the lower surface free energy barrier to be overcome.

These formation processes are occurring throughout the formation chamber of the cluster source whilst being swept towards the nozzle by the carrier gasses. During this time the cluster structure is also formed. Energy barriers that exist between stable states and the cooling process of clusters helps the cluster to reach a thermodynamic equilibrium prior to deposition. However, it is often the case that kinetics halts the process of thermodynamic equilibrium being reached. It has been shown in Chapter 2 that there are many quasi-spherical structures for clusters which offer the lowest energy minima, however, as discussed previously there are energetically favoured formation processes that may favour the formation of different structures. In this case the kinetics of cluster formation do not allow the cluster to reach its thermodynamic equilibrium, leaving the cluster structure in a metastable minimum. Sticking probabilities and surface atom diffusion are two examples of this. The solid state diffusion mechanisms at play here are discussed in greater detail in Chapter 6.

Using inert gas condensation techniques it is possible to exert a certain amount of control over the growth of clusters. Gracia-Pinilla *et al* [98] performed an investigation into the size of DC sputtered inert gas condensed clusters whilst maintaining a strict control over the experimental conditions in which they were produced. By varying the He and Ar gas flow rate (and hence pressure) observations were made with regards the size of clusters produced. Mean cluster size increased with the increase of Ar flow up to a point where size was reduced again. The growth rate of clusters will increase with a high Ar flow as it will promote the sputter rate of the target material, however, too much Ar flow and the clusters maybe swept through the formation chamber too quickly to form larger clusters; the probability of cluster forming collisions will reduce due to lack of time to do so. Cluster size effects were also investigated for He flow rate, the mean cluster size was found to reduce with increasing flow of He. A strong dependance on cluster mass and magnetron power was also observed; whereby increasing the power to the magnetron increased the beam intensity due to a higher ionisation rate, thus increasing cluster size.

Aggregation length can be thought of as the time spent in the formation chamber, thus, larger clusters are produced when a longer formation chamber is provided. In this case it was possible to control the maximum diameter for Cu clusters between 1nm and 15 nm by increasing the growth distance from 30 to 130 mm [98].

All of the variables mentioned previously can offer control over the size of clusters formed, the results seen however are dependent on the target material as cluster size maybe influenced by physical properties such as binding or ionisation energy [93].

3.3.2 Formation at Substrate Surfaces

The study of cluster/atomic movement on surfaces has been researched in great detail both experimentally and theoretically. Clusters may diffuse across a substrate surface by many established diffusion mechanisms [85] which are dependent on cluster size, substrate type, temperature and many other conditions. The diffusion of atoms or clusters can result in the formation of new structures on surfaces or an alternative cluster morphology for an individual cluster enabled via diffusion.

Mechanisms for cluster diffusion can be assorted into two main categories: the motion of the cluster due to the movement of individual atoms; and the motion of the cluster due to the simultaneous motion of a group of cluster atoms [85]. Individual mechanisms include; a) leapfrog diffusion, whereby an atom is promoted to the surface of a cluster and diffuses across it one atom at a time to new nearest neighbour sites. b) Evaporation-condensation mechanism, where an atom evaporates from the cluster and condensates as an ad-atom in a new location on the cluster, thus resulting in a change of the clusters centre of mass. Examples of diffusion mechanisms involving simultaneous many atom movements include; a) gliding, where the entire cluster moves as a whole b) shearing, whereby part of the cluster undergoes a concerted movement and c) dislocation, this is where two regions of the cluster have formed a stacking fault and are separated by a dislocation. The rows of atoms in the cluster then move to eliminate this stacking fault and again, results in the movement of the cluster's centre of mass. This last type of diffusion is responsible for long range cluster diffusion [85].

Diffusive motion can give rise to the nucleation of clusters or atoms to form larger structures on surfaces. In general the diffusion constant for solids, D, can be given as substrate unit cells per second and is expressed by,

$$D = D_0 e^{-\frac{E_d}{kT}}, \tag{3.5}$$

where T is the temperature, D_0 is a pre-factor constant, k is Boltzmann's constant, and E_d is the diffusion energy barrier [99]. The later is determined by both the nature of the substrate where the cluster is located, and the nature of the cluster itself, i.e. bond strength between the substrate and the cluster atoms.

Finding a suitable substrate to control or promote diffusion is essential in determining the final morphology of nanostructures on the surface. For example, the atomically flat planes of HOPG with step edges as nucleation sites can be used for clusters to diffuse to [86]. In a study by Degen *et al* [100] a thin Alumina film was grown on a Ni_3Al (111) substrate and used as a template for the growth of Pd clusters. Here the long ranged super-structure is used to provide periodic traps of nucleation sites for Pd cluster growth. It is mentioned how the reduction of the substrate temperature would provide a smaller diffusion coefficient for the Pd clusters, therefore leading to a higher density of nuclei that are able to be stabilised at the trapping centers of the substrate. A good review of structure formation via cluster deposition can be found in work by Jensen [101]. Jensen discusses the use of defects on a surface, with the total number of cluster islands formed upon a substrate being equal to the number of defects that the substrate supplies, regardless of the diffusivity of the clusters. An example of such a substrate is amorphous carbon (a-C), where the rough surface provides larger energy barriers to be overcome for diffusion to take place [102]. Clusters deposited for experiments presented in this thesis are on a-C due to the nature of its defect rich surface (amongst other reasons discussed in Chapter 4) which limits cluster diffusion, hence individual size-selected clusters can be studied.

As a general rule it is found that larger clusters are less mobile on a surface [103], and evidence is found for this in work by Di Vece *et al* [102]. This study found that when a sample of large and small size selected Au clusters on a-C substrate is heated to 200°C, all clusters below a certain diameter were no longer found upon the surface, indicating

that small clusters are much more mobile than larger ones. The expected diameter peak for the larger diameter clusters was still found in this case, but in some cases a smaller diameter is measured. This is attributed to the evaporation diffusion mechanism whereby some atoms leave a cluster and diffuse to join a larger cluster agglomerate. Conversely, large clusters have also been found to diffuse rapidly upon a graphite surface. In a study by Bardotti *et al* [104] large Sb and Au clusters (2300 and 250 atoms) diffused rapidly despite their large size. This effect is attributed to the whole cluster rotating upon the surface as a diffusive mechanism, having not found any explanation from current diffusion theory. Molecular dynamics studies of large Lennard-Jones clusters have also been simulated to diffuse rapidly on a crystalline surface [105]. The diffusion mechanism is explained as internal vibrations of the cluster and substrate to create a force on the cluster and allow it to diffuse by overcoming a weak external potential.

3.4   Sample Preparation: Deposition   of   Clusters   on   a-C substrate

3.4.1   Size Selected Pd Clusters

The deposition stage of the cluster source has previously been mentioned in section 3.2.4 of this chapter, where cluster beam intensities and mass spectra were described. This section provides information into the final stage of the complex cluster formation process.

The lens prior to the sample holder enables the cluster deposition area to be varied. For example, defocusing the beam will give a wider deposition area but at the expense of surface cluster density. In the case of this experiment the cluster beam was not defocussed but left at the tuned settings for maximum cluster yield. It has been found, in agreement with previous work [6], that the cluster density on the surface is reduced away from the centre of the TEM grid. Clusters have been deposited onto amorphous carbon (a-C) coated TEM grids from Agar scientific. The central area of each grid is marked with two inwardly facing triangles and there are four square areas of a-C surrounding this area. In order to ensure that a good cluster density was observed during experiments, analysis was only performed on one of these central grid areas. This was

achieved by moving the sample stage within the microscopes so that the central grid area was illuminated by the focused electron beam prior to imaging.

The deposition energy of clusters incident upon a substrate is determined by the magnitude of the negative bias applied to the sample holder. In order to study the morphology or structure of clusters, this is a factor that must be considered with much care, as the energy of the impinging cluster to the substrate will determine how much of the gas phase morphology of the cluster is retained. There are several outcomes to cluster impact upon a substrate, as discussed in many theses, text books and review articles concerning cluster physics [81, 89, 99, 106, 107]. Factors to consider which may contribute to these outcomes include cluster size, the angle at which the cluster approaches the surface and the type of substrate being used. A schematic of the fundamental processes for cluster-substrate interactions can be seen in Figure 3.7. The processes are outlined as follows, high energy impacts: reflection; sputtering; implantation; and fragmentation. Upon impact with the surface the cluster's atoms not involved with the immediate impact of the cluster (which have been abruptly stopped by the substrate) will bunch up due to them still possessing the initial velocity of the cluster. Collisions with the impact cluster atoms will lead to a heating of the cluster and the surface atoms involved with the collision may become molten. Thus the release of pressure post impact may result in the backscattering of atoms, spreading, or the breaking of bonds. Low energy impacts such as soft landing occur when the cluster sticks at its impact point and any deformation induced by the collision is elastic so the cluster keeps its identity. Cluster wetting is also a feature of low energy impact whereby the impact causes plastic deformation of the cluster [99].

Low energy cluster beam deposition (LECBD) or soft-landing, has been studied using molecular dynamical simulations [108] and predicts subtle changes to cluster structure during deposition onto carbon substrates. Unable to confirm this prediction precisely, but to gain some experimental evidence towards it, Couillard *et al* [109] show that for low energy deposition of Au clusters onto a-C substrates the spherical morphology is retained, for clusters of a few nanometres in size. Although the energy per atom required for soft landing clusters varies for different materials, it is widely considered to be around 1-2 eV per atom [81]. Conversely, should the deposition energy be increased it is possible to pin metallic clusters to the substrate [110]. Di Vece *et al* [110] found
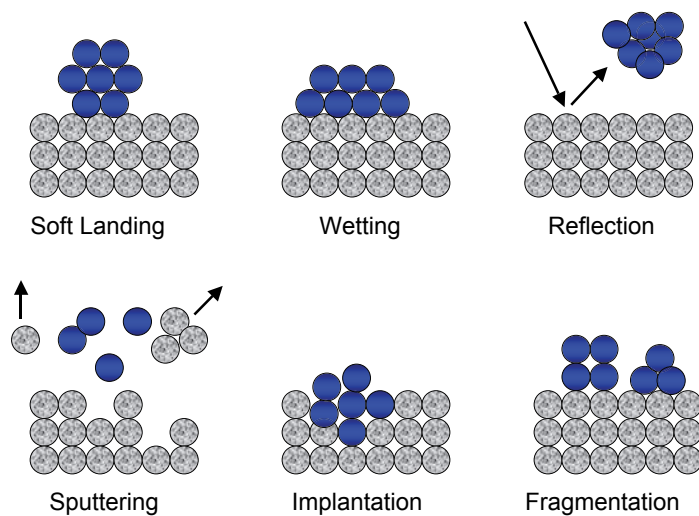
FIGURE 3.7: Illustration of cluster - surface interaction processes, figure adapted from
Ref. [99]

that pinning energies for gold (Au) and Nickel (Ni) clusters to be 15.5 eV/atom and
5.5 eV/atom respectively, a sharp contrast in energies for the two different elements.
The two methods show two extremes of deposition energy effects, and whilst both retain
the mass selection of the cluster. Pinning sees a considerable perturbation of the gas
phase morphology. The cluster does, however, remain stationary upon the surface of the
substrate, unlike soft landing deposition which may leave the cluster prone to processes
such as diffusion or coalescence [111]. The use of graphite pre-modified with defect sites
or defect rich a-C supports is sometimes used to reduce the diffusive processes of clusters
upon a substrate surface, allowing the study of isolated, low energy deposited clusters
in great detail. It is also proposed that cryogenic substrate temperatures can freeze the
post collision process thus not allowing any further cluster - substrate interaction which
may result in morphological change of the cluster [99].

Hsieh *et al* [106] summarised molecular dynamics simulations for Cu, Ni, Al and Si
clusters deposited on different substrate surfaces and the results are shown in Figure
3.8. This study talks of defining the hardness of the impact by taking a ratio of the

cluster binding energy and that of the substrate (R), which can then represent the scenario of a soft cluster landing on a hard surface and visa versa.
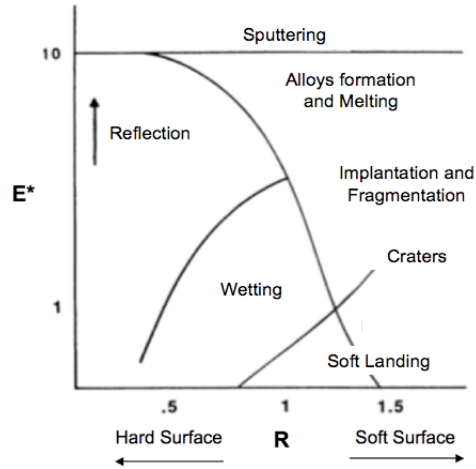
FIGURE 3.8: Cluster-surface interaction regimes as predicted by molecular dynamics simulations. R is the ratio of the binding energy of the cluster to that of the substrate and E* is the ratio of kinetic energy per atom in the cluster to binding energy of the substrate. Figure adapted from Ref. [106]

All clusters concerning this thesis have been deposited with the aim of retaining gas phase structure, therefore LECBD has been implemented and parameters chosen accordingly. An accelerating potential of 500 eV has been used for all cluster sizes keeping the energy per atom sufficiently low for this purpose. For example, taking the largest cluster investigated within this thesis, a Pd_{10000} cluster, the deposition energy per atom is 0.05 eV. The smallest cluster, Pd_{454} corresponds to 1.1 eV per atom. The inner sputtering chamber was cooled to 90 K and settings were tuned to maximise the beam current for each cluster size.

The a-C TEM grids on which all clusters were deposited allowed easy transfer to and from the Tecnai F20 Microscope. To avoid contamination of samples, sample holders were cleaned in a sonic bath for 10 minutes using acetone and then isopropanol. Sample holders were then dried by nitrogen gas flow before being inserted with grids into the deposition chamber. All grids were handled with tweezers, transported in air but stored under vacuum conditions in the load lock section of the cluster source. A sample is typically stored at $\approx 10^{-6}$ mbar.

3.4.2 Catalytic Clusters

The preparation of industrial catalytic Pd particles has been conducted by Johnson Matthey Ltd. Due to commercial sensitivity it has not been possible to obtain further information about the production of catalytic samples. The samples studies were on catalyst support materials Al_2O_3 and carbon blacks. Support materials such as these (carbon and oxides) are often used, as they have a high surface area and are micro/mesoporous. The design of support materials can promote the activity of metal catalysts and stabalise the catalysts against sintering during the high temperatures of a reaction [58].

Samples were in a powder format on arrival; deposition of this directly onto a TEM grid enabled some Pd particles and surrounding carbon to stick to the substrate surface via a van de Waals force. Upon HAADF STEM investigation it was possible to see at low magnifications where the sample was retained upon the substrate. Upon zooming in, it was then immediately apparent that the Pd catalyst support material, carbon blacks, was clumping in great quantities around the Pd particles, thus masking their projection under the electron beam. An example of this can be seen in Figure 3.9 (a).
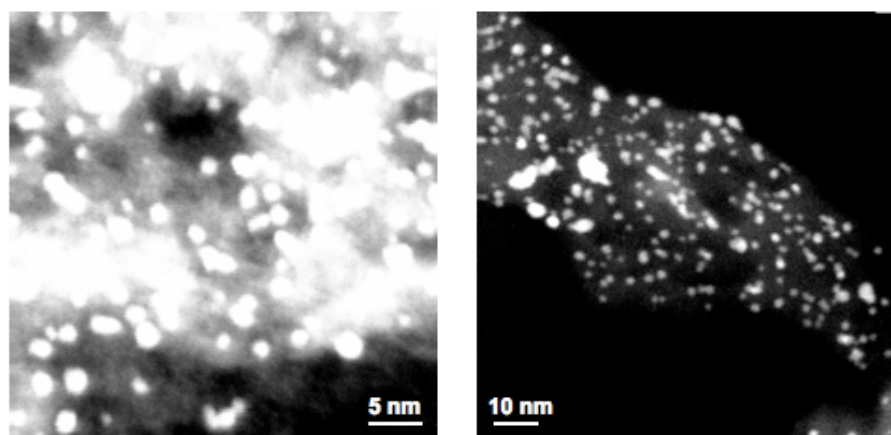
FIGURE 3.9: HAADF-STEM micrographs representing initial investigations into the optimum deposition procedure of Industrial Pd catalyst particles on carbon blacks. Taken with the Tecnai F20 microscope. a) Image of sample powder placed directly onto TEM grid, b) Image of sample after deposition parameters were performed, as described in the text.

In order to quantitatively analyse the catalytic Pd particles a new deposition method was developed. Via trial and error techniques, successful results were obtained in order to perform the intended experiments. Here, a small amount of industrial catalyst powder

was added to 4 ml of ethanol. The solution was then ultrasonicated for 10 minutes, after which, 5 μl of the solution was deposited onto a TEM grid and left to dry. This method enabled the Pd catalytic particles to be more evenly distributed upon the substrate surface with less build up of support material surrounding the Pd particles. The presence of too much support material masked their suitability for imaging in STEM, as seen in Figure 3.9 (a). The results of this method can be seen in Figure 3.9 (b), where there is minimal build up of carbon deposits surrounding particles, and the range of particle sizes can be much more clearly seen. Moreover, this approach enabled quantitative analysis of these samples, which is presented in chapter 5.

Chapter 4

Scanning Transmission Electron Microscopy and Transmission Electron Microscopy

4.1 Introduction

In 1931 the first TEM was built by Ruska and Knoll. This achievement was honoured by a Nobel prize in physics in 1986 [112] for Ruska which he shared with the inventors of the STM, Binnig and Roher [3]. The electron microscope was a ground breaking invention in that for the first time it was possible to achieve a better resolution than that of an optical microscope. Since then, methods used in TEM/STEM have improved continuously, and in recent years aberration corrected machines have become available [57, 113]. The use of these methods has been widely implemented to investigate or characterise clusters in recent years [5, 114–116].

Electron microscopy works on the principle that electrons can be focused using magnetic lenses, and thus a beam of electrons can be produced. Electron beams are usually in the energy range from 80 to 500 keV [18] and are transmitted through the sample under investigation. There are many scattering and interaction processes which electrons undergo upon contact with the sample and can be detected using many different

techniques, this will be discussed in this chapter, with specific interest to high angle scattered electrons in STEM.

This chapter will be split into three sections. Section 1 gives an introduction into the theory behind the working of scanning/tansmission electron microscopes with emphasis on the properties of electrons and image formation. From this, the second section will then introduce the two microscopes used for experiments presented within this thesis, a FEI Tecnai F20 and a Jeol 2100F with C_s corrector. The physical hardware and components of the microscopes will be describes within this section. The third and final section discusses the practical use of the two microscopes for the purpose of the experiments presented in Chapters 5, 6 and 7. This will address the processes involved in taking STEM measurements, factors which must be considered for quantitative STEM micrograph analysis, and a description of the analysis methods used for the analysis of data presented within this thesis. Within Section 3, where ever possible my own data has been presented, data taken from other sources is referenced where necessary. All work concerning electron microscopy has been conducted using the microscopes described in Section 2 of this chapter at the Nanoscale Physics Research Laboratory, University of Birmingham.

4.2 Section 1: TEM/STEM

4.2.1 Fundamental Properties of Electrons

It is widely known that electrons show both particle and wavelike characteristics, both of which are demonstrated within an TEM/STEM. For example, a microscope operating at about 100 keV will have a beam of electrons travelling about half the speed of light (c). This corresponds to a distance between electrons of 0.16cm [12], thus there is never more than one electron in the sample at any one time. Electrons will still however, undergo diffraction and interference, both of which are properties of waves.

The wavelength λ can be related to the particle momentum p through the Planks constant, h. Shown in equation 4.1,

$$\lambda = \frac{h}{p} \tag{4.1}$$

Within the instrument, electrons are accelerated through a potential V, giving each electron a kinetic energy E_k=eV. This potential is equal to the kinetic energy, thus we can equate the momentum to the electron mass, m and velocity, v. This step can be seen in equation 4.2.

$$eV = \frac{mv^2}{2} \qquad\qquad p = mv = (2meV)^{1/2} \tag{4.2}$$

Thus substituting 4.2 into equation 4.1, the electron wavelength is represented in terms of the accelerating voltage in the instrument.

$$\lambda = \frac{h}{(2meV)^{1/2}} \tag{4.3}$$

From equation 4.3 it can be seen that by increasing the accelerating voltage it is possible to decrease the wavelength of the electrons. The treatment of this principle given here is effective for explanation but neglects relativistic effects. For microscopes operating at 100 kV and above (all images within this thesis are taken at 200kV) the velocity of electrons is > 0.5c, thus relativistic effects cannot be ignored. Equation 4.4 is a modified version of 4.3 including relativistic effects. At larger accelerating voltages, larger relativistic effects will be seen [12].

$$\lambda = \frac{h}{[2meV(1 + \frac{eV}{2mc^2})]^{1/2}} \tag{4.4}$$

The advantages of using electrons rather than photons to study materials is clear due to the increase in spatial resolution at high energies. The use of electrons however presents challenges in understanding their interaction with material. For instance electrons can be scattered by gas molecules, thus the environment in which the electron beam is created must be evacuated. Specific electron interactions with clusters directly relevant to this study will be discussed in more detail as this chapter progresses, but it is important at this stage to note the many different mechanisms in which electrons can interact

with matter in electron microscopy, as opposed to visible light microscopes, where the assumption is often made that there is little interaction with the sample [117].

Electrons having passed though a sample can be classified into three categories; elastically scattered; inelastically scattered and electrons which have not been interacted with [117]. A probability that an electron is scattered by the sample material, can be described as either the cross section, σ_{total}, or the mean free path, λ. The cross section, σ_{atom} is the apparent area surrounding an atom in which the electron can interact, the probability of interaction with the sample surface , σ_{total}, is dependent on the thickness of the sample, the number density of atoms in the sample area, and σ_{atom} [117]. The mean free path is an alternative way of describing scattering interactions, whereby, instead of an area, a length is given. It is the average distance between interactions of an electron with the sample atoms. It is defined as the reciprocal of σ_{total} [12]. So for thin samples an electron may scatter once or not at all, but for thick samples multiple scattering events may occur.

The type of scattering then becomes important, as in order to deduce information about the sample, understanding of the scattering processes is required. Elastically scattered electrons can be thought of as deviated from their original path, but with no loss of energy. Inelastic scattering is the same but with a loss of energy for the electron. Other ways to classify the electron scattering is as coherent or incoherent. The latter meaning the electons are scattered and no longer have any phase relationship with the incident beam, and the former, applies to those that remain in step phase [12]. Elastic scattering is usually coherent but at higher angles becomes more incoherent. This point will be presented later when discussing the detection of high angle scattered electrons, as used for results presented in this thesis.

After interaction with the sample the electrons are then used to form images and diffraction patterns in order to gain information about the material being studied. As presented by Williams and Carter [12], diffraction is the deviation of a wave at the edge of an obstacle in its path, whereas scattering is the process by which particles are deflected as a result of a collision. Thus we see the wave particle duality applied to electrons interacting with mass. These effects are then measured by detectors, micrographs produced, and analysis can then be performed. The rest of this chapter presents these events with

specific relevance to this study. Image formation, electron detection and image analysis is discussed.

4.2.2 Image Formation in TEM

Image formation in TEM is best described by Abbe's theory and is displayed in Figure 4.1. In this illustration the system is simplified to a single lens system due to the fact that the resolution of a TEM is mainly determined by the objective lens. A real TEM system contains further intermediate and projection lenses. The theory of image formation processes in TEM are widely covered in the literature, good examples can be found in the works of Williams and Carter [12], Zhang [118] and Reimer and Kohl [119].

The surface of the specimen is illuminated by a parallel or near parallel electron beam. The lattices of the specimen then diffract the electron beam, forming beams traveling in multiple directions. The electron-surface interactions are governed by quantum mechanical diffraction theory beyond the scope of this thesis, the resultant effect however, is that the electron waves undergo phase and amplitude changes. The scattered electrons are then collected by an objective lens which is used to form an image, a Fourier transform of the sample is produced at the focal point of the lens. Depending on the method of imaging needed; the objective aperture can be adjusted in size to select different areas of the projected Fourier spectrum. For example, a narrow aperture only allows the unscattered and narrowly deviated beam through, and is known as bright field imaging (BF). Conversely, to get dark field (DF) imaging, only highly deviated electrons are taken into account, excluding the central spot. The commonly used phase imaging is performed when a large aperture is used and high resolution can be obtained.

The electron wave is forward scattered through the specimen with a transmitted wavefunction $\psi(R)$. Propagation through the objective lens then results in the beams being focussed on the back-focal plane, the electron wave here would be represented by its Fourier transform, $\Psi(K)$. K represents the frequency vector perpendicular to the optical axis and is sometimes considered in terms of the scattering angle, θ ($K = \theta/\lambda$; λ is the wavelength of electrons) and R represents the real vector. The electrons that have been scattered at an angle θ will undergo a phase shift due to spherical and chromatic
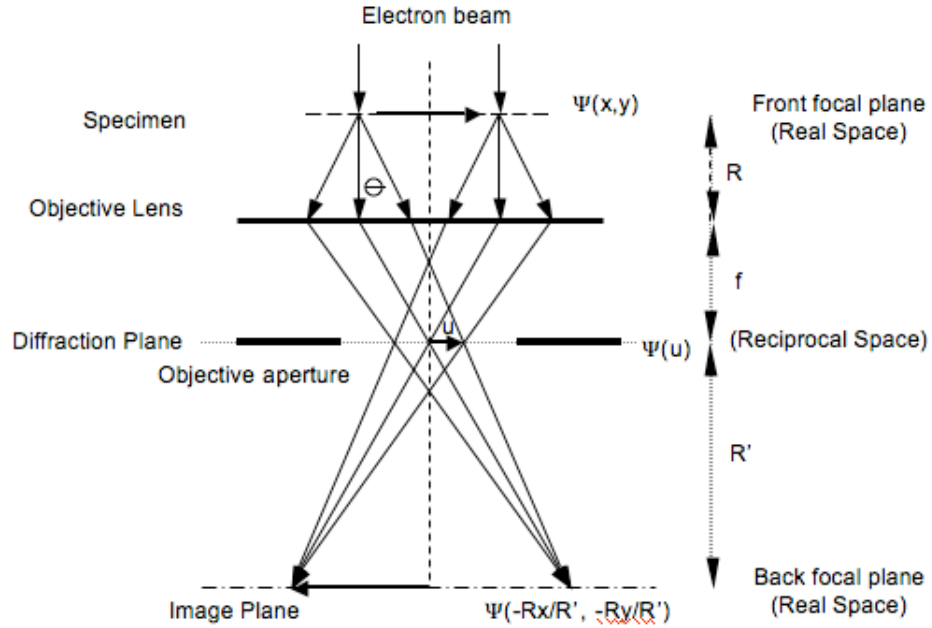
FIGURE 4.1: Abbe's theory of image formation demonstrated in a one lens TEM. Figure adapted from Wang [120]

aberrations of the lens. A function A(K) (lens function) can be multiplied to $\Psi(K)$ to allow for this effect.

The electron wave at the image plane is then given by taking another Fourier transform, $\Im[\Psi(K)A(K)]$. In effect, the image amplitudes seen in the image plane are based on the inverse Fourier transform of $\Psi(K)$ with the added function A(K) accounted for, i.e. the image contrast in TEM micrographs results from the scattering of electrons within the sample, and from the transfer properties of the optical system itself.

So we have seen that the electron image is a result of the inteference between the scattered beams at different angles, and that the interference pattern is affected by the phase modulation caused by the aberration of the objective lens. The image is calculated according to equation 4.5,

$$I(R) = |\psi(R) \otimes \Im[A(K)]|^2. \tag{4.5}$$

By considering the weak-phase object approximation (WPOA) [12], where only thin samples are considered and weak scattering is assumed, it is possible to obtain an analytical expression for the image intensity. Using the WPOA the electron wave upon

exiting the sample is given by,

$$\psi(R) = exp[-i\sigma V_p(R)] \approx 1 - i\sigma V_p(R), \tag{4.6}$$

where,

$$\sigma = \frac{\pi}{\lambda E} \tag{4.7}$$

Within equation 4.7, σ represents the interaction constant, E is the electron energy and V_p is the projected potential. This is obtained by integrating the sample potential along the optical axis (z direction),

$$V_p(R) = \int V(R, z)dz \tag{4.8}$$

If the spherical aberration and defocus is taken into account, then the lens function is,

$$A(K) = H(K)exp[i\chi(K)], \tag{4.9}$$

where,

$$\chi(K) = \pi\lambda\Delta z|K|^2 + \frac{1}{2}\lambda^3 C_s|K|^4, \tag{4.10}$$

here, Δz is the defocus, C_s the coefficient of spherical aberration and λ is the wavelength of the electrons. The objective aperture is represented as a top-hat function, H(K) and the phase shift is χ(K). Using equations 4.9 and 4.6 an expression is obtained for the intensity to the first order:

$$I(R) \approx 1 + 2\sigma V_p(R) \otimes \Im[H(K)\sin\chi(K)] \tag{4.11}$$

It is shown then that a convolution between the projected potential and an impulse response from the instrument is responsible for the contrast in a weak-phase object. In

Fourier space, the spatial frequencies of $2\sigma V_p(R)$ will therefore be multiplied by $H(K)\sin\chi(K)$, which is known as the transfer function, $T(K)$. For a more detailed description of the transfer function see reference [12].

This transfer function is applicable if the sample is a weak-phase object, the function then describes the contrast level in the TEM micrograph. For example, when the $T(K)$ is negative, there is positive phase contrast which results in atoms appearing dark against a bright background. When $T(K)$ is positive, the reverse happens and bright atoms are seen against a dark background and when $T(K)=0$, there will be no detail in the image for that value of K. This is due to the subtraction or addition of amplitudes given to the forward scattered beam by the phase shift function [12], which has been shown to complicate the transfer function through its dependance on defocus, electron wavelength and the C_s of the lens. It is also oscillatory with K (see equation 4.9). Optimisation of the transfer function occurred in 1949, when Scherzer balanced the effect of spherical aberration against a particular negative value of defocus [121]. This is known as the Scherzer defocus (Δz_{sch}),

$$\Delta z_{sch} = -1.2(C_s\lambda)^{\frac{1}{2}} \tag{4.12}$$

In summary, image formation in conventional TEM proceeds through the process of taking the Fourier transform of the forward scattered electron wave at the exit face of the sample, multiplying it by the lens transfer function and taking the inverse Fourier transform of the amplitude in the back focal plane. The image produced is made more complex by modifications made by the lens system, but contrast is achieved through coherent interference of the scattered waves from the sample. The difficulty in quantitative interpretation of TEM micrographs arrises due to the fact that only exit wave intensities and not phase information can be recorded. TEM can however provide detailed structural images of clusters, and a more quantitative approach can be made by selecting different types of scattered electron from the sample. Such a method is called scanning TEM (STEM) and is discussed in the next section.

4.2.3   Image Formation in STEM

All images presented within the results chapters of this thesis are produced through HAADF-STEM. STEM differs from TEM greatly in the fact that to form an image from a specimen it is not necessary to refocus scattered electrons. The image is formed by detecting the electron flux scattered in any direction as a function of probe position [115]. This principle is best explained by the principle of reciprocity.

4.2.3.1   The Principle of Reciprocity

The principle of reciprocity states that the wave amplitude at point P due to a point source at Q is identical to the wave amplitude at Q due to a source at point P [122]. Figure 4.2 illustrates this for the electron microscope. This figure demonstrates that the components needed for STEM are the same as in TEM, but the ray diagram in TEM is just the reciprocal of STEM, thus many of the principles described in the last section can be carried over to STEM. The electron beam in STEM mode is focused to a sharp point via a set of condenser lenses and an objective lens. An objective aperture is used to limit the angle of illumination from the incident probe prior to interaction with the specimen and rastered across the sample using a set of scan coils. Detectors are situated on the other side collecting the scattered electrons. In TEM the electron beam is widened and electrons interact with the specimen as discussed previously. The electrons are then focused on the detector.
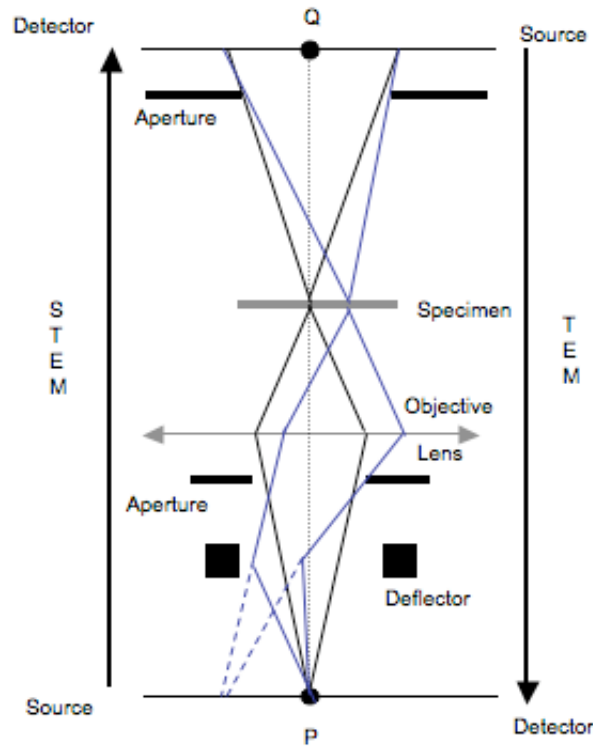
FIGURE 4.2: Ray diagram illustrating the theory of reciprocity Diagram shows that STEM is the reciprocal of TEM. Figure adapted from Liu [122].

4.2.3.2 STEM

The finely focused electron probe interacts with the specimen by scattering off its nuclei and electrons. As the electron beam exits the sample its amplitude distribution can be described by the wave function $\psi(\mathbf{K})$. $\mathbf{K}$ represents a two dimensional vector in the reciprocal space; $\mathbf{K} = 2\sin(\theta/2)/\lambda$ where λ is the wavelength of the incident electrons and θ the scattering angle. Variations of $\psi(\mathbf{K})$ carry information about the electron-sample interactions as the electron probe is scanned across the surface. It is however, not possible to directly measure $\psi(\mathbf{K})$, instead, images of samples are formed by collecting the scattered or transmitted electrons. $\psi(\mathbf{K})$ is related to the image intensity, $I(\mathbf{X})$, as a function of beam position $\mathbf{X}$, as shown in equation 4.13. $D(\mathbf{K})$ is the transmission function of the detector and $\psi(\mathbf{K},\mathbf{X})$ is the amplitude function.

$$I(\mathbf{X}) = \int D(\mathbf{K}) \mid \psi(\mathbf{K},\mathbf{X}) \mid^2 d\mathbf{K} \qquad (4.13)$$
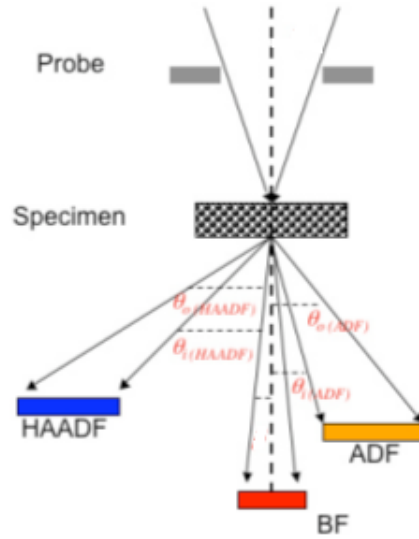
FIGURE 4.3: Electron scattering in STEM showing the position of detectors. The HAADF detector, used for this research is positioned far from the optical axis, see text for details

Multiple detectors can be arranged after the sample stage in STEM to provide different information about the sample, examples of these include a BF detector (as mentioned in TEM image formation), an energy-dispersive X-ray detector (EDX), and electron energy loss spectrometer (EELS). The predominant detection method utilised for experiments presented in this thesis is the high angle annular dark field detector (HAADF), which is able to detect single electrons scattered at a range of high angles from the sample. This form of detection is also known as Z-contrast imaging. A schematic of STEM detectors can be seen in 4.3.

Electrons scattered at high angles often originate from the interaction with an atomic nucleus of an atom within the specimen. These interactions are considered to be Rutherford scattering of electrons. This is because the scattering is highly dependant on the atomic number of the scattering atom and hence the term "Z-contrast" imaging in HAADF-STEM. For this type of incoherently scattered electron, no phase relations exist and the the image intensity varies approximately with Z^2 of the specimen [123]. The angular distribution of scattering from an atom with an atomic number, Z, to an angle θ, may be approximated by the Rutherford cross-section [12];

$$\frac{d\sigma(\theta)}{d\Omega} = \frac{e^4 Z^2}{16(E_0)^2 \sin^4 \frac{\theta}{2}} \qquad (4.14)$$

where σ is the scattering cross section of one atom, E_0 the beam energy and Ω the solid angle of collection. The total scattered electron intensity from interaction with the atoms of a cluster can be compared to the total intensity integrated over the area that the cluster occupies. For incoherent electrons scattered at high angle the total intensity, I, from a cluster is dependant only on the number of atoms within the cluster, N, and the electron beam energy. Hence it is possible to study and obtain information about the size of the imaged cluster from its integrated intensity. In reality, it is not always the case that all electrons are incoherently scattered. This is due to electron-material interactions such at multiple scattering effects and electron channeling. Section 3 of this chapter addresses these issues and discusses them with relevance to quantitative HAADF-STEM imaging.

Figure 4.4 (a) shows a HAADF-STEM image of size-selected Pd clusters that have formed through aggregation (or love as the heart shape may suggest!). The line scan shown in Figure 4.4 (b) shows how this type of image is sensitive to even a low number of Pd atoms, at the edge of the cluster, away from the bulk structural formation, a small number of Pd atoms can be seen resting on the a-C film. These atoms can then be used as a calibrating factor, any other intensity peaks of the same height can also be identified as containing the same number of atoms. If the column in question is identified as being an individual Pd atom then each column in the image can be quantified in terms of the number of atoms it contains. The higher the intensity peak, the more atoms that are contained in that atomic column, as seen towards the right hand side of the line scan [5, 124].

Figure 4.5 illustrates how HAADF-STEM images do not reverse contrast through defocus. The figure displays in both (a) and (b) how the defocus value can be changed to an optimum focus value which will reveal best contrast for structural features of clusters at different heights upon the substrate. Even when out of focus (the small clusters in (a) and the large cluster in (b)) contrast is not reversed, and would not do so for any defocus value. This is characteristic of incoherent images and is indeed advantageous.

For incoherent imaging, the intensity is a convolution of a function representing the cross section of a specific area of the sample, O(R) and a resolution function, which, for the case of STEM is the probe intensity profile, $P^2(R)$ [118, 124]. In other words, the
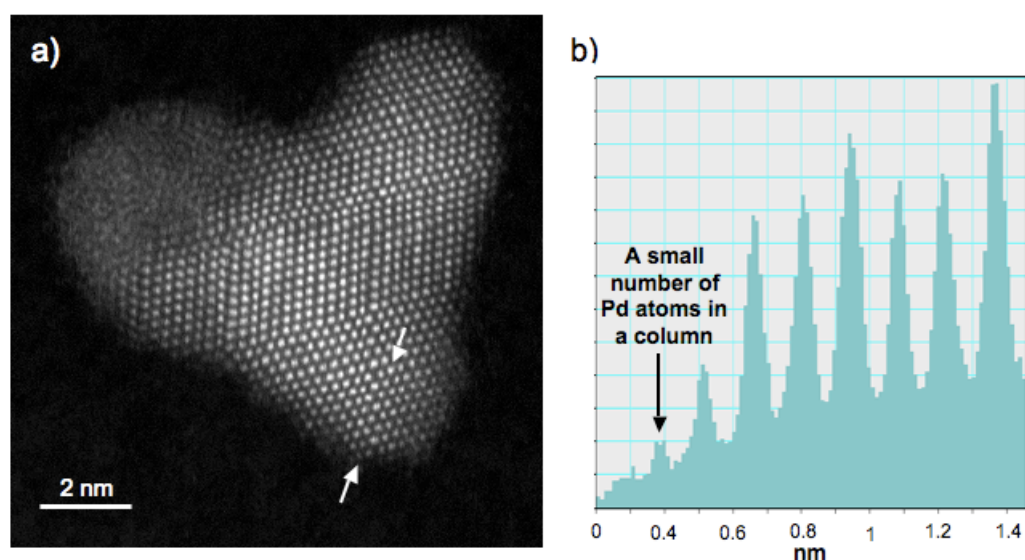
FIGURE 4.4: a)HAADF STEM image of aggregated size-selected Pd clusters, arrows illustrate the line profile position shown in (b). Image taken using Jeol 2100F with C_s corrector, 200 kV, inner and outer collection angles 52 to 140 mrad respectively. b) Scattered electron intensity line profile. The y axis represents the scattered electron intensity (arb. units.) Column containing a small number of Pd atoms highlighted at edge of cluster, see text for details.
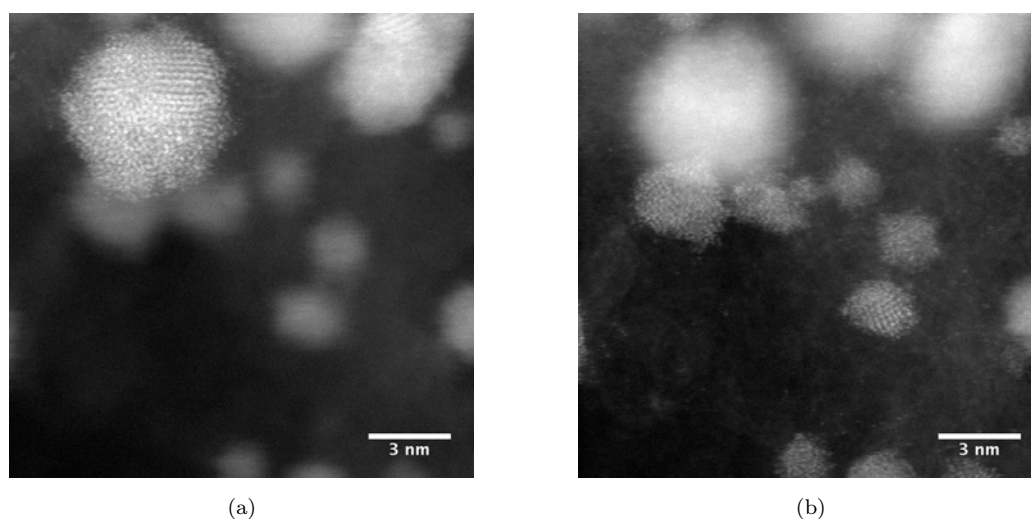
FIGURE 4.5: HAADF STEM images of industrial Pd catalyst particles: Figure illustrates how optimum contrast conditions are met at specific defocus and that contrast reversal is not present for HAADF-STEM images at varying defocus values. Images taken using FEI 2100F with C_s corrector, 200 kV, inner and outer collection angles 52 to 140 mrad respectively.

intensity is a mixture of your sample positions and how well you can resolve the sample positions. This can be written as,

$$I(R) = O(R) \otimes P^2(R), .\tag{4.15}$$

Obtaining an image of the cluster seen in Figure 4.4 with the bright field detector in STEM is the equivalent of image capture in TEM, a coherent phase contrast image. This image would display all the features seen in the HAADF-STEM image but the edge of the particle may be blurred due to delocalisation. This is where the location of a fringe is not necessarily correspondent to the location of the lattice plane [12]. As discussed previously, the image would also reverse contrast for different defocus values. Due to the BF image constituting of coherently scattered waves, it is very difficult to distinguish individual atoms around a cluster. This is because the pattern made by the substrate is indistinguishable from the scattered signal from the atom. For Z-contrast images however, the difference in atomic number from the Pd atom (Z=46) to the carbon atoms (Z=6) makes the contrast between the two easily identifiable.

To define what is meant by an incoherent image, one can look towards the main difference in BF and HAADF or ADF images, that is, the collection angle at which the electrons are detected after interaction with the sample. Most of the forward scattered waves will remain coherent with the unscattered beam and interference patterns can be formed. As all atomic spacing (d) in materials is between 1 and 3 $\mathring{A}$, this leads to diffraction angles at integer values, n, of λ/d [20, 124]. Most first order diffraction angles occur at $\leq$ 10 mrad [12, 118] making BF detectors sensitive to these electrons. But for a HAADF detector, the interference patterns are not measured, instead the signal from the integration of the many diffraction peaks over the scan range is recorded. Thus, large detection angles correspond to contrast based upon intensities and not phase, and such is the definition of an incoherent image. If one takes into account the fact that high angle scattering can be classified as electrons scattered at angles past the bragg scattered peaks ($\geq$10 mrad) then it is clear that the path difference between electrons scattered by atoms in the x/y plane (transverse) are much greater than those along the beam direction (z or longitudinal). This is shown in Figure 4.6. An electron beam entering a sample at angle θ will show phase differences for atoms in the x and z directions of $x\sin\theta$ and $z(1\text{-}\cos\theta)$ respectively. For small θ however, scattering angles are $x\theta$ and $z^2/2$. The latter is much smaller, showing how longitudinal coherency is much more difficult to break using detector geometry alone [118].
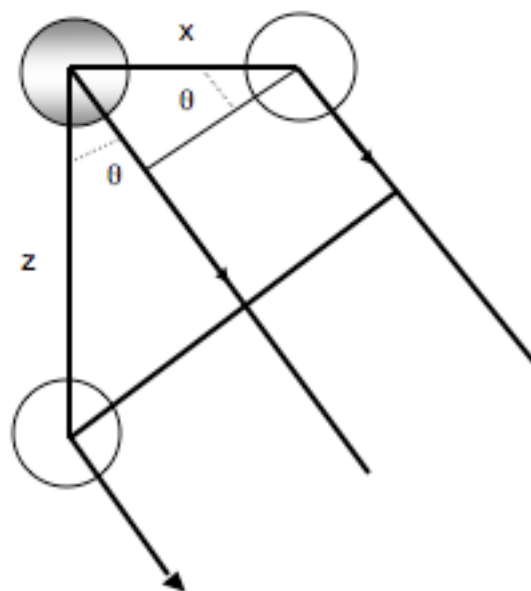
FIGURE 4.6: Path differences of scattered electrons from sample atoms in transverse (x) and longitudinal (z) directions. Smaller phase shifts for small angle approximations in the longitudinal direction make coherency much more difficult to break using detector geometry. Figure adapted from reference [118]

The effect of thermal diffuse scattering (TDS) [12] allows longitudinal coherency to be broken. TDS is vibrations of the sample atoms due to electron-phonon interaction. From vibration of atoms along an atomic column in transverse directions, scattered electrons have random phase differences as each electron will interact with the atoms at a slightly different position.

Thus far, STEM imaging with the HAADF detector has been discussed in detail and one can see its suitability for cluster investigation, especially clusters made of materials with large atomic numbers. But the identification of the chemical composition of a sample has not been discussed. A method known as dispersive X-ray spectroscopy (EDX) within STEM can be employed to do this. This method relies upon the emission of X-rays from the sample due to an ejection of an inner shell electron from the sample atom, following interaction with the electron beam. The ejection of such an electron leaves a vacancy which is promptly filled by an electron from an outer shell, in doing so this process releases an X-ray. The energy of this X-ray is characteristic to the electron orbitals involved and to the atomic structure of the sample from which they were emitted. Therefore the element can be identified by its unique X-ray signal. Signals are detected using an energy dispersive spectrometer and for a detailed account of their workings

see reference [117]. The position of the detector within the microscope is before the sample within its line of sight and must be as close to the sample as possible without obstructing the electron beams path. This is because X-rays cannot be deflected, and signal strength is improved by having detectors in close proximity. The substrate itself will produce a large amount of X-ray signal in comparison to that of a small cluster under investigation, however, if the substrate has no elemental similarities to the cluster of interest then it is possible to analyse the cluster quantitatively despite the large signal from the support.

4.2.4 Probe Formation and Lens Aberrations

The optimal spatial resolution achieved by a STEM is directly determined by the size of the electron probe. This is in turn dependant on the spherical aberration coefficient, the wavelength of the electrons, the defocus of the beam and the size of the objective aperture.

Correcting lens aberrations allows the objective aperture to be opened up, which in turn promotes a higher resolution. This is because electrons passing through a very small point, such as the objective aperture, suffer from diffraction, and the small point projects as an Airy disc, limiting the resolution [117]. It is only in relatively recent years that small probe sizes have been achievable and atomic resolution obtained and made commercially available in TEM/STEM [125]. Magnetic lenses used in microscope columns are normally based upon a circular geometry and all suffer from aberration, which in turn limits the apertures that can be used, and hence lessens the resolution that can be achieved. Multipole lenses can now be used to correct for these effects in conjunction with computational auto tuning to correct for high order aberrations that would be unachievable manually.

Any lens suffers from aberrations that can be classified into two groups: chromatic aberrations which depend on the wavelengths of the electrons passing through it; and monochromatic aberrations which will effect electrons independent of their wavelength. Any aberration distorts the quality of the image at every point of the sample, and each type acts differently. Chromatic aberrations occur if the electron beam contains electrons with a spectrum of wavelengths. Each electron will be deviated by the lens to a degree
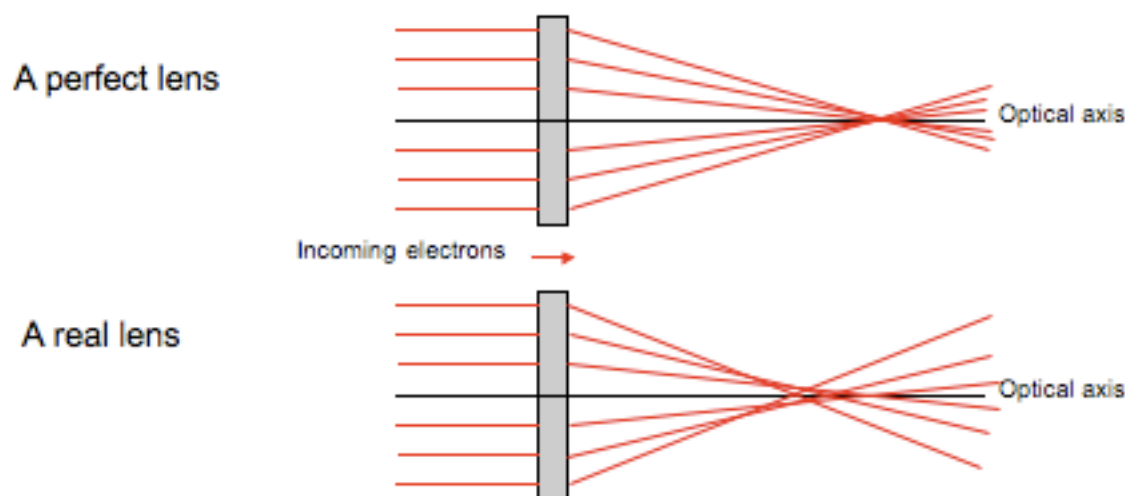
FIGURE 4.7: An electron path diagram displaying the effects of spherical aberration. The lower half of the figure shows how electrons are brought to focus nearer the lens the further away from the optical axis that they enter it.

based upon its associated wavelength. Hence, different wavelengths cause different focal points, which causes a loss of quality within the image.

Monochromatic aberrations occur due to different path lengths of electrons from the lens to the focal point. The most important one of these in electron microscopy is spherical aberration. Spherical aberrations are caused by the lens field acting inhomogeneously on the off optical axis rays [12]. This means that the further away from the optical axis (aligned perpendicular and central to the lens field) that the electron is upon entering, the more strongly it is bent back toward the axis. Therefore this does not allow the lens to focus all electrons at a specific point. Instead an object is imaged as a disk of finite size, hence the limitations of a microscope to magnify detail accurately. A schematic of this effect is illustrated in Figure 4.7. It has been shown in equation 4.9 that the C_s component directly affects the lens transfer function, so reducing this through the use of correctors enables more detail of the sample to be obtained.

Astigmatism is caused by non-uniform magnetic fields acting upon electrons passing through the lens and consequently has similar effects upon the electron beam to spherical aberration. There are however other ways in which astigmatism may arise within the microscope column independent of lens effects. Apertures that are introduced into the system can disturb the field if not correctly centered around the optical axis, and if

these apertures are not entirely clean then the contamination present, can charge up and deviate the electron beam.

Two different microscopes have been used within the experiments presented in this thesis and are summarised in the next section. For STEM images taken with the Jeol 2100F microscope the spherical aberration has been reduced using a C_s corrector and has a beam size of 0.9 Å. For images taken with the Tecnai F20 microscope the beam size is ≈ 4 Å.

4.3 Section 2: The Two Microscopes

4.3.1 FEI Tecnai F20 (S)TEM and Jeol 2100F with C_s Corrector

All images presented within the results chapters of this thesis have been recorded using a STEM with HAADF detector attachment. For the first two years of investigations (Sept 2007 to March 2009) imaging was performed using a FEI Tecnai F20 at the University of Birmingham. From June 2009 this microscope was replaced by a Jeol 2100F with C_s corrector. Results from both microscopes are presented within this thesis operating with a 200 keV electron beam. The basic principles of both microscopes are the same but operation controls and procedures vary, this is largely due to the presence of the spherical aberration corrector within the Jeol instrument.

The Microscope's columns consists of five sections; the electron source, illumination stage, sample stage, magnification stage and detection. Figure 4.8 shows the main components inside the Tecnai F20 microscope whilst Figure 4.9 and Figure 4.10 give cross sections and simplified component locations of the Jeol 2100F microscope respectively. The main components are discussed in this section and the figures given to easily distinguish the difference between the two machines.

4.3.1.1 Electron Source

Samples are illuminated by electrons which are required to be highly coherent, bright and energetic. Older microscopes originally used thermionic emission [12] to extract electrons. This method involves the heating of a material to give the electrons enough

energy to overcome its work-function. Both the Tecnai and Jeol instruments, however, achieve much higher beam currents through the use of a Schottky Field Emission Gun (FEG).

Traditionally FEGs consist of a sharp tungsten tip used as a cathode with respect to two anodes. The FEG is therefore placed in a strong extraction voltage of several kV so that electrons are drawn out from the tip end due to the generated electric field. The first anode provides the extraction voltage whilst the second anode accelerates the electrons to 200kV. It should be noted that the combined fields of the anodes produce a crossover of the electron beam as they act as an electrostatic lens [12]. Both instruments use this type of FEG but have a layer of Zirconia Oxide surrounding the tungsten which lowers the work function. High vacuum conditions are required so as to achieve good surface cleanliness and the tip is heated to aid electron emission as well as providing the secondary function of avoiding contamination.
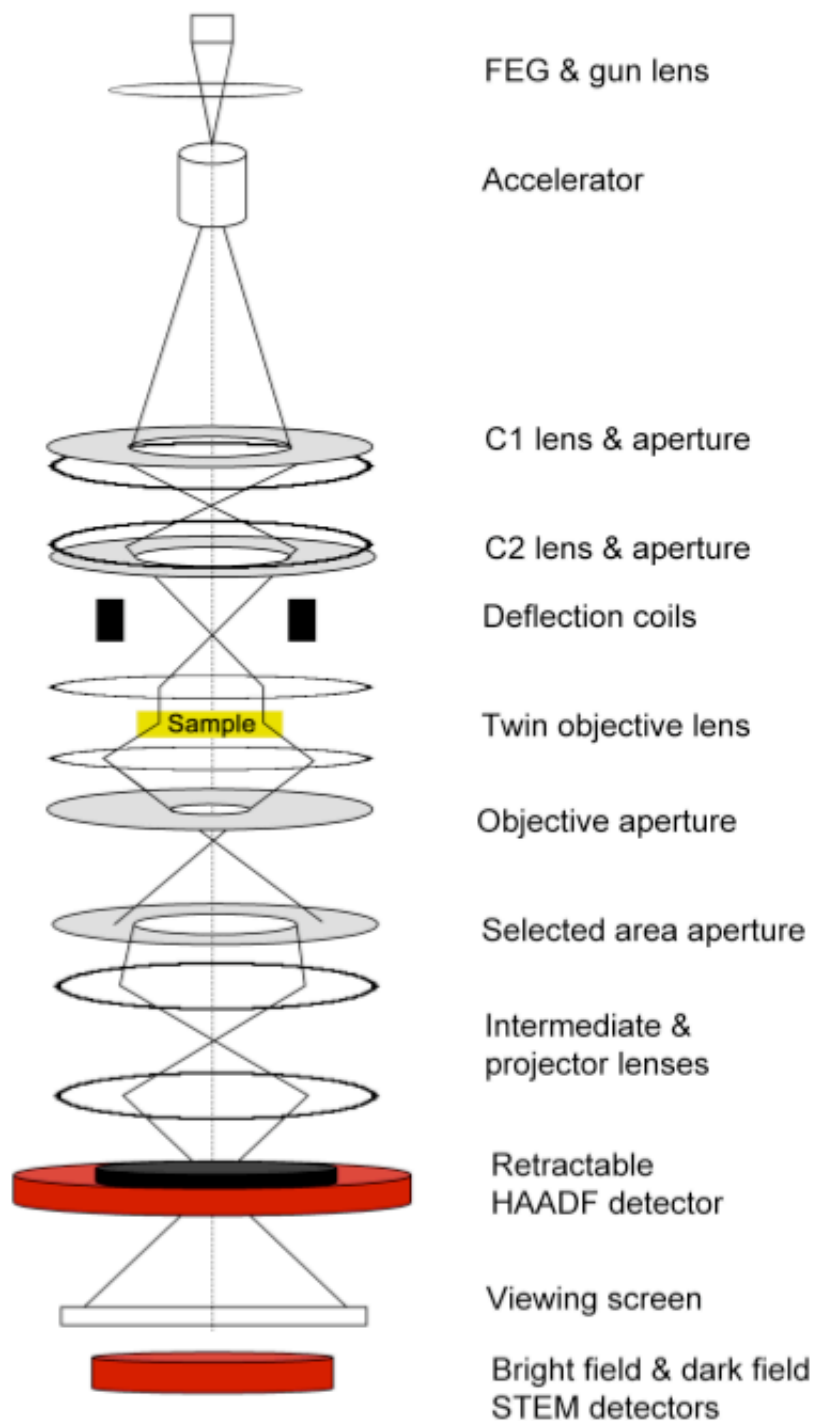
FIGURE 4.8: Schematic diagram showing the positions of the main components within the Tecnai F20 microscope column. The components necessary for TEM imaging are highlighted in addition to the detectors used in STEM [6].

4.3.1.2 Illumination: Lenses, Deflector Coils and Stigmators

With the exception of the electrostatic lens used at the gun all lenses within the columns of both microscopes are electromagnetic. These lenses consist of three components: lens coils, a magnetic circuit, and a cooling system. The magnetic field is produced by an electric current flowing in the coils and the distribution of this field is determined by the shape of the magnetic circuit. The magnetic circuit is a piece of magnetic alloy which contains the coils in which the electric current flows. The shape of this has to be precisely machined in order to achieve the exact desired effect on the electron beam. The flow of electric current inevitably produces heat, this would make the system unstable if it were not cooled by the water flow around the lens. This water flow has a carefully monitored flow rate and temperature in order to achieve cooling without disturbance to the electron beam.

The electrons are focused into a beam by the lenses, having been emitted from the electron gun by electron optics. Deflection coils are used to make sure that the beam is centered upon the optical axis and the two condenser lenses, C1 and C2, set the intensity of the illumination. The condenser lenses, in conjunction with the first objective lens, create a near parallel beam incident on the sample. In STEM the first objective lens (for the Tecnai) or the condenser minilens (for the Jeol) must be strong so as to create a focused beam upon the sample and AC scan coils manipulate the beam to be scanned across the sample.

It is common for lenses to focus the electron beam to a greater degree in one direction. This causes an asymmetry of the beam called astigmatism and can be corrected for by the stigmators in the microscope column. Stigmators have a quadrupole geometry, with each opposite pairing focusing or defocusing the electron beam using a magnetic field. For example, using stigmators an elliptical beam can be made circular.

A major difference in the illumination stage of the Jeol microscope from the Tecnai is the presence of a spherical aberration corrector unit. Its placement in the column can be seen in Figure 4.10 with an inset for a schematic of the lens configuration. Effectively it splits the beam into axial and field rays which follow differing paths through the hexapole lenses. The lenses over and under-correct for a number of orders of the C_s coefficient and when the beams converge the C_s coefficient is much reduced thus allowing

Electron gun

Electron gun 1st beam deflector coil

Electron gun 2nd beam deflector coil

Electron gun chamber isolation valve

1st condenser lens coil

2nd condenser lens coil

Goniometer

Specimen holder

Objective lens coil

Selected area aperture assembly

Intermediate lens stigmator coil

Projector lens beam deflector coil

Binocular microscope

Viewing window

Viewing chamber

Supply magazine

Receiving magazine

Accelerating tube

Gas inlet

Condenser-lens stigmator

Condenser-lens 1st beam deflector coil

Condenser-lens 2nd beam deflector coil

Condenser minilens (CM lens) coil

Objective aperture assembly

Objective lens stigmator coil

Objective minilens (OM lens) coil

1st image shift coil

2nd image shift coil

Intermediate-lens coil

Projector-lens coil

Viewing-chamber isolation valve

High-resolution diffraction chamber

Small screen

Large screen

Camera chamber

FIGURE 4.9: Detailed cross section of Jeol 2100F microscope, image taken from Jeol Instruction manual
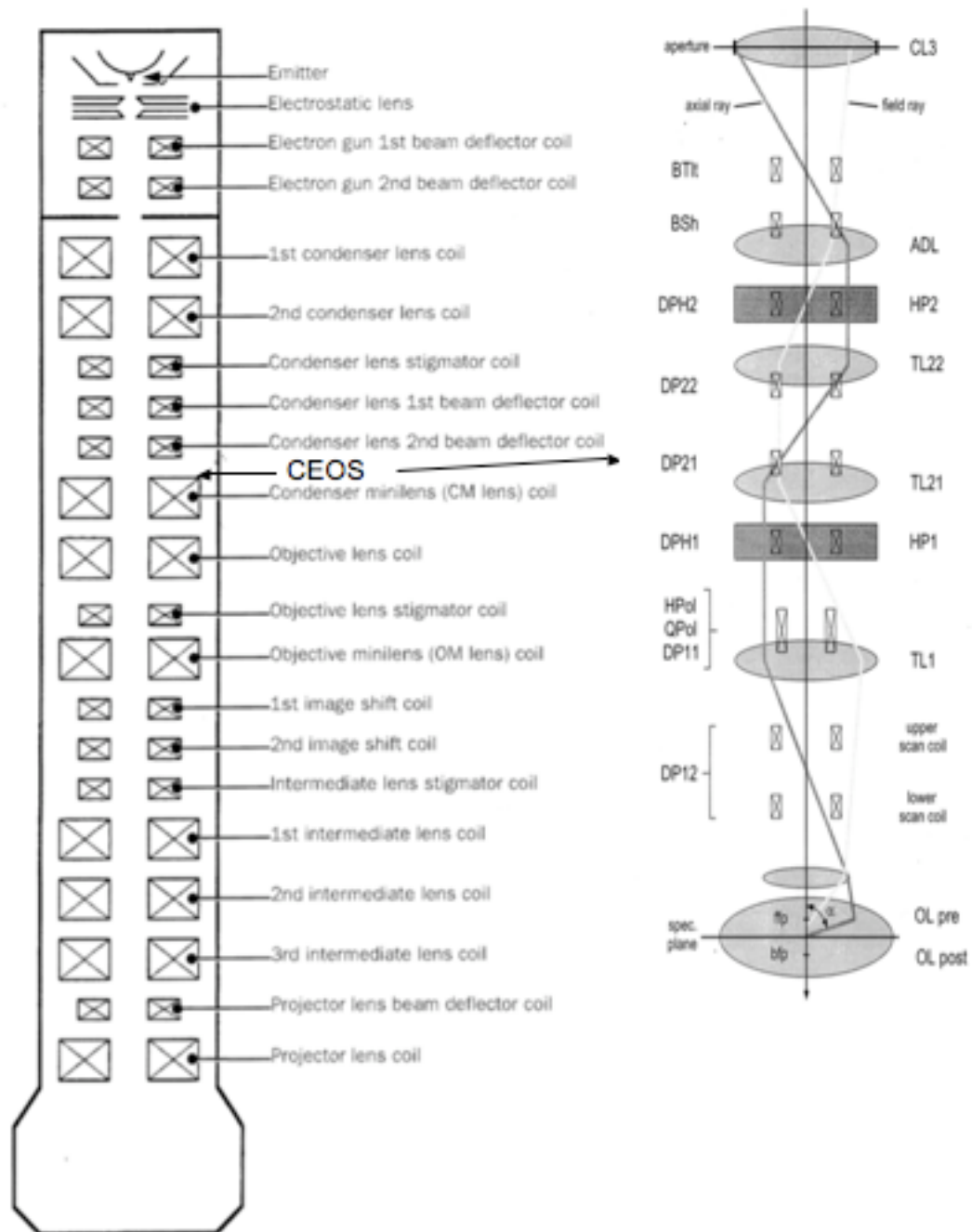
FIGURE 4.10: Left hand side: Lens and Coil locations within the Jeol Microscope, the CEOS spherical aberration corrector is placed between the condenser system and the condenser minilens (Image taken from Jeol Instruction manual). Right hand side: the schematic for the aberration corrector. The axial ray represents the electron beam traveling along the optical axis and the field ray represents the electron beam which has been influenced by aberrations within the illumination system (image taken from CEOS user manual).

better resolution in STEM. From the section discussing aberrations it is known that the electrons entering the lens at high angles to the optical axis are most sensitive to the aberrations. The electron beam is only scattered weakly at these angles thus their aberrations remain undetected in the on-axis image. So measurement of the aberration magnitude using on-axis images solely, is not sufficient [126]. To solve this problem one can take a tableau. A tableau is formed by tilting the incident beam around the optical axis through a series of azimuthal angles[127]. For each angle a Fourier transform is calculated of the recorded image. For the CEOS corrector a standard sample of Au nanoparticles on a a-C TEM grid is used for the alignment procedure. The aberrations are apparent in the recorded images as a change of shape and size of the clusters. The shape and size change is apparent by comparison of the clusters imaged at the full range of angles (circular around each side of Figure 4.11) and comparison of the two sides of the tableau, showing the under focused (UF) and over focused (OF) beam. This change is induced by a defocus and astigmatism of the beam at each angle. The measurement of the aberration values to the third order then allows correction to take place. A tableau example is shown in Figure 4.11 of the Jeol standard Au nanoparticle sample, the outer tilt angle is 18 mrad, but a tilt angle of 21 mrad is achievable in this system.
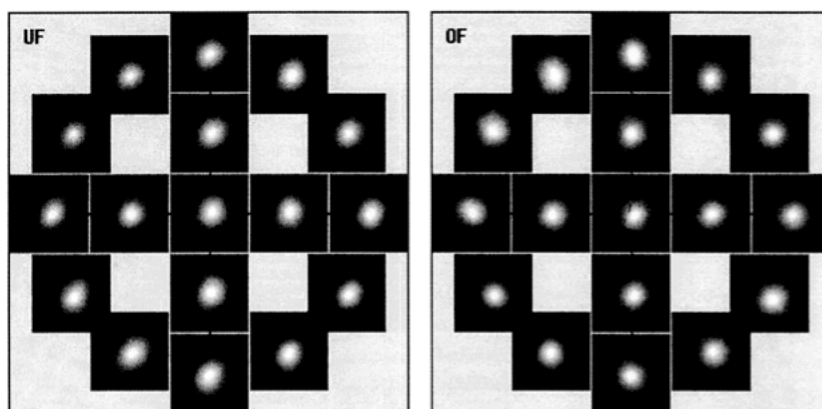
FIGURE 4.11: A tableau example taken using the CEOS STEM C_s corrector using a standard sample of Au nanoparticles provided by Jeol. The right hand side represents the over focused (OF) electron probe and the left hand side the under focused (UF) electron probe. Different tilt angles are shown for each focus level in the images displayed, see text for details. The outer tilt is 18 mrad, a fully corrected illumination system produces a tableau of identical nanoparticle images.

4.3.1.3   Sample Stage

All clusters are deposited onto 3mm TEM grids suitable for insertion into the column chamber by fitting them on a single tilt sample holder. The holder has the ability to tilt in order to aid sample alignment with respect to the electron beam. The sample is positioned between the upper and lower pole pieces of the objective lens in the Tecnai and Figure 4.9 displays the sample position in the Jeol microscope. Its surrounding area is cooled by liquid nitrogen cold fingers to improve the vacuum around the sample thus reducing contamination.

4.3.1.4   Magnification

For TEM imaging and the formation of diffraction patterns, the exiting electron beam is focused at this stage using more electron optics. The intermediate and projector lenses are used for magnification and imaging in TEM mode and the selected area aperture allows diffraction patterns to be formed.

4.3.1.5   Detection

The Tecnai has an additional high angle annular dark field detector (HAADF) which is utilised for all imaging presented within this thesis. It may be retracted from the column when not in use. It is shaped like a ring and is positioned above the viewing screen to collect electrons scattered at high angles from the sample. The HAADF detector consists of a scintillator that is optically coupled to a photomultiplier tube and detection has been optimised for single electron detection [111]. The HAADF detector used in the Tecnai was a Fischione 3000 model and the Jeol system uses a Jeol EM-24560 Dark Field Image Observation Device.

A Tecnai F20 microscope from the Electron Microscopy Centre at the University of Birmingham was also used within an experiment presented in chapter 6 of this thesis. This microscope was identical to the one used in the Nanoscale Physics Research Laboratory but was fitted with the capability of EDX analysis. This was performed with a Oxford X-Max 80 mm^2 SDD detector with a solid angle of 0.175 sr [128].

Both systems consist of a fluorescent viewing screen which is used to see the electron beam during alignment. The Jeol microscope also has a US 1000 camera fitted under the retractable viewing screen, which can be used in conjunction with the viewing screen to observe the Ronchigram for detailed alignment.

4.3.1.6   Vacuum System

The vacuum system for the microscopes are separated into three parts by small apertures. The three parts are differentially pumped and are known as the chamber, the column and the gun. Pressures in the chamber (with the aid of liquid nitrogen) reach 10^{-7} mbar and in the gun region 10^{-10} mbar. The generation of a vacuum inside the microscope is essential to the cleanliness of the sample, the insulation of the electronic optical components and for the propagation of the electrons.

4.4   Section 3:   Practical Use of STEM for Nanocluster Imaging

4.4.1   Imaging Pd Nanoclusters in STEM - for Quantitative Analysis

Imaging nanoclusters in STEM mode presents the many technological challenges of tuning many parameters for each different sample in order to produce images such as those presented within this thesis for quantitative analysis. This next section looks into the process of taking measurements in STEM; highlighting the need for complete understanding of the practicalities of image formation in the laboratory and how measurements have been analysed. Both microscopes were located in a laboratory where mechanical and electromagnetic interference was minimised. This was done predominantly by locating the microscopes in a sound proof booth whilst using an electric field cancellation system.

Firstly the substrate support of clusters should be considered. Carbon covered Cu grids were used for all samples presented here. They were purchased from Agar Scientific and have a nominal carbon thickness of $\approx$ 20 nm. Chapter 3 discussed the suitability of a-C for the deposition of clusters, but this substrate holds other properties that make it

convenient for study using a STEM. Amorphous carbon can be considered as transparent to the electron beam [12]. Amorphous carbon (a-C) has no crystalline structure and thus cannot interfere with the imaging of the supported Pd clusters. For Z-contrast imaging carbon is also well suited to nobel metal cluster investigation as its low atomic number of 6 provides little intensity in comparison to the Pd clusters within the HAADF- STEM image, thus providing excellent contrast allowing more accurate quantitative analysis.

As mentioned in chapter 3, all samples have been stored so as to keep them free from contaminants. Contamination can be a problem in STEM imaging due to the interaction between electron beam and any contaminants present upon the sample. Main contaminants are mobile hydrocarbons. Interaction with the electron beam means that they diffuse across the surface of the substrate towards an area being imaged. They manifest themselves on the STEM image as bright areas where the electron beam has scanned and can be seen in Figure 4.12. This effect disrupts the ability to perform analysis on the image due to the large amount of electron scattering from the contaminants, making clusters in contaminated areas difficult to distinguish. It has been found that for samples prone to contamination, the signal to noise ratio can be improved for detailed cluster investigation. Experiments have been conducted to reduce the effect of contamination using the Tecnai microscope. It has been found that leaving the area of interest under a wide electron beam in TEM mode at a magnification of 150x for 12 hours greatly reduces the build up of contaminants during prolonged STEM imaging. The contaminants under the low magnification electron beam are "pinned" to the surface by the interacting electrons and thus their mobility reduced when STEM imaging begins. The majority of samples imaged and presented in this thesis did not require such preparation. For the Jeol microscope a similar method can be employed, but widening the beam by switching to TEM mode is ill advisable as this turns off the aberration correction unit, meaning that it would have to be realigned when returning to the sample. Instead, using free lens control the power of the C1 lens is reduced to spread the beam in the same way as mentioned above. This would only be performed for 20 minutes to 1 hour. Plasma cleaning of the sample prior to imaging is also a method often employed for the reduction of surface contaminants. Should this method be available it would be advisable to use it with caution when performing cluster investigations, as the full effects of the cleaning process on small cluster structure are not known and could cause damage to the sample.
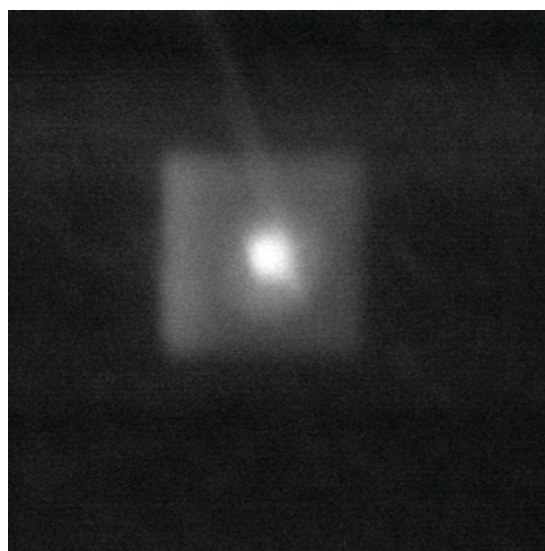
FIGURE 4.12: Low magnification STEM image of a blank a-C TEM grid. Effects of contamination can clearly be seen as the brighter area that had been scanned previously at a higher magnification. Image 20 nm by 20 nm.

Plasma cleaning was not used here.

During STEM imaging in both microscopes it was sometimes seen that the sample would suffer from mechanical drift. The sample holders allow movement of the sample under the electron beam, mechanically for large movement and using a piezo stage for fine movements. If the sample grid was not fully in place within the holder it was prone to drift, especially when the stage was being moved. At large magnifications this caused burring of the atomic features of clusters due to the movement of atoms between the time taken for each scan line. It was found that sample drift could be avoided if the sample was put into the column the night before a morning experiment, thus allowed the sample grid to reach equilibrium on the sample stage before imaging.

The majority of images taken with the Tecnai microscope analysed and presented within this thesis were taken at a magnification of 1.8 Mx. At high STEM magnifications the scan coils within the microscope feel the effect of mechanical and electromagnetic instabilities to a greater degree than at lower magnifications. A magnification of 1.8 Mx provides a level of detail high enough to make quantitative measurement of nanoscale structures such as clusters, whilst not experiencing much instability. It is also the case that to quantify the detected signal in HAADF-STEM reliably, the size of the pixels making up the image must be smaller than the spatial dimension of the scanning electron beam [122, 129]. When this criteria is met, integrating over a large range of

pixels is accurate due to each pixel carrying a small amount of information about the overall specimen. For instance, if the pixel size were larger than that of the beam, it would negate the purpose of using a sharply focused electron beam. With regards to the present study using the Tecnai microscope, each image was taken with 512×512 pixels, with the magnification of 1.8 Mx this gives a pixel size of 0.099 nm. A range of high magnification images were taken with the Jeol microscope; 15 Mx was the most used magnification for individual cluster structures. This corresponds to much smaller pixel sizes than seen with the Tecnai, for example, a 512×512 pixel image at this magnification gives a pixel size of 0.017 nm. Whilst the same image taken at the higher resolution of 1024×1024 pixels gives a pixel size of 0.008 nm.

P.E. Baston [57] investigated individual Au atom movement under the influence of the electron beam and Okamoto *et al* [114] state that the ability to quantify the size of individual nanostructures is primarily determined by the stability of the nanoclusters under the electron beam. For this reason when imaging using the Tecnai microscope repeat scans (x10) were performed upon samples prior to imaging and no evidence was found for a change in shape or movement of clusters. The increase in beam current for the Jeol microscope however subjects the cluster to much more intense energy and can result in atom movement. It is for this reason that image resolution was changed from 512 to 1024 pixels. This enables the scan time of the electron beam to be lessened or increased when needed, reducing the energy given to atoms within the cluster under investigation. When searching the sample and focusing the beam prior to recording the scan time was reduced by using 256×256 pixel resolution. The intention for many experiments is to establish the gas phase morphology of the cluster, and interaction with the beam for a prolonged time period would modify some atomic positions. Thus it can be considered that imaging Pd clusters using this microscope is a one shot approach due to the nature of atomic movement after one micrograph had been recorded.

The principle that spatial resolution in STEM is determined by probe size has been discussed previously. It is therefore essential that the user of a microscope has the ability to reliably reproduce a good alignment of the electron beam to obtain a small and well shaped electron probe. All STEM was performed using the nanoprobe mode with the C3 aperture and a large gun lens setting. Alignment and tuning was performed in order to give the best possible electron probe for cluster imaging. It is important to get the

smallest electron probe possible whilst retaining enough beam current for a good signal to noise ratio. A Ronchigram is an excellent tool for determining the electron probe shape and identifying aberrations [130]. The diffraction pattern in STEM is formed from a convergent beam. The central spot is a shadow image of the illuminated area, this is known as the Ronchigram. Figure 4.13 displays an example of a Ronchigram achieved after alignment in the Jeol system.
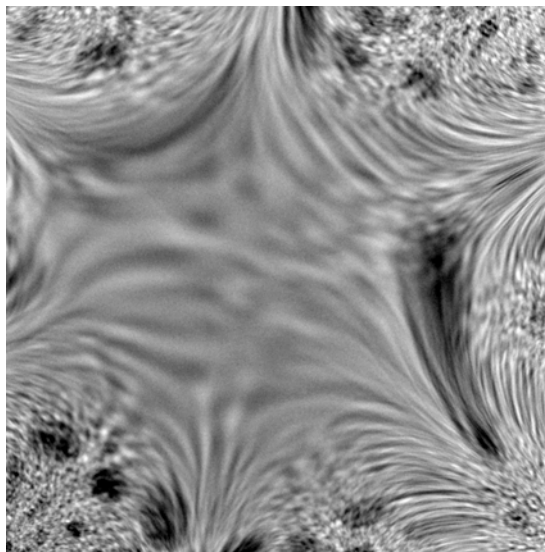
FIGURE 4.13: Electron Ronchigram from the Jeol 2100F microscope after beam alignment and aberration correction protocol. The image was taken using the Jeol Au nanoparticles standard sample with no condenser aperture inserted. See text for details.

The Ronchigram (Figure 4.13) image is taken with no condenser aperture inserted, thus allowing the entire part of the shadow image to be seen so that the lens aberrations can be corrected for. The central area appears flat (no contrast), showing a high magnification shadow of the amorphous substrate. This region is the area of the electron probe that is unaffected by spherical aberration. The area within this region is then selected for imaging by inserting a condenser aperture. The size of this region determines the size of the aperture that can be inserted, a larger region and thus aperture will give a better beam current incident on the sample whilst retaining a well formed probe shape, thus giving better signal to noise ratio and improved spatial resolution. Outside of this region is where the beam is affected by lens aberrations. The lines seen towards the edge of the image are due to the electron beams deviation from gaussian focus as a function of their angle through the lens [131]. It is important that the ronchigram is symmetrical; 6 fold symmetry is required by manual alignment of the beam initially, followed by achieving 12

fold symmetry after correcting for higher order aberrations using computational analysis in CEOS. A symmetrical ronchigram indicates that the probe is free of stigmatism (see Figure 4.15 (b) for an example of this aberration) and is centered about the optical axis. It should be noted that a Ronchigram taken with the Tecnai instrument would be circular, the symmetry seen here from the Jeol instrument is due to the non-circular geometry of the lens system within the spherical aberration corrector unit of the column (CEOS). A Tecnai ronchigram would also not have a region of zero contrast owing to the spherical aberrations of the lens system always being present in the absence of a corrector unit. An example of a Ronchigram taken using a Tecnai F20 microscope displaying these featuers can be see in Figure 4.14.
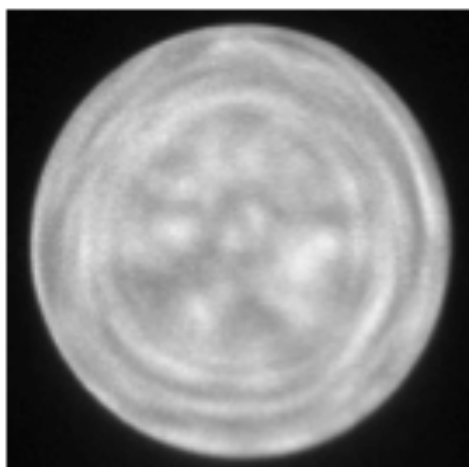
FIGURE 4.14: Electron Ronchigram from the Tecnai F20 microscope after beam alignment. See text for details.

When an object is imaged that is the same size or smaller than the electron probe being used to image it, the projected image is predominantly just that of the probe, this is known as object-probe convolution. For this reason, the smallest probe possible is desirable, however, a balance has to be met between probe size and electron beam current. Within both microscopes probe size could be changed by varying the spot size via the user interface. For the Tecnai, spot sizes could be picked from 1 (largest) to 11 (smallest), a spot size of 9 was used for all imaging due to the greater beam current available than at smaller sizes and high stability at this setting experienced by all users. The Jeol machine operated at a spot size, or SMMAG mode (as within the user interface) of 8c, this was recommended by the Jeol engineers. As mentioned previously, these spot sizes correspond to probe sizes of 4 Å and 0.9 Å respectively.

It was mentioned in a previous section how for STEM imaging there is no contrast reversal due to a non-oscillatory contrast transfer function. This was seen in Figure 4.5 where no matter the defocus value of the probe the contrast remained clear. However, as the probe defocus value changes, the edge of some clusters become blurred as others become sharp. Figure 4.15 (a) also shows an example of this from the Tecnai microscope, here a size-selected Pd_{212} cluster is imaged as a hollow disk when away from optimum focus. The defocus of the electron beam can therefore lead to errors in cluster size and integrated intensity measurement in HAADF-STEM. Care was taken to avoid this by achieving optimum focus for every cluster imaged. And by taking many data points to build up a statistical database of measurements, the standard deviation can represent the error based upon cluster measurements. Error calculations are discussed in the next section of this chapter.

(a)   (b)
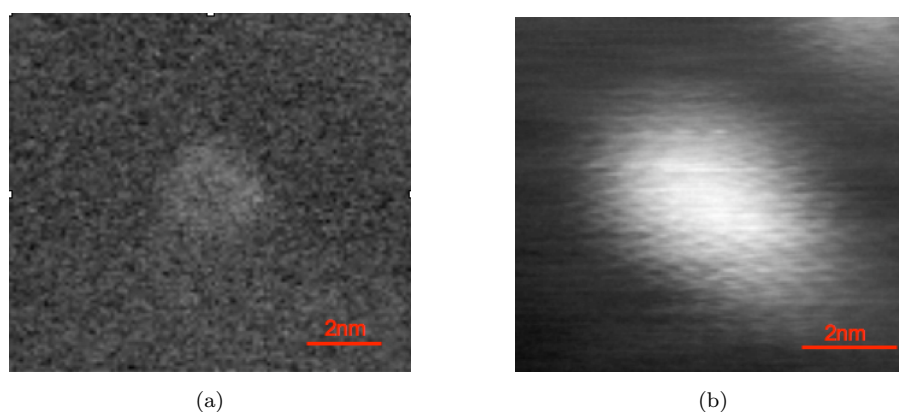
FIGURE 4.15: Examples of improper electron beam alignment using the Tecnai F20 Microscope in STEM, (a) non-optimal focus and (b) astigmatism: An Au cluster evaporated by an Edwards evaporator, it is seen to be stretched in the lower right corner due to this aberration.

Whether the probe converges above or below the sample is known as under or over focus. This terminology can be used to observe the difference in resolution achieved in the Jeol over the Tecnai microscope. As well as having better spatial resolution in the x- and y-directions, the Jeol microscope also has better resolution in the z-direction. A small change in defocus value on the Tecnai, leads to a larger change in the apparent probe size for the object and thus a poorer resolution than in the Jeol instrument. Figure 4.16 demonstrates this point schematically. Here both objects are imaged at the same defocus value, but because the beam converges more sharply on the Jeol instrument to a smaller point, the object is still in focus, although not optimally, due to a relatively

small probe still incident on the cluster surface. For the Tecnai system in the same situation, this defocus value leads to a more dramatic loss of features due to the probe size becoming a similar size to that of the object.
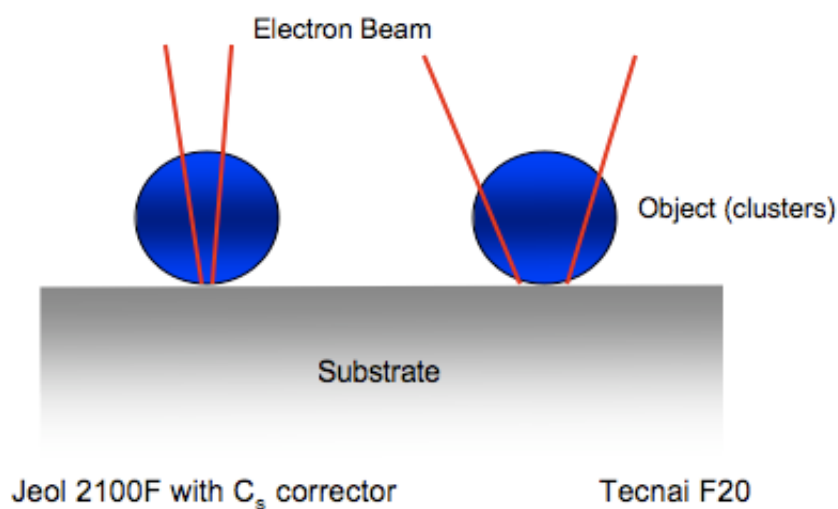
FIGURE 4.16: Graphical representation of a single defocus value in both the Tecnai and Jeol instruments to demonstrate resolution in the z-direction. Both objects are imaged at the same defocus value, but because the beam converges more sharply on the Jeol instrument to a smaller point, the object is still in focus, although not optimally, due to a relatively small probe still incident on the cluster surface. For the Tecnai system in the same situation, this defocus value leads to a more dramatic loss of object features due to the probe size becoming a similar size to that of the object.

Achieving the correct signal to noise ratio must also be considered at the detection stage where it affects the choice of collection angles used for the HAADF detector. Both instruments come with preset camera lengths that can be changed via the user interface for the detection of scattered electrons as required. It is shown in equation 4.14 that the scattering at high angles is proportional to Z^2. Experimentally though this is not entirely the case. Camera length is the effective distance between the sample and the detector [12] and by varying it, the inner and outer collection angles of the HAADF detector are changed. It has been discussed previously that incoherent imaging can only be imaged for high angle scattered electrons, thus the detection angles cannot be so small as to pick up the Bragg diffraction peaks or undisturbed electron beam or Z-contrast relationship would be lost. This is to say that the Z^2 relationship would not hold true, but instead would take some other power exponent value, lets say Z^α. However, for electrons scattered and detected at high angles, α would have a value of ≈ 2, but signal

would be lost as relatively few electrons would be detected. Thus a compromise between the power exponent value of the Z-dependance and signal to noise relationship has to be achieved for quantitative HAADF-STEM imaging.

Figure 4.17 (a) shows how the integrated HAADF intensity for Pd_{923} clusters changes with camera length in the Tecnai F20 microscope, with large camera lengths (smaller detection angles) leading to a greater number of detected electrons. Images displayed in Figure 4.17 (c) and (d) show this dependance visibly within the micrographs. The micrograph of industrial Pd catalyst taken with a camera length 120 mm has a much weaker signal of scattered electrons from clusters than that taken at 520 mm. In this case it is the inner detection angle that is of most importance as this is the angle which will be most likely to detect coherently scattered electrons. Figure 4.17 (b) demonstrates that as the inner detection angle is increased the integrated HAADF intensity for Pd clusters is reduced [132].

A more quantitative measurement of the Z-dependance for a certain camera length can be done by determining how close to Z^2 the scattering is. This is done by calculating ratios of the integrated intensities of two equally sized clusters of different material. For example, Wang *et al* [132] performed experiments using the Tecnai F20 microscope at Birmingham finding that for camera lengths of 285 mm the Z dependance was $Z^{1.32}$. For Pd clusters analysed within this study using the Tecnai instrument a camera length of 285 mm has been used consistently, this corresponds to inner and outer detection angles of 25 to 127 mrad respectively. At large camera lengths, contrast reversal of Pd clusters was started to be seen due to the detection of coherent electrons. At small camera lengths the scattered electron signal became too weak to distinguish cluster perimeters accurately with respect to the substrate (noise), especially for smaller Pd clusters. Hence the intermediate value of 285 mm was chosen. For the Jeol instrument a camera length of 10 or 12 cm has been employed for the same reasons. This corresponds to an inner collection angles of 52 and 61 mrad and an outer collection angle of 140 and 163 mrad respectively.

Experimental variables such as camera length are vital when considering the quantitative interpretation of scattered signal from clusters in order to achieve the quantitative HAADF-STEM interpretation of images. However, this becomes redundant should the detector not be capable of single electron sensitivity and have an output voltage that is

(a)

(b)

(c) (d)
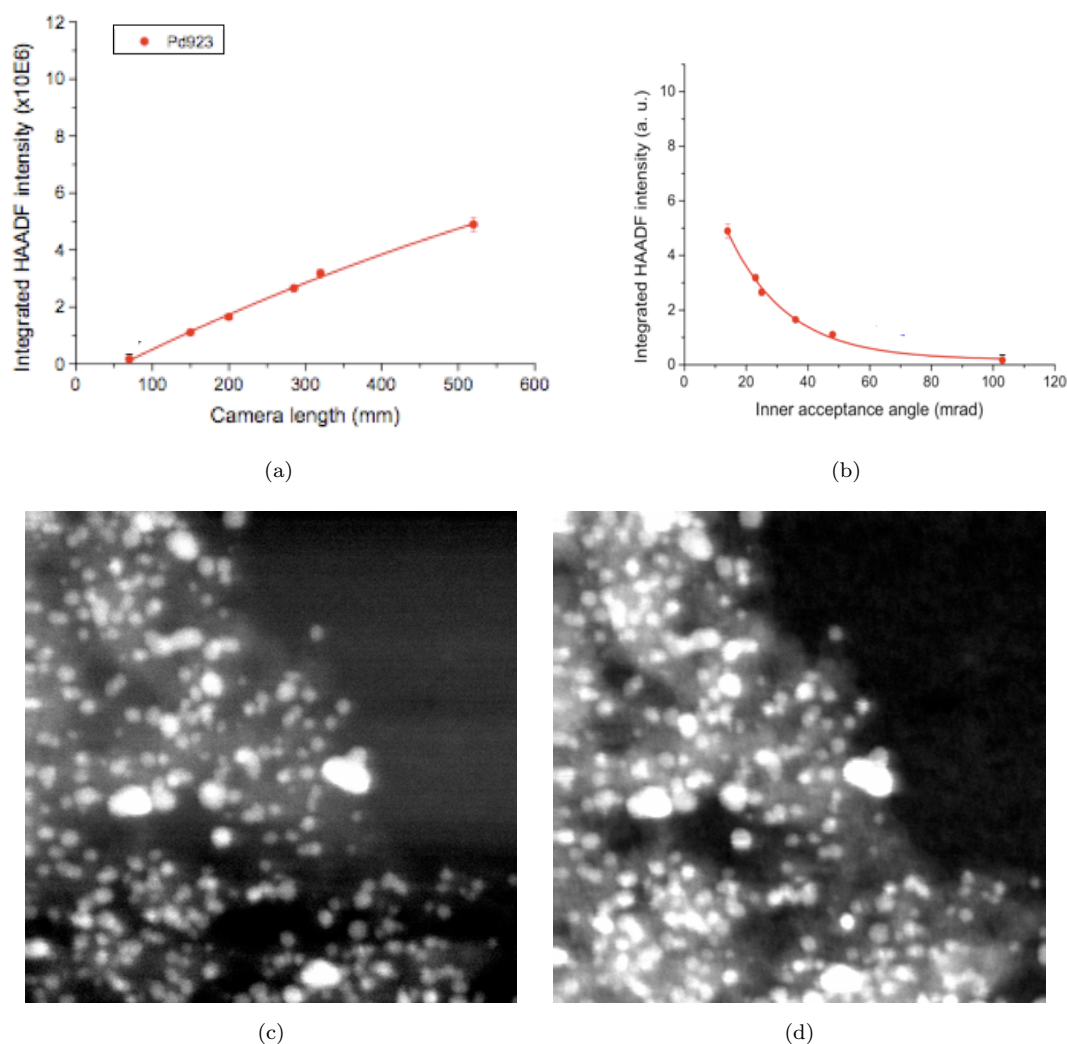
FIGURE 4.17: All figures represent data acquired with the Tecnai F20 microscope (a) A plot to show camera length as a function of integrated intensity of Pd$_{923}$ clusters using the HAADF detector in STEM mode. (b) A plot to show the inner acceptance angle of the HAADF detector as a function of the integrated intensity of Pd$_{923}$ clusters. Figure adapted from reference [132]. (c) and (d) HAADF-STEM micrographs of industrial Pd catalyst particles taken with camera lengths 120 mm and 520 mm respectively. Both images are of the size 73 × 73 nm.

proportional to the scattered intensity received [133]. For the case of both microscopes used within this study, each HAADF detector was capable of such measurement enabling the quantitative interpretation of HAADF STEM micrographs.

When imaging clusters in HAADF-STEM and recording their scattered intensity one should be aware of the channeling effect. Electron channelling occurs when the sample imaged has a crystal structure orientated with a zone axis parallel to the electron beam [134]. In this explanation the electron beam tends to stick close to the atomic columns

when transmitted through the cluster [12]. This results in the scattered intensity of electrons from the cluster being maximised and the cluster appearing brighter in the recorded micrograph than a cluster of the same size and element, but in an off-axis orientation. With relevance to this study, one would look for differences in intensity for all clusters made of Pd which may have arisen from this effect, however, generally these effects are small [116]. A good example of channelling can be found in an investigation done at Birmingham University using the Tecnai F20 microscope. Figure 4.18 shows HAADF-STEM images of bimetallic CuAg nanoparticles in (a) and Cu nanoparticles alone in (b). The scattered intensity variation is seen for the CuAg nanoparticles could be attributed to the increased scattering intensity that would be seen for Ag atoms due to its higher atomic number than Cu. However, the image of Cu nanoparticles alone shows similar intensity variations, hence the effect seen in (a) is likely not to be from Z-contrast effects alone. These images were taken with a camera length of 520 mm corresponding to a inner collection angle of 12 mrad, hence, as discussed before, they are prone to Bragg scattered electrons. The investigation discusses how the correct camera length should be chosen to avoid these effects and also how tilting the sample can allow identification of channelling effects. If the intensity variation disappears when the sample is tilted, then the scattered intensity from the new orientation of the cluster may now be interpreted as Z-contrast.
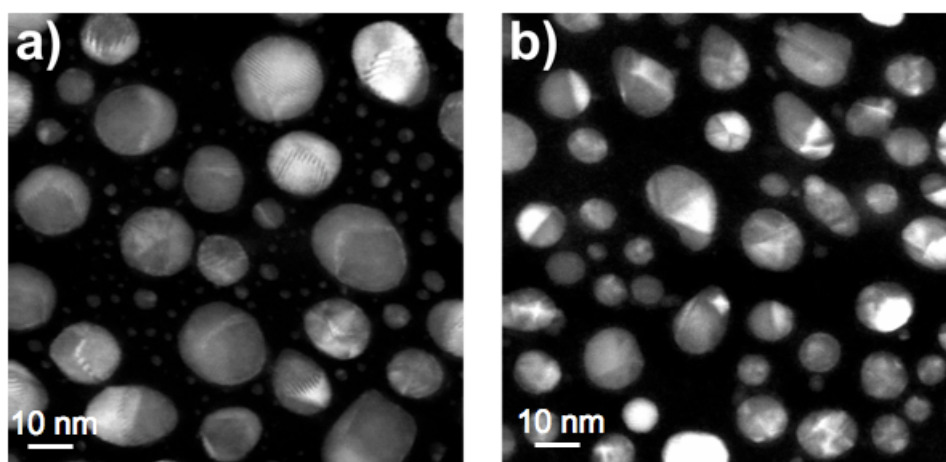
FIGURE 4.18: HAADF-STEM images taken with the Tecnai F20 at Birmingham University. Camera length of 520 mm used (inner collection angle 12 mrad). (a) CuAg nanoparticles (b) Cu nanopartilces [134].

Care has been taken to avoid possible distortion of the interpretation of HAADF scattered electrons within this study due to the channelling effect. Any cluster with a

suspected uncharacteristic bright region has been excluded from integrated intensity analysis; however this was found to be rare for the camera length used in this study. With the quantity of clusters imaged, this has not been an issue in terms of data acquisition.

Other experimental aspects that are worth considering within HAADF-STEM experiments will be discussed within the results chapters of this thesis, here an overview of setting up the microscope in order to perform the experiments is presented.

4.4.2 Image Processing - Methods of Analysis

Analysis of HAADF-STEM images taken with the FEI Tecnai F20 microscope was performed using an image analysis program called ImageJ [135]. For images taken with the Jeol 2100F microscope the program called Digital Micrograph (DM) was also used [136]. Measurements of integrated cluster intensity, diameter and aspect ratio have all been applied to clusters investigated within this study, each subsection to follow describes how these measurements were taken as well as the other options which were considered.

4.4.2.1 Measurements of Intensity

There were two ways which the integrated HAADF intensity from a Pd cluster could be measured. By integrated HAADF intensity one refers to the number of electron counts received by the HAADF detector as scattered there by the entire mass of an individual cluster. Both methods involve a background subtraction protocol, since the scattered intensity recorded from a cluster will also be due to a small amount of scattering arising from the a-C support. The first method described is the one employed within this study.

The HAADF image intensity was recorded by tracing around the perimeter of each individual cluster, recording the intensity, and performing a background correction arising from the a-C support. The perimeter drawn around individual clusters for intensity analysis was moved to an adjacent site of the cluster in question. Image intensity of the pixels surrounding the cluster was then recorded with the area occupied by the

perimeter being the same as the surface area of the cluster itself. Background subtraction was then achieved by repeating this process three times, averaging the surrounding intenities and subtracting this value from that of the original cluster intensity. This value was then taken as the total integrated intensity of the cluster. Here, the intensity contribution provided by the a-C support material on which the cluster rested had been estimated and then removed, thus a more accurate value of cluster intensity obtained. This procedure is summarised in Figure 4.19 (a) and by the following equation;

$$I_{cluster} = I_1 - (\frac{(I_2 + I_3 + I_4)}{3})$$ (4.16)

Another method for cluster integrated intensity measurement takes the following approach. The perimeter of the cluster is traced and intensity recorded, giving an area A_1 and intensity I_1. A second perimeter is traced around the cluster but is larger than A_1 so as to include some of the surrounding a-C support. This gives an area A_2 and an intensity measurement of I_2. The cluster integrated intensity is then given by equation 4.17 and is shown schematically in Figure 4.20 (a),

$$I_{cluster} = I_1 - (I_2 \times \frac{A_1}{A_2})$$ (4.17)

Figure 4.19 (b) and Figure 4.20 (b) display histograms showing the distribution of integrated intensity measurements for Pd_{3500} clusters for both methods described. As is clear from the results, there is little difference in either method. The first method used gives a average cluster value of $(12.2 \pm 1.6) \times 10^4$ and the second method gives $(11.6 \pm 1.4) \times 10^4$. In both cases the standard deviation is used for error about the mean. Due to the similarity of these results and with no way of quantifying the accuracy of either method, the practicality of integrated intensity measurement had to be considered when deciding which to use. Many of the clusters displayed in the electron micrographs under analysis within this study have neighbouring clusters close to the perimeter of the cluster awaiting analysis. A prime example of this can be seen in Figure 4.19 (a) where a Pd_{887} cluster is seen next to a Pd_{10000} cluster which is being analysed. Thus using the second method of integrated intensity measurement in this case would not be practical. Hence the method chosen for this study is the first one described in this section. Background
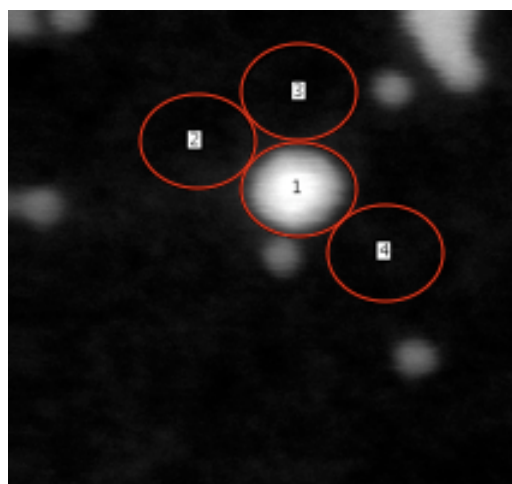
(a)
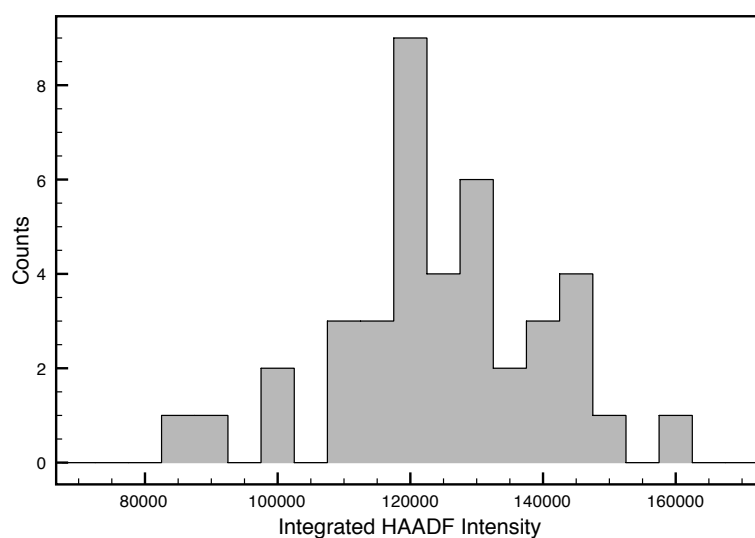
(b)

FIGURE 4.19: (a) HAADF-STEM image of Pd_{10000} and Pd_{887} clusters to display the method used for integrated intensity measurement (50×50 nm). The regions marked with red circles have the same area as each other (representing the area within the perimeter of the cluster under analysis) and are numbered from 1 to 4. This corresponds to the intensities measured using equation 4.16. (b) A histogram of measured integrated intensities for 40 Pd_{3500} clusters measured using this method.

subtraction protocol of this kind has to be employed as the contribution to the intensity provided by the support is not uniform, and has to be estimated via the nearest sites surrounding the cluster in question.
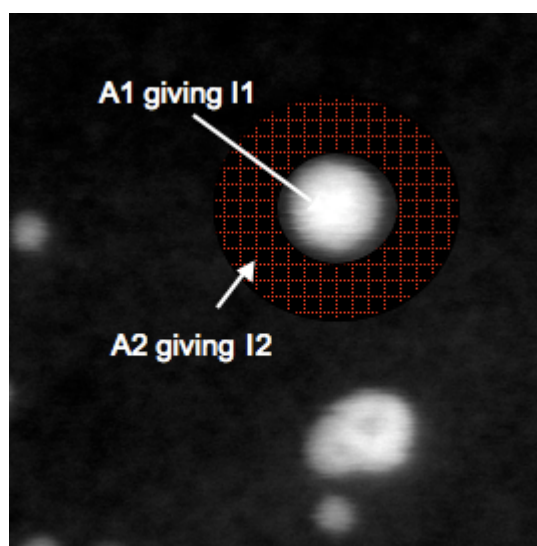
(a)
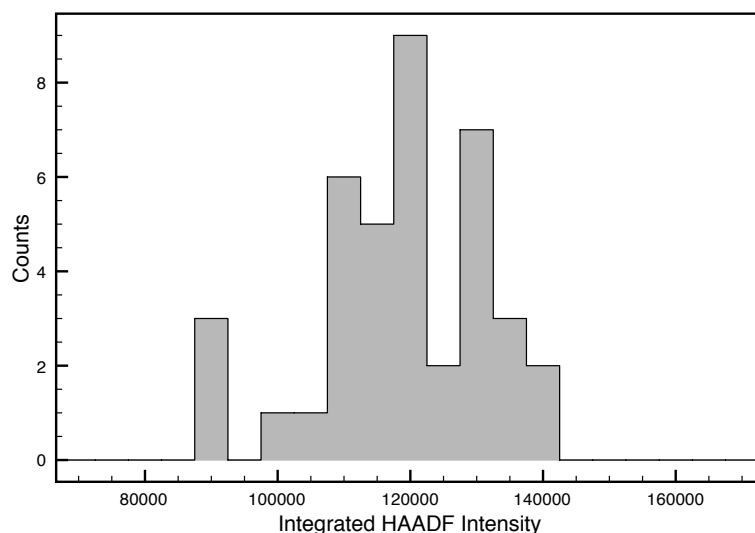
(b)

FIGURE 4.20: (a) HAADF-STEM image of Pd_{10000} cluster used to display the method of alternative integrated intensity measurement (50×50 nm). The figure displays labels corresponding to equation 4.17 and details are found in the text. (b) A histogram of measured integrated intensities for 40 clusters of one size measured using this method.

4.4.2.2 Measuring Cluster Diameter and Aspect Ratio

Diameter measurements were taken for all clusters with a circular projection under the electron beam. Due to the circular projection, the diameter measurement could be performed simultaneously with that of integrated intensity. By tracing the perimeter of the cluster, the area, A, of it can be determined easily via the program ImageJ. This area

can then be converted into a diameter measurement due to the relationship $A = \pi r^2$, where r is the radius and is equal to half the diameter.

For clusters seen that did not have a circular projection an alternative method of defining the cluster shape was required. Within the literature, defining irregular morphology uses different methods. An interesting use of two dimensionless determinations is that used by Korolev and Isaac [137] in determining the roundness and aspect ratio of ice clouds. Here many irregular morphologies are seen so just using the aspect ratio of the structure does not give a true representation of ice cloud morphology. This is where the roundness value, β comes in; it is determined by:

$$\beta = \frac{4S_{meas}}{\pi D_{max}^2}, \tag{4.18}$$

where S_{meas} is the area of the projection of the object and D_{max} is the maximum dimension of the object shape. Alternatively, Bele *et al* [138] defines the circularity of clusters as the equivalent circular circumference over the particle perimeter. Values for this range from 0 for totally irregular clusters to 1 for an ideal circular cluster. This study also utilised a computational method known as local adaptive threshold (LAT) to study many more clusters from TEM images than would normally be done using the by-eye by-hand method [138]. LAT used more complex methods to determine the cluster perimeters than is needed in Z-contrast imaging due to the nature of contrast for bright field images.

In this thesis, clusters seen to have non circular projections under the electron beam have been analysed using two methods, that of aspect ratio and cirularity. For the case of size selected Pd clusters the method used was to define the aspect ratio. In this case, the clusters were not irregular or asymmetric in projection, but all appear elongated along one axis. Therefore the choice of aspect ratio analysis is relevant as the results symbolise the magnitude of the deviation along the elongated axis. If circularity was used, then the resultant data would only signify the deviation from circular projection. For example, a cluster elongated along one axis may have the same circularity value as a cluster with a very asymmetrical projection, but where elongation has occurred in multiple directions. So circularity would not quantify the data for size selected Pd clusters in the correct manner. This data can be found in chapter 6. For Pd catalytic

particles investigated using the Jeol 2100F microscope, however, some were found to be very irregular in shape. In this case the aspect ratio measurement is not suitable as it would not represent the deviations away from either the defined x or y axis. Circularity is used in order to quantify the deviation from circular projection. Figure 4.21 displays examples of two clusters where both aspect ratio (a) and circularity (b) were required for different purposes.

Aspect ratio measurements were taken by drawing a multiline profile (11 lines) over a cluster's shortest dimension but passing through the central point of the cluster. The line profile produced was a projection of the intensity over the length of the line and the edge of the cluster was easily visible due to Z-contrast making Pd easily distinguishable from the a-C support. This length was determined by taking 10th width full maximum at each end of the profile. The length value was displayed within the image processing software by positioning the mouse at the required spot, and then clicking and dragging it to the opposite end of the profile. This step was then repeated for the clusters longest dimension. The aspect ratio is given by the longest length of the cluster divided by the shortest length. Aspect ratios of 1 represent circularly projected clusters, ratios of 1.1 to 1.5 maybe thought of as egg-shaped in projection and values above this elongated. This type of measurement could be performed using both ImageJ and DM. Circularity measurements were calculated by taking the equivalent circular area of the particle and dividing it by the projected area of the particle. The perimeter of the particle was traced to obtain the projected area measurement and the circular projection was drawn surrounding the particle in question. This is best described by illustration and can be seen in figure 4.21 (b). The area inside the circle surrounding this cluster is the measurement taken.

For the measurement of atomic distances when analysing images taken with atomic resolution the program DM was used. A multi line profile can be drawn over atomic columns of the cluster seen in the image. The distance between the peaks of the atomic column profiles can then be measured using the same method as used to determine the length of the aspect ratio profiles.
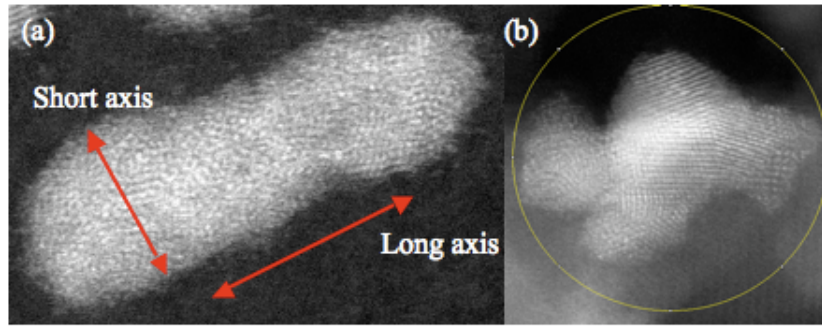
FIGURE 4.21: HAADF-STEM micrographs of clusters (a) Pd_{10000} and (b) Pd catalyst particle on Al_2O_3 taken with the Jeol 2100F with C_s corrector microscope. The cluster in (a) is suitable for aspect ratio analysis. The cluster in (b) is suitable for circularity analysis. The circle shown in (b) represents the equivalant circular area of the particle. See text for details.

4.4.2.3 Error Analysis

For all samples, between 200 to 300 clusters were analysed when measuring HAADF intensity and diameter. For aspect ratio measurements 60 to 100 clusters were measured of each size. The calculated error for manual measurement of cluster diameter was calculated using the equation below.

$$\sigma_{d_{av}}^2 = \frac{(\sigma(x)^2 + \sigma(y)^2)}{2^2} \tag{4.19}$$

When multiple results were calculated, the standard deviation, s, from the average was used. This can be seen in the equation below where x_i is the manually measured diameter, x_{av} is the average diameter of cluster size and N is the number of clusters measured.

$$s^2 = \frac{1}{N-1}\Sigma(x_i - x_{av})^2 \tag{4.20}$$

Standard deviation was also used to calculate errors for HAADF intensity distributions, due to its direct relationship with the half width half maximum (HWHM) of a Gaussian distribution as seen in the following chapters [139]. Errors taken for individual cluster integrated intensity measurements were minimal given that incoherent scattering was achieved. Contributions of error arising from background intensity measurement exist because the true intensity from the a-C atoms beneath any cluster was not directly

measured. However, this error is difficult to quantify and has been reduced by averaging the intensity values of areas surrounding the clusters. Any errors calculated on the number of atoms, N, within a cluster are to $\pm 4\%$ of its N value.

The main source of error for any measurements concerning this study is due to the non-uniform a-C substrate. Statistical analysis of clusters has been employed to reduce this and the error values display the size range whithin which the measured integrated intensity or cluster diameter are most likely to lie. There are some errors that have arisen which are difficult to quantify. For example, detector noise and the rotation of clusters or movement of single atoms upon the cluster surface under the electron beam. These errors are thought to be minimal however and where relevant are discussed in further depth together with the presented results.

The integrated HAADF intensity data is presented in histograms showing the distribution of values recorded for each cluster mass. The bin size is chosen to best represent the distribution of intensity values within the measured range. A bin size too large would not display the distribution of data sufficiently. Equally, a bin size too small, whilst giving the same statistical conclusions as any bin size represented within the results, would not graphically represent the data in a way so as to easily distinguish the peaks.

Chapter 5

Size and Shape of Industrial Pd Catalytic Particles using Size-Selected Clusters as a Mass Standard

5.1 Introduction

It is well established that the performance of catalyst particles is closely related to their size and shape [140, 141]. In a review article by Haruta [142] concerning the use of Au as a catalyst it is stated that the performance of a catalyst of any metal is dependent on three factors: the contact between the Au and the support; the type of support; and the size of the particles. The formation of structures with low surface to volume ratios are thermodynamically preferred, hence bulk materials Pd represents the lowest energy structural configuration. So in producing nanoparticles for use as a catalyst there will be a tendency to agglomerate where possible to minimise this ratio. The presence of stabilisers is required to prevent this happening by providing barriers between catalytic particles and in some cases assisting in structural control [67]. The Pd catalyst under investigation in this chapter is suspended in a carbon blacks support, but in the final section of this chapter the support material of Al_2O_3 is also studied. To

date the reasons stated in Haruta's review have been the main source of explanation for the catalytic activity of noble metal nanoparticles. More fundamental investigations as to how the activity is determined in terms of structure also exist. At the atomic scale, there are preferential structural features that favour catalytic activity [143–146]. It is often considered that the low co-ordination sites of nanoparticles offer the most useful sites for any specific reaction. For example, reactivity in methoxycarbonylation process using PVP stabilised Pd particles was found to increase with the fraction of surface atoms at corners or edges in a study by Gniewek *et al* [68]. Both experimental and theoretical studies also show an increase in catalytic activity for small Au nanoparticles with low co-ordination atoms for the CO oxidation reaction [11, 147]. Other structural features have also been found to favour catalytic activity in Pd nanoparticles. Taking the hydrogenation process for example, here the (111) face of the Pd nanoparticle is utilised for this reaction [67]. For the case of the cube-octahedron, as the particle size increases, the only surface atoms to increase in number are those of the (111) face. The overall effect is that there will be a smaller percentage of surface atoms as well as edge or vertex atoms. Thus it is apparent that the most efficient structure for catalysis is dependent on the reaction that needs to take place, however, as a general rule, the size and support material of the catalyst can be a good indicator of its reactivity.

In order to develop efficient catalysts, it is of extreme importance to correlate catalytic properties of clusters with their size and shape, as well their atomic structures at each stage of design, synthesis and catalytic reaction. Experimentally the structural determination of catalytic particles on surfaces is a challenging task. In particular, industrial catalytic clusters often have a wide size range and show a variety of shapes. Within Pd catalysts prepared by Chen *et al* [148] for the aerobic oxidation of alcohols a size range of 2.2 to 10 nm particles were found, with only the samples containing a large amount of 3.6 - 4.3 nm sized particles giving the best reactivity. Good reviews into the range of structures seen within metallic catalytic samples and Pd nanoparticles can be found in the works of Narayanan *et al* [143] and Piccolo *et al* [149]. In both reviews, structures, characterised by TEM, were found ranging from elongated nanoprisms, cubes, multiply twinned and tetrahedral particles.

Transmission electron microscopy based techniques provide excellent ways of caracterising such clusters [114, 150]. Moreover, work developed from the 70's onwards by

Treacy *et al* [129, 151] highlighted the advantages of utilising high angle annular dark field scanning transmission electron microscopy (HAADF-STEM) technique for catalytic particles. In 1978 the first utilisation of this method for catalyst characterisation was published. This showed how the Z-contrast images provided better contrast, revealing structural features in more detail, than conventional TEM or hollow cone dark field imaging. In 1989 Treacy *et al* developed this method and were able to quantify catalytic particle sizes by showing how Rutherford scattered electrons were proportional to the number of atoms probed by the beam. This had great advantages over conventional size characterisation where data was reliant on dimensional measurements. The mass of Pt catalyst nanoparticles was derived for sizes up to 3.5 nm by computation of the HAADF intensity increment per atom. However, the mass measurements had a large associated error due to the need to make assumptions regarding particle morphology.

STEM is also known as Z-contrast imaging since, at high scattering angles, the cross sections depend strongly on atomic number, Z [152–154]. This was discussed in detail in Chapter 4. It provides incoherent images, and there is no contrast reversal with sample thickness, hence image interpretation is more straight forward than phase contrast imaging. This technique has recently gained significant popularity in catalyst characterisation following the advancement of aberration corrected transmission electron microscopy [155]. This will be discussed in greater detail in the final section of this chapter. Recent reports have focused on three-dimensional structure of real catalysts. For example STEM tomography has been performed on Pd, Pt and Ta catalysts by taking a series of images at different tilt angles [156–158]. The final morphology of the particle can then be seen through a re-construction of the series of two-dimensional images. Investigations into Pd/Ru and Pd catalysts by Midgley *et al* [153] and Benlekbir *et al* [159] using STEM tomography have been able to reconstruct the catalytic particle shape and position within the support to within 1 nm^3 and 2 nm^3 respectively. The detailed morphology of the catalysts is apparent, though the exercise is rather time-consuming.

Another approach aims at placing the scattering cross-section on an absolute scale by measuring the incident electron beam current [133]. Here, quantitative HAADF-STEM imaging was performed by normalising scattered intensities to the incident beam; comparison to theoretical simulations showed good agreement with the experimental results.

Quantitative STEM images then allow three-dimensional information about the materials to be extracted. The beam current measurement is normally unavailable in many laboratories. Where measurement of this kind is not possible, theoretical values or assumptions have been introduced. In one such study by Yang *et al* [150], the HAADF images were converted to elastic scattering cross sections. A detailed knowledge of the detector efficiency, and direct comparison to theoretical cross sections, allows the number of atoms within a catalytic particle to be determined. Other theoretical approaches can be found in the form of exit wave reconstruction. Gontard *et al* [160] uses aberration corrected TEM in conjunction with exit wave reconstruction to identify the active sites of a commercial Pt catalyst.

In order to gain quantitative interpretations of HAADF-STEM images a calibration factor is required so that scattered intensities can be normalised. From the study above into current methodology in this field, it is apparent that these techniques require extra equipment within the microscope column (for the case of incident beam measurement), or theoretical comparisons (exit wave reconstruction and cross section calculation). For the case of tomography, distinct advantages exist in the structural detail produced, nevertheless it is a time consuming process to study the wide variety of structures present in a catalytic sample. For results presented in this chapter, an alternative approach to the evaluation of catalyst particles is taken by using clusters of a pre-determined size, formed in the gas phase and soft landed on a-C surfaces, as mass standards in STEM imaging. In this case scattered intensities of size-selected clusters are used to place the unknown particle intensity on a scale, and measurements allow three dimensional data to be extracted from the sample. Normalisation factors are also present to ensure microscope conditions are kept consistent. This method will be described in detail in the following paragraphs. The potential of this technique is exploited for a real Pd industrial catalyst, provided by Johnsson Matthey.

The details of sample preparation of both the size selected clusters and catalysis particles can be found in Chapter 3. Size selected Pd cluster sizes of N = 454, 887, 1103, 1389, 2046, 2622, 3000, 3500, 4500 ($\pm$ 4 %) were used as mass standards for the characterisation of commercial catalyst, Pd on carbon (sample number 87L). For details of analysis methods and experimental preparation within the STEM see Chapter 4.

5.2 Measurement of Size Selected Clusters and Catalytic Particles

Figure 5.1 displays a collection of HAADF-STEM images of the industrial Pd catalyst. This figure gives a good overview of the typical Pd particle areas and sizes of Pd catalytic particles that underwent study. Figure 5.1 (b) is a magnification of the central area shown in (d), which provides a good low magnification image of the Pd catalyst sample. Figure 5.1 (a) and (c) are example images that would be used for integrated intensity and diameter analysis. Intensity and diameter analysis was performed using the protocol described in Chapter 4: Section 3 of this thesis.
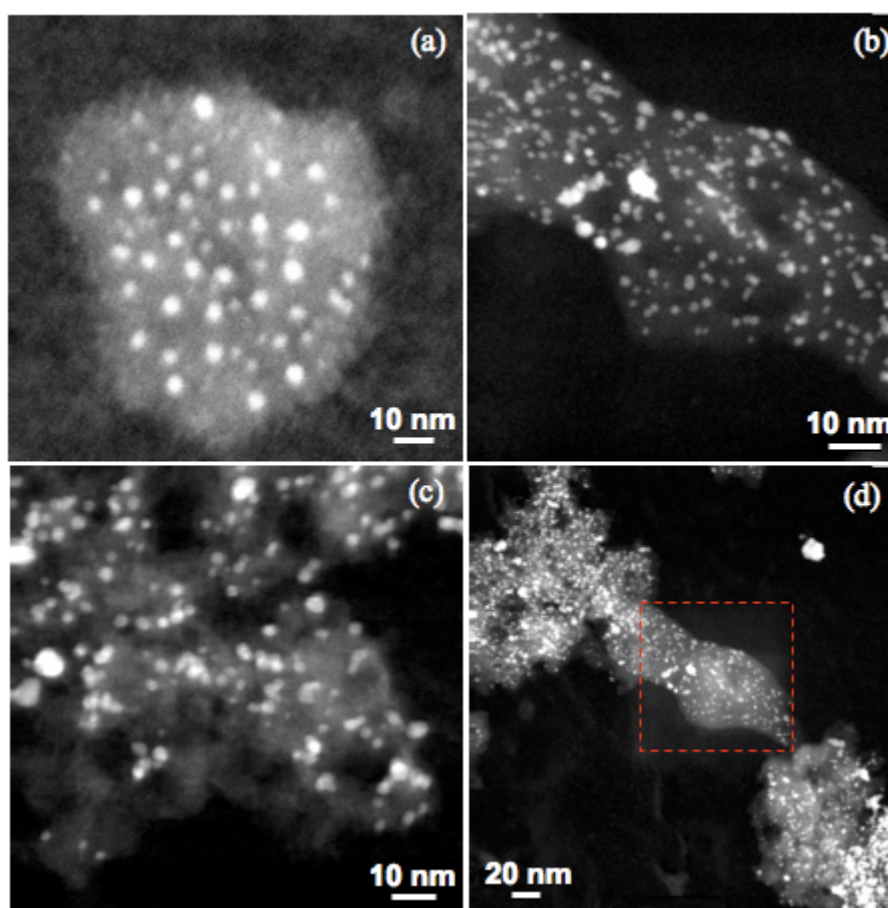
FIGURE 5.1: HAADF-STEM images of an industrial Pd catalyst deposited on an a-C surface via the deposition method described in chapter 3. (b) is a magnification of the central area of (d), marked with a red border, which shows a low magnification image of the catalyst giving a good idea of cluster distribution. (a) and (c) are typical images used for integrated intensity analysis and diameter measurement.

The diameter distribution of the Pd catalyst particles is shown in Figure 5.2 (a). Diameters were measured using the method described in section 4.4.2.2 of this thesis. Most particles lie within the range 1.6 to 2.6 nm in diameter. One cannot extract full three-dimensional structural information from the diameter measurement alone, since they represent a two-dimensional projection. To characterise the catalyst particles more fully, the HAADF intensity integrated over each particle is carefully analysed using the software package ImageJ and plotted in Figure 5.2 (b). Background subtraction protocol means the intensity contribution from the unevenness of the support is minimised.
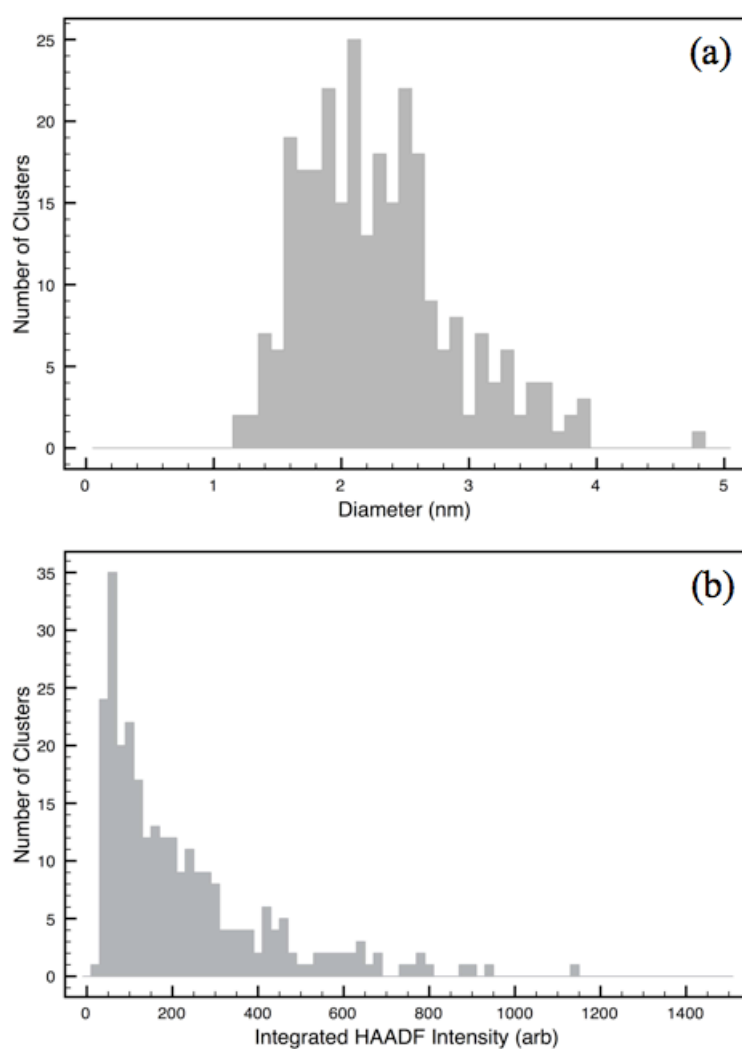
FIGURE 5.2: (a)Histogram of measured diameters of Pd catalyst particles. (b) Histogram of the integrated HAADF intensity of the corresponding catalytic particles.

To translate the nanoparticle intensities of the industrial catalyst into the number of

atoms in the particles, size selected clusters are used as a standard for the HAADF-STEM intensities. Although much care was taken to ensure microscope conditions remained constant throughout the experiment, as described in chapter 4, due to the time scale of the data collection it was important to introduce a factor that could quantify any changing conditions. To deal with any fluctuations in the microscope conditions, the integrated intensity data for the Pd clusters were calibrated against a particular size of cluster, Pd_{887}. Each data set taken could be normalised to this cluster size by imaging the Pd_{887} cluster alongside each sample. For size selected clusters this was done by co-deposition of Pd_{887} and Pd_N clusters on each sample grid. For the Pd catalyst particles a Pd_{887} standard sample was imaged immediately prior to Pd catalyst imaging and microscope conditions monitored throughout the experiments. Figures 5.3 (a) and 5.4 (a) present HAADF-STEM images for samples where size selected Pd_{887} clusters are co-deposited with Pd_{2046} and Pd_{3000} respectively, on the same TEM grid. The HAADF intensity histograms display unambiguously two well separated peaks for Pd_{887} and Pd_{2046} in Figure 5.3 (b) and for Pd_{887} and Pd_{3000} in Figure 5.4 (b). A histogram representing diameter measurements for Pd_{887} and Pd_{2046} clusters is shown in Figure 5.3 (c). Again, two clear peaks are seen represented by each size of cluster. For diameter measurements on size selected clusters, only those with circular projections were measured. Any deviation from this projection is presented and discussed in Chapter 6.

Fig 5.5 shows a plot of size selected cluster diameter vs integrated intensity to the third. Plotting HAADF intensity to the third gives a linear relationship due to the integrated scattered electron intensity being proportional to the number of scattering atoms present. Thus, the intensity is proportional to the cluster volume, and hence can be plotted as seen in Figure 5.5. This plot illustrates how size selected clusters are more readily distinguishable from their integrated intensity values than the diameter measurement. Although some overlap exists within the error bars for integrated intensity values, this relationship is apparent. For larger cluster sizes than those presented here, this point would be even more valid. The intensity measurement will increase with greater magnitude than diameter for clusters of increasing size. It should be considered though, that at a certain point the proportionality between HAADF intensity and N may break down due to sample thickness (see Chapter 4). The data plotted for clusters with different N values is readily distinguishable by intensity but with similar diameter
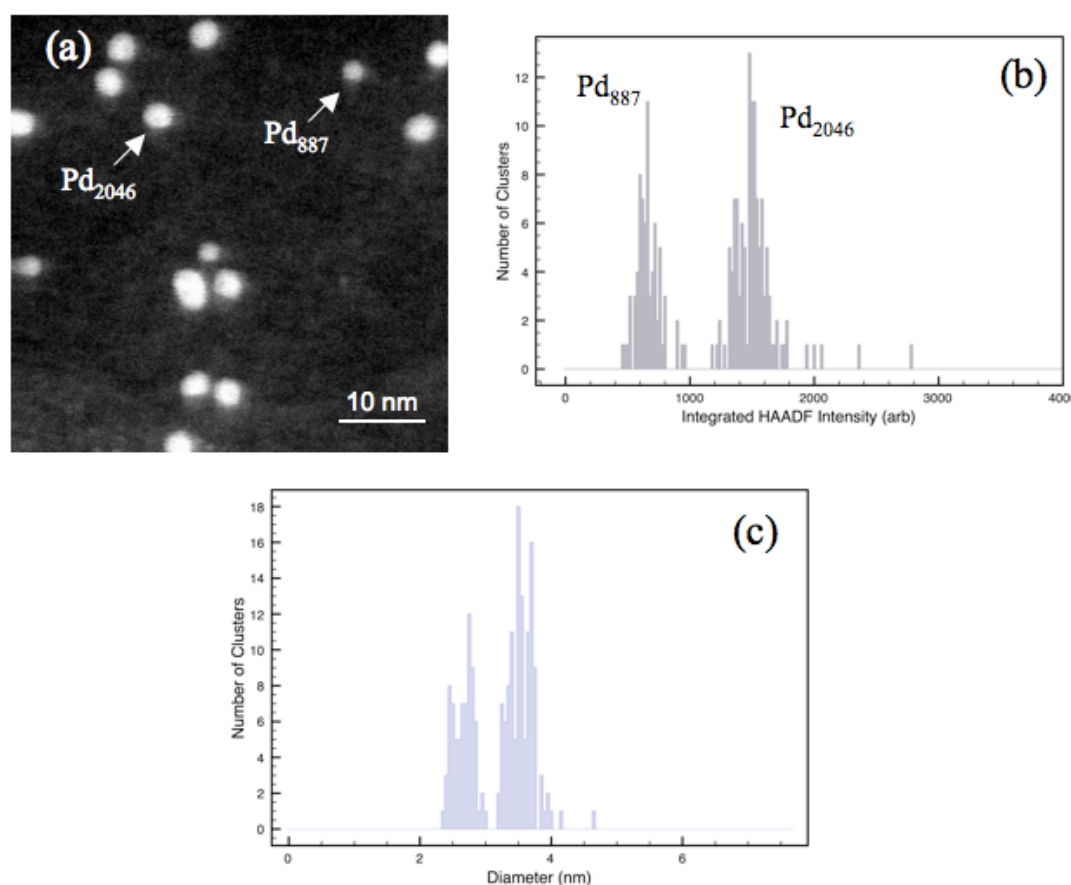
FIGURE 5.3: HAADF STEM image (a), a histogram of integrated cluster intensity (b) and a histogram of cluster diameters (c), for a mixed sample of Pd_{887} and Pd_{2046} clusters. Pd_{887} is used as a calibration against all other Pd cluster sizes.

measurements. This may make identification of size selected clusters difficult based upon diameter measurements alone, hence the integrated intensity measurement is also an integral part of cluster size characterisation.

5.3 Integrated Intensity vs Number of Atoms

From the measurements of integrated HAADF intensity, the number of atoms contained in the Pd catalytic particles can be determined. Measurement of the incoherently scattered electron intensity and cluster size, N, has been exploited to establish the relationship between the two variables, under the specific experimental conditions set. The calibration factor, Pd_{887} has been imaged alongside each cluster or catalytic particle to account for fluctuations in experimental conditions. Figure 5.6 displays the HAADF intensity integrated over the size selected clusters as a function of the number of atoms, N,
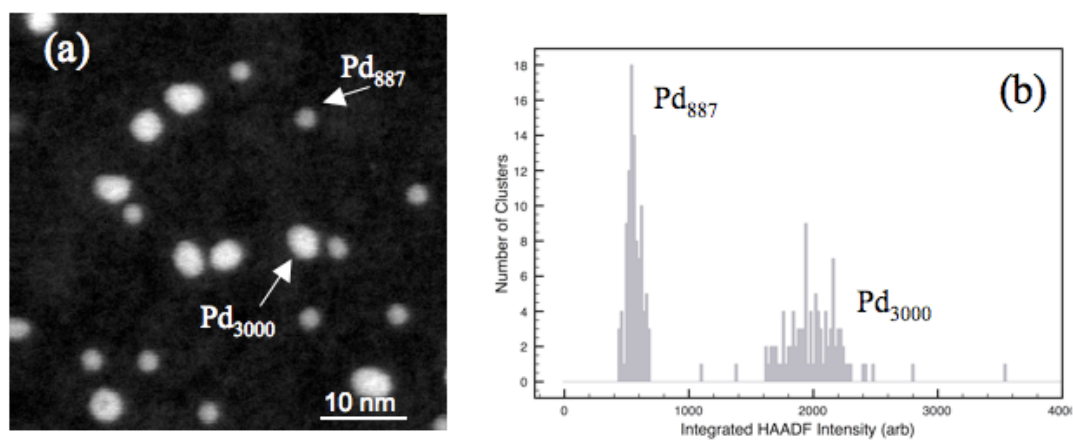
FIGURE 5.4: HAADF STEM image (a) and a histogram of integrated cluster intensity (b) for a mixed sample of Pd_{887} and Pd_{3000} clusters.
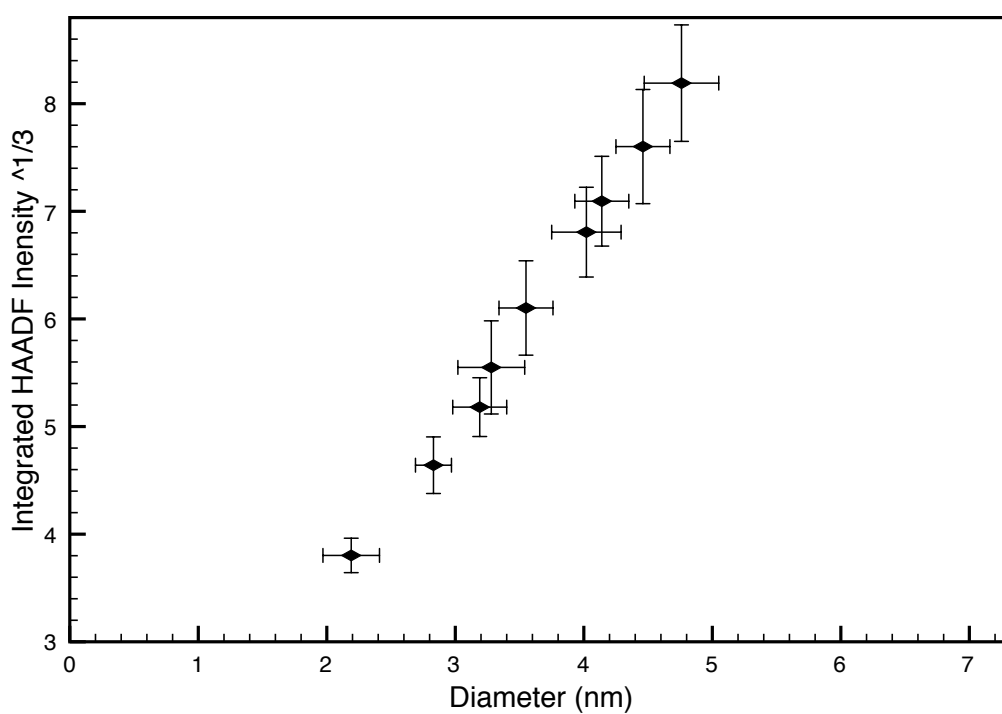
FIGURE 5.5: Integrated HAADF intensity as a function of cluster diameter for size selected cluster measurements.

contained in each cluster. This relation can be used as the calibration curve for Pd. The plotted intensities and error bars for each size selected cluster are based upon the mean value, and the standard deviation of the distribution recorded for each size. The dashed line in Figure 5.6 is a linear fit to the data points plotted. There is a steady increase in the intensity with the number of atoms to $N \approx 4500$. This is a much more extended

range than reported previously for Pd, where the relationship was only investigated up to 55 atoms [161]. Using this relationship, it is possible to determine the size range in terms of the number of atoms, in the industrial Pd catalyst particles investigated, providing the sample is imaged under identical microscope conditions. Inset of Figure 5.6 shows a magnified area of the main plot, this is to illustrate the corresponding range of the measured intensities for the Pd catalyst sample. The arrows point to the catalyst sample containing particles between 30 and 1700 atoms. This calibration curve may now be used for the characterisation of any Pd sample where the number of atoms is unknown, providing that the microscope conditions are as close as possible to the plotted data set and a calibration sample, Pd_{887}, is used to allow for any fluctuations.
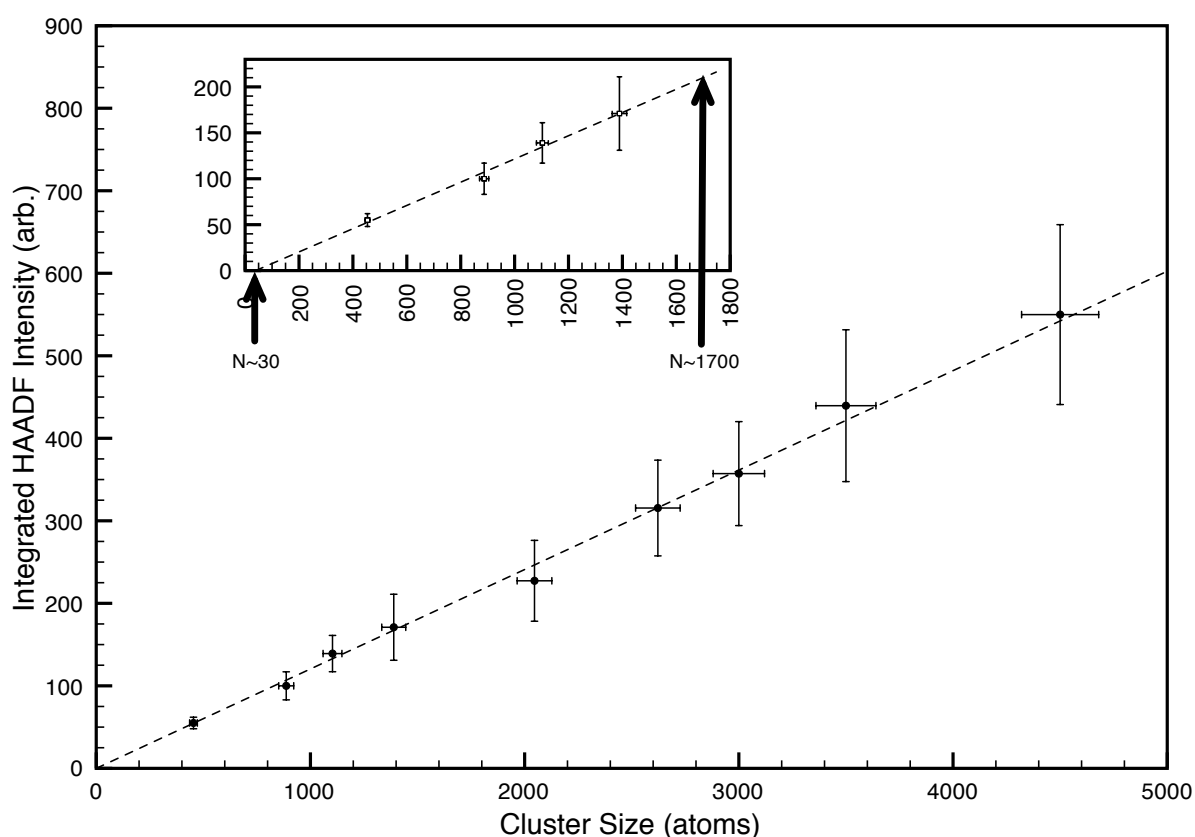
FIGURE 5.6: The HAADF intensity integrated over clusters as a function of the number (N) of Pd atoms in the cluster. The error bars on the y-axis were taken from the standard deviation of the distribution measured using HAADF-STEM and x-axis error bars are 4 % of N determined by the mass resolution of the time-of-flight mass selector. The corresponding range of integrated intensities measured for the industrial Pd catalyst is highlighted by the arrows (shown in the inset) along the line of best fit. It shows that within this Pd sample, particles have a size range of 30 to 1700 atoms.

5.4 Pd Catalyst: Structure and Size Characterisation

Having calibrated the number of atoms in the industrial Pd catalytic sample against those in the size selected Pd samples, one can now address the three-dimensional shape of the clusters, by relating integrated intensity and diameter (D) measurements. The STEM imaging shows that the catalytic Pd nanoparticles all have approximately circular two dimensional projection. Two-dimensional flat (i.e. raft like) morphologies can be ruled out by visually inspecting the HAADF-STEM intensity variation within each cluster. However, it is difficult to distinguish spherical and hemispherical shapes of small particles without carefully quantifying the image intensities. Two models of the nanoparticle shape are considered. Based upon simple geometric considerations that were first introduced in chapter 2, one plots in Figure 5.7, the projected cluster diameter as a function of $N^{\frac{1}{3}}$ in both the spherical cluster approximation, $D_s = 2R_a N^{\frac{1}{3}}$, and the hemispherical cluster approximation, $D_h = 2R_a(2N)^{\frac{1}{3}}$, where R_a is the atomic radius calculated from the lattice parameter for bulk Pd, 0.389 nm [162].

The data points for the size selected Pd clusters in Figure 5.7 are the mean values measured for each size. The linear fit to the cluster data (the thick dashed line), which includes the origin, lies close to but just above the spherical cluster approximation. This suggests only a small deformation of the size selected clusters created in the gas phase when they are soft-landed on the amorphous carbon substrate, allowing them to retain a quasi-spherical structure. By contrast, the data points for the industrial Pd catalyst particles in Figure 5.7 are clearly suggestive of a hemispherical rather than spherical cluster shape. These data points represent 280 nanoparticles. Furthermore, it is noticeable that the most of the data points lie above the hemispherical cluster model. This implies that, overall, the industrial Pd nanoparticles are somewhat more flattened than an idealised hemispherical shape.
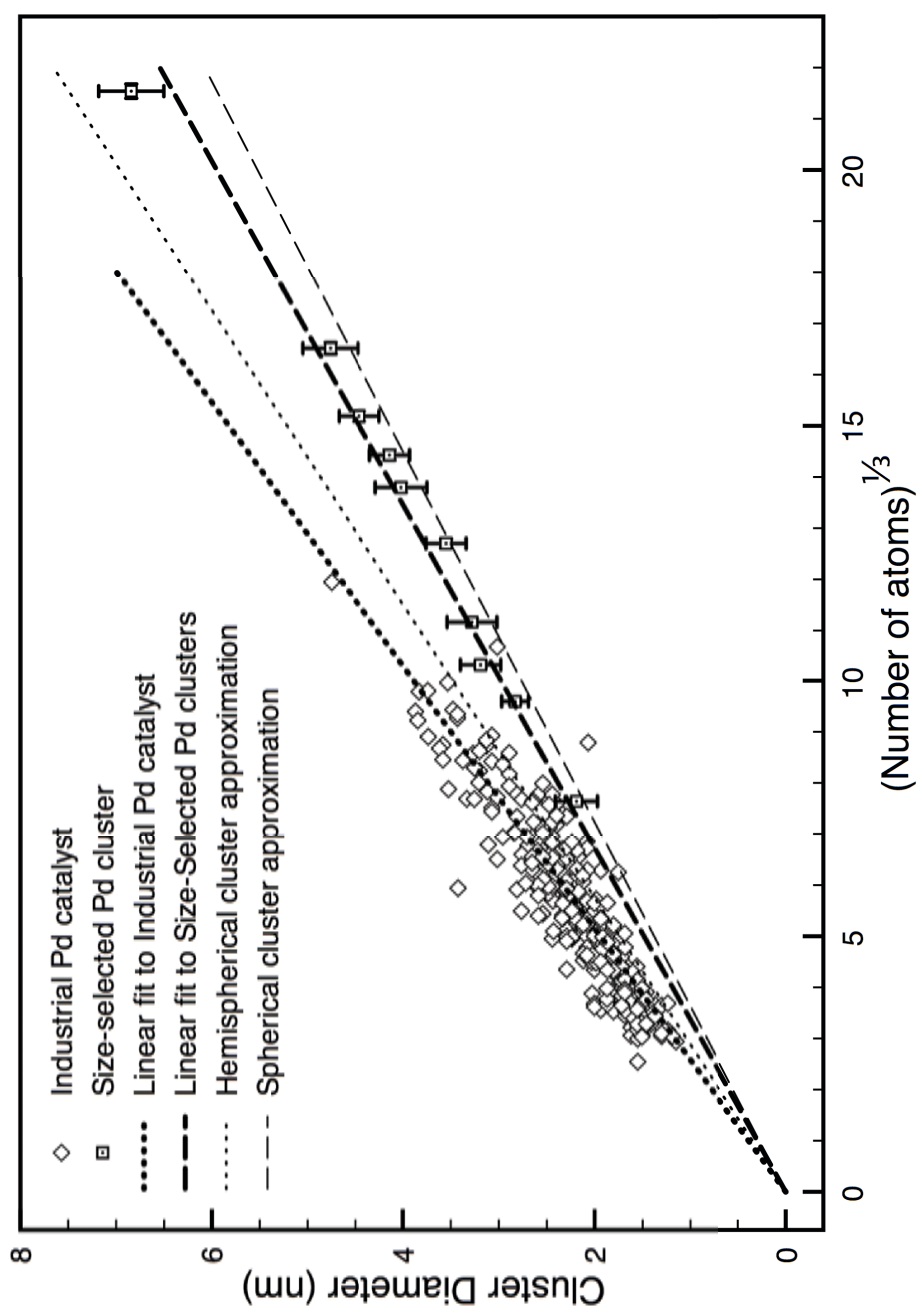
FIGURE 5.7: Comparison between size selected Pd cluster data and 280 industrial Pd catalyst particles in terms of the number of atoms and diameter. Thin-dashed and thin-dotted lines represent the spherical and hemispherical cluster approximations, respectively. Thick-dashed and thick-dotted lines are the linear fits to the size selected clusters and industrial Pd particle data, respectively.

5.5 Discussion

The shape of the catalyst particles will depend on a number of factors including the catalyst material, support and synthesis process. However, it is worth noting that the finding for Pd on carbon black is similar to that of Yang *et al* [150] for PtRu$_5$ catalytic clusters on similar supports. Yang *et al* attribute the oblate shape to the stable bond between Ru and C but not Pt and C. However, the clear difference in this work between the pre-formed Pd clusters and the industrial Pd catalysts highlights the importance of the particle formation process on the shape. In this case, both types of Pd particles are on carbon supports (thin a-C film vs. carbon black). In an investigation by Li *et al* [163] the size effects of PVP-Pd nanoparticles was investigated in catalytic suzuki reactions. In this case it is suggested that the higher catalytic activity of smaller particles is due to the increase in the number of vertex and edge atoms in comparison to their larger counterparts. The smallest Pd particles showed lower activity, however, and it is postulated that this is due to poisoning of the catalyst via strong adsorption of the reaction intermediates. The point of interest to take from this is that these conclusions are drawn from stating that the particle size distributions (taken by diameter measurements via TEM) show a roughly spherical particle morphology when supported on an a-C grid. This investigation's conclusions may have changed should intensity measurements been made available, as a more detailed structural conclusion could have been drawn, as has been shown in the results from this chapter.

Though the work presented in this chapter so far was conducted with Pd on carbon supports, it should be pointed out that the technique described is applicable to other supports often used for catalytic samples, such as MgO, TiO$_2$ or aluminium oxide. The method yeilds better results when used for heavier elements on light supports, since HAADF-STEM is a Z-contrast imaging technique. This novel method has recently been developed within studies by Young *et al* [74] and tested on Au nanoparticles prepared by wet chemical and thermal evaporation methods. In conjunction with this previous work on size selected Au clusters [5, 74], where a near linear relationship was found for Au integrated HAADF intensities of cluster sizes up to ≈4000 atoms, it is envisaged that the monatomic dependance of the HAADF-STEM image intensity on cluster size up to ≈5000 atoms may apply to a wide range of elements. This method is most useful

in establishing the main features of the morphology of small particles with a significant distribution in size, a situation commonly encountered in the industrial production of catalysts. It is of importance to note that the ease and efficiency of this method, is designed to be useful to commercial experimentalists, where a reliable and quick characterisation of catalytic particles is required. This broad brush approach could also provide a useful starting point for a more detailed charaterisation of supported catalysts when required. One limit on the accuracy of the size determination in terms of the number of atoms within the clusters is the mass resolution of the size selected cluster source, which is set at $\pm$ 4% in the present study, but can be improved. This method complements sophisticated three-dimensional microscopy techniques, such as TEM/STEM electron tomography [156, 157] or HRTEM exit-wave reconstruction [160]. This approach may be especially valuable if combined with detailed atomic resolution characterisation using aberration corrected STEM. Results concerning this type of characterisation can be seen in chapter 7 and within the next section with relevance to catalytic particles. It is still worthy of note that, although the aberration corrected microscope offers enhanced spatial resolution and image contrast, the intense probe can cause movement or modification of the clusters, especially those with a diameter less than 2 nm. Conventional STEM, with a less intense beam, should lead to less cluster damage.

For measurements of integrated HAADF intensity on size-selected clusters there is an increase in the spread of data with size, N. This can be seen in Figure 5.4 (b) for example, where there is a narrow peak for Pd_{887}, and a wider spread of intensities for Pd_{3000}. The spread in integrated intensities for any population of Pd_N cluster reflects the magnitude of the mass-selection resolution, providing that minimal errors are incurred from image recording and background subtraction, and that incoherent imaging is achieved. The spread of data as cluster size increases is, however, larger than the calculated mass-resolution of the mass selection device. This could be attributed to the cluster source mass resolution not being consistent for clusters of large sizes. Theoretically this is not the case, see Chapter 3 for discussion. However, it is impossible to check with mass spectrum acquisition at the source due to the nature of beam currents for specific large cluster sizes being present amongst a large envelope of similar sized clusters. Resolvable peaks for mass resolution only exist in mass spectrums for small clusters. Other reasons for this data spread could have arisen from measurement in STEM. Uncertainties may

have arisen due to rotation or vibration of the clusters during scanning. This effect may lead to slight over-counting of atoms by the detector from the apparent larger cluster size. The effects of coherent scattering should be considered also. Bragg scattering may contribute to the detected intensity from high order diffracted electrons. These effects are expected to be minimal due to the quantity of incoherent signal detected at the collection angles used but may still contribute. Care was taken to select the collection angles so as to achieve the correct compromise between the type of scattering (incoherent/coherent) and magnitude of signal received. This was described in detail in chapter 4.

5.6 Pd Catalysts on Varying Support Materials

In 1984 Boudart [164] stated that for catalytic particles of a size below 1 nm, the metal-support interaction is expected to be important, and that much remained to be done to understand the nature of these interactions. Since then much research has been performed into the improvement of catalysts via the nature of the support material, a good review of this can be found in Catalytic Chemistry by B. C. Gates [165]. Many industrial catalysts exist as highly dispersed aggregates on a support material, as are the samples under investigation here. One role of the support material is to reduce costs. Catalytic materials are often expensive, so exposing as many of the surface atoms or reactant sites available to the reactants as possible and preventing aggregation and sintering is desirable [165]. Supports such as Aluminium Oxide (Al_2O_3) and Carbon Black (C) are typical of industrial catalysts due to their robust nature to withstand activation processes and catalytic reactions. These two support materials are compared in this study.

Methods of atomic structural catalyst particle characterisation have been discussed within the introduction section to this chapter, and Chapter 7 of this thesis presents the advantages of spherical aberration correction in STEM for atomic structural characterisation of small clusters. The use of a smaller probe in C_s corrected STEM provides a much more intense beam than that of the uncorrected microscope. As a consequence of this, better contrast between elements of differing atomic numbers becomes apparent. Due to the industrial Pd catalyst samples being upon support materials, Pd particles

cannot be imaged directly resting upon the a-C support. It has been shown already how sample preparation methods to reduce the surrounding C support or HAADF-STEM imaging were taken in Chapter 3 of this thesis. For the case of Al_2O_3 supporting material, the atomic numbers of these elements are higher than that of C (Z = 8 for O and 13 for Al), thus, using the aberration corrected Jeol 2100F microscope allowed good contrast between the catalytic particles and the support in STEM analysis. At this stage in the experiment it was not possible to use the Tecnai F20 microscope due to the equipment change in the laboratory. Unfortunately this meant that the Pd catalytic particles on different supports could not be "weighed" using the Pd calibration curve, due to a vast difference in all imaging parameters. The purpose of this section is to show the morphological change in catalytic Pd particles in the two different support materials. C_s corrected STEM assists with this by providing a well defined Pd particle perimeter.

Figure 5.8 illustrates four low magnification HAADF-STEM images taken of Pd on Al_2O_3 in (a) and (b) and of Pd on C in (c) and (d). One can see the clear difference in the nature of the two different catalysts from these images. The Al_2O_3 support showing a much more well defined perimeter than its C counterpart. The Pd particles on the Al_2O_3 support appear at first glance to be much more irregular in structure than the circular projections seen for Pd particles on C. Images taken at higher magnification are shown in Figure 5.9, and visually illustrate this point further. The irregular structure of Pd particles seen in Figure 5.8 (a) belong to the sample with the Al_2O_3 support, whilst the circular like projections of the particles in Figure 5.8 (b) belong to the sample with the C support.

As explained and discussed in Chapter 4, the asymmetrical projection of the Pd particles does not lend itself to aspect ratio determination; instead, circularity is used as a way of quantifying the deviation away from circular projection. Analysis of Pd particles from both samples was performed using this method. The results from this analysis can be seen in Figure 5.10. Each individual cluster measurement is represented by a data point along the x-axis whilst the circularity of the cluster is plotted along the y-axis, ranging from 1 for perfectly circular to 3.2 for the cluster with the least circular projection. It is clear that the majority data points for Pd particles on C are near circular in projection, as shown in the previous section, corresponding to a hemispherical/raft like morphology.
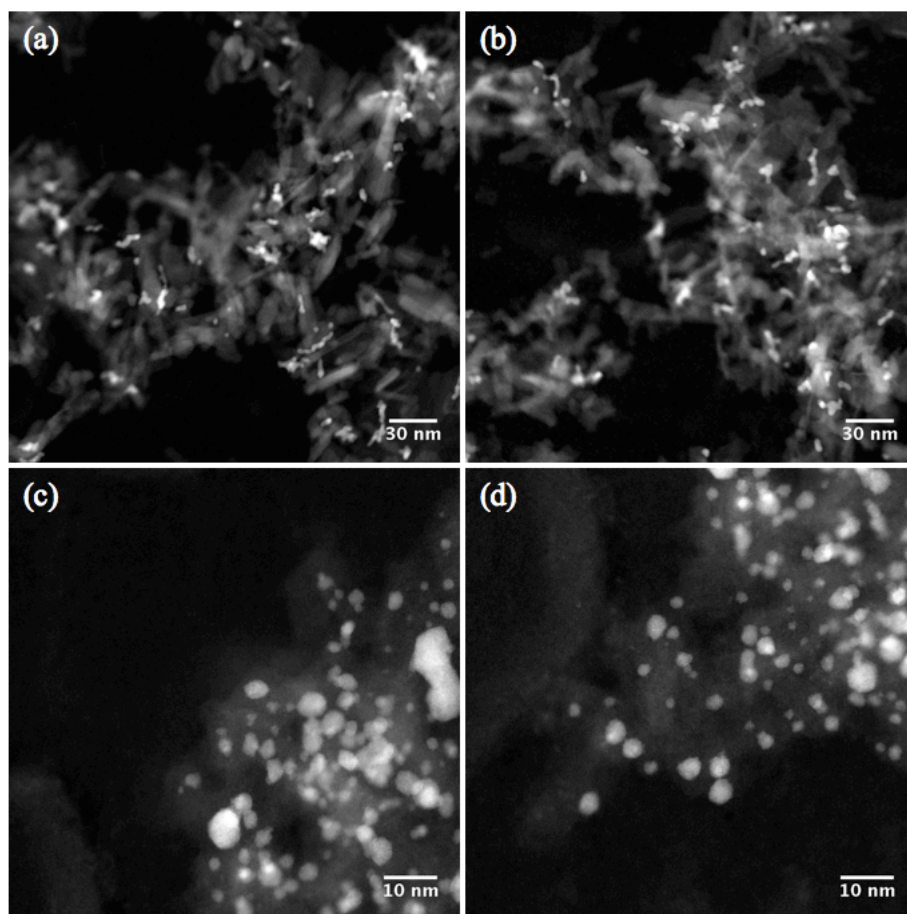
FIGURE 5.8: Low magnification HAADF-STEM images taken of Pd on Al_2O_3 in (a) and (b) and of Pd on C in (c) and (d).

However, in comparison the Pd particles on Al_2O_3 support show a strong deviation from circular projection for the majority of the data points, with only 11% of clusters with a circularity of ≈ 1. Due to the sensitive commercial nature of the catalysts samples no information about their creation process was given. However, the analysis performed has given important information about the Pd catalyst particles in differing support materials. The lack of circularity seen for Pd particles on the Al_2O_3 support is a clear demonstration of the role that the supporting material plays in the morphology of the catalytic particles. This is then important, as control over the structure of a particle allows control over its purpose within catalysis. It is possible that the lack of circularity is due to the nature of the support material, causing the Pd particles to agglomerate thus causing the observed asymmetry. It is of great scientific interest that catalyst structures can be characterised in this way, as specific structures may provide an increased number of reaction sites.
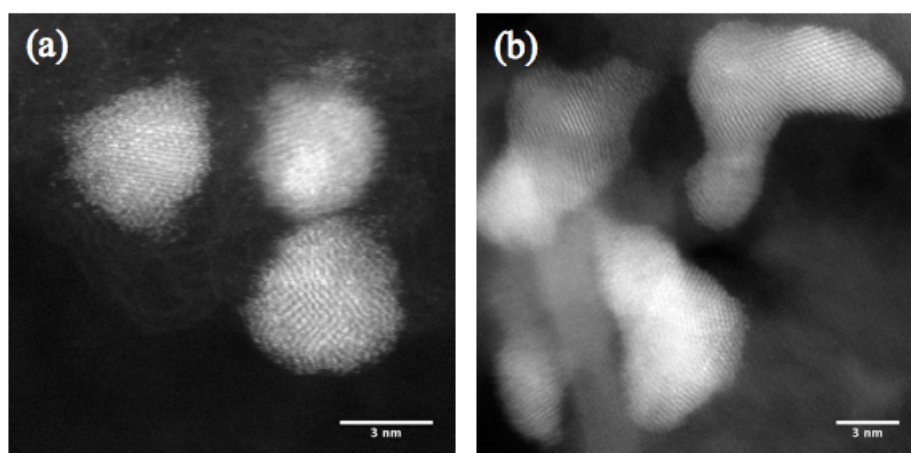
FIGURE 5.9: HAADF-STEM images taken of Pd particles on C, in (a), and of Pd particles on Al$_2$O$_3$, in (b). Images offer a visible illustration of the typical projections of Pd catalyic particles on the two different supports: asymmetrical for the case of (b) and circular like for the case of (a).
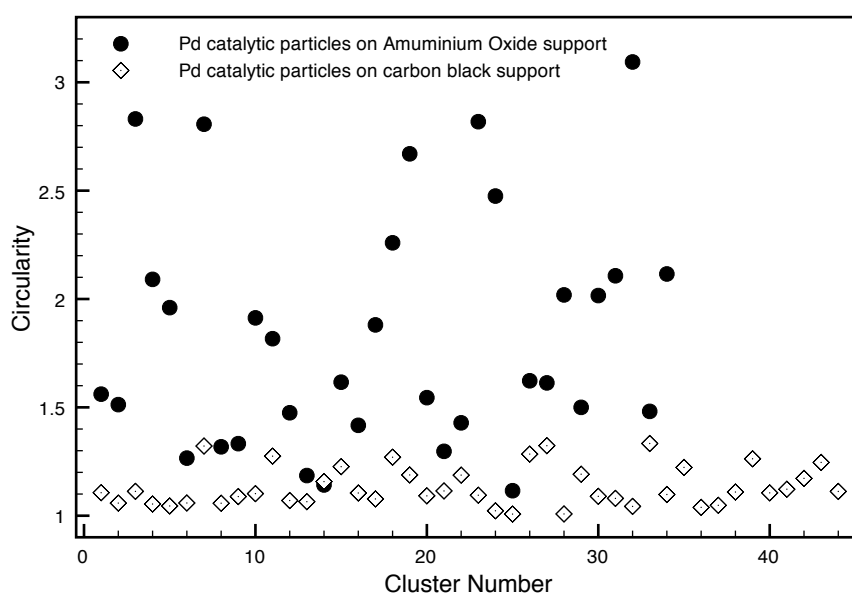
FIGURE 5.10: A plot to illustrate the circularity of cluster from two industrial Pd catalytic samples, shown in legend. Each data point represents an individual Pd particle, see text for discussion.

5.7   Summary

The work presented in this chapter demonstrates that it is possible to characterise the size and morphology of industrial (Pd) catalyst particles (on carbon black) using a combination of HAADF-STEM and size selected (Pd) clusters as mass standards. The method exploits the relationship between cluster image intensity and pre-selected cluster

size (number of atoms). This "calibration" can then be applied to catalytic nanoparticles with unknown size and shape. Comparison of the quantitative image intensity and particle diameter with simple geometric models allows us to gain insight not only into the size (number of atoms), but also the morphology of the catalyst particles. It is found that the industrial Pd catalyst particles are close to hemispherical in shape (a bit flatter), whereas the size selected Pd clusters formed in the gas phase retain approximately spherical form when soft-landed on an amorphous carbon film. The speed and utility of this method introduced here may allow practical evaluation of clusters at each stage of catalyst design, production and use. It has been shown that this method can provide information concerning the structure and size of a catalyst in a quick and efficient manner. These morphological conclusions may affect the catalysts suitability for a given purpose. The information can be gained quickly with this approach and fed-back into the system for improvement in catalytic design.

Moreover, in combination with the new generation of spherical aberration corrected STEM instruments, new insights into more intricate structural details of such samples can become accessible, thus allowing specific structural models to be tested. The asymmetrical nature of the structure seen for the sample of Pd on Al_2O_3 means that one needs to build more realistic structural models that reflect the complex nature of different catalytic particle morphology in order for this sample to undergo the full characterisation method described in this chapter. The particle size distribution could be calculated in terms of number of atoms with ease, however, comparison with simple structural models such as the SCA would not be possible due to its asymmetry.

A feasibility study into the atomic structure of both Pd catalytic samples has been performed using the Jeol 2100F microscope. It is found that in comparison to size-selected clusters, the presence of Pd particles orientated with alignment so as to reveal individual atomic columns is rare. This is perhaps due to the presence of the surrounding support material masking some structural features, or perhaps the nature of the Pd particle structure itself. Figure 5.11 displays some examples of HAADF-STEM images taken in the feasibility study for detailed structural characterisation. These images do not represent the majority, but illustrate the best images recorded showing structural features. Figure 5.11 (a) and (c) shows a Pd catalyst particle on carbon with good alignment under the electron beam displaying atomic columns. A (111) face is seen in

particle (a) and a three-dimensional intensity plot of the particle is shown in (b). The particle is slightly asymmetrical in nature with the top half of the particle being larger than the lower half (as seen by the magnitude of the brightness). The larger particle in (c) shows (111) face with well aligned atomic columns all in one direction. Figure 5.11 (d) illustrates a Pd particle within the Al_2O_3 support. For some samples, using C_s corrected STEM may reveal the different crystallographic domains that make up the ramified structures seen within this sample, and then offer clues as to the active faces within the catalyst. However, it can also be that the crystal structure of the supporting material in the case of Al_2O_3, may hinder the structural characterisation of Pd particles if the particles are not well separated from the support. This would be more of a problem for a TEM study, as the lack of Z-contrast would not allow a clear distinction of structures originating from the supporting material or catalytic cluster. For clusters aligned well under the electron beam it may be possible to measure nearest neighbour distances for Pd structures with differing support material. This could be important in verifying both experimental and theoretical reports into the contraction of atomic distances at outer layers of nanostructured particles (as presented in chapter 2).
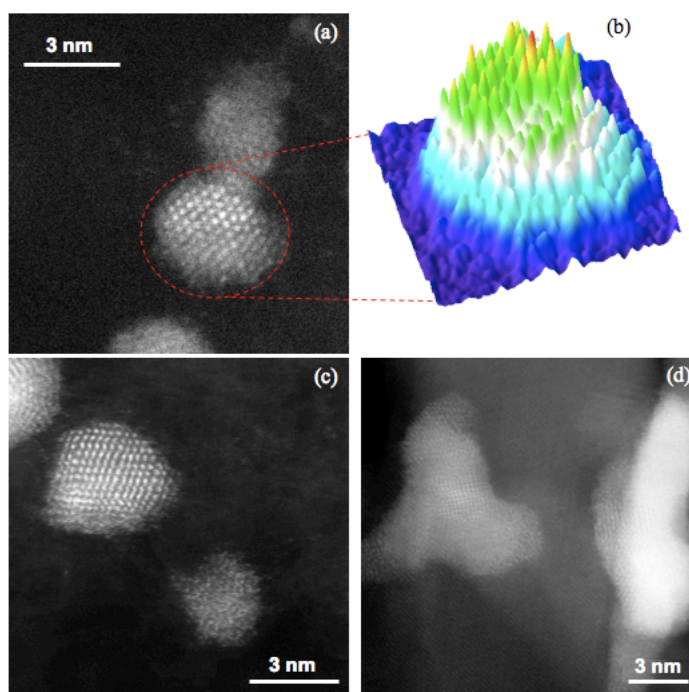
FIGURE 5.11: HAADF-STEM data of Pd catalyst particles taken with the Jeol 2100F microscope for the purpose of a feasibility study into the merits of aberration corrected STEM for atomic structural characterisation of Pd catalysts. (a) and (c) are Pd particles on C supports and (d) is a Pd particle on Al_2O_3 support. (b) is a three dimensional intensity plot of the cluster in (a), shown circled.

It is shown from the feasibility study into the merits of catalyst structural determination using aberration corrected STEM that structural features can be identified with extensive searching of the catalytic sample. The difficulties and merits of this method are discussed in Chapter 7 in great detail where this is employed in an experiment to characterise the atomic structure of size selected cluster, Pd_{887}. The use of C_s corrected STEM for structural characterisation of entire catalyitic samples is very time consuming and it is recommended to be used, where required, in conjunction with the "broad brush" methods developed within this chapter. These methods may then be of great use to the catalysis community offering information at each stage of catalyst design, production, and use.

Chapter 6

Size Dependent Morphology of Pd Atomic Clusters

6.1   Introduction

A main feature of this thesis throughout has been how structure determines function, and Pd clusters are all subject to structural suitability for the given application. Hence, shape controlled synthesis of Pd is a challenging task, but doing so would provide an opportunity to evaluate their properties for, for example, plasmonic, electronic, energy storage and catalytic applications [166]. Chemical methods have been employed to synthesise Pd clusters with structural control by Xiong *et al* [166], producing well defined structures ranging from five-fold twinned rods to cubes or bars. Solution phase synthesis of Pd nanostructures with organic surfactant has been employed by Watt *et al* [167] to control particle morphology using a pressure reaction vessel. The study showed that they could shift from a thermodynamic growth regime, favouring isotropic morphologies, to a kinetic growth regime, resulting in branch-like morphologies. With the technology to size select the number of atoms within a cluster available, the ability to link size (number of atoms) and morphology has become apparent. On experimental time scales it is often kinetics, rather than thermodynamics, that obscures the most stable state of a cluster [14].

This chapter addresses some of the structural features of size selected Pd clusters revealed by HAADF-STEM analysis. The primary aim here is to demonstrate the usefulness of HAADF-STEM at identifying cluster sizes regardless of their morphology, as well as the suitability of this technique for the identification of structural features. The secondary aim is to identify formation mechanisms of Pd cluster structures and suggest reasons for the creation of the structural features seen under HAADF-STEM analysis.

The results of this study will be presented in two parts: one addressing the elongation of size selected Pd clusters, and the other looking into the formation of internal changes within clusters. The physics theory and literature behind cluster formation was discussed in detail in the formation of clusters section within Chapter 3, which also included a description of the Birmingham cluster beam source that is used for the creation of samples under study in this chapter. It is recommended that these sections are consulted for the background regarding the results presented here. Further literature regarding the control of cluster structure and experimental similarities to these results are presented and discussed within the discussion sections of each part of this chapter.

6.2 Elongated Pd Cluster Structure

This section presents the findings of a controlled experimental investigation into some variables inherent on cluster formation. HAADF STEM is used to show that there is a strong correlation between cluster size and shape. In Chapter 5 HAADF-STEM was shown to be an efficient technique to obtain the three dimensional morphology of nanoparticles and this chapter is a continuation upon this theme. Here it is used as a tool to determine not only the morphology of the cluster in two dimensional projection, but also its mass from integrated intensity measurement. The advantage of this method over conventional TEM is that one can determine the consistency of pre-determined size, in terms of number of atoms (N), regardless of the cluster morphology.

6.2.1 Results

Pd clusters with 887, 1389, 2046, 2622, 3000, 3500, 4500 and 10000 atoms were formed by gas phase condensation of radio frequency magnetron sputtered Pd atoms. All clusters were deposited as described within the cluster formation chapter of this thesis. The temperature inside the formation chamber was 90 K, as measured by a K-type thermocouple, and the deposition at 500 eV upon a-C substrates ensured that the energy was low enough to prevent fragmentation of the cluster upon impact with the substrate [168]. This result is also verified in Chapter 5 where size selected clusters of smaller sizes, and hence more energy per atom than those used here, were seen to retain quasi-spherical gas phase morphology using the same deposition energy. All clusters were imaged using the 200 KV Tecnai F20 STEM, with the exception of Pd_{10000} clusters for which aberration corrected STEM was implemented. This is discussed within the text, and settings used can be found within Chapter 4 of this thesis.

Figure 6.1 shows typical HAADF-STEM images of (a) Pd_{4500} and Pd_{887} (b) Pd_{3000} and Pd_{887}. The smaller clusters with circular projection in both (a) and (b) represent (a) Pd_{887} clusters. Visibly distinguishable from their Pd_{887} counterparts are both Pd_{4500} and Pd_{3000} clusters, their range of circular to oblate projections being apparent. Figure 6.1 (c) highlights this in greater detail, showing a three-dimensional representation of the intensity profile from the highlighted red area in (a) where two Pd_{4500} clusters can be seen with different morphology, one elongated and one circular.

Having a pre-determined cluster size means that there should also be a representative integrated scattering intensity for each cluster size. To characterise the Pd clusters, the HAADF intensity integrated over each particle is carefully analysed using the software package ImageJ. Background subtraction protocol means that the intensity contribution from the unevenness of the support is minimised. Aspect ratio measurements (long axis / short axis) provide an indication of the magnitude of elongation along a single axis. Figure 6.2 plots integrated HAADF intensity as a function of aspect ratio for individual clusters with N= 2046, 2622, 3500, 4500 from (a) to (d). Each data point represents an individual cluster measurement, with the dotted line representing the average integrated cluster intensity value associated with that cluster size. It is clear from Figure 6.2 that cluster sizes show little deviation from their mean values but clusters can have a variety of
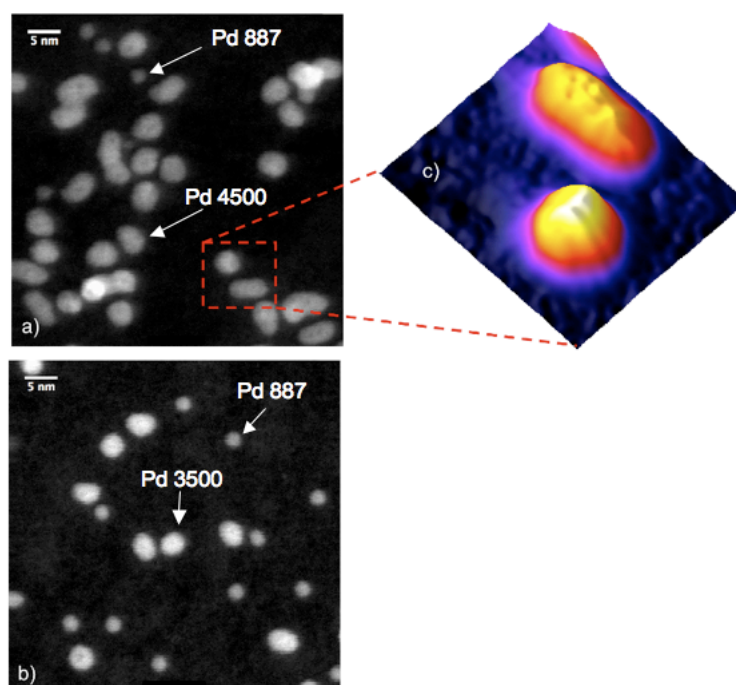
FIGURE 6.1: Typical HAADF-STEM images of (a) Pd_{4500} and Pd_{887} (b) Pd_{3000} and Pd_{887}. Images taken using the Tecnai F20 microscope. (c) A three-dimensional representation of the dashed area shown in (a). Two Pd_{4500} clusters are shown, with elongated and circular projections.

different aspect ratios, moving from circular projections of aspect ratio ≈ 1 (for Pd_{2046}), to more elongated structures with aspect ratios of up to 1.9 in the larger cluster sizes. As a result, factors which may have caused post gas phase morphological change, such as aggregation due to the surface mobility of clusters, can be ruled out, as the mass selection resolution is verified regardless of the cluster morphology. HAADF-STEM images are also shown adjacent to the plots in Figure 6.2 to give examples of clusters of the specific size in question. For (c) and (d) some larger irregular shapes are apparent in the micrographs. The corresponding integrated intensity values for these clusters are not shown within the plots as they are much larger than the two sizes present on the sample and so are not representative of the sizes being considered here. It is possibly the case that the projected area and intensity measurements of these clusters represent two or more Pd clusters that have been incident upon the substrate surface at the same position. The clusters at this point may merge, or sit on top of each other, revealing a bright area where the Pd sample area is thicker. This can be seen in (d) at the top right of the micrograph, where perhaps three clusters overlap in a central area (bright spot), and the remaining cluster structures are revealed propagating from this spot.

Only clusters that were separated from interaction with other clusters were analysed in this study so as to avoid distortion of the results through cluster-cluster interactions.

The aspect ratio data shown reveals each Pd cluster size having a range of different morphologies, from near circular to elongated projections. Here cluster orientation upon the substrate surface should be considered; as it is conceivable that all clusters could be elongated, but the true structure masked in the micrographs by orientation upon the surface. Taking a Pd_{10000} cluster with an elongated morphology for example, this cluster would appear elongated in projection if lying upon its long axis, however, it's morphology would appear circular if the cluster were standing upright upon its end. The cluster would however have the same integrated intensity measurement in both instances as this is determined by its size and not the orientation upon the substrate. The measurement that would differ between these possibilities would be the diameter. A check as to the feasability of this argument can be performed. The diameter of Pd_{10000} clusters with circular projections was measured to be in the range of 6.1 to 7.2 nm, this is illustrated in the histogram displayed in Figure 6.3. If one takes the upper limit of this range (7.2 nm) and assume a spherical morphology then this corresponds to a volume of 195 nm^3. If this specific cluster projection was of an elongated structure, for example, a cylinder with an aspect ratio of 2, then the corresponding measurement of diameter would be 5 nm. The lower limit for Pd_{10000} cluster diameters was 6.5 nm, which lies well outside the range of the corresponding cylindrical model diameters. The likelihood of upright cylindrical orientation occurring consistently for all samples is also small, and does not fit with the results presented in Chapter 5, where a wide range of size selected clusters with circular projection were shown to fit well with the spherical cluster approximation model for the same sample set as presented here. To conclude, based upon the measured diameters, it is thought that the orientation of the elongated clusters seen within this experiment is horizontal (long axis) on the substrate surface, and that the circular projections seen for any cluster size represent a quasi-spherical morphology. The measured diameter for circular projections of quasi-spherical clusters is distinguishable between the diameters for an elongated morphology standing upright, whilst still retaining the same, or very similar, integrated intensity measurement.

To illustrate the size-dependant morphology, Figure 6.4 plots the aspect ratio as a function of cluster size. It is found that, for Pd clusters of sizes $\geq$ 2000 atoms, clusters
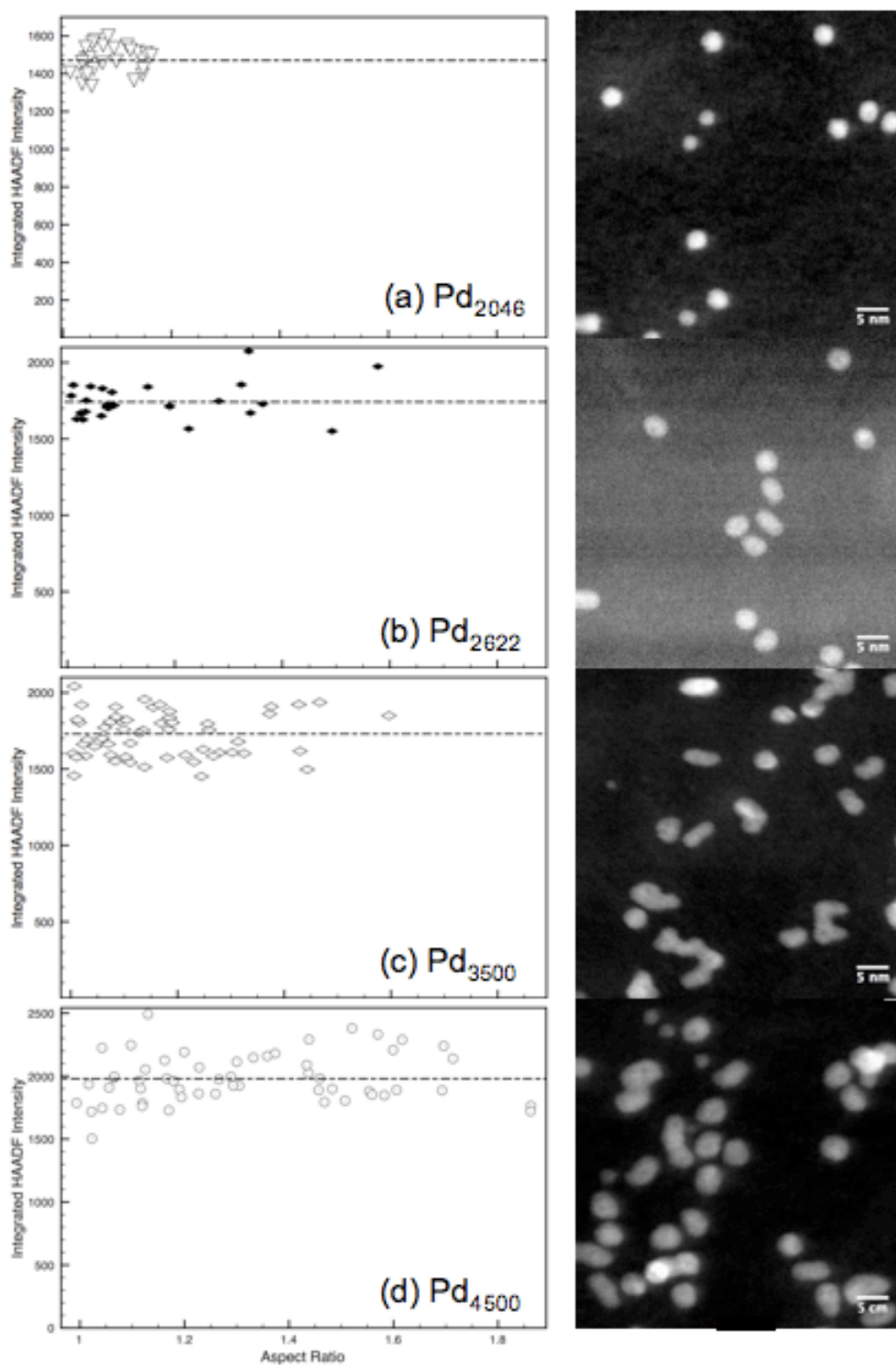
FIGURE 6.2: Integrated HAADF intensity from individual clusters as a function of aspect ratio for individual clusters ranging from N= 2046, 2622, 3500, 4500 from (a) to (d). The dashed line represents the average integrated HAADF intensity value for each cluster size. The x-axis represents circular projection at the aspect ratio of 1, to increasingly elongated structures further to the right along the axis. Respective Pd cluster HAADF-STEM images are also shown adjacent to the plots.
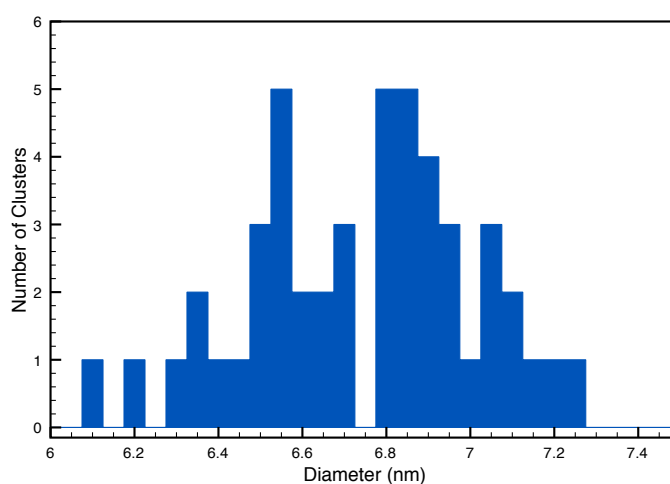
FIGURE 6.3: A histogram showing the measured diameters of Pd_{10000} clusters with circular projection.

start to depart from their quasi-spherical shape and present elongated morphologies. It is also apparent that the larger the cluster, the wider the range of cluster morphologies observed. This is illustrated in the inset of Figure 6.4, where a histogram displays the number of counts for the range of aspect ratios measured for Pd_{10000} clusters, corresponding to the far right data point in the main plot indicating that aspect ratio varies from 1 up to a maximum of 5 for this cluster size. Errors here were calculated from the standard deviation of the measured aspect ratio range for each size of cluster and become steadily larger with increasing cluster size demonstrating a wider spread of data. However, there is no indication of increased integrated intensity measurement with aspect ratio for all sizes of Pd cluster. Thus from the evidence presented so far, it is believed that this variation is representative of gas phase morphology. Chapter 5 also concluded that the size selected Pd clusters with circular projection retained their gas phase morphology. This was concluded by comparison with the spherical cluster approximation, with diameter and integrated intensity measurements showing a good fit to the structural model.

Further investigation into Pd_{10000} clusters was performed using the Jeol 2100F with C_s corrector, to verify previous results and offer a higher resolution for structural insight. Inserted into Figure 6.5 are examples of Pd_{10000} clusters with their associated aspect ratio and integrated intensity measurement labeled. These values can be found labelled within the main plot, which displays integrated intensity as a function of aspect ratio
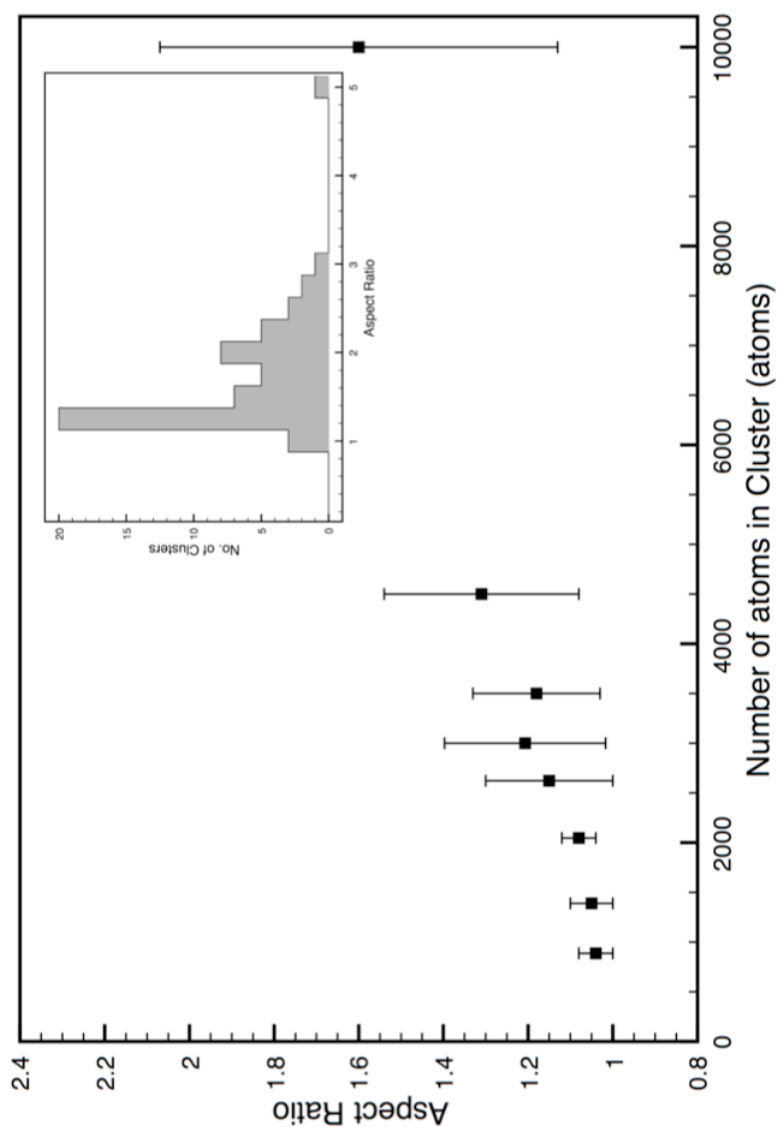
FIGURE 6.4: Comparison of size selected Pd cluster aspect ratio across the mass range of Pd_{887} to Pd_{10000}. The data points represent the average aspect ratio measurement for a Pd cluster of that size. An increase in aspect ratio is seen for higher cluster masses. The error bars represent the range of structures seen for any particular size and are calculated by the standard deviation away from the mean. Inset is a histogram representing the measured aspect ratios for Pd_{10000} clusters. This plot corresponds to the far right data point on the main plot.

for the Pd_{10000} clusters imaged with the Jeol microscope. The inserts show examples of clusters with circular projection (aspect ratio = 1) to those that are elongated (aspect ratio = 3.1), whilst retaining a similar integrated intensity values, thus verifying the previous data taken using the Tecnai microscope.
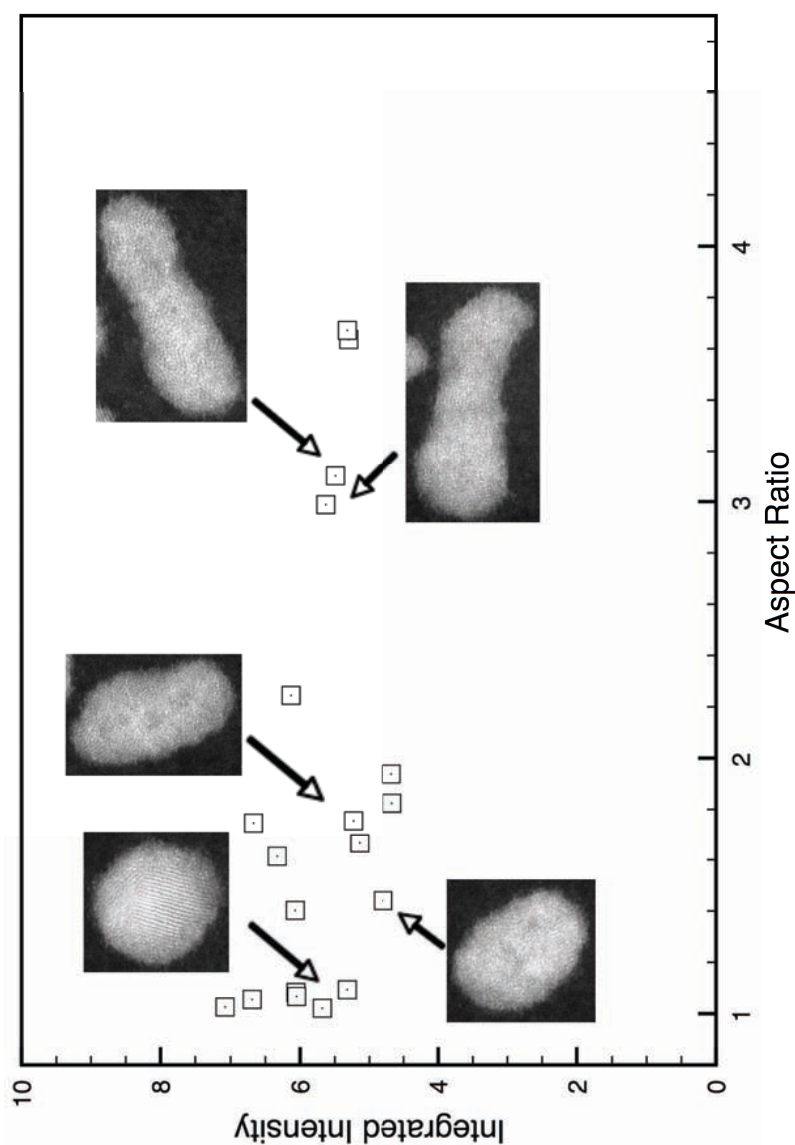
FIGURE 6.5: Integrated HAADF image intensity from individual Pd_{10000} clusters as a function of their aspect ratio. All data taken using the Jeol 2100F C_s corrected microscope and examples of Pd_{10000} cluster images are shown inset, with the corresponding values labeled.

A more detailed analysis of Pd_{10000} clusters suggests that those projecting elongated morphology appear to be made up of seed clusters that have partially sintered to form the overall cluster structure. This is shown in Figure 6.6, where two different Pd_{10000} cluster examples are given, and a copy image of the cluster displayed to highlight the structural features. This analysis outlines the large seed clusters, which have partially sintered prior to exiting the cluster formation chamber and being deposited upon the substrate surface. This process results in a neck like formation, indicative of partial or

interrupted sintering. Further structural features of size selected clusters can be seen in Figure 6.6. A dip in intensity can be noticed in the central region of the large seed that forms the Pd_{10000} cluster shown in the top row of this figure. This structural feature will be investigated in greater detail within the second half of this chapter.
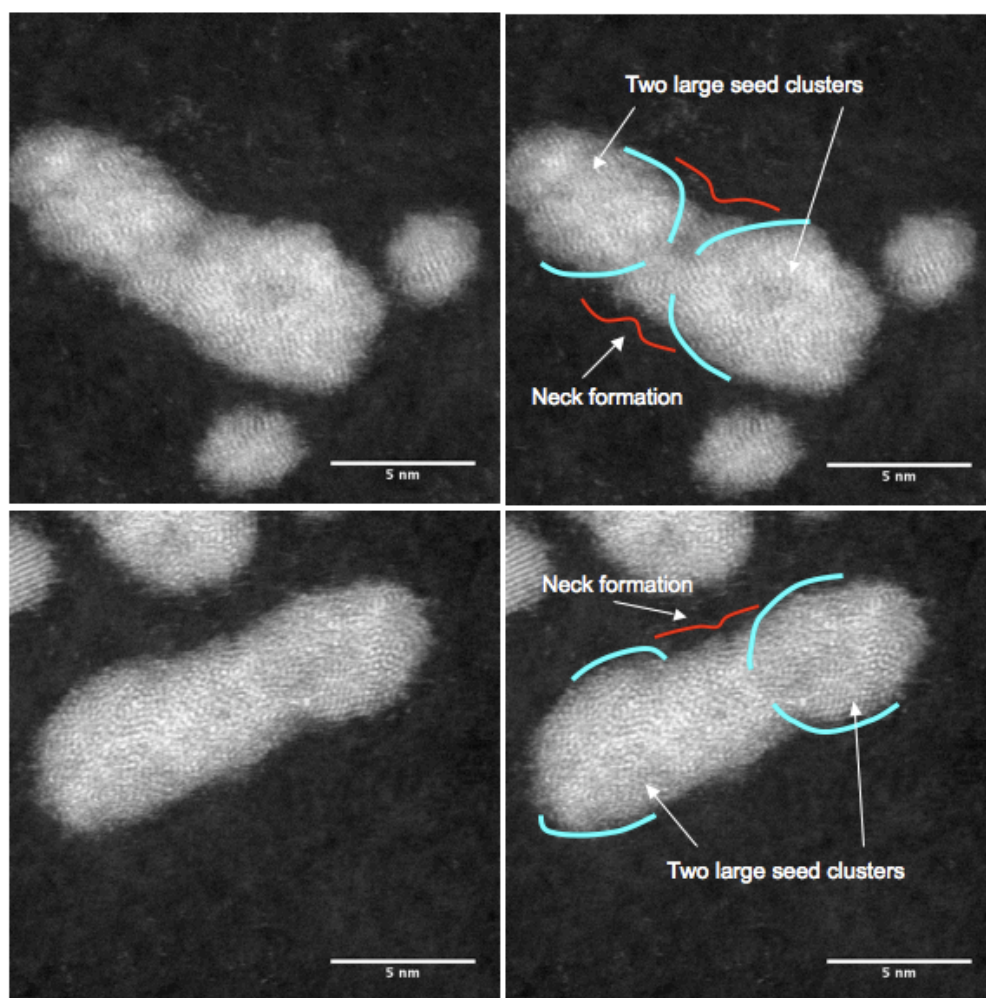
FIGURE 6.6: Two elongated Pd_{10000} cluster examples: The images on the left hand side are original HAADF-STEM data, whilst the images on the right hand side are copies of the image with structural features of interest highlighted and labelled. see text for discussion.

6.2.2 Discussion

It is generally considered that cluster formation via gas condensation is a result of atomic addition and/or "seed" cluster aggregation. In the present case the aggregation is aided by Ar/He carrier gas. A large percentage of clusters with elongated shape shown in this study suggest that some clusters are in a non-equilibrium state. This could be understood if the time between seed cluster collisions is shorter than that of the time taken for the cluster to sinter to a spherical structure, then elongated morphologies may form. From two-dimensional projection, evidence has been observed for partially sintered "large seed" clusters contributing to the overall morphology of elongated Pd clusters. Smaller clusters made from smaller "seeds" would require shorter time to reach equilibrium structure prior to deposition. For Pd, the onset of elongated morphology is seen for clusters ≥ 2000 atoms, much earlier than what has been reported for Au clusters at sizes ≥ 6000 atoms [6]. It should be noted though that direct comparison of the two data sets for Pd and Au is difficult due to their being differences is the cluster formation conditions. It is very often the case that within the cluster source variables such as the condition of the target material, for example, effect the optimum tuning for any cluster size. Thus, exact replication of formation conditions for two different materials is extremely challenging. However, one possibility for this earlier on-set could be that Pd is more prone to residual gases in the formation chamber than Au, or perhaps, that there were more residual gases in the formation chamber when the Pd clusters were formed. The residual gas molecules could reduce the atomic surface diffusion rate, leading to an increase in sintering time and, hence, an earlier on-set of elongated morphologies. It is apparent then that there is a competition between formation mechanisms within the condensation chamber; the sticking of larger seed clusters together, providing a tendency to elongated morphology, and the sintering and coalescence of two seeds, which strives for more compact morphologies.

Experimentally, the presence of smaller seed clusters constituting to the final morphology of size-selected clusters has also been reported by Alayan *et al* [71] for Pt nanoclusters. The formation process described there in is also supported by this study; that is that the sintering process of two seeds can be frozen due to a larger curvature area to fill, caused by additional seed impacts. In order to achieve an equilibrium state, curvature, and hence surface tension, need to be minimised, therefore, partly coalesced clusters are seen.

Wegner *et al* [96] discusses, with regards to metallic clusters, how sintering mechanisms play a vital role in cluster beam formation and are dependant on material, temperature and particle size. Zachariah *et al* [35] found that nanoparticle sintering via molecular dynamics studies also supports this argument, stating that vapour phase growth of clusters has a tendency to form agglomerated morphologies, more so than spherical ones. This occurrence is attributed to the sintering time being greater than the time for particle-particle collisions. A schematic from this study to illustrate these formation mechanisms can be seen in Figure 6.7(a). This illustration shows how agglomerated (or in this case, elongated) clusters arise when forming in the gas phase; the non-spherical morphologies shown being that of groups of "seed" clusters stuck together. The initial collision which results in the sticking of seed clusters causes a rapid temerature rise, the morphology will then change further as the resulting structure attempts to coalesce further causing a more gradual temperature rise. This coalescence mechanism progresses through surface atoms of the cluster filling in the neck region between the seed clusters [35, 169]. This is illustrated in Figure 6.7(b). Experimentally, evidence of this formation mechanism are seen for Pd_{10000} clusters as shown in Figure 6.6.

Lando *et al* [170] provide similar cluster formation theories for Ag clusters formed by diffusion on a HOPG surface. The study states that the evolution of cluster morphology is a competition between the time constraints; that of the time between impacts and the coalescence time to fuse into one larger cluster. Control of the morphology in this case is achieved by introducing impurities into the clusters, thereby increasing the atom mobility at the surface of cluster islands. Similar results were found by Olynick *et al* and Stappert *et al* [171, 172] where the presence of oxygen on Cu and FePt clusters respectively, is shown to slow the coalescence process greatly and thus alter the cluster structure. In this case the presence of the oxygen reduces the free energy of the system, thus reducing the size of the critical radius (see equations 3.2 and 3.3 in chapter 3) and in turn producing smaller seed particles [172]. As a consequence the sputtered material forms smaller nucleation seeds, resulting in more seeds being present within the nucleation zone. This then leads to more particle-particle collisions in any given time period, and hence agglomerated morphologies are formed.

The quantity of Pd seeds in the condensation chamber, and indeed their size, is greatly sensitive to the fine-tuning of the cluster beam source. Parameters such as nozzle size,
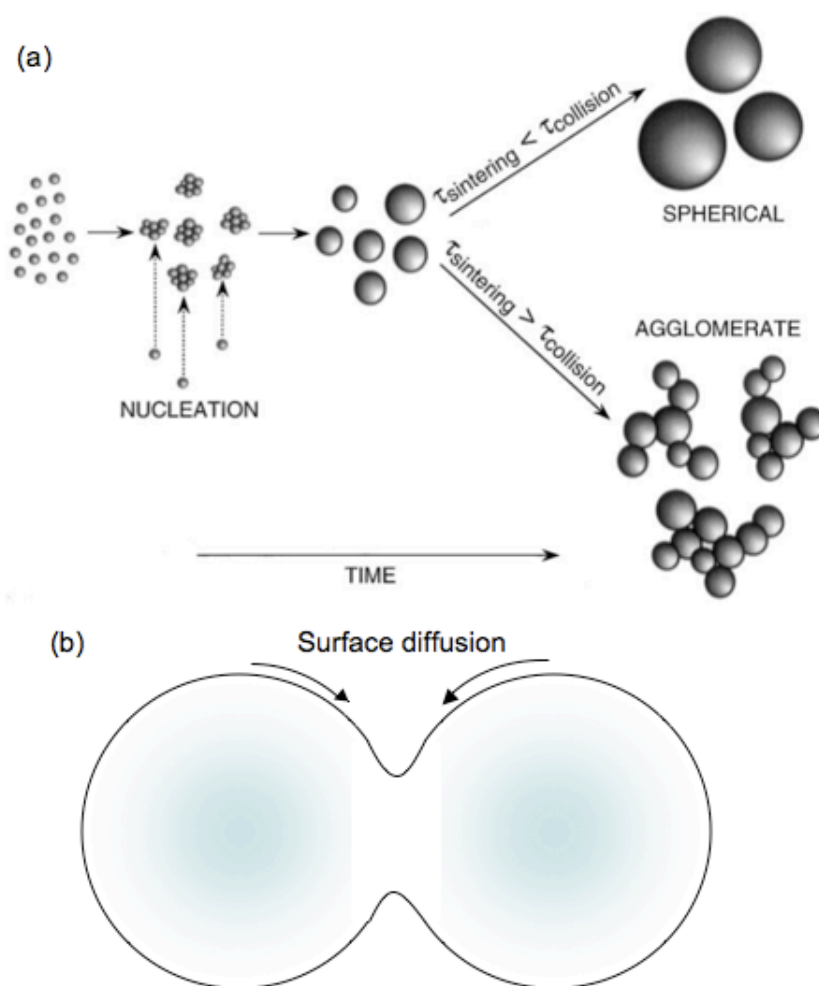
FIGURE 6.7: (a) A schematic of the evolution of gas phase cluster growth taken from reference [35] to explain the onset of elongated morphology within size selected Pd clusters (b) A schematic of two Pd "seed" clusters coalescing via surface diffusion of Pd atoms at the surface to fill the neck region, thus maximising surface to volume ratio and eventually achieving a quasi-spherical shape.

Ar gas flow rate, power to the magnetron, and He gas pressure all affect the measured cluster beam current. The larger the cluster size, the higher the magnitude of deviation in cluster beam current seen when settings are altered from the highly tuned conditions ideal for each size. Perez-Tijerina *et al* [173] utilized control over such variables to produce Au/Pd clusters with a high degree of monodisperity. In this study, clusters were created by inert-gas condensation with control over the Ar flow rate and power to the magnetron. The cause of oblate and elongated structures found for Pd clusters is in agreement from experimental and theoretical studies within the literature. To gain a better understanding as to the specific size dependance of these effects for a variety of

different elements further work is required. This is presented in the final section of this chapter.

6.3 Size Dependent Kirkendall Effect Observed in Size-Selected Pd Clusters

6.3.1 Results

Another striking structural feature discovered in the HAADF-STEM investigation using the Tecnai F20 microscope on Pd size selected clusters is shown in Figure 6.8. The presence of circular-like dips in intensity, positioned within the clusters, is seen within the micrographs and illustrated within the line profiles shown in this figure. The presence of these dips is found to be cluster size dependent. None of these features have been found for Pd clusters containing less than 2622 atoms, but for this size and above are seen to be present in just over one quarter of clusters. The presence of these features does not appear to be sensitive to any particular structural form. These intensity dips, central within a Pd cluster, have been seen in those of circular as well as oblate projection. Often the position of the dip is off centre to the clusters. For elongated clusters the cluster projection often contains more than one dip, possibly due to the number of these features being linked to the number of seed clusters that the larger cluster is made from. Consistent with this is the fact that multiple holes are seen for Pd_{10000} clusters, but rarely seen for cluster sizes lower than this. All of the key characteristics of these features are shown in Figure 6.8.

Due to the spatial resolution of the Tecnai F20 electron probe, specific perimeter inspection of the intensity dips is not possible. For this reason aberration corrected STEM was employed for further investigation. Examples of Pd clusters imaged using this microscope can be seen in Figure 6.9. The clusters presented show the intensity dip in question with a clear perimeter, confirming their circular projection and allowing further analysis to be performed. A striking feature of Figure 6.9 (b) is that the periodicity of the atomic structure seen in the Pd_{10000} cluster is continued across the entire area of the intensity dip. This common finding illustrates that the dip in intensity is not positioned at the top (surface) of the clusters, else there would be a noticeable change
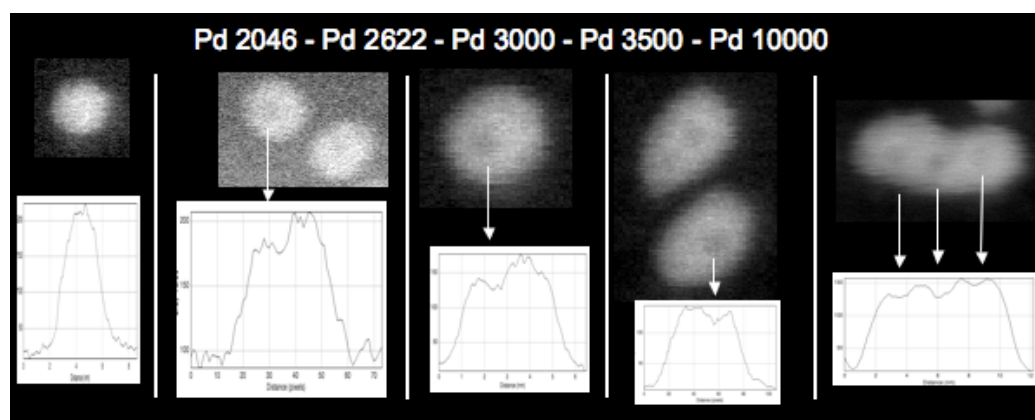
FIGURE 6.8: An illustration of the size dependance of "the dip in intensity circular-like projection" seen for size selected Pd clusters. the feature is not seen for cluster sizes below 2622 atoms for this sample range, but is observed in clusters above this size with varying morphology. HAADF-STEM cluster images are shown taken using the Tecnai F20 microscope, and the corresponding intensity profiles taken horizontally across the clusters are shown below to illustrate the intensity dip.

in the arrangement of the atomic columns seen within the image. Instead, the feature must be positioned within the cluster itself. The projected area of the intensity dip in clusters of all sizes was measured by tracing the perimeter of the area in ImageJ. The average area was measured to be 1.50 nm^2, with a standard deviation about this value of 0.37 nm^2. This value was found to be reasonably consistent throughout the entire range of cluster sizes from Pd$_{2622}$ to Pd$_{10000}$. The entire range of measured sizes can be seen within Figure 6.10, which plots the projected area of the structural feature against the percentage of total cluster area of the cluster that it belongs to. It is clear from this plot that no real relationship can be determined between the two parameters, and the average size of the feature measurement remains fairly consistent regardless of the cluster size.

Figure 6.11 (a) and (b) displays two HAADF-STEM Pd clusters containing 3500 and 4500 atoms respectively. Below each image is a line profile of the projected intensity propagating along the arrows displayed across the clusters. The lattice fringes and atomic columns of the Pd clusters can be seen within the profile along with a distinct dip in intensity around the centre where the structural feature is located within the cluster. Again, the atomic arrangement is seen to be consistent over both the intensity dip and the surrounding area.

The information gained from image analysis thus far still leaves unknowns such as the
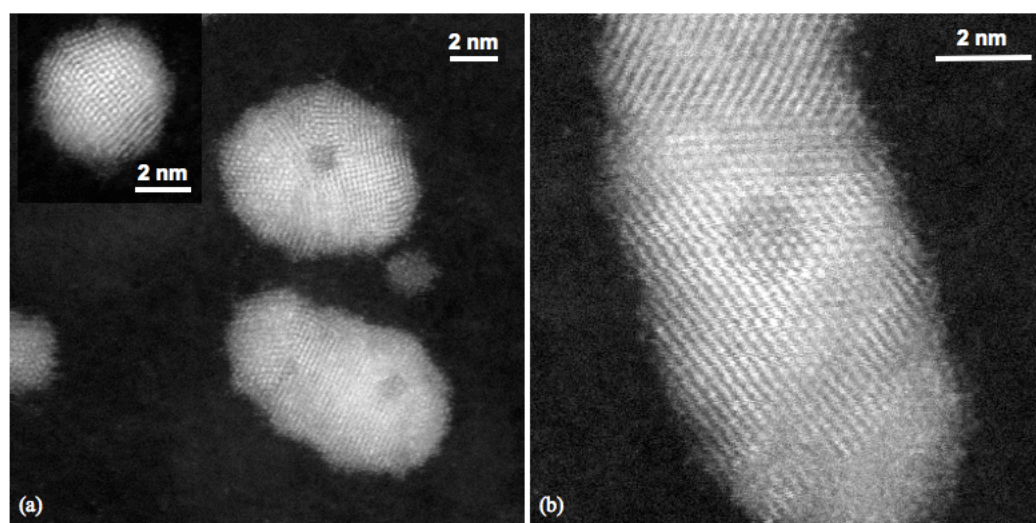
FIGURE 6.9: HAADF-STEM images of Pd clusters showing a clear circular projection of a dip in intensity within the main cluster body (a) Pd_{4500} clusters and (b) Pd_{10000} cluster. Inset of (a) is an example Pd_{2622} cluster with no intensity dip for reference. Images taken on the Jeol 2100F with C_s corrector, see text for discussion.
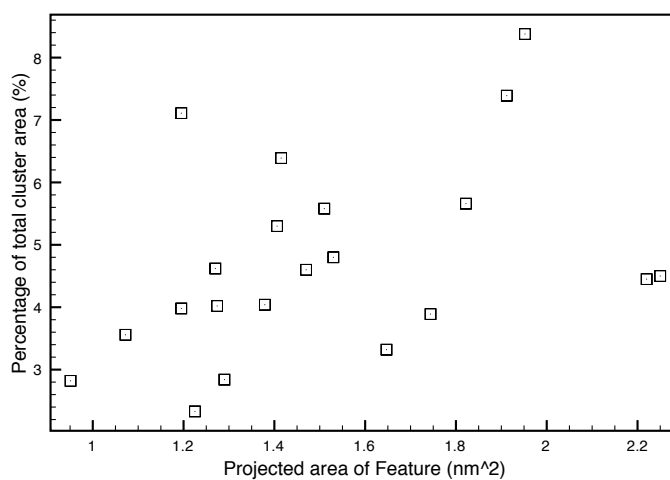
FIGURE 6.10: A plot of the projected area of the structural feature against the percentage of total cluster area that it takes up of the cluster it was observed in. See text for discussion.

nature of what is being seen, and why it is there. It is not known what causes these dips in intensity, however, a number of possibilities exist. A dip in intensity could be attributed to a lack of Pd atoms for that specific area in comparison to the size of the atomic columns in the rest of the cluster. The intensity dip does not allow us to reveal the exact location of its cause along the z-axis. The periodicity of the atomic structure over the feature seen in C_s corrected HAADF-STEM analysis (see Figures 6.9 and 6.11), does allow one to determine that its position is not at the cluster surface. Thus it can be
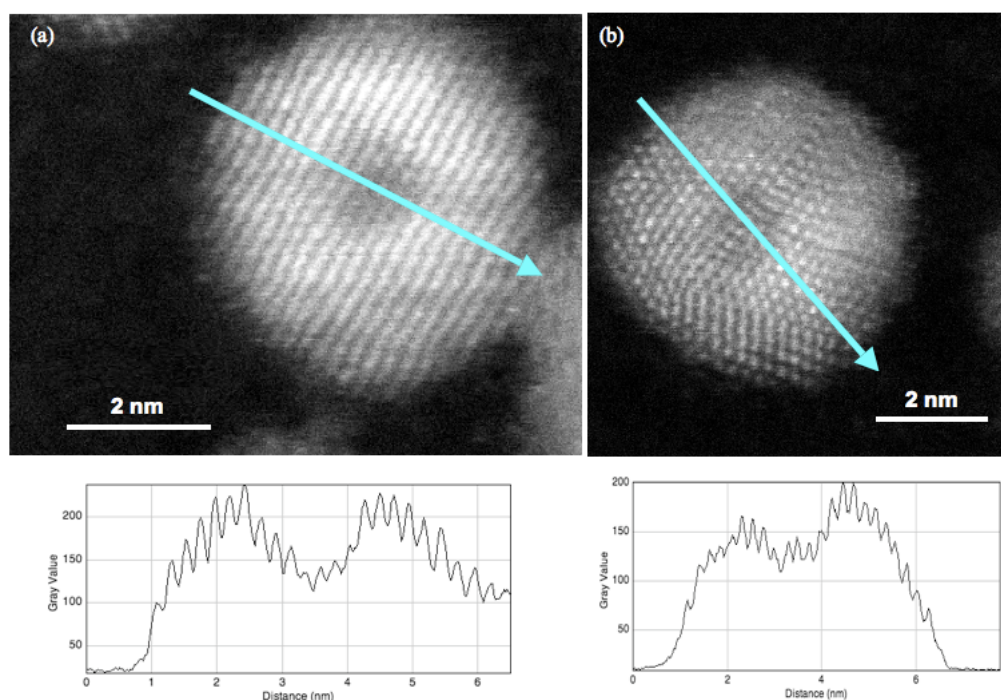
FIGURE 6.11: (a) and (b) displays two HAADF-STEM Pd clusters containing 3500 and 4500 atoms respectively. Line profiles are shown representative of the arrows draw across each cluster. The dip in intensity caused by the feature under investigation is clearly shown within these plots.

concluded that the feature seen is a spherical like area or void within the cluster. The dip in intensity could also be attributed to a material of a lower atomic number being present within the cluster. An inner scattering collection angle of 61 mrad is used for the HAADF detector in this investigation, according to the theory, excellent Z-contrast should be achieved between atoms of different elements. Therefore it is proposed that the dip in intensity seen could possibly be from the presence of another material, such as oxygen or Pd oxide.

To investigate this proposed theory energy dispersive X-ray analysis (EDX) was performed upon the sample containing Pd_{4500} clusters. The experiment using EDX was performed using the following steps: a cluster was found using HAADF-STEM in the Tecnai F20 microscope with EDX attachment with a prominent dip in intensity feature that could be seen. The electron beam was then placed over three spots and EDX spectra were taken. The first was taken directly over the centre of the intensity dip, the second half way between the dip and the cluster perimeter, and the final spectrum was recorded upon the a-C substrate, far away from any Pd clusters. An examples of this process can be seen in Figure 6.12. This figure displays the HAADF-STEM image of the

cluster with the corresponding beam position labelled within the image that was used for EDX analysis. The spectrum taken is then shown on the right hand side, and the corresponding data is shown in the centre.
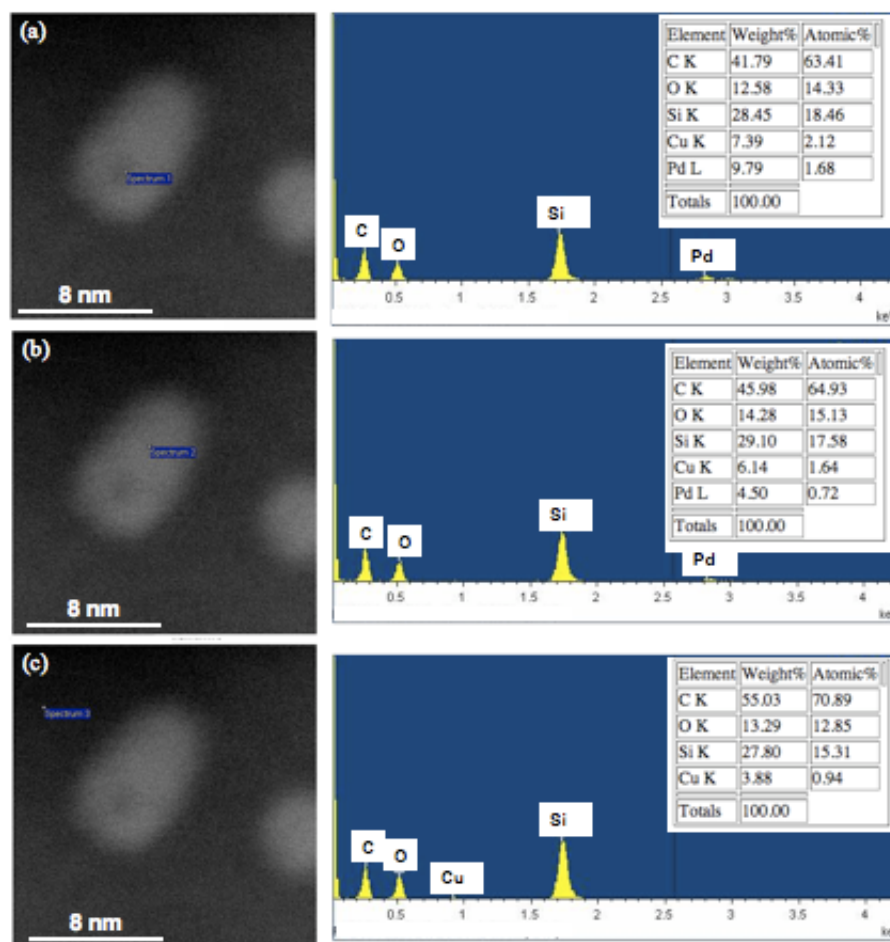
FIGURE 6.12: Example results from EDX analysis of size selected clusters. HAADF-STEM images are shown to with the electron beam position labelled for EDX spectra aquisition. The spectrums and data are also displayed, see text for details

The purpose of this experiment was to see if the presence of other elements apart from Pd was present within the cluster, specifically located around the structural feature under investigation. The results showed that Pd and O were present within the cluster area regardless of where the probe was positioned. No Pd signal was detected when the spectrum was recorded for the substrate, as would be expected. The presence of C is from the substrate itself, along with Cu from the grid which the substrate sits upon. Si is present due to its use within the manufacturing processes of the TEM grids. There has been no noticeable increase in O signal from the EDX experiments for spectrums recorded within the "cluster voids". The signal detected from the first probed area (void)

in comparison to the signals recorded for the bulk cluster area vary with regards to Pd and O amounts. No trend could be distinguished between the two but the presence of both elements within the cluster confirmed.

6.3.2   Discussion

From research into the literature, voids within nanoparticles have been seen for clusters of other elements such as Al, Cu, Pb and Fe. In all cases the structural feature is attributed to the Kirkendall effect. Kirkendall was the first to report the net transport of mass across an interface between two metal types [174]. The reason given for this mass transport was that of vacancy exchange, and not through the direct interchange of atoms. At the interface of two metal species there will be a mismatch in the diffusion rates of both elements. This will result in the net diffusion of atoms from one side of the interface to the other, and as diffusion takes place, vacancies will be left in their place. These vacancies will appear to move in the opposite direction to the diffusing atoms, eventually accumulating to form a void. For example, a study by Nakamura *et al* [175] used TEM to study the formation of hollow metal oxide clusters of Cu, Al and Pb. For the case of Cu and Al clusters the rapid diffusion towards the outward area of the cluster of metal ions through the oxide layer results in a hollow void forming in the centre of the cluster. This was true for clusters of all sizes with the exception of Al clusters greater than 8 nm in diameter. At this size range a metal core was created with a surrounding oxide layer. For the case of Pb, the difference in diffusivity (D) of the metal ions and the oxygen atoms ($D_{Pb} < D_O$) results in the formation of solid Pb oxide clusters. In an investigation by Gaiduk *et al* [176], the synthesis of hollow SnO_2 nanoislands was performed by controlling the samples oxygen exposure. The voids in this case were found to be larger for cluster sizes of above 10 nm in diameter. This particular study assumes that the absorption of oxygen atoms on the oxide surface causes the creation of an electric field. The electric field then promotes the Kirkendall effect leading to the formation of the voids, which is found to be dependent on the temperature of the clusters and the ambiance of the thermal treatment that the clusters undergo. So the formation of voids within clusters is found to be both element and size dependent as well as being influenced by the temperature and ambiance of the cluster formation. Wang *et al* [177] recorded the critical size range for void formation in the oxidation of Fe clusters

by TEM analysis. It was found here that for clusters smaller than 8 nm in diameter a void is present in the centre of the cluster with the rest of the material fully oxidised, this was confirmed by EDX analysis of the clusters. For clusters larger than 8 nm a core shell structure was found with a surface oxide layer and Fe core.

Until now, there are no repeats in the literature recording the Kirkendall effect for Pd clusters. Evidence has been found in the literature of TEM investigations revealing voids, much in the same way as the STEM results have here, with elemental composition of the clusters confirmed by EDX analysis. The experimental findings presented within this section are thus: the elemental composition of the size selected Pd clusters has been found to be of Pd and O; the location of the feature is within the cluster, and the feature is size dependent, only appearing on clusters with $N \geq 2622$. It is concluded from the evidence and findings within the literature that the structural feature seen is that of a void within the clusters. This has been caused by the Kirkendall effect, whereby the presence of O within the Pd has caused voids to form within the cluster as the process of vacancy exchange takes place due to atomic diffusion of the two species, Pd and O.

The next step in the investigation into void formation in size selected Pd clusters is to design an experiment with strict control over the factors relevant to the formation of these structural features. For instance, control over the atmospheric or oxygen exposure of Pd clusters may reveal at what level the kirkendall effect is observed with clusters. Also, whilst maintaining a constant oxygen exposure a wider range of Pd cluster sizes could be investigated to determine the specific onset of void formation. Future experiments are discussed within the next section of this chapter.

It has already been postulated, in the first half of this chapter, that the presence of oxygen within the formation chamber may slow the sintering rate of merging seed clusters and therefore lead to elongated structures of features. If this is the case then the void formation may perhaps have occurred prior to deposition, depending on the timescales of the void formation. It could be thought that the formation of voids may have occurred over a longer timescale but from oxidisation in the gas phase, hence explaining why only $\approx 50\%$ clusters are seen to have developed the feature. Oxidation of Pd clusters has been shown by Stevens *et al* [178] from magnetron sputtered clusters exposure to the atmosphere after deposition. In this case the Pd particles developed an outside oxide layer around a Pd core and no evidence of the Kirkendall effect was seen. Although the

clusters used in this study were stored under vacuum conditions, transportation of the samples to the microscopes was done under ambient conditions where oxidation may have occurred. So this experiment cannot confirm when the first exposure to oxygen may have occurred.

Once again within this thesis we return to the idea that structure determines function, and voids within clusters as discussed from the literature is no exception. Applications suited to such cluster structures that have been proposed are the use of the void as a site for a nanoscale reactor in catalysis [179] or in bio medical applications with it used as a drug delivery system [174]. In the later case the stress that is induced on the solid from an enlargement of the void in its centre causes the creation of a porous material, suitable for bio-medical applications.

6.4 Summary

The morphology of Pd clusters formed via gas-condensation has been shown unambiguously, via HAADF-STEM, to be strongly size-dependent, with the formation mechanism undergoing a competition between the rate of solid state diffusion processes and the time interval between cluster seed impacts. It is envisaged that one may select not only the cluster size but also the cluster shape via tuning kinetic parameters, such as temperature, gas carrier pressure as well as cluster flight time. The outcome of this work suggests that further investigation along this line would not only provide insight into fundamental understanding of cluster formation, but also a platform to explore practical applications of deposited size-selected clusters. Amongst the many tunable parameters inherent within the cluster source upon cluster creation it is suggested that the most effective future experiment into the structural formation of oblate or elongated clusters be through the variation of condensation length. This would allow the other tuning parameters to be kept constant for a single sized Pd cluster, whilst changing the time scales allowed in its formation. Hence this experiment may confirm the theory that the cluster is not given enough time to sinter to form an equilibrium structure before formation stops upon exiting the chamber. Unfortunately, at this time the current cluster source at the University of Birmingham does not have this capability, but it should be considered as a modification in the future.

The second part of the experiment involved the investigation into the dip in intensity seen at the centre of size selected clusters above N = 2622. This experiment has shown that due to oxygen exposure of the size selected Pd clusters a void has formed within the cluster via the Kirkendall effect. The size of the voids has been shown via HAADF-STEM analysis and they are seen clearly within the micrographs to be inherent on clusters of a certain size. The continuation of the structural periodicity seen over the area of the intensity dip using C_s corrected STEM illustrates that the void is positioned somewhere within the cluster structure and is not a crater on the cluster surface. Energy dispersive X-ray analysis has confirmed the presence of both Pd and O within the cluster structure, providing evidence for the means for the Kirkendall effect to take place. Evidence for this effect seen in Pd clusters has not previously been presented within the literature. A more detailed experiment is suggested to investigate the presence of voids within size selected Pd clusters. There are many experimental factors that could be investigated. The literature suggests that the void creation is subject to the temperature of the cluster, the size of the cluster and the atmosphere that it is exposed to. A thorough investigation all three factors should be considered and investigated using HAADF-STEM analysis. With regards to the modulation of oxygen exposure, equipment is not available within this lab to perform such an experiment, but one could perhaps measure the exposure to air by means of time left out of vacuum. A heating stage could also be employed during this exposure and the results then recorded. A wider range of sample sizes could be investigated in order to determine the specific onset in terms of size for this structural feature.

By understanding the nature of structural features observed one can begin to control the desired features and tailor the structures for use within the desired application. This chapter has proposed, for the case of Pd, formation mechanisms which cause irregular structural features such as elongation and voids. The use of HAADF-STEM has been shown to be a valuable tool to use for morphological analysis of clusters, showing capabilities to determine the cluster size, irrespective of morphology, and offering information beyond the topology of the cluster structure by collecting coherently scattered electrons transmitted through the sample.

Chapter 7

Atomic Structure of Supported Size Selected Cluster: Pd$_{887}$

7.1 Introduction

This chapter presents work done into the detailed structural characterisation of size-selected cluster, Pd$_{887}$, using a spherical aberration corrected STEM. The objective here is to deepen our understanding of the atomic structure of supported clusters. Atomic structure is vitally important as it is well known that specific features of cluster structures are related to their catalytic activity [140, 141], and thermodynamic or electronic properties [180]. Chapter 5 set out a detailed review of STEM based characterisation techniques. The results of Chapter 5 showed that the size-selected Pd clusters have a close agreement to the spherical cluster approximation under the experimental conditions used. These results were then used for the structural characterisation of unknown Pd particles using the high-resolution mass selected clusters as a mass balance via quantitative analysis of HAADF-STEM images. It is the incoherent nature of these images that allow this nanometrology to be performed and three-dimensional data obtained for Pd clusters and particles. In the same way, and with higher resolution possible with the Jeol microscope, it may be possible to gain three-dimensional data from images of Pd clusters where the intensity of the electrons scattered by each atomic column is related to the number of atoms they contain. The ability to see atomic column positions also

allows comparison with simulated structures that a cluster could potentially form. These experimental goals are presented and discussed within this chapter.

Theoretical studies into cluster structure are capable of producing exact atomic structures, with the positions of each atom within the cluster known. However, the limited resolution of STEM, and the sheer complexity of the number of possibilities for atom positions within a cluster, severely restricts the ability to match experimental results with theoretical predictions. Aberration corrected HAADF-STEM is however, the most suitable tool to offer insight into the three-dimensional details of nanostructures at an atomistic scale. The gap that exists between experiment and theory is a scientific problem that has to be addressed, and this chapter presents a method developed to do so, and offers insight into the many difficulties that arise when trying to achieve experimental structural determination of nanoclusters. For instance, it was shown in Chapter 6 that cluster formation mechanisms play a large role in the morphology of the cluster, and that the number of variables determining the resultant structure are many. Storage conditions of the cluster and its interaction with the substrate can also affect its structure prior to imaging under STEM. Even after these factors have been taken into consideration, when studying the cluster in the microscope the orientation of the cluster under the electron beam greatly affects the user's ability to characterise it as a specific structure, by masking important structural features.

Whilst a-C has many advantages as a substrate (see Chapter 3 and 4), the roughness of its surface means that clusters will be orientated at a variety of angles. Take the Marks decahedron for example; work by Scherbarchov *et al* [180] shows how this structure will be metastable when sitting upon a substrate surface on its (100), (111) or perched on re-entrant facet corners. This is shown schematically in Figure 7.1. In addition to this, Figure 7.2 illustrates how a cluster can present itself under the electron beam in random orientations due to the nature of the a-C substrate irrespective of its tendency to sit in any particular way.

All of these variables would be extremely difficult to model within a theoretical simulation and thus making the gap between experiment and theory difficult to bridge. An example of theoretical simulation and experimental study can be found in the work of Li
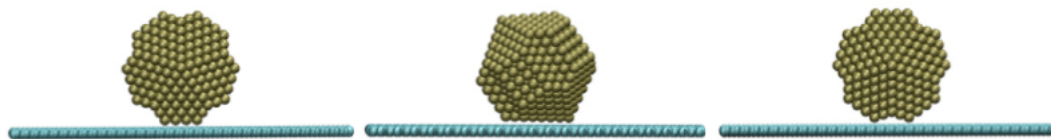
FIGURE 7.1: Metastable orientations of a supported Marks decahedron Pd$_{887}$ cluster: Cluster rests upon the (100), (111), or re-entrant facets as shown from left to right. Figure taken from reference [180].
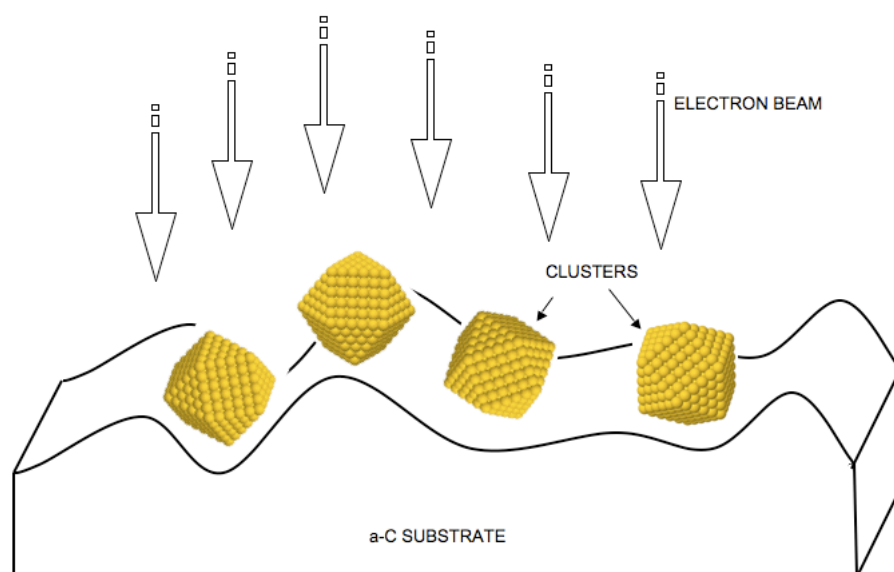
FIGURE 7.2: Clusters upon an a-C substrate. The orientation of a cluster upon the substrate with respect to the electron beam is random due to the irregular surface of the a-C substrate that they are deposited on.

et al [5], as mentioned in Chapter 2. The comparison of image simulation and HAADF-STEM analysis identified geometries such as ino-decahedra, cubocatahedra and icosahedra for the size selected cluster Au$_{309}$. These findings were consistent with theoretical modeling of the cluster system, with many different closely packed energy minima found for the Au$_{309}$ ± 6 atom cluster. Similar techniques are employed within this chapter for Pd$_{887}$ clusters. The symmetry present in proposed cluster structures (see Chapter 2 for a review) provides distinguishing features that can be identified when imaging clusters in TEM or STEM. These features can then be compared to the theoretical models to ease interpretation procedures. For example, work by Flores *et al* [181] presents a system that can identify structural features of metal nanoparticles at different orientations from TEM micrographs using digital image processing. Features are attributed to different structural types such as decahedral, icosahedral, fcc, twinned and amorphous particles.

Jose-Yacaman *et al* has performed many studies into the structural determination of nanoclusters using HRTEM and cluster modeling. One such study found Pd nanoparticles deposited onto an MgO substrate to be grouped into fcc, decahedral and icosahedral structural motifs [54]. Other investigations by the same author [182] found the presence of amorphous Pd nanoparticles at sizes of 1-5 nm under HRTEM study. The clusters not identified as amorphous in this study were grouped into the common structural motifs already mentioned in Chapter 2. In a study by Ascencio *et al* [53] electron microscopy and theoretical micrographs are compared for gold nanoparticles a few nanometers in diameter, finding all the above mentioned structures. It is worth noting that this study states that although calculations were performed for Au, there should be very little difference for other noble metals. Hence, it is possible to establish from the literature the specific structural features that correspond to specific structural motifs, and that the TEM is an excellent tool for such analysis. The C$_s$ corrected HAADF-STEM offers new insight into cluster analysis though, not suffering from phase contrast and offering three-dimensional information about the cluster structure at the atomic scale

General factors to consider for the quantitative analysis of HAADF-STEM images can be found in Chapter 4. When imaging at atomic resolution there are certain variables within the experimental parameters that need more careful consideration as their importance is emphasised under these more sensitive conditions. If one is looking to quantify atomic column depths via detection of single atoms, much in the same way that size selected clusters are used to quantify particles of unknown size in Chapter 5, then the following experimental parameters have to be taken into account: 1) the beam current should not vary during the scan period when recording an image, 2) the probe position should not fluctuate away from its intended scan route, 3) microscope parameters, such as astigmatism and defocus value should be stable thus preventing any change of shape of the probe during imaging, and 4) the column must be clean and under vacuum so as to prevent the settling of any hydrocarbon contamination on the sample. In a study into atom by atom mapping of the structural and chemical composition of materials using aberration corrected microscopy by Krivanek *et al* [183], when imaging single atoms a convolution of the sample structure and the probe size was observed. They also indicated the presence of a non-gaussian probe tail. These effects were negated by processing the data using fast fourier transforms as a quick route to the deconvolution

of the probe. Another interesting investigation into quantitative C$_s$ corrected HAADF-STEM can be found in the work of Kotaka *et al* [113]. Atomic column intensity ratio dependance on defocus, convergent semi-angles, specimen thickness and detector gain were carried out for the SrTiO$_3$(001) surface. The study finds that the main difficulties of such experiments lie in the ability to find optimum focus and the presence of residual aberrations at larger convergent semi-angles. It has been mentioned previously that the energy transferred to the sample from an electron beam can cause movement of atoms or knock on damage, particularly for lighter elements such as O or C. It has been shown though that sample damage can be greatly reduced by operating at 60 keV and a probe size of 1 Å achieved [184].

All the investigations mentioned above were performed on well known crystal structures, however, cluster morphology is quasi-crystal and, on occasions, non uniform. Although it has been shown that clusters imaged with a circular projection are within a quasi-spherical regime, clusters deviating from predicted compact structural motifs require greater understanding of how the nature of such deviation can occur to atomistic levels of detail. Aberration corrected STEM can be extremely useful for this type of analysis.

Pd clusters are of specific scientific interest to catalysis, with industrial catalysts already consisting of nanometer sized particles with complex structures [140]. For clusters with sizes above 100 atoms, the size dependance on physical properties is relatively smooth in comparison to smaller clusters [180]. The fluctuating surface to volume ratio of cluster structures gives rise to the non-bulk crystalline effects, which in turn provide properties of great usefulness. Pd$_{887}$ is a cluster within the specific size range of interest to the catalytic community (diameter found to be ≈2.83 nm, see Chapter 5), but it also holds interest to the scientific community with regards to its structure. The specific size is predicted to be a closed shell for the Marks decahedron [180], although it is apparent from the literature that many structural motifs exist in close proximity to each other within this size range, based upon the specific cluster system energies. With many theoretical investigations for Pd being limited to sizes of up to 100 atoms [14], and the majority of current industrial Pd catalyst sizes being larger than this, experimental evidence for structures at sizes such as Pd$_{887}$ are of importance. It has been shown in Chapter 5 how soft landing of the clusters is thought to preserve the gas phase morphology of the cluster; this was essential to this investigation as the structure needs to be preserved if

results are to be useful to real world scenarios where clusters may be suspended rather that deposited upon a surface. It is worth noting, however, the potential for interaction between cluster and substrate (see Chapter 3 and discussion in this chapter).

7.2 Identifying Structures

7.2.1 Experimental method

This section explains the experiment conducted into the structure of the size selected cluster, Pd_{887}. All imaging was performed on the Jeol 2100F microscope with C_s corrector at 200 keV. For quantitative analysis every effort was made to ensure that all imaging variables mentioned in the last section were kept constant. A camera length of 12 cm was used for all Pd_{887} cluster images and all images were recorded at a size of 512 by 512 pixels. Images were taken at 15 M or 20 M times magnification corresponding to a pixel size of 0.022504 nm and 0.016878 nm respectively. The dwell time on each pixel was 38 μs and images were acquired in line sync mode, which means that the start of each new scan line was synchronised with the AC mains. The gain of the detector was kept constant (contrast/brightness) and there was no noticeable fluctuation in the beam current during imaging. The most difficult of variables to control was to keep the probe always within optimum focus, although it is thought that this was achieved to the best standard possible through careful imaging. The shape of the probe also may have been subject to first order astigmatism effects during the experiment. To combat this the Ronchigram was checked at regular time intervals throughout imaging, and any astigmatism present removed by adjusting the alignment of the beam. For some experiments the purpose was not to record images for quantitative analysis, but to look in great detail at the structure Pd_{887} clusters aligned in good orientation with the electron beam. For images presented of this nature the contrast and brightness of the detector was adjusted so as to obtain the clearest image possible for comparison with simulated data. Experimentally, Pd_{887} clusters were deposited with a deposition energy of 0.564 eV/atom and have an error in N of $\pm$ 35 atoms due to the mass resolution of the time of flight mass selector in the Birmingham cluster source.

7.2.2 Simulation Method

Theoretical cluster models have been prepared for comparison with experimental results. Cluster models that were chosen were those of geometric shell structures including the Truncated Octahedron (TO), Cubo-octahedron (CO), Icosahedron (Icos), and Marks decahedron (Mdh), due to their frequent occurrence from experimental observation in the literature and theoretical predictions for Pd clusters of this size range. Due to the size of the Pd$_{887}$ cluster and limited computational power, simulations involving full quantum mechanical calculations were not possible. Instead, as the structures are of high symmetry by nature, they are calculated by growth vectors from each atom point. The model is then minimised using a Gupta potential [185] and used to find the atom positions for the lowest energy structure available for the designated cluster size. This work was performed by Professor R.L. Johnston and A. Logsdail of the School of Chemistry, University of Birmingham. These co-ordinates were then imported into a program written in MATLAB version 7.9.0 (code courtesy of Dongshen He of the Nanoscale Physics Research Laboratory, University of Birmingham). This program enabled HAADF-STEM images to be simulated for each structural motif. The simulated images produced were of a size 512 by 512 pixels. For each pixel in the x and y directions the intensity contribution to the image is calculated by a Gaussian function approximating the electron probe. For the z-direction (in and out of the page) the intensity calculated is a linear function of the single atom intensity, e.g. an atomic column of 4 atoms will have four times the intensity of a single atom. The program is ideal for comparison with experimentally imaged clusters as it produces a series of simulated images taken by rotating the cluster at specified degree steps. Thus the random orientation of clusters under the electron beam can be accounted for and structural features to be identified for comparison. For each structural motif rotations around each axis in 4 or 5 degree steps were taken and simulated HAADF-STEM images produced. It is important to note that for simulated images only relative image contrast is given and other microscope parameters, with the exception of probe size, or the effects of coherent scattering, are omitted. Simulations were run using the University of Birmingham's Blue BEAR computer cluster.
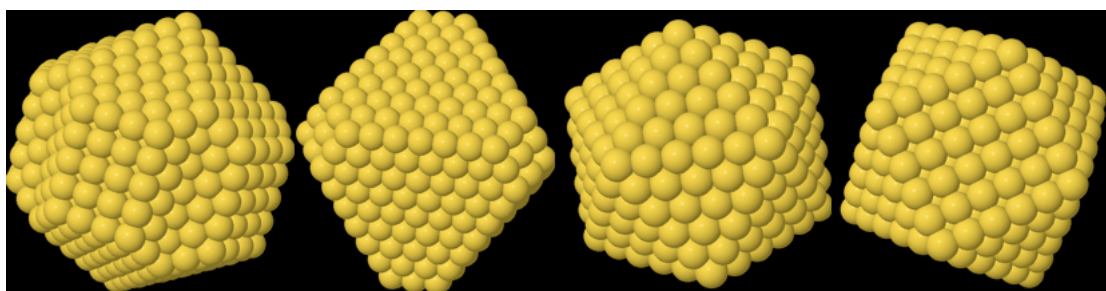
FIGURE 7.3: Hard ball models of cluster structures commonly seen in Pd nanoclusters less than 1000 atoms in size. From left to right: Marks Decahedron (887 atoms), Tructated Octahedron (861 atoms), Icosahedron (561 atoms) and Cubo-octahedron (561 atoms). Models created by inputing structural co-ordinated into Jmol (freeware program: http://jmol.sourceforge.net/).

7.2.3   Results

7.2.3.1   Unknown Cluster Structure

A total of 161 Pd$_{887}$ clusters were investigated for comparison with the simulated images. Out of this sample 86 % of clusters were found to have an irregular morphology, with no discernible features for comparison with structural models and an ambiguous atomic column contrast. Examples of such clusters can be seen in Figure 7.4. It is worth noting that, although structural columns are not identifiable due to cluster orientation or structure, the advantages of a small probe size are clear. The signal to noise ratio is much improved upon than in previous images shown that were taken with the Tecnai microscope, leading to well defined cluster outline and lattice imaging potential. The top left image in Figure 7.4 shows clusters with a 6-sided projection, many of which were seen within the sample range. It is difficult to analyse this specific orientation of cluster due to icosahedral, decahedral and cobo-octahedral clusters all potentially projecting this same hexagonal outline thus meaning that the particular structure of these clusters remains unidentified [24].

Within this group of unknown structures there exists clusters that are aligned well under the electron beam revealing structural features. Such a cluster can be seen in Figure 7.5. Here the cluster appears to present a (100) square face towards the top of the cluster, with (111) triangular sides surrounding it. This structure did not fit any models within the experiment and its structure could not be determined.
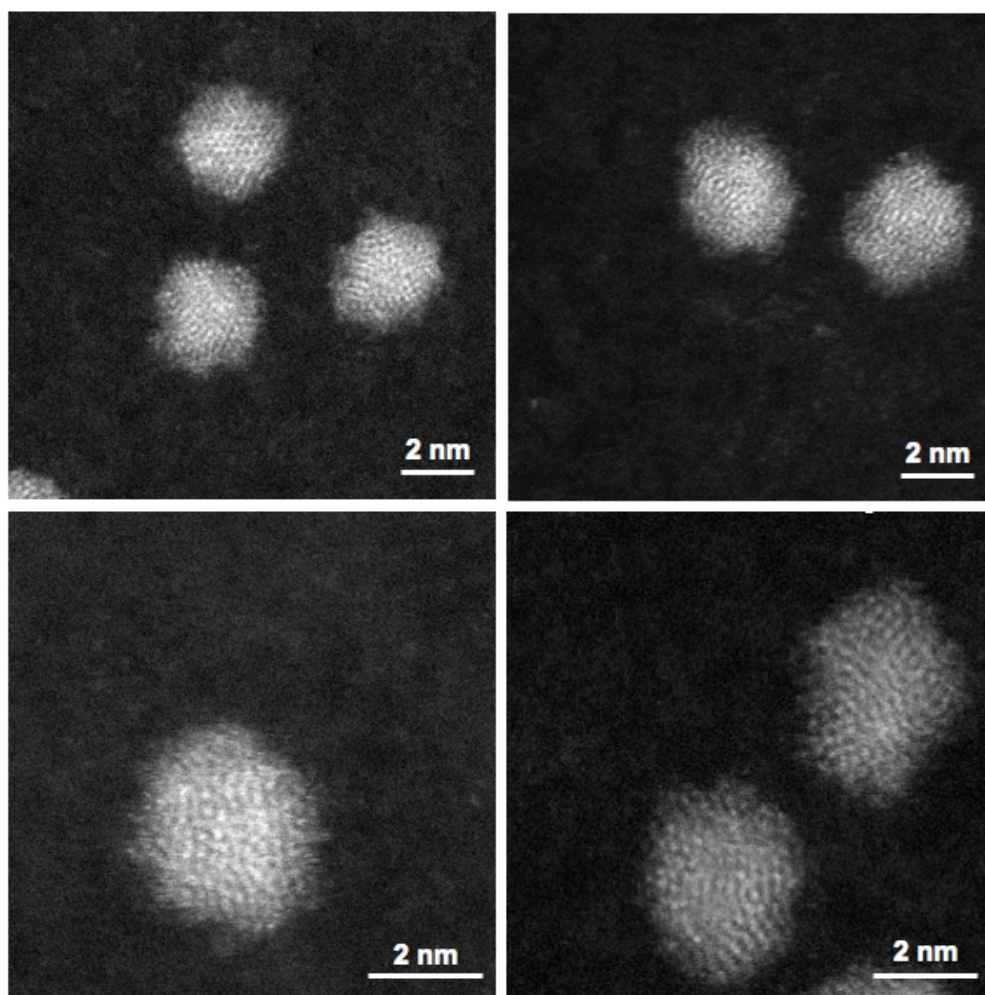
FIGURE 7.4: Pd$_{887}$ clusters with irregular morphology, no discernible structural features present for comparison with theoretical models. This cluster type accounted for 86 % of clusters imaged.
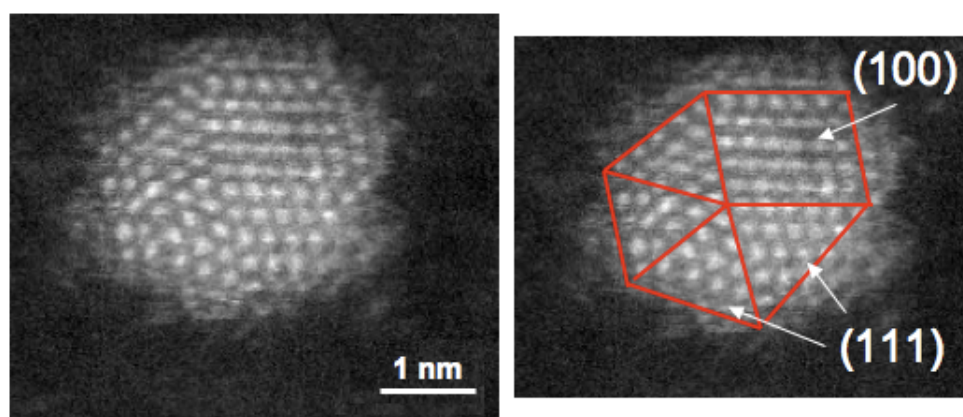
FIGURE 7.5: A well ordered Pd$_{887}$ cluster of unknown structural motif. The right hand side of the Figure displays the clear crytalographic faces of the cluster's structure as discussed in the text.

Further Pd$_{887}$ clusters within this classification can be seen in Figure 7.6. Figure 7.6 (a) shows a cluster that has good orientation with the electron beam towards the top of the cluster, displaying atomic columns. However, half way down the scan this structure is lost and the image appears streaky. The presence of single atoms near the cluster perimeter surrounding this area tells us that the image is still in focus, so the change in cluster morphology is surprising. One explanation for this is perhaps that structural re-orientaion or rotation of the cluster occurs during the scan, caused by the high energy of the electron beam interacting with the cluster. Imaging Pd$_{887}$ clusters in this manner does not allow adjustment of focus and astigmatism during the scan or scans previous to the recording of the image. The cluster just described is good evidence of how structural features of a cluster's gas phase morphology may be lost due to interaction with the electron beam. This means the imaging of such clusters is in effect a one shot affair, if the purpose of the experiment is to study the gas phase morphology. However, one advantage of STEM imaging is that it displays imaging results in real time. The induced heating of a cluster as a consequence of the electron beam interaction, and resulting structural change, can therefore be studied as it happens through repeated scans. In comparison, TEM studies of such events would only be capable of showing the before and after of the cluster's structural adjustments. Figure 7.6 (b) and (c) display clusters with a well defined perimeter and structural features that could not be associated to a known structural motif, and Figure 7.6 (d) shows a clusters which has well defined symmetrical edges about the central region with apparent disorder, or misalignment with the electron beam, throughout the remainder of the cluster.

The final cluster worthy of note shows well aligned structure under the electron beam but is of unknown morphology, is displayed in Figure 7.7 (a). Chapter 2, Figure 2.3 displayed forms of decahedral morphology showing the top down view of these cluster types having 5 -fold symmetry about their central axis. This cluster displays the characteristics of 5-fold symmetry but tilted away from the central axis to the right hand side. This is demonstrated in Figure 7.7 (b), with the lines of symmetry drawn on to the cluster for illustration. The well aligned atomic columns can be seen projecting from a central point, although the triangular (111) faces are not all visible around the axis of symmetry due to the cluster orientation upon the substrate. No structural match with simulated data could be found for this cluster.
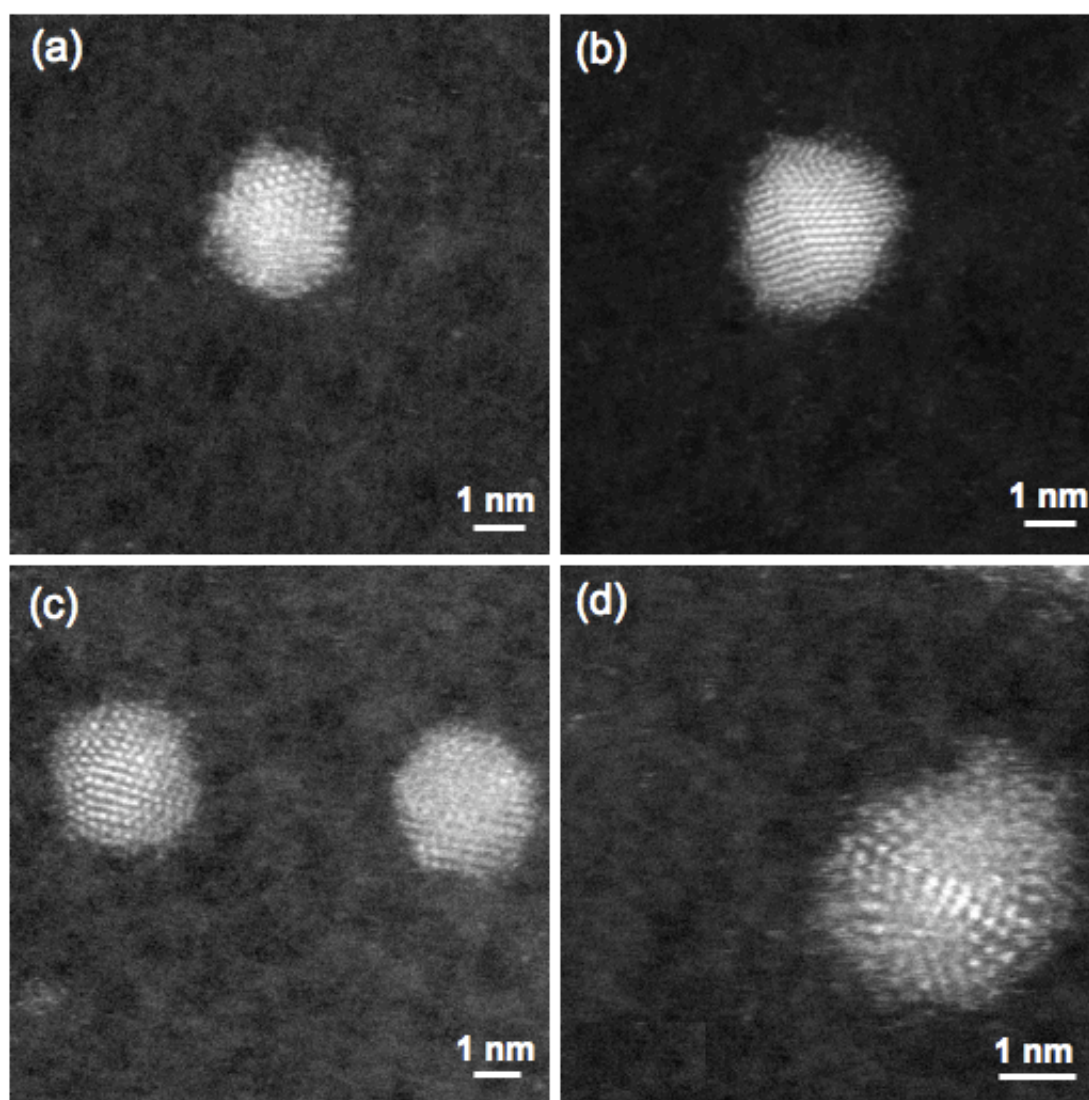
FIGURE 7.6: HAADF-STEM micrographs of Pd$_{887}$ clusters of an ordered nature but with no assigned structural motif. Note that (a) displays a good example of cluster-probe interaction, see text for details.

Where the structural motif could be recognised, comparison has been made to appropriate simulated images and their corresponding fast fourier transform (FFT). The following subsections give examples of this for a range of different shapes.

7.2.3.2 Cubo-octahedron

The cluster shown in Figure 7.8 presents a hexagonal outline typical of an fcc structured cubo-octahedron. The experimentally imaged Pd$_{887}$ cluster is shown in the bottom left
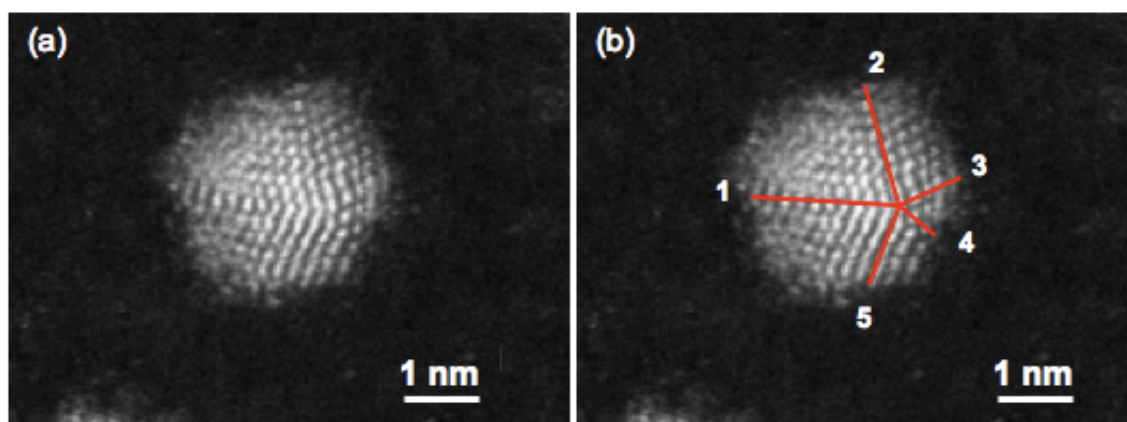
FIGURE 7.7: HAADF-STEM images of Pd$_{887}$ cluster (a) The off-axis five fold symmetry visible within the cluster, no structural model could be found to fit this specific cluster. (b) Cluster orientation is illustrated, as mentioned in the text, with the five lines of symmetry drawn on the cluster for illustration.

of the figure with the simulated image of a Pd$_{561}$ cluster bottom right, in the same orientation as the imaged cluster. The cluster presents both (100) and (111) facets as labelled in the hardball model in Figure 7.8, where the model cluster is shown exactly as it sits upon the substrate surface. The corresponding fast fourier transforms of both experimental and simulated clusters are shown above the cluster images. The spot geometry of the simulation is similar to the diffraction pattern of the cluster image. FFT comparison is extremely helpful in determining the cystallographic features of a cluster, especially in the cases where image contrast is complex and hard to distinguish. In this case the resemblance of the real and simulated FFT's is clear when the micrograph comparison is perhaps less clear, confirming the structure to be that of the cubo-octahedron. The hard ball model is also shown for reference. Three Pd$_{887}$ clusters with cobo-octahedron morphology were found within this study.

7.2.3.3 Icosahedron

A total of five icosahedrons were found within the sample and a good example of such a structure can be found in Figure 7.9. Due to the complex nature of cluster orientation possibilities upon the surface and the arrangement of atoms for the icosahedron model it is difficult to identify such structures within the sample. It is seen in the simulation that, for most orientations, the icosahedron is not a linear columnar aggregation of atoms. A
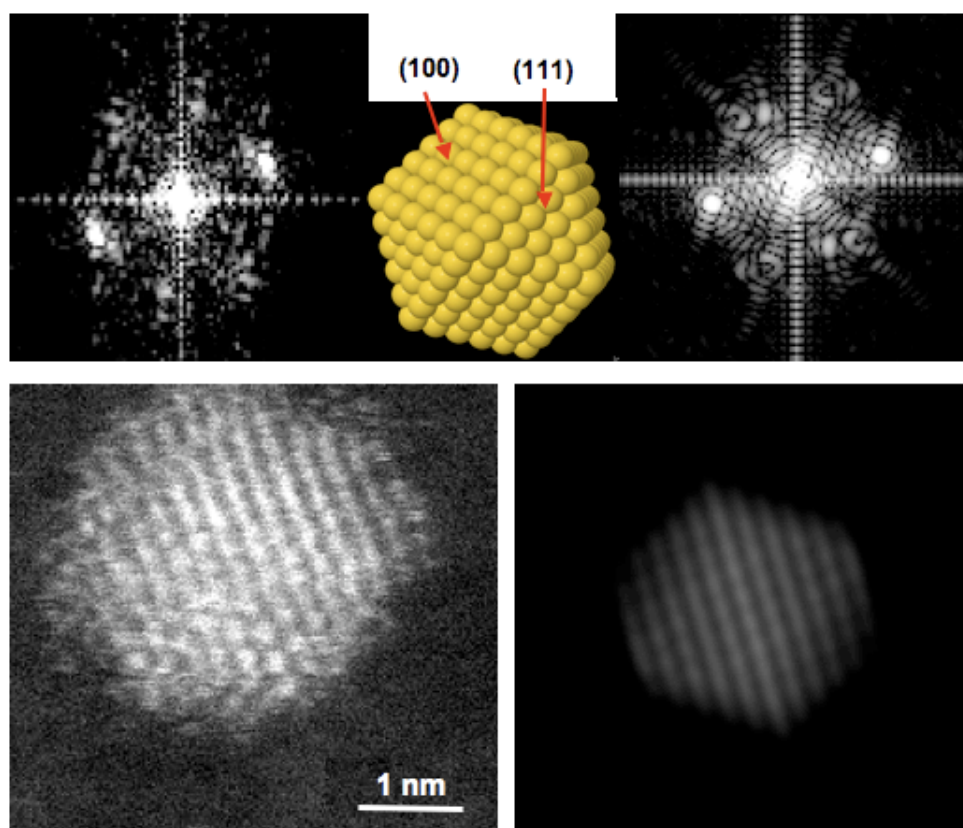
FIGURE 7.8: An example of a Pd$_{887}$ cluster with a cubo-octahedron morphology. The left hand side represents the experimental data of a Pd$_{887}$ cluster and the right hand side the simulated data of a Pd$_{561}$ cluster. Both real and simulated clusters present both (111) and (100) facets and show an excellent match between the FFT's. The hard ball model is also shown for structural reference with the same orientation as the clusters shown in the micrographs.

specific feature that distinguishes the icosahedron is the presence of bright atoms surrounded by a circular motif of surrounding atoms. This feature can be seen twice in the experimental image of the Pd$_{887}$ cluster in Figure 7.9 (bottom left of figure), comparing well to equivalent features in the adjacent simulated image of the Pd$_{561}$ cluster. Closed geometric shells for the icosahedron occur at N= 13, 55, 147, 309, 561 and 923, so it is perhaps unlikely that a perfect icosahedron would be found within this sample of Pd$_{887}$ clusters. It is apparent, however, that whilst direct experimental and simulation image comparisons are rare for this structure in this study, the distinguishing feature of an icosahedron does reveal itself on occasions. It is possible that poly-icosahedron are being observed. Further examples of this can be seen in Figure 7.10, where the distinguishing features of the icosahedron mentioned in this section can again be seen in the experimental cluster images.
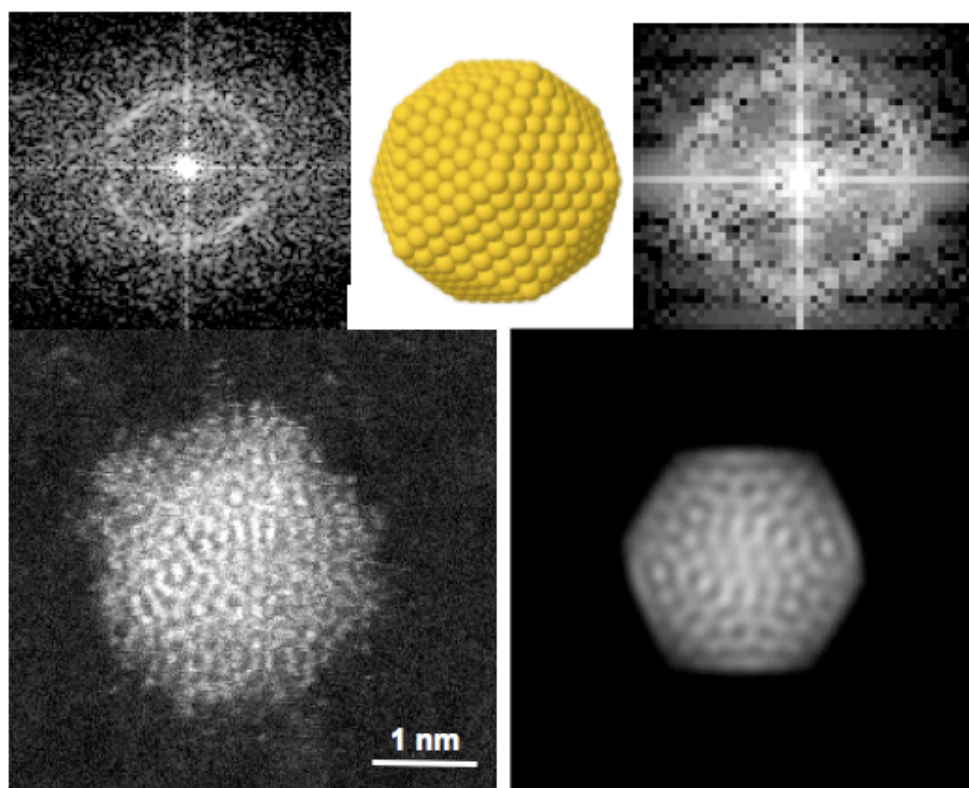
FIGURE 7.9: Right hand side: an example of a Pd$_{887}$ cluster with Icosahredral morphology. Left hand side: an example of a Pd$_{561}$ cluster with icosahedral morphology. The hard ball icosahedron model is also shown for reference. See text for details.
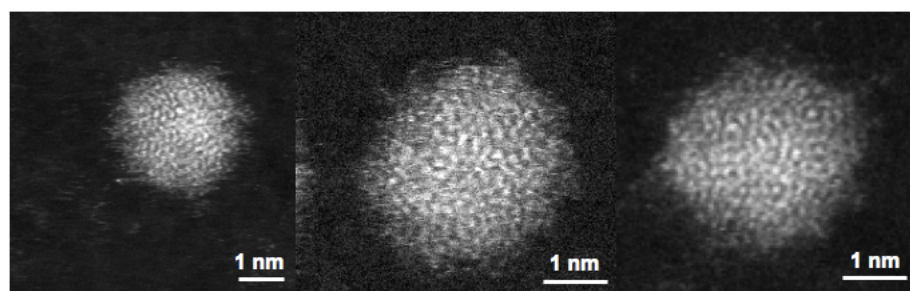
FIGURE 7.10: Experimental Pd$_{887}$ cluster images showing features of the icosahedral structural motif, see text for details.

7.2.3.4 Marks Decahedron

A further structure found in this study was that of the Marks decahedron (Mdh). Pd$_{887}$ is proposed to be closed shell structure for the Mdh but only a single cluster could be attributed to this specific morphology; this is shown in Figure 7.11. Comparison between experimental and simulated images show the appearance of two re-entrant facets of the Mdh, presented as blurred areas towards the bottom of the cluster in its current orientation. A third re-entrant facet can also be seen centrally at the top of the cluster.

The hard ball model for the Mdh is shown also is Figure 7.11 in the same orientation as the experimental cluster. The apex of the cluster can be seen with the five fold lines of symmetry originating from this point. Agreement of the FFT's confirms this structural motif and orientation upon the substrate surface.
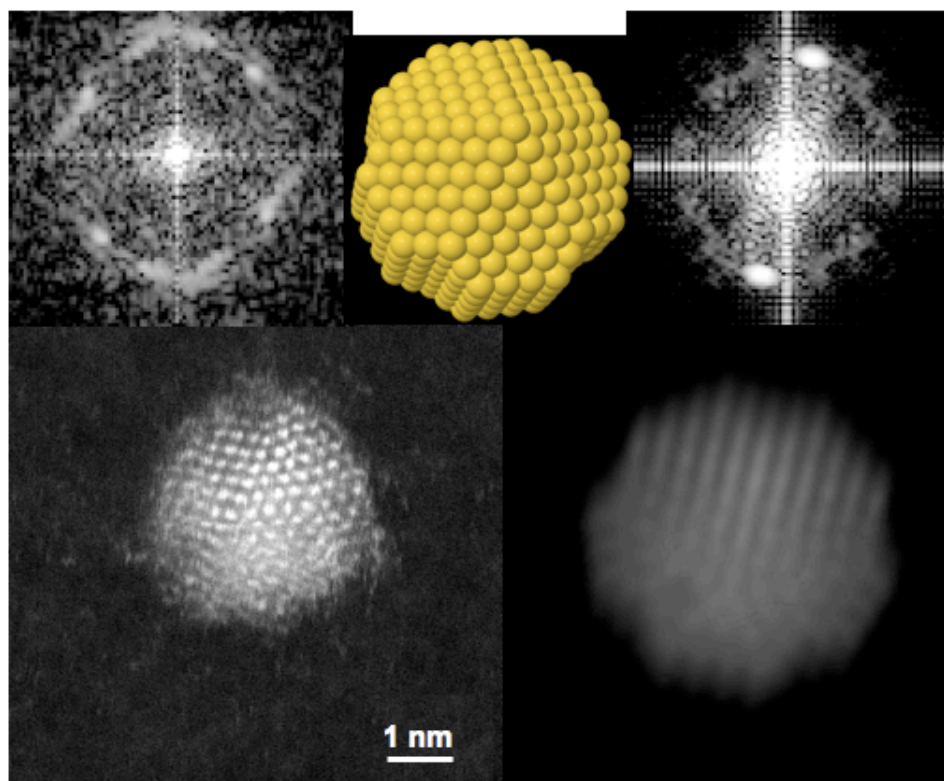
FIGURE 7.11: Pd$_{887}$ cluster with the structure of a Marks decahedron. Experimental (left) and simulated (right) images and FFTs are displayed in good agreement with each other. Two re-entrant facets of the Mdh can be seen at the base of the cluster. The hard ball Mdh model is shown for reference.

7.2.4 Truncated Octahedron

Within the simulations performed for global minima structures of varying sizes there exists a structure very close in size to the Marks Decahedron at size N=887. This is the Truncated Octahedron (TO), which occurs at size N= 861, a value within the error range for the Pd$_{887}$ size selected clusters from our cluster source. Like the cubo-octahedron this is also constructed from fcc packing. Four such particles were found within the cluster sample, an example of which is given in Figure 7.12, where the experimental and simulated images show the cluster with two (111) faces facing the electron beam. The hard ball model of this structure displays this orientation for comparison. It is

interesting to note a feature of the cluster in the experimental image, where the slight distortion of the cluster is apparent horizontally along its centre is due to noise whilst recording the image; above and below this line it is apparent that the columns in the lower half are brighter than those in the upper half. In comparison the simulated image presents no such variation with the TO structure symmetrical about this central line. This is due to the HAADF-STEM imaged TO structure being asymmetrical about its centre, with the lower half of the cluster containing more atoms in each column than the top half.
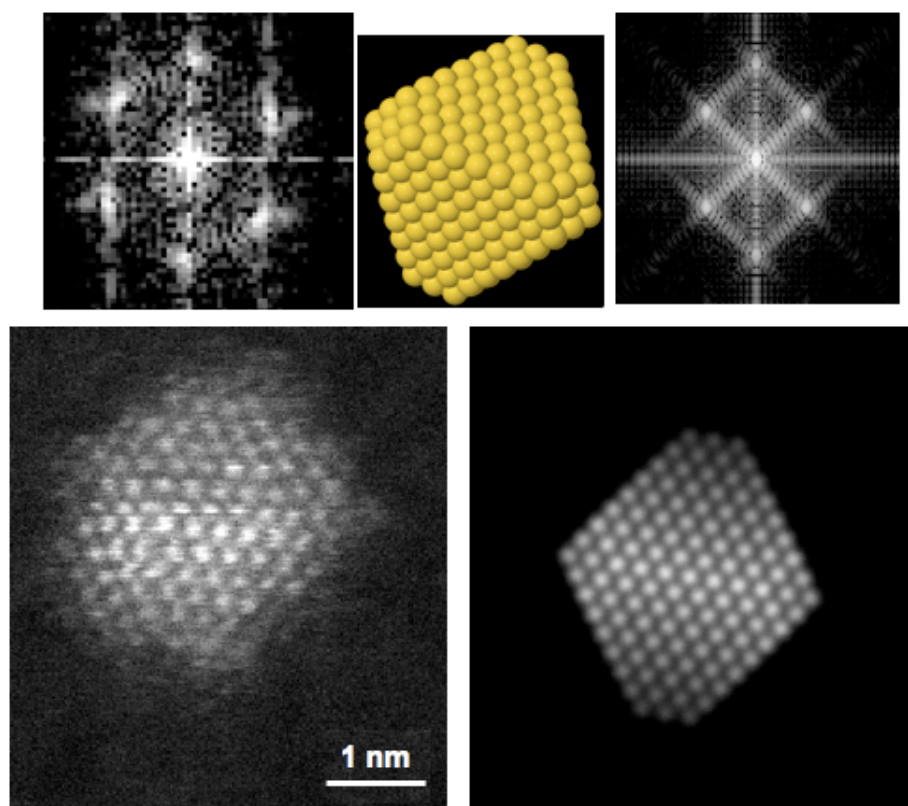
FIGURE 7.12: Pd$_{887}$ cluster with the structure of a truncated octahedron with two (111) faces displayed under the electron beam. Experimental results are shown on the left hand side and simulations on the right. For discussion see text.

7.2.5 Discussion

The need to experimentally characterise cluster structure at the atomic scale has been discussed in detail throughout this thesis. The gap between theory and experiment needs to be bridged in order to be able to design nanostructures for application and use within real world scenarios such as catalysis. The mass selection available within the cluster

source at the Birmingham laboratory has allowed a unique opportunity to compare Pd clusters of a known size with theoretical structures within similar size regimes. There is, however, a distribution of cluster mass arising due to the mass resolution of the cluster source, inherent in the Pd$_{887}$ clusters studied within this chapter. This is illustrated by the integrated HAADF intensity distribution shown in the histogram in Figure 7.14.
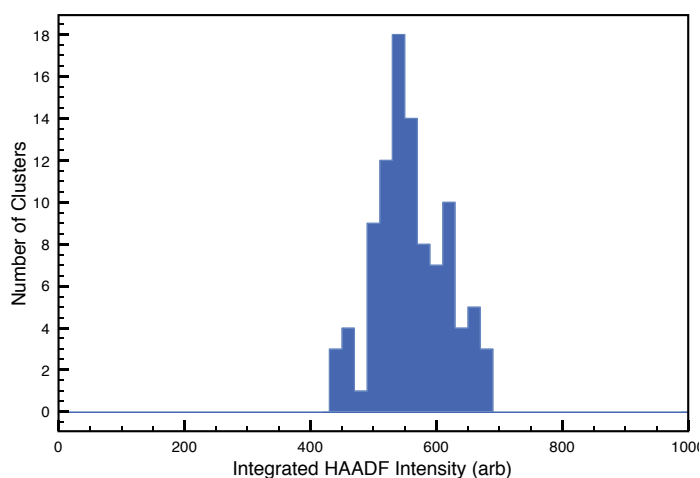
FIGURE 7.13: A histogram showing the integrated intensity measurements of Pd$_{887}$ clusters.

It is apparent from Figure 7.14 that the exact size in terms of N cannot be fully known within the size selection process for any clusters under investigation. The error placed upon the mass resolution of the cluster source is ± 4 %. How much influence this error in N has on the structural outcomes of the Pd$_{887}$ clusters is difficult to determine. For example, if the experimental parameters were entirely suited to the formation of the proposed Marks decahedron for a Pd$_{887}$ cluster, then any deviation of N about this number may lead to the formation of an unclosed geometric shell. The balance of internal/external strain on the cluster would then lead to the introduction of new facets, leading to a distorted and incomplete version of the Marks decahedron or perhaps a entirely new form of structure. This represents another difficulty in experimentally verifying proposed structural models, even with the atomic resolution enabling us to do so.

This issue is coupled with the random orientation of clusters upon the substrate surface, making the structural features unique to each structural motif difficult to identify if not correctly orientated under the electron beam. In other words, in practice, there exits

a narrow distribution of sizes and many orientations that a Pd$_{887}$ cluster may take, leading to many different structural possibilities resulting in exact identification issues in characterisation. To combat these effects, many different structural motifs have been simulated to aid the recognition of structural features seen experimentally. However, yet more motifs are needed to widen the possibilities of finding a match between theory and experiment.

The use of C$_s$ corrected STEM has been extremely useful in the structural determination of Pd$_{887}$ clusters from two-dimensional projection and comparison with simulated images. Clusters have been successfully identified with cubo-octahedral, icosahedral, Marks decahedral and truncated octahedral morphologies. However, it is unfortunate that a large percentage of clusters fell into the category where their structure could not be determined. Many of these showed good alignment under the electron beam, revealing interesting structural features, but still could not be identified with certainty. The inclusion of more theoretical simulations could help to identify such morphologies and achieve better knowledge of supported Pd cluster structure. The classification of some cluster structures as amorphous has been avoided due to the lack of a larger range of simulated data for comparison. However, it is feasible that many of the 86% unknown supported Pd$_{887}$ cluster structures are disordered and amorphous in nature. For many structures where no diffraction spots within the FFT could be easily identified, and no clear discernible features seen within the image, this could well be the case. It would require more investigation via simulation before definite conclusions could be drawn. Evidence suggestive of disorder in Pd$_{887}$ can be found when comparing the data presented so far in this chapter to that of a similar study into Au$_{887}$ [186]; this study used the same techniques for characterisation as presented in this chapter. A total of 40 % of clusters were assigned a structural motif, in comparison to the 14 % found for Pd. This result is suggestive that Au may be more structurally ordered than Pd.

For clusters where an associated structure was identified it is found that there is a mix between crystalline and non-crystalline morphologies; this highlights the competition between these motifs for this size range of cluster. It is clear that this method of structural identification could benefit greatly from automation, as has been performed by Flores *et al* [181] for TEM studies of clusters. It is thought that this may improve the experimental method by reducing the time taken to perform analysis and also make

the experiment accessible to many more cluster experimentalists, as the identification of structural features often requires an experienced eye. The nature of the system itself presents problems of structural characterisation, but the method has been shown to have successful applications in nanocluster characterisation at the atomic scale. The method presented is believed to be the best way to structurally characterise clusters at the atomic scale given the issues surrounding atomic characterisation that do not lend well to alternative characterisation methods. For example, tomography would not be suitable as a resolution of ≈1 nm would not be sufficiently detailed to reveal structural features vital to clusters with applications in catalysis, where individual atom positions are required to be known. Multi-slice imaging could achieve the desired resolution but would not be suitable for this type of characterisation due to the movement of atoms and structural change that the cluster would undergo through interaction with the electron beam during the multiple images taken inherent on this technique.

In summary, this chapter has highlighted the usefulness of C$_s$ corrected STEM as a powerful tool for detailed structural determination of supported nanoclusters. Through the combination of simulation and experiment, the characterisation of cluster structure has been succesfully demonstrated and the difficulties surrounding the nature of the experiment discussed. With the ability to characterise sample structures one can begin to understand the nature of their formation under specific conditions. This in turn can lead to comparison of specific structures with associated properties such as catalytic activity.

7.3 Three-dimensional Measurement at the Atomic Scale

Both the literature [53, 54] and this study demonstrate that projected cluster images allow reasonable assessment of cluster structure. The identification of single atoms has not yet been approached within this thesis and can be a useful ability in C$_s$ corrected HAADF-STEM imaging, in comparison, single atoms are difficult to image readily with conventional HRTEM studies. Single atoms can usually be found close to a cluster perimeter, having fallen from the cluster during impact with the substrate, or perhaps undergone the evaporative process during heating induced by the electron beam. The soft-landing of Pd$_{887}$ clusters at very low energy per atom means that these atoms are

not as frequently observed as might otherwise be the case, restricting the population available for statistical analysis. It has been discussed previously how the intensity of a given point within a HAADF-STEM micrograph is directly related to the number of atoms situated at that point, provided a thin sample is used. Hence by recording intensity values for single atoms, one should be able to compare this intensity to the varying intensity of multiple atomic columns, thus calculating column depth in terms of number of single atoms. Van Benthem *et al* [187] has shown that the HAADF intensity increases linearly with atomic column depth for up to 6±2 atoms of Au. This was established using Z-contrast simulations and through focal series images of nanocrystals. Quantitative depth resolution has also been established for Au$_{309}$ clusters by Young [6], column depths of 9 Au atoms were found in clusters via comparison with simulated Z-contrast images. A study by Wang *et al* [161] uses an atom counting HAADF-STEM method to verify the size of monolayer protected Au clusters of a proposed size by comparison to size-selected gold clusters, this was done for clusters containing up to 38 Au atoms in total. No such studies have been found within the literature for Pd clusters.

Quantitative image analysis was performed for Pd$_{887}$ clusters using the Jeol 2100F microscope as described in the following paragraphs. The integrated HAADF intensity distribution can be seen in Figure 7.14 (a). Only clusters that were well separated were analysed in order to inhibit the possibility of material transfer by diffusion from one cluster to another in close proximity. The mean intensity value for a Pd$_{887}$ clusters was found to be 759 ± 154. Figure 7.14 (b) shows the histogram for measured intensities of single atoms. The mean single atoms intensity was found to be 0.64 ± 0.19.

Single atoms were identified near to the cluster perimeters by utilising false colour function within the ImageJ software. The contrast and brightness of the image could also be adjusted to reveal single atom locations with greater ease. Examples of this single atom identification method can be seen in Figure 7.15, (a) and (b) are 3-dimensional representations of the HAADF-STEM micrographs; the single atoms can be clearly seen circled in white. Figure 7.15 (c) and (d) show standard images with colour adjustment to assist in the identification of single Pd atoms.

By dividing the average total intensity for a Pd$_{887}$ cluster by that of the average single atom intensity we may see how many atoms the cluster contains, as long as the measurements are accurate and the intensity relationship with size holds true. According
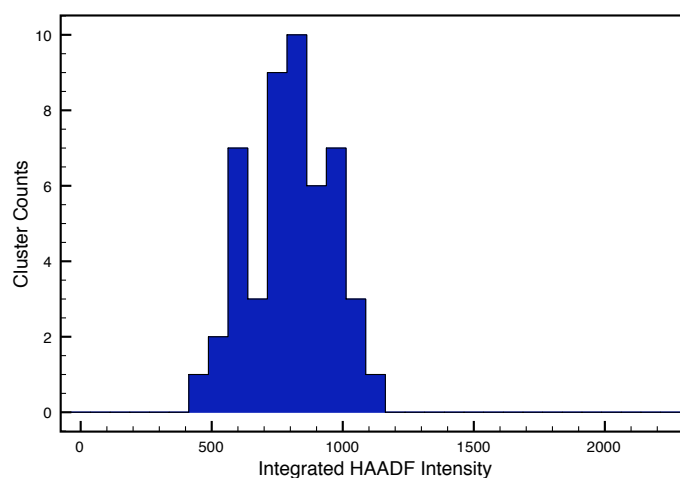
(a)
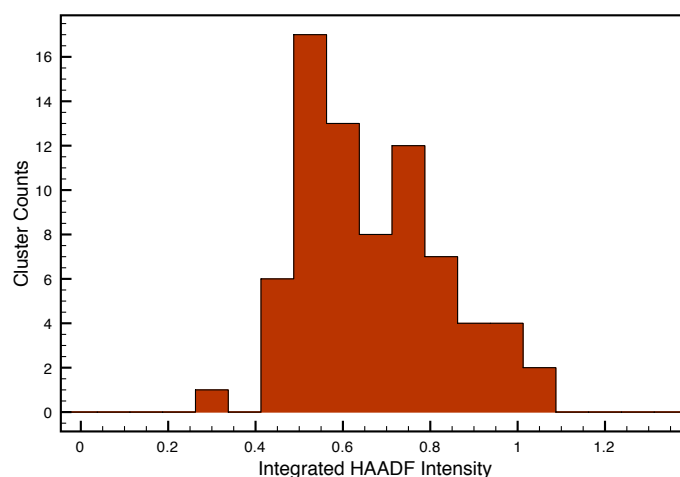
(b)

FIGURE 7.14: (a) Histogram of integrated HAADF intensity for Pd$_{887}$ clusters imaged with the Jeol 2100F microscope. (b) Histogram of integrated HAADF intensity for single Pd atoms found in close proximity to the Pd$_{887}$ cluster perimeters.

to the measured results the Pd$_{887}$ cluster contains 1186 atoms, a value which is far outside the upper error limit for N from the mass selection of the size-selected clusters. In parallel to this investigation column mapping of two well aligned clusters was also performed. Based upon the scattered intensity from a single Pd atom, the integrated intensity from each visible column of a Pd$_{887}$ cluster was measured. It is assumed that the background intensity for each column was that of the average background value for each single atom measured, as each column sits upon the substrate surface with an area of one atom. Figure 7.16 displays the two clusters investigated, the HAADF-STEM
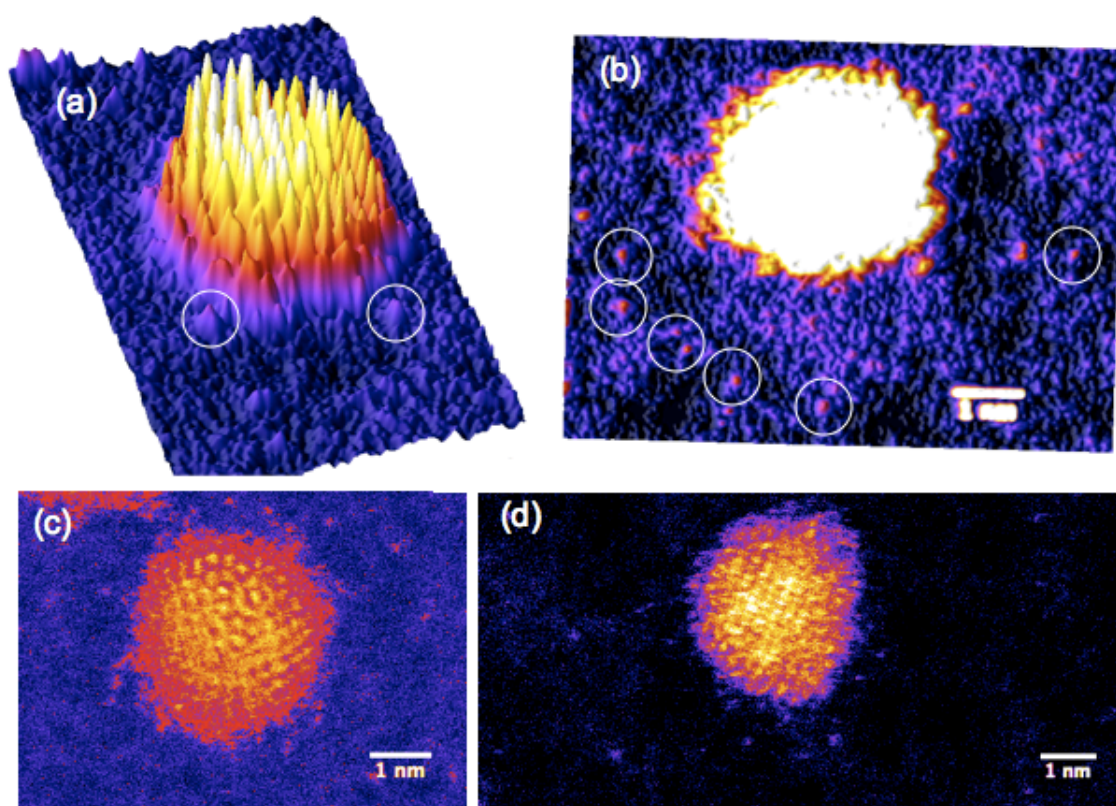
FIGURE 7.15: (a) and (b) are 3-dimensional representations of the HAADF-STEM micrographs, the single atoms can be clearly seen circled in white in close proximity to the Pd$_{887}$ cluster. The contrast adjustment in (b) illustrates the presence of single atoms more clearly than a standard micrograph. (c) and (d) are standard HAADF-STEM micrographs with false colour applied.

micrograph is given in each case, with the adjacent image showing the labelled columns that underwent quantitative analysis. The intensity of each column was measured and the background intensity subtracted. The number of atoms in the column was then calculated by the average single atom intensity. For example a column with integrated intensity value of 4.07 minus the average single atom background of 1.46, divided by the average single atom intensity, 0.64, gives a result of the column containing 4.08 atoms. It is not possible to map the entire cluster in this way as not all of the cluster can be resolved in terms of atomic columns; much of the cluster perimeter appears less well defined than the central regions, and could not be measured. There is also scattered intensity between the atomic columns that has not been accounted for in this analysis if one just takes the atom perimeter of the column as an intensity measurement. This is discussed further in the next section of this chapter. The column sum for Figure 7.16 (a) amounts to 490 atoms, and for Figure 7.16 (b), it amounts to 548 atoms. Both

results deviate significantly from the expected (887 $\pm$ 53) atom value. However, the analysis represented by Figure 7.16 illustrates the points made regarding the difficulties experienced when counting the total number of atoms in a cluster via atomic column mapping, as previously discussed.
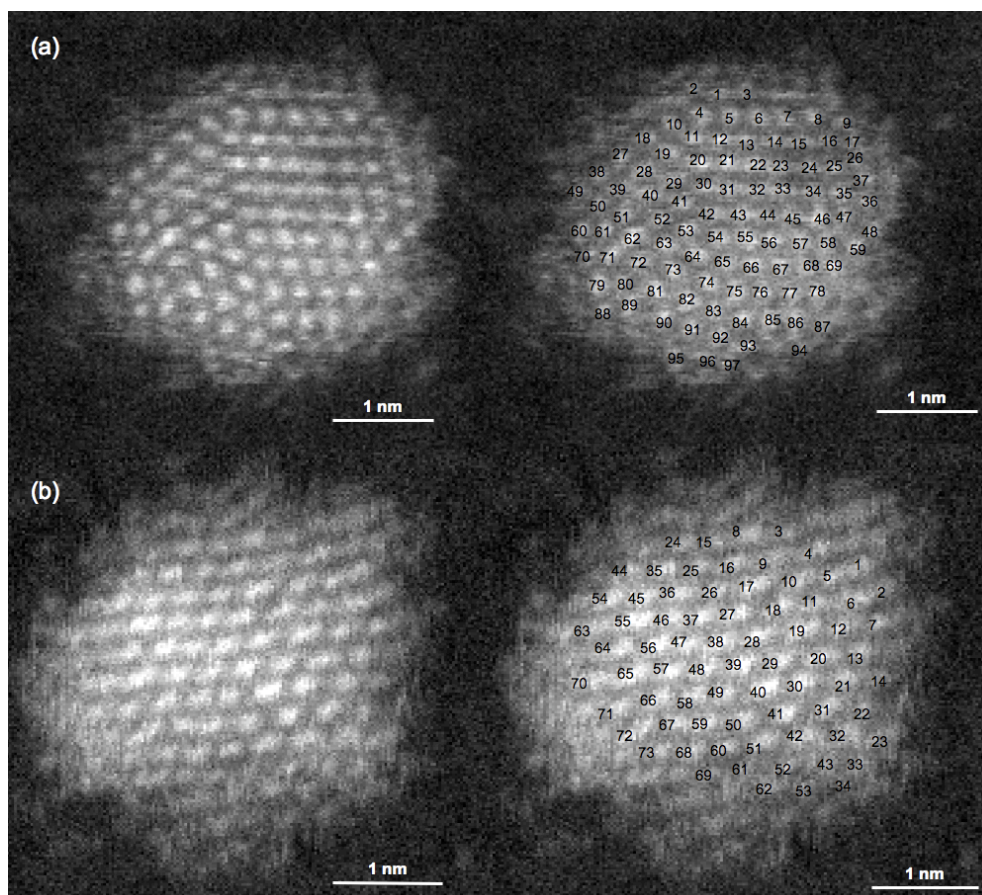
FIGURE 7.16: Both (a) and (b) shown the original HAAF-STEM micrograph of Pd$_{887}$ clusters used for column mapping on the left hand side. The right hand side displays the same cluster but with each column that underwent analysis labeled. See text for details and discussion.

7.3.1 Discussion

This last section has highlighted some of the experimental difficulties in single atom detection and its use in quantifying cluster size and atomic column depth. The experiment has raised some important points that must be considered if this method is to be implemented for Pd clusters. These points are discussed in the following paragraphs.

Clear errors have been demonstrated between the expected correlation between single Pd atom intensity and size selected cluster. Each possibility for error in this experiment

must be considered. Starting at the root of the experiment, one must decide if there are errors within the sample preparation. In this case the largest source of error is within the mass resolution of the time of flight mass spectrometer. However, the mass resolution of the cluster source was verified during sample production by recording a mass spectrum and is therefore unlikely to be so large as to effect these results. Also it is the case that the diameter measurements of size-selected cluster Pd$_{887}$ are consistent across all samples, indicating that a large error in N for clusters studied in this experiment is not valid. Hence, it is believed that the error must arise through the measurements taken rather than being inherent in sample preparation. It is mentioned previously how background subtraction is the largest source of error when taking HAADF intensity measurements. For size-selected clusters the background intensity contributes a small percentage to that of the overall integrated intensity measurement from the cluster as a whole. However, for single atom measurements there will exist an intrinsic error because the background contribution is proportionally larger (consistently above 100%) in comparison to the integrated intensity of the single atom itself. Thus, assuming a constant background for single atoms may not be appropriate and a more intuitive method may be required to be developed. One could also see how it could be easily possible to identify as single atoms within a HAADF-STEM micrograph features that could in reality consist of two atoms stacked together, hence giving a much larger spread in recorded data values effecting the average single atom intensity result. However, should this have been the case two well defined peaks would have been expected within the plot shown in Figure 7.14 (b).

As well as errors in measurement technique, one must consider the errors arising from the microscope itself. It is stated in the introduction section of this chapter that some criteria must be met in order to achieve accurate quantitative analysis of C$_s$ corrected HAADF-STEM micrographs and it may be the case that this experiment fell short of these requirements. Taking the electron probe for example, it is possible that the probe shape was not completely constant throughout the experiment leading to a false projection of single atom perimeters. During imaging consistent manual adjustment of the low order astigmatism is required throughout the imaging period, and, as this is a manual process, by its nature there may have been human error inherent in it. This has the consequence that the probe size may not always have been optimised, leading to a convolution effect of the probe and single Pd atoms, thus affecting their projection

within the micrographs. Although these probe effects do not alter the scattered intensity detected from a single atom, they do affect the projected area of the atoms. Thus the value for the background may be over estimated. Although every effort was made to minimise these effects it is possible that some may have occurred and thus affected the outcome of this experiment. It is also stated within the criteria that there must be no probe movement during the scan. This criteria may be broken in a reverse manner through the movement of single atoms under the electron probe, giving the same effect as a jittering probe position. If the single atom were to move in a direction along the scan line of the probe during imaging, quicker than the movement of the probe, it is easy to see how the scattered intensity from that atom will be different than if it were at rest, as the atom may appear to be scanned a number of times along the path of the probe, or indeed less than a single time if the atom movement is in the opposite direction to the scan.

When studying the results of the column mapping experiment it is thought that the error in background subtraction technique for single atoms caused results that differ from those expected. The fact that not all of the cluster could be measured due to many atoms close to the cluster perimeter not being clear within the columnar arrangement. This could be attributed to the movement of atoms near the cluster edges, where atoms are less tightly bound (less nearest neighbours). This movement inhibits the ability to resolve the positions of the atoms in the micrograph and thus the image appears fuzzy at cluster edges. Also the intensity between the columns, perhaps arising from the probe tail [183], was not accounted for, thus affecting the accuracy of the results. This experiment has demonstrated some of the difficulties arising in atomic column depth quantification and single atom detection. Quantification of these errors or their removal will assist detailed structural characterisation at the atomic scale. Comparison of experimental data to simulated Z-contrast images for the exact cluster structure under investigation would greatly assist in the estimation of error sizes from the experimental data. Atomic depth determination is seen as a promising method judging from studies within the literature for Au, however, this experiment has highlighted its complex nature with regards to Pd within this particular experimental set up. The atomic number of Pd makes single atom detection more difficult in comparison to Au (Z = 46 and 79 respectively) as the Z-contrast intensity for Au is much higher than that of Pd. The

application of appropriate filters to HAADF-STEM micrographs via FFT may allow the reduction of beam convolution effects and more accurate single atom position location and intensity measurements [183].

The nature of three dimensional quantification of atoms and atomic columns has been shown to be complex with regards to sources of potential errors in measurement and analysis. This experiment has aided the understanding of the errors and the technique for future experiments. Finding the solution of these issues for this type of experiment could lead to an even deeper understanding of supported cluster structure and maybe crucial in the understanding of catalytic mechanisms. This experiment has also highlighted the difficulty in structural control of clusters of a very narrow size range, it has, however, shown that polyhedral morphologies can be retained through soft landing upon an a-C substrate.

Chapter 8

Conclusions and Outlook

8.1 Conclusions

The main theme of the work described in this thesis has been the study of supported Pd nanostructures via scanning transmission electron microscopy (STEM). The ability to mass select Pd clusters in terms of the number of atoms has provided unique opportunities to develop the fundamental understanding of cluster deposition and nanostructure characterisation. Mass selected clusters have been shown to be ideal candidates for use as mass standards in the development of nanometrology techniques for the characterisation of commercial catalytic samples. They have also proven to be valuable tools for detailed study of the atomic structure of clusters by providing a unique opportunity to allow the comparison of experimental and theoretical results. This study has considered such techniques in detail and has also presented insight into the current output of the Birmingham Cluster source for Pd, under the experimental conditions used, highlighting unique size dependent structural features and providing an excellent framework for future studies to be built upon.

The concept of cluster structure determining function has arisen on many occasions throughout this thesis, especially for cluster applications within the field of catalysis. It has also long been known that the nature of HAADF-STEM makes it a desirable method for the imaging of small nanostructures such as clusters. With these two points in mind an experiment was designed to characterise the unknown size and structure

of industrial Pd catalyst particles, offering insight via quantification of HAADF-STEM micrographs and comparison to simple structural models. The use of size selection for Pd clusters has made the understanding and quantification of HAADF-STEM imaging possible as the scattered electrons at high angles may be directly compared to the number of atoms contained within a Pd cluster. The nanoscale structures produced, for the size range of clusters investigated, are devoid of long range crystallographic symmetry and appear "thin" to the incoming electrons. Thus, these clusters made quantification possible by minimising issues surrounding the quantification of HAADF-STEM micrographs such as electron channeling and thickness attenuation. For the case of the Tecnai F20 microscope, imaging parameters were tuned to enable the relationship of integrated HAADF intensity analysis of size selected Pd clusters and N. This was then implemented, with a calibration factor (Pd_{887}), to determine the morphology of commercial Pd catalyst particles provided by Johnson Matthey plc and can be found in Chapter 5 of this thesis. A monatomic relationship was found between cluster size, N, and integrated intensity for Pd clusters up to 5000 atoms. The morphology of catalyst particles was found to be hemispherical in nature via diameter and integrated intensity measurement. The success of this method lies with its efficiency and the speed with which a catalytic sample can be characterised for any element, provided the imaging parameters are accounted for and the mass standard relationship in place. The method may be of great use within the commercial sector to evaluate catalytic particles at each stage of design, production and use.

The high resolution of the mass selection in Pd clusters enabled mass spectrometry measurements to be made with accuracy and allowed cluster size to be determined independent of cluster or particle morphology. HAADF-STEM investigation was able to verify the mass selection, confirming that the cluster structures were a result of gas-phase growth rather than post-depositon surface diffusion and coalescence processes. This in turn allowed key structural features of size selected Pd clusters to be identified for specific cluster masses. The morphology of Pd clusters formed via gas-condensation was shown to be unambiguously size-dependent, with the onset of oblate and elongated clusters found to occur at a size of N $\approx$ 2000. The formation mechanism for the Pd clusters is a competition between the rate of solid state diffusion processes and the time interval between cluster seed impacts. It is envisaged, therefore, that one may select

not only the cluster size but also the cluster shape via the tuning of kinetic parameters, such as temperature, carrier gas pressure and cluster flight time.

HAADF-STEM investigation also revealed further size dependent features of Pd size selected clusters. A dip in intensity of circular projection was observed to be positioned within clusters with 2622 atoms and above. Investigation using energy dispersive X-ray analysis confirmed the presence of Pd and O constituents within the clusters. The intensity dip was identified as a void within the mass of the clusters formed by the mis-match of diffusion coefficients of the Pd an O species within the cluster. A void is formed via vacancy exchange through what is known as the Kirkendall effect, this effect has not yet been mentioned within the literature for the case of Pd. The Z-contrast nature of HAADF-STEM imaging makes this an ideal method to reveal such structural features.

All size-selected Pd clusters were soft landed upon a-C surfaces for experiments presented within this thesis. Evidence of retention of gas-phase morphology was presented in Chapter 5 whereby clusters with circular projection under HAADF-STEM analysis were found to be a good fit to the spherical cluster approximation. This indicated that, under low-energy deposition, a quasi-spherical morphology was retained and minimal deformation upon impact with the substrate surface occurred. Further to this the elongated morphologies were verified to be of consistent size selected mass within Chapter 6. Backed by this evidence, the structure of size selected cluster Pd_{887} was analysed with the confidence that the structural features had not been modified greatly through interaction with the substrate.

It is apparent from the literature surrounding the structural characterisation of supported clusters that a gap exists between theory and experiment. A better understanding of supported nanostructures is essential to their advancement into practical applications. Using aberration corrected HAADF-STEM and cluster size selection, a viable method of structural characterisation via comparison between experimental and simulated cluster images has been employed for supported cluster Pd_{887}. A detailed HAADF-STEM investigation into the structure of supported Pd_{887} clusters has been compared with simulated HAADF-STEM images of clusters, within a similar size range of well known structural motifs simulated using global minimum techniques. Using this method structures have been identified within the Pd_{887} sample to be of either icosohedral, truncated octahedral,

cub-octahedral or Marks decahedral morphology. Many clusters within the range were found to be structurally unclassifiable, however, the nature of the system itself provides significant challenges in detailed structural identification. Therefore, the clusters that could not be structurally identified have been discussed in detail with regards to the methods developed within this thesis for the experimental characterisation of supported Pd clusters. The feasibility of single atom detection using C_s corrected STEM, and its uses to quantify the depth of atomic columns within Pd_{887} clusters, has been studied with the aim of extracting the maximum information possible from any cluster under investigation. Experimental problems have been addressed when accurately comparing the scattered intensity from an atomic column to that of a single atom. Difficulties arise from the accurate background subtraction of single atom intensities, and the ability to image an entire cluster that shows good consistent alignment under the electron beam. This particular study has shown some of the issues surrounding three dimensional atomic positioning using HAADF-STEM and serves as suggestions for future experiments of this type.

The use of both STEM and aberration corrected STEM in this study allowed detailed characterisation of clusters that may be used to interpret their potential use for application. Studies have shown that this method of incoherent imaging allows a variety of different structural analysis to be performed: from broad brush techniques characterising catalyst particles using mass standards, to the detailed identification of structural features present in clusters. This analysis further develops our fundamental understanding of cluster formation and may allow the structural tuning of the cluster formation process. Also the improved spatial resolution of C_s corrected STEM, and cluster mass selection capabilities have shown how it is possible to bridge the gap between theory and experiment, by direct comparison of proposed structural motifs for any particular size of cluster with atomic resolution images. It has been shown that the improved spatial resolution of aberration correction in STEM can provide detailed structural information of great value to the community by identifying atomic column arrangements. With the ability to control cluster size and shape, and perform detailed structural characterisation, advancements can be made in the applications and use of nanostructures in real world scenarios, such as catalysis.

8.2   Future Work

The implementation of the nanometrology method for structure and size characterisation of commercial catalyst samples within industry would be a desirable long term outcome from this work. The efficiency of this technique may make it possible to perform structural evaluation at different stages of the catalyst life cycle, thus providing important feedback to the commercial designer. The technique could also be widened to other catalytic elements, and also perhaps to span a wider or more specific size range. The versatility of this method allows such flexibility for future studies. The ability to image catalytic particles with atomic structural detail using C_s corrected STEM may allow the identification of structural features responsible for particular catalytic functions. It would be of great interest to perform in-situ studies of catalyst particles, both before and after reaction, using HAADF-STEM as a tool for both elemental and structural characterisation.

The current set up of the Birmingham cluster source is highly desirable and flexible, allowing the design of experiments to be tailored for specific needs, such as those presented within this thesis. Whether it be size selection, varying the element to be investigated, or the energetics of deposition, all such variables can be accounted for in experimental design. It has been found though, that control of cluster morphology for Pd clusters in excess of 2000 atoms is difficult to establish, creating oblate and elongated shape deviation from the predicted lowest energy gas-phase structures. The mass selection, however, was retained, as verified by HAADF-STEM analysis. It has been found that the source operating parameters are very sensitive to the structural cluster formations produced, and a detailed future experiment should follow with regards to this, as control over cluster size and structure may lead to useful design of application specific nanostructures. Chapter 6 discussed the specific features identified within this study, offering insight into the literature regarding cluster formation and proposed mechanisms for the Pd size selected clusters under investigation. The adjustment of a single variable within the cluster source during cluster creation often has a domino effect on other variables that is not linear in nature. For example, it has been discussed how alteration of the Ar gas flow rate would effect cluster formation, but in turn, this would effect the pressure within the formation chamber and may lead to the loss of beam current for the selected

cluster size. It is not always predictable how one adjustment may alter another two or three steps down the line, as there are many factors to consider. It is proposed that the most efficient way to investigate the formation of specific structures at any size is to allow the adjustment of the distance within the formation chamber within which the clusters form. In effect this would enable the time taken to reach equilibrium morphology to be studied for any element of any size, whilst allowing other parameters to be kept constant. This requires re-engineering of the current system, but doing so would provide a large step towards structural control of clusters.

Concerning the formation of voids within the size selected Pd clusters: there is a need to establish more specific details of this structural feature. Experiments can be designed to determine, 1) the onset of the Kirkendall effect by controlled cluster exposure to oxygen for a single sized cluster, 2) the size specific onset of the Kirkendall effect through exposure to oxygen at the same level for a wider range of Pd cluster sizes, 3) EELS mapping using the C_s corrected Jeol 2100F STEM could perhaps offer a more detailed insight into the chemical make up of the Pd clusters than the EDX experiment presented within this thesis. This technique was attempted in experiments for this thesis but was not successful due to sample drift. With regards to the first of the three suggested experiments, it is of interest to note if these features form within the cluster source due to oxygen exposure. This could be determined by the incorporation of a vacuum transportation system from the source to the microscope. This would avoid the potential contamination of Pd clusters by oxygen in the atmosphere and would reveal if any residual O were present in the formation chamber of the cluster source. If this were the case then it maybe possible to control the O level, and hence gain a level structural control. Modification of the microscope column would be required for this experiment to be possible. This could be incorporated into the experiment proposed in the paragraph above designed to develop control over nanostructure growth.

The principle difficulties arising from the structural identification of Pd_{887} clusters arose from the mass resolution of the cluster source. Small variations in the cluster size may lead to different structural forms being adopted by the clusters in question. An improvement of the mass resolution will therefore enable even greater control over structural features seen within clusters of a certain size. The current mass resolution for samples prepared for studies presented in this thesis gives an error in N of ± 4 %, the new

cluster source currently being installed in the laboratory has a much improved mass resolution of $\pm$ 1 %. Future studies regarding the analysis of such clusters may benefit from the inclusion of more simulated structural motifs at global minimums for sizes that include the number of atoms arising from the error in mass selection. Then perhaps the slightly disordered, or asymmetrical clusters could be identified via comparison with HAADF-STEM images. The experiments highlighted some difficulties in terms of single atom detection and the use of single atom intensities for accurate comparison to column depth intensities within Pd_{887} clusters. It is thought that this method can also benefit from comparison to simulated HAADF-STEM micrographs of the experimental cluster under investigation. If the cluster structure was identified, and the microscope conditions simulated, then one could compare the simulated results to the experimental data. This would provide a good clue as to the accuracy of the experimental estimation of column depths, and indeed would reveal a third dimension (z) into the determination of its exact structural motif. In conjunction with this, the study may benefit from a detailed investigation of the experimental parameters, such as camera length, for the Jeol 2100F microscope used during imaging Pd_{887} clusters. For instance, the use of a larger camera length would reveal if any effects such as multiple-scattering were occurring within Pd_{887} clusters from the previous settings, perhaps giving a more realistic integrated intensity value and hence cluster size (N), when compared with the measured single atom intensities.

A whole range of experiments are available for design which may offer extensive advancements in cluster production for application via HAADF-STEM analysis. The aberration corrected STEM's spatial resolution and it's ability to image in Z-contrast make it an ideal candidate for the characterisation of alloyed clusters. Such clusters are of great interest as the presence of differing materials is one approach in tuning specific features for application, but this is dependent on their arrangement, and with resolution in three dimensions, and Z-contrast, HAADF-STEM could be a powerful tool in the characterisation of such materials. This could be started in this laboratory through the purchasing of a alloyed target for the cluster source, and in conjunction with the formation control experiments could provide detailed knowledge of such alloyed structures.

Bibliography

[1] J. V. Barth, G. Costantini, and K. Kern. Engineering atomic and molecular nanostructures at surfaces. *Nature*, 437(7059):671–679, 2005.

[2] D. Mijatovic, J. C. T. Eijkel, and A. van den Berg. Technologies for nanofluidic systems: top-down vs. bottom-up-a review. *Lab Chip*, 5(5):492–500, 2005.

[3] G. Binnig and H. Rohrer. Scanning tunneling microscopy. *Surf. Sci.*, 152-153(Part 1):17–26, 1985.

[4] G. Binnig, C. F. Quate, and C. Gerber. Atomic force microscope. *Phys. Rev. Lett.*, 56(9):930–933, 1986.

[5] Z. Y. Li, N. P. Young, M. Di Vece, S. Palomba, R. E. Palmer, A. L. Bleloch, B. C. Curley, R. L. Johnston, J. Jiang, and J. Yuan. Three-dimensional atomic-scale structure of size-selected gold nanoclusters. *Nature*, 451(7174):46–48, 2008.

[6] N. P. Young. *A Quantitative Electron Microscopy Study of Supported Atomic NanoClusters*. PhD thesis, The University of Birmingham, August 2007.

[7] H. J. Freund. Model studies on heterogeneous catalysts at the atomic level. *Catal. Today*, 100(1-2):3–9, 2005.

[8] A. W. Castleman and P. Jena. Clusters: A bridge between disciplines. *Proc. Nat. Acad. Sci.*, 103(28):10552–10553, July 2006.

[9] J. A. Collins, C. Xirouchaki, R. E. Palmer, J. K. Heath, and C. H. Jones. Clusters for biology: immobilization of proteins by size-selected metal clusters. *App. Surf. Sci.*, 226(1-3):197–208, 2004.

[10] M. Salerno. Plasmon polaritons in metal nanostructures: the opto-electronic rout to nanotechnology. *Opto Elec. Rev.*, 10(3):217–224, 2002.

[11] B. Hvolbæk, T. V. W. Janssens, B. S. Clausen, H. Falsig, C. H. Christensen, and J. K. Nørskov. Catalytic activity of gold nanoparticles. *Nano Today*, 2(4):14–18, 2007.

[12] D. B. Williams and C. B. Carter. *Transmission Electron Microscopy*. Plenum Press, 1996.

[13] A. R. Tao, S. Habas, and P. Yang. Shape control of colloidal metal nanocrystals. *Small*, 4:310–325, 2008.

[14] F. Baletto and R. Ferrando. Structural properties of nanoclusters: Energetic, thermodynamic, and kinetic effects. *Rev. Mod. Phys.*, 77(1):371–423, 2005.

[15] R. Ferrando, J. Jellinek, and R. L. Johnston. Nanoalloys: from theory to applications of alloy clusters and nanoparticles. *Chem. Rev.*, 108(3):846–910, 2008.

[16] J. P. K. Doye and D. J. Wales. Magic numbers and growth sequences of small face-centered-cubic and decahedral clusters. *Chem. Phys. Lett.*, 247(4-6):339–347, 1995.

[17] I. Robinson. Coherent diffraction: Giant molecules or tiny crystals? *Nat. Mater.*, 7(4):275–276, 2008.

[18] L. D. Marks. Experimental studies of small particle structures. *Rep. Prog. Phys.*, 57:603–649, 1994.

[19] A. G. Zacarias, M. Castro, J. M. Tour, and J. M. Seminario. Lowest energy states of small palladium clusters using density functional theory and standard ab initio methods. a route to understanding metallic nanoprobes. *Journal of Phy. Chem. A.*, 103:7692–7700, 1999.

[20] Kittel. *Introduction to Solid State Physics*. John Wiley and Sons. Inc, Toronto, 6 edition, 1986.

[21] R. L. Johnston. *Atomic and Molecular Clusters*. Taylor and Francis, London, 2002.

[22] A. S. Barnard. A thermodynamic model for the shape and stability of twinned nanostructures. *J. Phys. Chem. B*, 110(48):24498–24504, 2006.

[23] C. L. Johnson, E. Snoeck, M. Ezcurdia, B. Rodriguez-Gonzalez, I. Pastoriza-Santos, L. M. Liz-Marzan, and M. J. Hytch. Effects of elastic anisotropy on strain distributions in decahedral gold nanoparticles. *Nat. Mater.*, 7(2):120–124, 2007.

[24] T. P. Martin. Shells of atoms. *Phys. Rep.*, 273(4):199–241, 1996.

[25] W. A. de Heer. The physics of simple metal clusters: experimental aspects and simple models. *Rev. Mod. Phys.*, 65(3):611–676, 1993.

[26] W. D. Knight, K. Clemenger, W. A. de Heer, A. Saunders, M. Y. Chou, and M. L. Cohen. Electronic shel structure and abundences of sodium clusters. *Phys. Rev. Lett.*, 52(24):2141, 1984.

[27] W. Zhang, Q. Ge, and L. Wang. Structure effects on the energetic, electron, and magnetic properties of palladium nanoparticles. *J. Chem. Phys.*, 118:5793–5801, 2003.

[28] N. Watari and S. Ohnishi. Atomic and electronic structures of palladium 13 and platinum 13 clusters. *Phys. Rev. B.*, 58:1665–1669, 1998.

[29] V. Kumar and Y. Kawazoe. Icosahedral growth, magnetic behavior, and absorbate-induced metal-nonmetal transition in palladium clusters. *Phys. Rev. B.*, 66:144413+, 2002.

[30] C. Barreteau, M. C. Desjonqueres, and D. Spanjaard. Theoretical study of the icosahedral to cuboctahedral structural transition in rhodium and palladium clusters. *Eur. Phys. J. D*, 11:395–402, 2000.

[31] A. P. Sutton and J. Chen. Long range finnis-sinclair potential. *Philos. Mag. Lett.*, 61:139+, 1990.

[32] F. Baletto, R. Ferrando, A. Fortunelli, F. Montalenti, and C. Mottet. Crossover among structural motifs in transition and noble-metal clusters. *Journ. Chem. Phys.*, 116(9):3856–3863, 2002.

[33] K. Michaelian, N. Rendon, and I. L. Garzon. Structure and energetics of nickel, silver, and gold nanoclusters. *Phys. Rev. B.*, 60(3):0163+, 1999.

[34] J. P. K. Doye. Identifying structural patterns in disordered metal clusters. *Phys. Rev. B.*, 68:195418+, 2003.

[35] M. R. Zachariah and M. J. Carrier. Molecular dynamics computation of gas-phase nanoparticle sintering: a comparison with phenomenological models. *J. Aerosol Sci.*, 30(9):1139–1151, 1999.

[36] M. M. Alvarez, J. T. Khoury, T. G. Schaff, M. Shafigullin, I. Vezmar, and R. L. Whetten. Critical sizes in the growth of gold clusters. *Chem. Phys. Lett.*, 266(1-2):91–98, 1997.

[37] L. D. Marks and P. M. Ajayan. Equilibrium shape of a buoyant particle. *J. Mater. Res.*, 5(7):1496–1501, 1990.

[38] P. M. Ajayan and L. D. Marks. Evidence for sinking of small particles into substrates and implications for hetrogeneous catalysis. *Nature*, 338:139–141, 1989.

[39] L. W. Mckeehan. The crystal structure of silver-palladium and silver-gold alloys. *Phys. Rev.*, 20(5):424+, 1922.

[40] R. Lamber, S. Wetjen, and N. I. Jaeger. Size dependance of the lattice parameter of small palladium particles. *Phys. Rev. B.*, 51(16):968–971.

[41] W. J. Huang, R. Sun, L. D. Tao, J. Menard, R. G. Nuzzo, and J. M. Zuo. Coordination-dependent surface atomic contraction in nanocrystals revealed by coherent diffraction. *Nat. Mater.*, 7:308, 2008.

[42] W. Qi, B. Huang, and M. Wang. Structure of unsupported small palladium nanoparticles. *Nanoscale Res. Lett.*, 4(3):269–273, 2009.

[43] R. Lamber, N. Jaeger, and G. Schulzekloff. Electron microscopy study of the interaction of nickel, palladium and platinum with carbon ii. interaction of palladium with amorphous carbon. *Surf. Sci.*, 227(1-2):15–23, 1990.

[44] K. Heinemann and H. Poppa. In-situ transmission electron microscopy evidence of lattice expansion of very small supported palladium particles. *Surf. Sci.*, 156:265–274, 1985.

[45] J. W. M. Jacobs and D. Schryvers. A high-resolution electron microscopy study of photodeposited paladium particles on tin oxide and thier oxidation in air. *J. Catal.*, 103:436–449, 1987.

[46] W. Vervisch, C. Mottet, and J. Goniakowski. Theoretical study of the atomic structure of palladium nanoclusters deposited on a magnesium oxide (100) surface. *Phys. Rev. B.*, 65(24):245411+, 2002.

[47] C. M. Wang, V. Shutthanandan, Y. Zhang, S. Thevuthasan, L. E. Thomas, W. J. Weber, and G. Duscher. Atomic level imaging of gold nanocluster dispersed in titanium oxide and strontium titanate. *Nucl. Instrum. Methods Phys. Res., Sect. B.*, 242(1-2):380–382, 2006.

[48] C. L. Kuo and P. Clancy. Melting and freezing characteristics and structural properties of supported and unsupported gold nanoclusters. *J. Phys. Chem. B.*, 109(28):13743–13754, 2005.

[49] K. Koga, T. Ikeshoji, and K. Sugawara. Size- and temperature-dependent structural transitions in gold nanoparticles. *Phys. Rev. Lett.*, 92(11):115507+, 2004.

[50] C. L. Cleveland, U. Landman, M. N. Shafigullin, P. W. Stephens, and R. L. Whetten. Structural evolution of larger gold clusters. *Zeitschrift für Phys. D*, 40(1):503–508, 1997.

[51] C. Cleveland and U. Landman. Structure of nickel clusters. *J. Chem. Phys.*, 11:7376–7396, 1991.

[52] H. Y. Jiang, W. S. Cai, and X. G. Shao. New lowest energy sequence of marks' decahedral lennard-jones clusters containing up to 10 000 atoms. *J. Phys. Chem. A.*, 107(21):4238–4243, 2003.

[53] J. Ascencio, C. Gutierrez-Wing, M. E. Espinosa, M. Marin, S. Tehuacanero, C. Zorrilla, and M. Jose-Yacaman. Structure determination of small particles by high resolution electron microscopy imaging: theory and experiment. *Surf. Sci.*, 396(1-3):349–368, 1998.

[54] M. José Yacamán, J. A. Ascencio, H. B. Liu, and J. Gardea Torresdey. Structure shape and stability of nanometric sized particles. *J. Vac. Sci. Technol., B*, 19(4):1091–1103, 2001.

[55] J. M. Soler, M. R. Beltrán, K. Michaelian, I. L. Garzón, P. Ordejón, D. S. Portal, and E. Artacho. Metallic bonding and cluster structure. *Phys. Rev. B.*, 61(8):5771–5780, 2000.

[56] S. Iijima and T. Ichihashi. Structural instability of ultrafine particles of metals. *Phys. Rev. Lett.*, 56(6):616+, 1986.

[57] P. E. Baston. Gold cluster behaviour using aberation corrected annular dark feild imaging. *Microsc. Microanal.*, 13, 2007.

[58] Y. Li and G. A. Somorjai. Nanoscale advances in catalysis and energy applications. *NanoLetters- in press.*

[59] Eric E. Finney and Richard G. Finke. Nanocluster nucleation and growth kinetic and mechanistic studies: A review emphasizing transition-metal nanoclusters. *J. Colloid Interface Sci.*, 317(2):351–374, 2008.

[60] C. B. Murray. Watching nanocrystals grow. *Science*, 324(5932):1276–1277, 2009.

[61] A. Zuttel. Materials for hydrogen storage. *Mater. Today*, 6(9):24–33, 2003.

[62] E. C. Walter, R. M. Penner, H. Liu, K. H. Ng, M. P. Zach, and F. Favier. Sensors from electrodeposited metal nanowires. *Surf. Interface Anal.*, 34(1):409–412, 2002.

[63] M. K. Starchevsky, S. L. Hladiy, Y. A. Pazdersky, M. N. Vargaftik, and I. I. Moiseev. Giant palladium-561 clusters: onset to new catalytic properties. *J. Mol. Catal. A: Chem.*, 146(1-2):229–236, 1999.

[64] T. S. Ahmadi, Z. L. Wang, T. C. Green, A. Henglein, and M. A. El-Sayed. Shape-controlled synthesis of colloidal platinum nanoparticles. *Science*, 272(5270):1924–1925, 1996.

[65] G. C. Bond. The origins of particle size effects in hetrogeneous catalysis. *Surf. Sci.*, pages 966–981, 1985.

[66] W. E. Kaden, T. Wu, W. A. Kunkel, and S. L. Anderson. Electronic structure controls reactivity of size-selected palladium clusters adsorbed on titanium oxide surfaces. *Science*, 326(5954):826–829, 2009.

[67] J. Durand, E. Teuma, and M. Gomez. An overview of paladium nanocatalysis: surface and molecular reactivity. *Eur. J. Inorg. Chem.*, 569:3577–3586, 2008.

[68] A. Gniewek, J. J. Ziolkowski, A. M. Trzeciak, and L. Kepinski. Influence of palladium colloid synthesis procedures on catalytic activity in methoxycarbonylation reaction. *J. Catal.*, 239:272–281, 2006.

[69] D. Schebarchov and S. C. Hendy. Solid-liquid phase coexistence and structural transitions in palladium clusters. *Phys. Rev. B.*, 73(12):121402+, 2006.

[70] B. von Issendorff and R. E. Palmer. A new high transmission infinite range mass selector for cluster and nanoparticle beams. *Rev. Sci. Instrum.*, 70(12):4497–4501, 1999.

[71] R. Alayan, L. Arnaud, M. Broyer, E. Cottancin, J. Lermé, J. L. Vialle, and M. Pellarin. Morphology and growth of metal clusters in the gas phase: A transition from spherical to ramified structures. *Phys. Rev. B*, 73(12), 2006.

[72] Q. Guo, P. Fallon, J. Yin, R. E. Palmer, N. Bampos, and J. K. M. Sanders. Growth of densely packed gold nanoparticles on graphite using molecular templates. *Adv. Mater.*, 15(13):1084–1087, 2003.

[73] K. Kimoto. A study of lithium clusters by means of a mass analyzer. *J. Phys. Soc. Jpn.*, 42(6):2071–2072, 1977.

[74] N. P. Young, Z. Y. Li, Y. Chen, S. Palomba, M. Di Vece, and R. E. Palmer. Weighing supported nanoparticles: Size-selected clusters as mass standards in nanometrology. *Phys. Rev. Lett.*, 101(24):246103+, 2008.

[75] J. C. Hutleen, D. A. Treichel, M. T. Smith, M. L. Duval, T. R. Jensen, and R. P. Van Duyune. Nanosphere lithography: size-tunable silver nanoparticel and surface cluster arrays. *J. Phys. Chem. B*, 103:3854–3863, 1999.

[76] J. Bosbach, D. Martin, F. Stietz, T. Wenzel, and F. Träger. Laser-induced manipulation of the size and shape of small metal particles: Towards monodisperse clusters on surfaces. *Eur. Phys. Journ. D.*, 9(1):613–617, 1999.

[77] D. Kenny. Nucleation and growth of carbon-60 thin films on graphite. *Surf. Sci.*, 447(1-3):126–132, 2000.

[78] T. K. Sau and A. L Rogach. Nonspherical noble metal nanoparticles: colloid-chemical synthesis and morphology control. *Adv. Mater.*, 22:1781–1804, 2010.

[79] P. Lu, T. Teranishi, K. Asakura, M. Miyake, and N. Toshima. Polymer-protected nickel/palladium bimetallic nano-clusters: Preparation, characterization

and catalysis for hydrogenation of nitrobenzene. *J. Phys. Chem. B.*, 103(44):9673–9682, 1999.

[80] X. M. Lin, H. M. Jaeger, C. M. Sorensen, and K. J. Klabunde. Formation of long-range-ordered nanocrystal superlattices on silicon nitride substrates. *J. Phys. Chem. B.*, 105(17):3353–3357, 2001.

[81] S. Pratontep. *Production and characterisation of size-selected nanoclusters on surfaces.* PhD thesis, The University of Birmingham, 2002.

[82] T. Bedson, R. E. Palmer, and J. P. Wilcoxon. Electron beam lithography in passivated gold nanoclusters. *Microelectron. Eng.*, 57-58, 2001.

[83] H. Xu, L. D. Menard, A. Frenkel, R. Nuzzo, D. Johnson, and J. Yang. The effect of substrates/ligands on metal nanocatalyts investigated by quantitative z-contrast imaging and high resolution electron microscopy. *Mater. Res. Soc. Symp. Proc.*, 876E, 2005.

[84] S. Link, Z. L. Wang, and M. A. El-Sayed. Alloy formation of gold-silver nanoparticles and dependence of the plasmon absorption on their composition. *J. Phys. Chem. B.*, 103:3529–3533, 1999.

[85] K. Oura, V. G. Lifshits, A. A. Saranin, A. V. Zotov, and M. Katayama. Surface science: An introduction. pages 404–408, 2003.

[86] N. P. Young, J. Palfreyman, and Z. Y. Li. Carbon 60-assisted growth of gold nanowires using a stepped graphite surface as template. *Small*, 2(1):71–74, 2006.

[87] R. A. Sperling and W. J. Parak. Surface modification, functionalization and bio-conjugation of colloidal inorganic nanoparticles. *Philos. Transac. Royal Soc. A-Math. Phys.Eng. Sci.*, 368(1915):1333–1383, 2010.

[88] H. Pauly. *Atom, molecule and cluster beams II.* Springer, Berlin, 2000.

[89] S. J. Carroll. *Deposition of size selected atomic clusters on surfaces.* PhD thesis, The University of Birmingham, June 1999.

[90] M. H. Schaffner, J. F. Jeanneret, F. Patthey, and W. D. Schneider. An ultrahigh vacuum sputter source for in situ deposition of size-selected clusters: silver on graphite. *J. Phys. D: App. Phys.*, 31(22):3177+, 1998.

[91] J. A. Alonso. *Structure and properties of atomic nanoclusters.* Imperial College Press, London, 2005.

[92] J. Bolton. *Electromagnetism.* Open University press, 2006.

[93] S. Pratontep, S. J. Carroll, C. Xirouchaki, M. Streun, and R. E. Palmer. Size-selected cluster beam source based on radio frequency mahnetron plasma sputtering and gas condensation. *Rev. Sci. Inst.*, 76:045103, 2005.

[94] P. Sigmund. Theory of sputtering. i. sputtering yield of amorphous and polycrystalline targets. *Phys. Rev. Online Arch. (Prola)*, 184(2):383–416, 1969.

[95] H. Haberland. *Clusters of atoms and molecules I.* Chemical Physics 56. Springer-Verlag, Berlin, 1994.

[96] K. Wegner, P. Piseri, H. Vahedi Tafreshi, and P. Milani. Cluster beam deposition: a tool for nanoscale science and technology. *J. Phys. D: App. Phys.*, 39(22):R439–R459, 2006.

[97] J. R. Waldram. *The theory of thermodynamics.* Cambridge University Press, 2 edition, 1987.

[98] M. Gracia-Pinilla, E. Martínez, G. Vidaurri, and E. Pérez-Tijerina. Deposition of size-selected copper nanoparticles by inert gas condensation. *Nanoscale Res. Lett.*, 5(1):180–188, 2010.

[99] K. H. Meiwes-Broer. *Metal Clusters at Surfaces.* Cluster Physics. Springer, 2000.

[100] S. Degen, C. Becker, and K. Wandelt. Thin alumina films on nickel3/aluminium alloy(111): A template for nanostructured palladium cluster growth. *Faraday. Discuss.*, 125:343–356, 2004.

[101] P. Jensen. Growth of nanostructures by cluster deposition: Experiments and simple models. *Rev. Mod. Phys.*, 71(5):1695–1735, 1999.

[102] M. Di Vece, N. P. Young, Z. Y. Li, Y. Chen, and R. E. Palmer. Co-deposition of atomic clusters of different size and composition. *Small*, 2(11):1270–1272, 2006.

[103] C. Brechignac, Ph Cahuzac, F. Carlier, M. de Frutos, A. Masson, C. Mory, C. Colliex, and B. Yoon. Size effects in nucleation and growth processes from preformed soft landed clusters. *Phys. Rev. B*, 57(4):R2084–R2087, 1998.

[104] L. Bardotti, P. Jensen, A. Horareau, M. Treilleux, B. Cabaud, A. Perez, and F. Casete Santos Aires. Diffusion and aggregation of large antimony and gold clusters deposited on graphite. *Surf. Sci.*, 367:276–292, 1996.

[105] P. Deltour, J-L. Barrat, and P. Jensen. Fast diffusion of lennard-jones cluster on crystalline surface. *Phys. Rev. Lett.*, 78(24):4597, 1997.

[106] H. Hsieh, R. S. Averback, H. Sellers, and C. P. Flynn. Molecular-dynamics simulations of collisions between energetic clusters of atoms and metal substrates. *Phys. Rev. B.*, 45(8):4417–4430, 1992.

[107] C. Xirouchaki. Pinning and implantation of size-selected metal clusters: a topical review. *Vacuum*, 66(2):167–173, 2002.

[108] S. J. Carroll, R. E. Palmer, P. A. Mulheran, S. Hobday, and R. Smith. Deposition and diffusion of size-selected (silver 400+) clusters on a stepped graphite surface. *App. Phys. A*, 67(6):613–619, 1998.

[109] M. Couillard, S. Pratontep, and R. E. Palmer. Metastable ordered arrays of size-selected silver clusters on graphite. *App. Phys. Lett.*, 82(16):2595–2597, 2003.

[110] M. Di Vece, S. Palomba, and R. E. Palmer. Pinning of size-selected gold and nickel nanoclusters on graphite. *Phys. Rev. B.*, 72(7), 2005.

[111] M. Couillard. *Electron Microscopy of Nanostructures resulting from the Deposition of Size-Selected metal Clusters*. PhD thesis, The University of Birmingham, 2002.

[112] E. Ruska. The development of the electron microscope and electron microscopy. *www.nobelprize.org/nobel_prizes/physics/laureates/1986/ruska-lecture*, December 1986.

[113] Y. Kotaka. Essential experimental parameters for quantitative structure analysis using spherical aberration-corrected high angle annular dark field transmission electron microscopy. *Ultramicros.*, 110(5):555–562, 2010.

[114] N. L. Okamoto, S. Mehraeen, A. Kulkarni, S. Nemana, B. C. Gates, and N. D. Browning. Determination of nanocluster size distributions from high angle annular dark field scanning transmission electron microscopy images. *Micros. Microanal.*, 13(Supplement S02):546–547, 2007.

[115] S. J. Pennycook and D. E. Jesson. High-resolution z-contrast imaging of crystals. *Ultramicros.*, 37(1-4):14–38, 1991.

[116] M. T. Otten. High-angle annular dark-field imaging on a scanning/transmission electron microscope system. *J. Electron Microsc. Tech.*, 17(2):221–230, 1991.

[117] P. J. Goodhew and F. J. Humphreys. *Electron Microscopy and Analysis*. Taylor and Francis, 2 edition, 1992.

[118] X. F. Zhang and Z. Zhange. *Progress in transmission elecron microscopy 1 : concepts and techniques*. Surface Science. Springer, 1999.

[119] L. Reimer and H. Kohl. *Transmission Electron Microscopy: Physics of Image Formation*. Optical Sciences. Springer, 5 edition, 2008.

[120] Z. L. Wang. *Characterization of Nanophase Materials*. Wiley - VCH, 2000.

[121] O. Scherzer. The theoretical resolution limit of the electron microscope. *J. App. Phys.*, 20:20, 1949.

[122] J. Liu. *Characterization of Nanophase Materials*. Wiley, 2000.

[123] S. C. Anderson, C. R. Birkland, G. R. Anstis, and D. J. H. Cockayne. An approach to quantitative compositional profiling at near-atomic resolution using high-angle annular dark field imaging. *Ultramicroscopy*, 69:83+, 1997.

[124] S. J. Pennycook. *Scanning Microscopy for Nanotechnology*. Springer, 2007.

[125] M. Haider, H. Rose, S. Uhlemann, E. Schwan, B. Kabius, and K. Urban. A spherical aberration corrected 200kv transmission electron microscope. *Ultramicro.*, 75:53–60, 1998.

[126] C. Hetherington. Aberration correction for transmission electron microscopy. *Mater. Today*, 7(12):50–55, 2004.

[127] F. Zemlin. Practical procedure for alignment of a high-resolution electron microscope. *Ultramicros.*, 4:241+, 1979.

[128] M. Chu. Analytical tranmission electron microscopy of materials using a large area silicone drift energy-dispersive x-ray spectroscopy detector. *Micros. Anal. Nanotechnol. Supp.*, (137):11–14, 2010.

[129] M. M. J. Treacy and S. B. Rice. Catalyst particle sizes from rutherford scattered intensities. *J. Micros.*, 156:211–234, 1989.

[130] Q. Ramasse and A. Bleloch. Diagnosis of aberrations from crystalline samples in scanning transmission electron microscopy. *Ultramicros.*, 106(1):37–56, 2005.

[131] Rodenburg. http://www.rodenburg.org/stem/t200.html, July 2010.

[132] Z. Wang, Z. Y. Li, A. Abdela, S. J. Park, D. Tang, and R. E. Palmer. Quantitative z-contrast imaging in scanning transmission elecron microscopy with size-selected clusters. *Phys. Rev. Lett. submitted to*, May 2010.

[133] J. M. LeBeau, S. D. Findlay, L. J. Allen, and S. Stemmer. Quantitative atomic resolution scanning transmission electron microscopy. *Phys. Rev. Lett.*, 100(20):206101+, 2008.

[134] C. Langlois, Z. W. Wang, D. Pearmain, C. Ricolleau, and Z. Y. Li. High angle annular dark field scanning transmission electron microscopy imaging of copper/silver core-shell nanoparticles. *J. Phys. Conf. Ser.*, 241:012043+, 2010.

[135] ImageJ. *URL: http://rsb.info.nih.gov/ij/docs/index.html*, Sept 2008.

[136] Digital Micrograph. *http://www.gatan.com/imaging/dig_micrograph.php, Sept* 2010.

[137] A. Korolev and G. Isaac. Roundness and aspect ratio of particles in ice clouds. *J. Atmos. Sci.*, 60:1795–1808, 2003.

[138] P. Bele, H. Uchida, K. Okaya, H. Yano, U. Stimming, and M. Watanabe. Transmission electron microscopy of monodisperse platinum2 ruthenium3/cobalt catalysts synthesized by the nanocapsule method. *Microsc. Anal.*, 24(4):5–7, 2010.

[139] L. Lyons. *A Practical Guide to Data Analysis for Physical Science Students.* Cambridge University Press, 1991.

[140] C. Henry. Catalytic activity of supported nanometer-sized metal clusters. *App. Surf. Sci.*, 164(1-4):252–259, 2000.

[141] G. A. Somorjai and J. Y. Park. Colloid science of metal nanoparticle catalysts in 2d and 3d structures. challenges of nucleation, growth, composition, particle shape, size control and their influence on activity and selectivity. *Top. Catal.*, 49:126–135, 2008.

[142] M. Haruta. Gold as a novel catalyst in the 21st century: preparation, working mechanism and applications. *Gold Bull.*, 37:27–37, 2004.

[143] R. Narayanan and M. A. El-Sayed. Catalysis with transition metal nanoparticels in colloidal solution: Nanoparticle shape dependance and stability. *J. Phys. Chem. B.*, 109:12663–12676, 2005.

[144] F. Studt, F. Abild-Pedersen, T. Bligaard, R. Z. Sorensen, C. H. Christensen, and J. K. Norskov. Identification of non-precious metal alloy catalysts for selective hydrogenation of acetylene. *Science*, 320:1320+, 2008.

[145] J. K. Norskov and C. H. Christensen. Toward efficient hydrogen production at surfaces. *Science*, 312:1322–1323, 2006.

[146] J. Zhu and M. Zach. Nanostructured materials for photocatalytic hydrogen production. *C.O.C.I.S*, 14:260–269, 2009.

[147] V. W. Janssens, A. Carlsson, A. Puig-Molina, and B. S. Clausen. Relation between nanoscale gold particle structure and activity for carbon monoxide oxidation on supported gold catalysts. *J. Catal.*, 240:108–113, 2006.

[148] J. Chen, Q. Zhang, Y. Wang, and H. Wan. Size-dependant catalytic activity of supported palladium nanoparticles for aerobic oxidation of alcohols. *Adv. Synth. Catal.*, 350:453–464, 2008.

[149] L. Piccolo, A. Valcarcel, M. Bausach, C. Thomazeau, D. Uzio, and G. Berhault. Tuning the shape of nanoparticles to control their catalytic properties: selective hydrogenation of 1,3-butadiene on palladium/aliminuim oxide. *Phys. Chem. Chem. Phys.*, 10(36):5504–5506, 2008.

[150] J. C. Yang, S. Bradley, and J. M. Gibson. The oblate morphology of supported platinum/ruthenium-5 on carbon black. *Mater. Charac.*, 51:101–107, 2003.

[151] M. M. J. Treacy, A. Howie, and C. J. Wilson. Z-contrast of platinum and palladium catalysts. *Philos. Mag.*, 38(5):569–585, 1978.

[152] Z. Y. Li, J. Yuan, Y. Chen, R. E. Palmer, and J. P. Wilcoxon. Direct imaging of core-shell structure in silver-gold bimetallic nanoparticles. *App. Phys. Lett.*, 87(24):243103+, 2005.

[153] P. A. Midgley, M. Weyland, J. M. Thomas, and B. F. G. Johnson. Z-contrast tomography: a technique in three-dimensional nanostructural analysis based on rutherford scattering. *Chem. Commun.*, (10):907–908, 2001.

[154] Z. Y. Li, J. P. Wilcoxon, F. Yin, Y. Chen, R. E. Palmer, and R. L. Johnston. Structures and optical properties of 4-5 nm bimetallic silver/gold nanoparticles. *Faraday Discuss.*, 138:363–373, 2008.

[155] S. J. L. Billinge and I. Levin. The problem with determining atomic structure at the nanoscale. *Science*, 316(5824):561–565, 2007.

[156] L. C. Gontard, R. E. Dunin-Borkowski, M. H. Gass, A. L. Bleloch, and D. Ozkaya. Three-dimensional shapes and structures of lamellar-twinned fcc nanoparticles using annular dark field scanning transmission electron microscopy. *J. Electron Microsc. (Tokyo)*, 58(3):167–174, 2009.

[157] M. Weyland, P. A. Midgley, and J. M. Thomas. Electron tomography of nanoparticle catalysts on porous supports: A new technique based on rutherford scattering. *J. Phys. Chem. B.*, 105(33):7882–7886, 2001.

[158] S. Mehraeen, N. L. Okamoto, D. G. Morgan, S. Nemana, B. C. Gates, H. Stahlberg, and N. D. Browning. Z-contrast tomography of nanoscale heterogeneous catalysts. *Microsc. Microanal.*, 13(Supplement S02):1326–1327, 2007.

[159] S. Benlekbir, T. Epicier, M. Bausach, M. Aouine, and G. Berhault. Scanning tansmission electron microscopy high angle annular dark field electron tomography of palladium nanoparticles with complex shapes. *Phil. Mag. Lett.*, 89(2):145–153, 2009.

[160] L. C. Gontard, L. Y. Chang, C. J. D. Hetherington, A. I. Kirkland, D. Ozkaya, and R. E. Dunin-Borkowski. Aberration-corrected imaging of active sites on industrial catalyst nanoparticles. *Angew. Chem. Int. Ed.*, 46(20):3683–3685, 2007.

[161] Z. W. Wang, O. Toikkanen, F. Yin, Z. Y. Li, B. M. Quinn, and R. E. Palmer. Counting the atoms in supported, monolayer protected gold clusters. *J.A.C.S*, 132:2854–2855, 2010.

[162] H. W. King. *Crystal Structures and Lattice Parameters of Allotropes of the Elements*. CRC, 89 edition, 2009.

[163] Y. Li, E. Boone, and M. A. El-Sayed. Size effects of pvp palladium nanoparticles on the catalytic suzuki reactions in aqueous solution. *Langmuir*, 18(12):4921–4925, 2002.

[164] M. Boudart and G. Djega-Mariadassou. *Kinetics of Heterogeneous Catalytic Reactions*. Princeton University Press, Princeton, NJ, 1984.

[165] B. C. Gates. *Catalytic Chemisrty*. Wiley, 1992.

[166] Y. Xiong and Y. Xia. Shape-controlled synthesis of metal nanostructures: the case of palladium. *Adv. Mater.*, 19:3385–3391, 2007.

[167] J. Watt, N. Young, S. Haigh, A. Kirkland, and R. D. Tilley. Synthesis and structural characterization of branched palladium nanostructures. *Adv. Mater.*, 21:2288–2293, 2009.

[168] S. Gibilisco, M. Di Vece, S. Palomba, G. Faraci, and R. E. Palmer. Pinning of size-selected palladium nanoclusters on graphite. *J. Chem. Phys.*, 125(8):084704+, 2006.

[169] S. Arcidiacono, N. R. Bieri, D. Poulikakos, and C. P. Grigoropoulos. On the coalescence of gold nanoparticles. *Int. Journ. of Multiphase Flow*, 30:979–994, 2004.

[170] A. Lando, N. Kebaili, Ph Cahuzac, C. Colliex, M. Couillard, A. Masson, M. Schmidt, and C. Brechignac. Chemically induced morphology change in cluster-based nanostructures. *Eur. Phys. J. D.*, 43:151–154, 2007.

[171] D. L. Olynick, J. M. Gibson, and R. S. Averback. Impurity-suppressed sintering in copper nanophase materials. *Philos. Mag. A.*, 77(5):1205–1221, 1998.

[172] S. Stappert, B. Rellinghaus, M. Acet, and E. F. Wassermann. Oxygen-mediated suppressoin of twinning in gas-phase prepared iron/platinum nanoparticles. *Eur. Phys. J. D.*, 24:351–354, 2003.

[173] E. Perez-Tijerina, M. G. Pinilla, S. Mejia-Rosales, U. Ortiz-Mendez, A. Torres, and M. Jose-Yacaman. Highly size-controlled synthesis of gold/palladium nanoparticles by inert-gas condensation. *Faraday Discuss.*, 138:353–362, 2008.

[174] K. An and T. Hyeon. Synthesis and biomedical applications of hollow nanostructures. *Nano Today*, 4(4):359–373, 2009.

[175] R. Nakamura, D. Tokozakura, H. Nakajima, J. G. Lee, and H. Mori. Hollow oxide formation by oxidation of aluminium and copper nanoparticles. *Journ. App. Phys.*, 101(7):074303+, 2007.

[176] P. I. Gaiduk, J. L. Hansen, and A. N. Larsen. Synthesis and analysis of hollow tin oxide nanoislands. *App. Phys. Lett.*, 92:193112+, 2008.

[177] C. M. Wang, D. R. Baer, L. E. Thomas, J. E. Amonette, Jiji Antony, You Qiang, and G. Duscher. Void formation during early stages of passivation: Initial oxidation of iron nanoparticles at room temperature. *J. App. Phys.*, 98(9):094308+, 2005.

[178] K. Stevens, B. Ingham, M. Toney, S. Brown, and A. Lassesson. Structure of palladium nanoclusters for hydrogen gas sensors. *Curr. App. Phys.*, 8(3-4):443–446, 2008.

[179] Y. Yin, R. M. Rioux, C. K. Erdonmez, S. Hughes, G. A. Somorjai, and A. P. Alivisatos. Formation of hollow nanocrystals through the nanoscale kirkendall effect. *Science*, 304(5671):711–714, 2004.

[180] D. Schebarchov, S. C. Hendy, and W. Polak. Molecular dynamics study of the melting of a supported 887-atom palladium decahedron. *J. Phys. Conden. Matt.*, 21:144204+, 2009.

[181] A. Flores, L. A. Robles, M. O. Arias, and J. A. Ascencio. Small metal nanoparticle recognition using digital image analysis and high resolution electron microscopy. *Micron*, 34(2):109–118, 2003.

[182] M. José-Yacamán, M. Marin-Almazo, and J. A. Ascencio. High resolution transmission electron microscopy studies on palladium nanoparticles. *J. Molec. Catal. A: Chem.*, 173(1-2):61–74, 2001.

[183] O. L. Krivanek, M. F. Chisholm, V. Nicolosi, T. J. Pennycook, G. J. Corbin, N. Dellby, M. F. Murfitt, C. S. Own, Z. S. Szilagyi, M. P. Oxley, S. T. Pantelides, and S. J. Pennycook. Atom-by-atom structural and chemical analysis by annular dark-field electron microscopy. *Nature*, 464:571–574, 2010.

[184] O. L. Kirvanek, N. Dellby, M. F. Murfitt, M. F. Chisholm, T. J. Pennycook, K. Suenaga, and M. F. Nicolosi. Gentle scanning transmission electron microscopy: Annular dark field imaging and electron energy loss spectroscopy at low primary energies. *Ultramicros.*, in press, 2010.

[185] R. P. Gupta. Lattice relaxation at a metal surface. *Phys. Rev. B.*, 23(12):6265–6270, 1981.

[186] D. He. Aberration corrected scanning transmission electron microscopy of size selected gold clusters and gold/platinum nanorods. Master's thesis, The University of Birmingham, 2010 to be submitted.

[187] K. van Benthem, Y. Peng, and S. J. Pennycook. Tomographic imaging of nanocrystals by aberration corrected scanning transmission electron microscopy. *Mater. Res. Soc. Symp. Proc.*, 839, 2005.